

**Differential Top Pair Production Cross-Section  
Measurements at  $\sqrt{s} = 7$  TeV with the ATLAS  
Detector at the LHC**

**THÈSE**

présentée à la Faculté des sciences de l'Université de Genève  
pour obtenir le grade de Docteur ès sciences, mention physique

par

**Ian James Watson**

*Australie*

Thèse N° 4697



**UNIVERSITÉ  
DE GENÈVE**

FACULTÉ DES SCIENCES

**Doctorat ès sciences  
Mention physique**

Thèse de *Monsieur Ian James WATSON*

intitulée :

**"Differential Top Pair Production Cross-Section Measurements  
at  $\sqrt{s} = 7$  TeV with the ATLAS Detector at the LHC"**

La Faculté des sciences, sur le préavis de Monsieur A. CLARK, professeur honoraire et directeur de thèse (Département de physique nucléaire et corpusculaire), Monsieur X. WU, professeur associé et codirecteur de thèse (Département de physique nucléaire et corpusculaire), Monsieur M. NESSI, suppléant professeur titulaire (Département de physique nucléaire et corpusculaire), Monsieur G. TAYLOR, professeur (School of Physics, University of Melbourne, Australia) et Monsieur T. CARLI, docteur (Département de physique, CERN – Organisation Européenne pour la Recherche Nucléaire, Genève, Suisse) autorise l'impression de la présente thèse, sans exprimer d'opinion sur les propositions qui y sont énoncées.

Genève, le 16 juillet 2014

Thèse - 4697 -

Le D<sup>é</sup>canat

N.B. - La thèse doit porter la déclaration précédente et remplir les conditions énumérées dans les "Informations relatives aux thèses de doctorat à l'Université de Genève".





# Abstract

The top quark is the most massive fundamental particle of the Standard Model of particle physics, and as the only quark to decay before hadronising gives a unique opportunity for studying QCD, the theory of the strong interaction. In this thesis, we study the  $t\bar{t}$  production cross-section as a function of several variables related to the produced top quarks. This thesis presents variables defined after the hadronisation of the top quark, and so are mostly independent of its theoretical description, unlike previous results which are corrected to the partonic variables. Using the ATLAS detector at the LHC, the measurements are performed for  $\sqrt{s} = 7$  TeV proton–proton collisions. The measurements are sensitive to various parameters entering the description of top quark production, including the Parton Distribution Functions, and so have good potential to be used in furthering our understanding of proton collision physics and for future tunings of the models used in describing the physics.

## Résumé

Le quark top, ou t-quark, est la particule la plus lourde du « Modèle Standard » de la physique des particules fondamentales, et, étant le seul quark qui désintègre avant d'hadroniser, ce quark nous présente une opportunité singulière d'étudier le QCD, la théorie de l'interaction forte. Dans cette thèse nous étudions la dépendance de la section efficace pour la production des paires sur certaines variables cinématique associés avec le t-quark ou les paires.

Au lieu de transformer les mesures expérimentales en utilisant un modèle (ou plusieurs modèles), cette thèse présente la définition d'une variable « pseudo-top », très corrélée avec la reconstruction du t-quark ou le paire mais reconstruite après l'hadronisation du t-quark, donc en utilisant des variables qui sont plus ou moins indépendantes de la dépendance théorique au niveau partonique.

L'analyse est réalisée avec l'expérience ATLAS au « Large Hadron Collider (LHC) » du CERN en utilisant les collisions  $pp$  avec une énergie de collision  $\sqrt{s} = 7$  TeV.

Les mesures différentielles du quantité « pseudo-top » sont sensibles aux paramètres de la production du t-quark, par exemple les distributions d'impulsion des partons dans le proton (en bref, les « parton distribution functions » ou « PDF »). Pour cette raison, les mesures permettent une comparaison avec les différents modèles QCD, donc elles peuvent améliorer notre connaissance de la production des t-quarks dans les collisions  $pp$  et de raffiner les modèles QCD dans l'avenir.

## Declaration

The work of this thesis is in many respects the culmination of decades of preparation by many thousands of physicists working on the LHC and ATLAS experiment. Chapters 2 and 3 cover an overview of the theory relevant for the thesis and experimental setup. The author was directly involved in the studies of section A.3, which documents the work of the layout task force, set to create a new design of the replacement inner detector due in 2023. It uses previous work on the Utopia layout, and handed over to simulation teams (of which the author was not a member) who obtained the results of section A.4. The analysis of chapters 5 and 6 was the author's primary focus during the course of the thesis and represents the original work done for the thesis. The author was also, in part, responsible for putting together and maintaining software related to the physics objects presented in chapter 4. This involved taking disparate recommendations provided by the top working group and random code snippets and interfaces provided by combined performance groups, and setting up a framework which takes in raw objects and corrects and scales them based on the dedicated studies of the group. The package thus presents the objects in a form suitable for performing physics analyses within the top group at ATLAS, such as the one the author performed for this thesis. The code is currently the standard code used in the ATLAS top group, and is now maintained by others.

Ian James Watson, Genève, June 2014



# Contents

<b>1. Introduction</b>	<b>3</b>
<b>2. The Top Quark in the Standard Model</b>	<b>7</b>
2.1. The Standard Model of Particle Physics	7
2.2. Pre-history of the Top Quark	14
2.2.1. The Top Quark Discovery	16
2.3. Hadron Collider Physics	18
2.4. Production of Top Quarks at Hadron Colliders	21
2.5. The decay of the top quark	24
2.6. Other Properties of the Top Quark	25
<b>3. The ATLAS Detector</b>	<b>29</b>
3.1. The LHC	29
3.2. ATLAS Overview	33
3.3. The Inner Tracking Detector	37
3.3.1. Track Reconstruction	39
3.4. The Calorimeters	41
3.5. The Muon Spectrometer	47
3.6. The Trigger System	48
3.6.1. Single Electron Trigger	50
3.6.2. Single Muon Trigger	52
<b>4. Object and Event Selection</b>	<b>55</b>
4.1. Object Reconstruction and Selection	56
4.1.1. Primary Vertex	56
4.1.2. Electrons	57
4.1.3. Muons	60
4.1.4. Jets	60
4.1.5. <i>b</i> -jet Identification	65

4.1.6. Missing Transverse Momentum . . . . .	68
4.1.7. Event-level selection . . . . .	70
4.2. Monte Carlo Simulation Samples . . . . .	72
4.2.1. Overview . . . . .	72
4.2.2. Simulated Samples . . . . .	75
4.3. Background Estimation . . . . .	79
4.3.1. Backgrounds from MC . . . . .	79
4.3.2. W+Jets Normalisation . . . . .	80
4.3.3. QCD Multijet Estimation . . . . .	84
4.3.4. Data/Monte Carlo Comparisons . . . . .	88
4.4. Particle-object selection . . . . .	89
<b>5. Pseudo-Top Definition</b>	<b>95</b>
5.1. Differential Distributions . . . . .	95
5.2. Issues with Current Top Analyses . . . . .	102
5.3. Pseudo-Top definition . . . . .	107
5.3.1. Matching . . . . .	107
5.3.2. Construction of the Pseudo-Top Observable . . . . .	109
5.3.3. Pseudo-Top Analysis Definition in Data . . . . .	122
<b>6. Differential <math>t\bar{t}</math> Cross-Section Analysis</b>	<b>129</b>
6.1. Corrections and unfolding . . . . .	129
6.1.1. Basic Cross-Section Measurement . . . . .	130
6.1.2. Unfolding to a Differential Cross-Section . . . . .	131
6.1.3. Unfolding configuration study . . . . .	133
6.1.4. Binning Procedure . . . . .	134
6.1.5. Correction Factors and Response Matrices . . . . .	137
6.2. Systematic Uncertainties . . . . .	139
6.2.1. Propagation of Uncertainties . . . . .	140
6.2.2. Sources of Systematic Uncertainty . . . . .	141
6.3. Results . . . . .	148
6.3.1. Particle Level Combination . . . . .	148
6.4. Discussion . . . . .	153
6.5. Extrapolation to top partons . . . . .	164
<b>7. Conclusion</b>	<b>169</b>
7.1. Future Work . . . . .	170

---

<b>A. Inner Detector Studies for the ATLAS Phase-II Upgrade</b>	<b>173</b>
A.1. The ATLAS Upgrade Schedule . . . . .	174
A.2. Inner Detector Requirements . . . . .	175
A.3. Studies . . . . .	177
A.4. The Letter of Intent Layout . . . . .	182
<b>B. Correction Factors and Response Matrices</b>	<b>185</b>
<b>C. Tables of Systematic Uncertainties</b>	<b>199</b>
<b>D. BLUE Combination Systematic Uncertainties</b>	<b>215</b>
<b>E. Additional Results</b>	<b>229</b>
E.1. Normalized Unfolded Results . . . . .	229
E.2. Combination Results with Alternate Signal Models . . . . .	233
<b>List of Figures</b>	<b>237</b>
<b>List of Tables</b>	<b>251</b>
<b>Bibliography</b>	<b>259</b>



# Chapter 1.

## Introduction

The last several generations of intense theoretical and experimental exploration into the elementary constituents of matter has led to a consistent and accurate description of particle physics in the form of the Standard Model (SM). In the SM, there are 12 point-like particles, described by fermionic quantum fields, that make up the basic constituents of matter. These particles interact through the exchange of gauge bosons arising as a result of the symmetries of the theory, and are apparent at low energies as the strong, weak and electromagnetic forces. The particles are divided into 6 leptons, which interact via the weak and electromagnetic force, and 6 quarks, which interact with all the forces. Mass is introduced into the SM through breaking the joint electroweak symmetry at low energies via the Higgs mechanism. The discovery of the Higgs Boson, predicted as a consequence of the Higgs mechanism, in 2012 by the experiments running on the LHC gave the most recent, spectacular verification of the SM.

The ATLAS detector is one of the two general purpose experiments at the LHC, designed to exploit the full range of physics available at the LHC. It is built around one of four points where protons, accelerated to unprecedented energies in either direction in the circular LHC, are collided. Through 2011 it collected data from these proton–proton collisions with a centre of mass energy of 7 TeV, several times the previous highest energy collisions studied. The analysis of the data collected allowed the aforementioned discovery of the Higgs boson, but it has also given experimentalists the opportunity to study other SM particles and search for signs of physics beyond the SM.

With a mass of 173 GeV, the top quark is the heaviest particle of the SM. It is much heavier than the 126 GeV Higgs boson or  $W$  and  $Z$  bosons of the weak force and an order of magnitude heavier than the next heaviest fermion, the  $b$ -quark, with a mass of around 4 GeV. Discovered only in 1994, it also provides interesting opportunities for

investigation at the LHC. Its extremely large mass (relative to the other fermions) has led to speculation that it may play a special role in electroweak symmetry breaking, or that it may have special links to physics beyond the SM (required to explain, for example, the origin of dark matter). Along with these speculations, the top quark is interesting as a probe of the SM’s theory of the strong force, Quantum Chromodynamics (QCD). Its large mass means that these decays operate at high energies, in a regime describable by perturbative calculations. Other quarks, operating in non-perturbative regimes where QCD has large couplings, form stable bound states, which partially decorrelate the kinematic and spin properties of the quarks at production through the particle exchanges which bind them together. The top quark, however, decays before this process occurs and transmits its production information to its decay products. The top quark is thus a uniquely sensitive probe of QCD.

Using the collision data from ATLAS, this thesis measures the differential production cross-section of pairs of top quarks as a function of their kinematics. Previous measurements have presented results extrapolated to the “parton-level”. This, first, requires correcting the reconstructed detector data to top quark kinematics describable only by simulation. This builds in the phenomenological models used to construct the simulation, which can therefore not be improved by the measurement. Secondly, it extrapolates from the experimentally accessible phase space to the full phase space of the top-pair production. As the experiment has access to only a small fraction of the phase space, these extrapolations limit the utility of the results. The limitations in this approach have led theorists to call for new experimental techniques in these measurements, asking for results with corrections accounting only for detector inefficiencies and limiting extrapolations to detector accessible regions.

Therefore, our analysis aims to reconstruct proxy observables using only the experimentally accessible information, both in the construction of the observables, and the phase-space corrections we apply to them. We call these observables “pseudo-top”. They are constructed from the physics objects defined in the detector and the stable final state particles of the simulation, and presented corrected only for detector inefficiencies. These results should therefore be usable as inputs to phenomenological model building and comparison and therefore provide new insight into the production and decay of top quarks in hadron collisions. This is the first study to analyse and measure distributions using this technique.

This thesis starts by describing the structure of the SM in chapter 2. Particular emphasis is placed on the role and physics of the top quark. In chapter 3, we introduce

the LHC and the ATLAS detector, the data of which are used in the later analysis chapters. In chapter 4, we describe how physics objects are reconstructed from the the data delivered by ATLAS. We also discuss how the simulations of the physics and detector are produced and used in the physics analysis and the estimation of the size of the background processes. In chapter 6, we present the preliminary studies, definition and data analysis of the pseudo-top, and present the results of measuring several differential cross-sections of the pseudo-top observable. The measurements are compared with several theoretical simulations which are used to model top quark production. We also discuss the sources of systematic uncertainties in the analysis, and how they are estimated. In chapter 7, we present the final conclusions and discuss future directions in which the research can be taken.



# Chapter 2.

## The Top Quark in the Standard Model

### 2.1. The Standard Model of Particle Physics

The developments over the past several decades have led to a theory of physics on the sub-nuclear scale which accounts for the vast majority of experimentally observed phenomena. This theory is the Standard Model (SM) of particle physics. The SM encompasses all the known physical forces except gravity, which has defied attempts for it to be incorporated into the quantum field framework of the SM. General overviews of the quantum field theory and the SM can be found in [1, 2]. The material on the historical development of the SM in this chapter is taken from [3].

The SM is a gauge quantum field theory. That is, it describes physical phenomena in terms of interacting quantum fields, where the fields are representations of a gauge group. In the case of the SM, this group is  $SU(3)_C \times SU(2) \times U(1)_Y$ . The gauge symmetry is required to hold locally. That is, the Lagrangian is required to be invariant under a gauge transformation allowed to vary smoothly over space-time. Starting with non-interacting fields, to obtain gauge symmetry, one needs to introduce massless bosonic fields and write down interaction terms between these gauge fields and the original fields. Forces can then be understood as interactions of the original fields with the gauge fields. By Noether's theorem, which says that every symmetry of the Lagrangian corresponds to a conserved quantity, there are conserved gauge currents corresponding to the symmetries of the theory. As a final remark, all the fields of the SM are gauge charged under the full symmetry group of the theory. This implies that mass terms cannot be written into the

theory without breaking the gauge symmetry, as  $m\bar{\psi}\psi$  terms do not form gauge singlets. Since we know that the particles have mass, there needs to be another way to introduce mass into the theory. This is provided by the famous Higgs mechanism which will be described later.

As an example, electromagnetism is described by fermion fields which obey a  $U(1)_{\text{EM}}$  symmetry. The free field Lagrangian density for a single field  $\psi$  is written

$$\mathcal{L} = \bar{\psi}\partial\psi \quad (2.1)$$

Then, in order for the Lagrangian density to remain invariant under a  $U(1)_{\text{EM}}$  gauge transformation  $\psi \rightarrow e^{iq\alpha(x)}\psi$ , where  $q$  is the electric charge and  $\alpha(x)$  is an arbitrary  $U(1)_{\text{EM}}$  gauge transformation, one needs to introduce a new massless bosonic field  $A^\mu$  which transforms  $A_\mu \rightarrow A_\mu - \partial_\mu\alpha(x)$  and couple the field to  $\psi$ , giving the Lagrangian density for EM as

$$\mathcal{L} = \bar{\psi}i\gamma^\mu\partial_\mu\psi - iq\bar{\psi}\gamma^\mu A_\mu\psi - \frac{1}{4}F^{\mu\nu}F_{\mu\nu} \quad (2.2)$$

where  $F^{\mu\nu} = \partial^\mu A^\nu - \partial^\nu A^\mu$  is the kinetic term for  $A^\mu$ . After quantisation, the quantum excitations of a field from the vacuum state are interpreted as particles; so, in this example, electromagnetism is the result of a fermion absorbing or emitting a photon. Physical calculations are typically made as a perturbative expansion in the coupling constant  $q$ . Beyond the first order of the expansion, ultraviolet and infra-red infinities appear, which leads to the need to renormalise the couplings. This leads to the running of the coupling constants, where the effective strength of the interactions is a function of the centre of mass energy of the incoming interacting particles.

The SM gauge group,  $SU(3)_C \times SU(2) \times U(1)_Y$ , breaks into two components:  $SU(3)_C$  which is the strong force gauge group, and  $SU(2) \times U(1)_Y$  which is the electroweak (EW) gauge group. There are 12 types of fermions in the SM and one scalar field, the Higgs field. The fermionic fields come in three generations, which are copies of the fields that only differ by their masses, and are divided into quarks and leptons. The known particles of the SM are shown in table 2.1. There are six quarks: up and down in the first generation, charm and strange in the second, and top and bottom in the third. Each quark is actually a triplet of fields in the fundamental representation of the strong force gauge group. The quarks also divide into left-handed doublets and right-handed singlets of the electroweak group. The six leptons are singlets under the strong force, and so do not interact with the

**Table 2.1:** The Standard Model particles [4]. Charges are in units of  $e$ , the absolute value of the charge of the electron. The masses of the neutrinos are small but non-zero. The mass of the light quarks ( $u, d, s$ ) are given for the  $\overline{MS}$  subtraction scheme at a scale  $\mu \approx 2$  GeV. There is an anti-particle for each fermion with oppositely-signed charge and quantum numbers. Each quark is a triplet under  $SU(3)$ , meaning that there are 3 fields for each quark, denoted red, blue and green. The leptons are singlets under  $SU(3)$  and therefore do not experience the strong force.

		Particle	Symbol	Charge	Spin	Mass
Fermions	Leptons	electron neutrino	$\nu_e$	0	$1/2$	$\lesssim 2$ eV
		muon neutrino	$\nu_\mu$	0	$1/2$	$\lesssim 2$ eV
		tau neutrino	$\nu_\tau$	0	$1/2$	$\lesssim 2$ eV
		electron	$e$	$-1$	$1/2$	511 keV
		muon	$\mu$	$-1$	$1/2$	106 MeV
		tau	$\tau$	$-1$	$1/2$	1.777 GeV
	Quarks	up	$u$	$+2/3$	$1/2$	2.3 MeV
		charm	$c$	$+2/3$	$1/2$	1.275 GeV
		top	$t$	$+2/3$	$1/2$	173.4 GeV
		down	$d$	$-1/3$	$1/2$	4.8 MeV
strange		$s$	$-1/3$	$1/2$	95 MeV	
bottom		$b$	$-1/3$	$1/2$	4.18 GeV	
Bosons	photon	$\gamma$	0	1	0	
	W boson	$W$	$\pm 1$	1	80.4 GeV	
	Z boson	$Z$	0	1	91.2 GeV	
	gluon	$g$	0	1	0	
	Higgs boson	$H$	0	0	125.5 GeV	

strong force gauge bosons, but also come in left-handed EW doublets and right-handed EW singlets. The leptons are the electron, electron neutrino, muon, muon neutrino, tau and tau neutrino. In the canonical version of the SM, the neutrinos only appear in the doublet, without a corresponding singlet. As will be shown, this implies that they are massless. Because of the observation of neutrino mixing, however, it is known they have some mass, although the mechanism by which they gain mass is not yet known. The neutrinos also have no hypercharge, so unlike the other fermions, it is possible to introduce a Majorana mass term, however it is unknown if this is the actual mechanism.

The QCD  $SU(3)_C$  group introduces eight gluon fields which transform under an adjoint representation of the  $SU(3)$  group. The QCD group has three colour charges

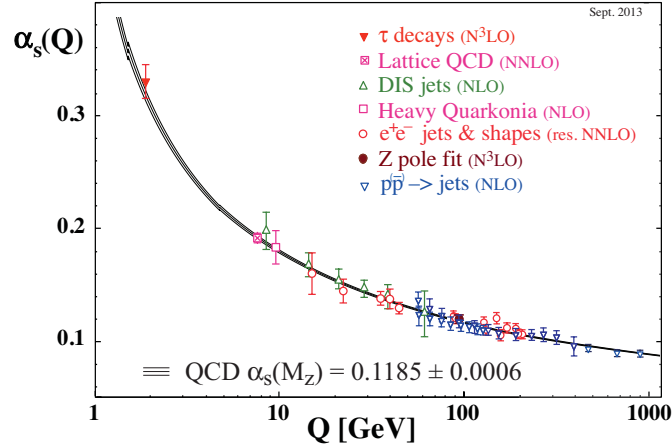


**Figure 2.1:** Summary of measurements of  $\alpha_S$  as a function of the energy scale  $Q$ . The respective degree of QCD perturbation theory used in the extraction of  $\alpha_s$  is indicated in brackets. Taken from [4].

denoted red, green and blue, and corresponding three anti-colour charges. The quark fermions carry colour charge, the anti-fermions anti-colour charges, and the gluons both a colour and anti-colour charge. Because they are colour charged, the gluons will experience self-interactions.<sup>1</sup> At low energies, the QCD coupling constant is of order unity, which means that the perturbative expansion breaks down. This leads to the idea of confinement, which requires that physically observed states occur only as colour singlets, requiring that the particles making up a physical state neutralise the colour charges together forming hadrons. This leads to the quark model, which describes the hadrons as mesons, a quark and anti-quark of the equivalent colour–anti-colour, and baryons, three quarks or three anti-quarks each of different colour which also forms a colour singlet. The quarks of these hadrons are held together by gluon exchange. At high energies, the energy-dependent effective QCD coupling becomes small, and so perturbation theory again holds. This leads to asymptotic freedom, where a high energy probe of a hadron interacts with constituents of the hadron independently of the rest of the hadron. Figure 2.1 shows the evolution of the strong coupling constant at various energy scales, showing an energy dependence consistent with the predictions from QCD.

The electroweak sector is described by the massless photon  $\gamma$  which is responsible for the familiar electromagnetic force, and the three massive gauge bosons, the  $W^\pm$ , and the  $Z^0$ , which make the weak force responsible for nuclear decays. As mentioned, mass terms

<sup>1</sup>Technically, this follows from  $SU(3)$  being non-Abelian.

in the Lagrangian are forbidden by gauge symmetry. These fields are introduced in the SM through the Higgs mechanism. The Higgs field is a doublet under the electroweak group  $\phi = (\phi^+, \phi^0)$  with the free-field Lagrangian

$$\mathcal{L}_{\text{Higgs}} = (\partial\phi)^\dagger(\partial\phi) - \mu\phi^\dagger\phi - \lambda(\phi^\dagger\phi)^2 \quad (2.3)$$

which is manifestly invariant under  $SU(2) \times U(1)_Y$ . After coupling to the electroweak sector, the ground state of the Higgs field is non-zero and invariant under gauge rotations of the Higgs fields. A choice of the ground state breaks the gauge invariance, so the Higgs field spontaneously breaks the gauge invariance at low energies from  $SU(2) \times U(1)_Y$  into  $U(1)_{\text{EM}}$ . The theory can then be rewritten as a perturbative expansion around the vacuum state  $|0\rangle$ , which by gauge invariance we are free to choose as being in the real direction of the bottom half of the doublet  $\langle\phi\rangle = \langle 0|\phi|0\rangle = \frac{1}{\sqrt{2}}(0, v)$  where  $v = 246$  GeV corresponds to the typical energy scale of electroweak interactions.  $\langle\phi\rangle$  is referred to as the vacuum expectation value (VEV). The unbroken  $SU(2) \times U(1)_Y$  gauge fields are  $W^{1,2,3}$  and  $B$ . After breaking, it is possible to rewrite the fields so that the massless  $W^{1,2}$  and the upper half of the Higgs doublet becomes the massive  $W^\pm$  (the Higgs fields providing the longitudinal components and the coupling to the VEV providing the mass). Similarly, the  $W^3$ ,  $B$  and the imaginary part of the lower half of the doublet combine and mix to form the massive  $Z^0$  and the massless  $\gamma$ . This leaves a single real scalar field from the doublet, the Higgs boson. This model of the electroweak sector is called the Glashow-Weinberg-Salam (GWS) theory [5–7].

Because the  $W^\pm$  and the  $Z^0$  masses are derived from mixing with the scalar Higgs doublet and the VEV, the SM can predict the masses of the bosons if the mixing angle between the  $W^3$  and  $B$  to form the  $Z^0$  and photon (called the Weinberg angle  $\theta_W$ ) is known. Before the discovery of the bosons, it was possible to obtain this angle from neutral weak-current interactions. For example the Gargamelle experiment was the first to find neutral current interactions  $\nu_\mu$  interacting with a neutron to produce a recoil  $\nu_\mu$  and hadrons through a  $Z^0$  boson exchange, giving results allowing a Weinberg angle  $\sin\theta_W = 0.3 - 0.4$  [8]. The subsequent discovery of the  $W$  and  $Z$  bosons, at UA1 [9, 10] and UA2 [11, 12] on the  $Spp\bar{p}S$  collider at CERN in 1983, in agreement with the predicted masses was strong evidence for the GWS theory.

Masses for the fermions can also be incorporated as couplings to the Higgs in the unbroken theory, which leads to mass terms through coupling to the Higgs VEV after

breaking.<sup>2</sup> This is done by coupling a fermion doublet to a fermion singlet and the Higgs doublet in a Yukawa term:

$$\mathcal{L}_{\text{Yukawa}} = -y_{ij}^d Q_{L,i} \phi d_{R,j} - y_{ij}^u Q_{L,i} \phi^* u_{L,j} + h.c. \quad (2.4)$$

where the  $Q_{L,i}$  enumerate the left-handed fermion doublets, the  $d_{R,i}$  are the down-type right-handed singlets (down, strange and bottom in the quarks, but for the SM with massless neutrinos there are no right-handed neutrinos) and the  $u_{R,i}$  enumerate the up-type right-handed singlets (electron, muon, tau), and the  $y_{ij}^d$  and  $y_{ij}^u$  are the Yukawa couplings between the up- and down-type fermions respectively. To conserve symmetry one can only couple quarks with quarks and leptons with leptons. After breaking, the Yukawa terms become mass terms through the VEV coupling and as a result couplings to the longitudinal portion of the electroweak bosons and the Higgs boson are obtained. This leads to the prediction that the strength of the Higgs couplings should be proportional to the mass of the fermions.

A boson with properties consistent with the Higgs was discovered by the ATLAS [13] and CMS [14] collaborations in 2013 in LHC  $pp$  collision data taken at  $\sqrt{s} = 7$  TeV and  $\sqrt{s} = 8$  TeV. Given that the top has a much larger coupling to the Higgs compared to other fermions, the dominant Higgs production mechanism in hadron colliders is gluon fusion through a top loop to Higgs. The experiments found excesses, in both the  $\gamma\gamma$  and four lepton mass distributions, consistent with a 125 GeV Higgs boson decaying through  $H \rightarrow \gamma\gamma$  and  $H \rightarrow ZZ^* \rightarrow llll$  respectively.

The coupling strength relationship for the fermionic masses has yet to be experimentally verified as of 2014. However, the ATLAS and CMS collaborations have evidence that the Higgs couples to fermions by observing evidence of the Higgs boson decaying to two taus. In this search, ATLAS observes an excess above the background only hypothesis with a significance of  $4.1\sigma$  [15], and CMS observes a excess with significance of  $3.2\sigma$  [16]. The excesses are consistent with that expected from a SM Higgs Boson with mass 125 GeV.

In order to obtain the physical states, the  $y_{ij}^{d,u}$  matrices must be diagonalised. After doing this in the quark sector, the interactions with the  $W^\pm$  bosons are rotated with respect to the mass basis by the  $3 \times 3$  unitary matrix, the Cabibbo-Kobayashi-Maskawa (CKM) matrix. The neutral current couplings in the SM respect the mass basis, so this

---

<sup>2</sup>Note that the majority of the mass of the hadrons is due to the energy carried by the gluon field holding the quarks together, rather than the Higgs mechanism which we are about to describe.

implies that the only source of inter-generational mixing is through the weak charged-current interactions. The elements of the CKM matrix represent the probability that one up-type fermion couples to a specific down-type fermion. The current measurement of size of the parameters give [4]:

$$\begin{pmatrix} |V_{ud}| & |V_{us}| & |V_{ub}| \\ |V_{cd}| & |V_{cs}| & |V_{cb}| \\ |V_{td}| & |V_{ts}| & |V_{tb}| \end{pmatrix} = \begin{pmatrix} 0.9743 & 0.2252 & 0.0087 \\ 0.2253 & 0.9734 & 0.0404 \\ 0.0035 & 0.0412 & 0.9991 \end{pmatrix} \quad (2.5)$$

The CKM matrix, being  $3 \times 3$ , complex and unitary, can be parametrised by three mixing angles, and a phase, which in the SM is the only source of CP violation. The parameters of the CKM matrix have been studied and constrained at the  $B$  factory experiments, BaBar [17] and Belle [18], and the CKM picture of the quark sector has been shown to be consistent with the measurements. This provides stringent constraints on beyond the SM physics, as generic new interactions introduce new CP violating phases, and a fourth generation would imply that the CKM matrix ought to be a  $4 \times 4$  unitary matrix and so the  $3 \times 3$  portion we probe can be non-unitary.

In the massless neutrino version of the SM, the matrices for the charged-current weak sector are diagonalized by the mass diagonalisation matrices, so no intergenerational mixing occurs. However, since it is well established that neutrinos oscillate [19, 20], it is at the same time established that neutrinos have mass. There are several mechanisms which could explain the neutrino mass. For example, since neutrinos are neutral under hypercharge, the addition of EW singlet right-handed neutrinos  $N_i$  is allowed and coupling with the left-handed SM neutrino generates a mass for both. This leads to small SM neutrino mass and new neutrino particle states with large mass (the so-called ‘‘Type-I seesaw mechanism’’ [21]). This, or any other proposed explanation, requires the addition of new particles beyond those currently known to the SM, and is the one of the best pieces of evidence that there is physics beyond the SM. The mixing in neutrinos is described by the PMNS matrix [22–24], the lepton sector analogue to the CKM matrix. The mixing angles have all been measured, but the size of the CP violation in the lepton sector has yet to be determined [25].

For all its success, the SM is not a complete theory of nature. It does not incorporate a description of gravity and attempts to add it in the same theoretical framework of the SM have failed. Due to the weakness of the gravitational force at the subatomic level, no experimental input is expected to be forthcoming, which leaves physicists at an

impasse, unable to describe gravity along with the other forces and without experimental guidance to induce new directions for ideas. The characteristic scale at which gravity becomes important, the Planck Scale  $\Lambda_{\text{planck}} \approx 10^{19}$  GeV is the definite energy that would need to be probed for beyond the SM physics due to gravity to appear. Between the scale currently probed at the LHC, on the order of a TeV, and the Planck Scale, the SM remains self-consistent, however there are also hints that new physics is needed in this range. For example, the rotational curve of galaxies implies that they contain much more mass than is visible, requiring a new form of matter not currently in the SM. This Dark Matter is also required to explain the formation of structures as the early universe evolved from the initial isotropic and homogeneous conditions to the present day distributions of stars and galaxies. The matter–anti-matter asymmetry in the universe also cannot be explained. CP violation is required to generate this asymmetry from the symmetric early universe and is partly provided in the CKM mixing. The currently measured values of CP violation, however, are not large enough to account for the size of the observed asymmetry. These and similar observations spur both theoreticians and experimentalists to search for new theories and new experiments that may revolutionise our understanding of the universe through the coming decades.

Having briefly outlined the SM of particle physics, let us now concentrate on one particular particle of the theory, the top quark, which is the subject of this thesis.

## 2.2. Pre-history of the Top Quark

The quark model was first proposed during the 1960s in order to explain the structure of the hadronic resonances being continuously discovered at the time [26]. Deep inelastic scattering experiments in the late 1960s gave evidence for the composite nature of the proton [27, 28]. In 1970, Glashow, Illiopoulos and Maiani showed that the non-observation of strangeness changing neutral currents could be explained if there was a fourth quark, the charm quark [29]. This was spectacularly confirmed by the discovery in 1974 of the  $J/\psi$  meson, the lowest lying  $c\bar{c}$  state, completing the second generation of the fermions. The discovery was made by the SLAC-LBL Mark I detector on the SPEAR  $e^+e^-$  collider measuring the  $e^+e^- \rightarrow \text{hadrons}$ ,  $e^+e^- \rightarrow e^+e^-$ , and  $e^+e^- \rightarrow \mu^+\mu^-$  cross-sections [30] and with a pair spectrometer using protons from Brookhaven’s alternating gradient synchrotron colliding with a Beryllium target and looking at the  $e^+e^- + X$  spectrum [31].

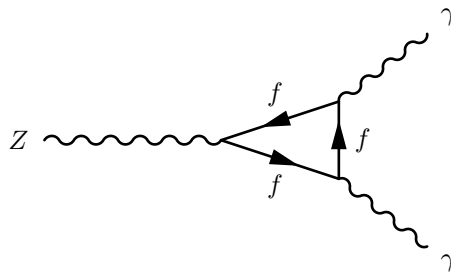


**Figure 2.2:** Feynman diagrams for the process  $Z \rightarrow \gamma\gamma$ .

Then, in 1975, the tau lepton was discovered [32], implying the existence of a third generation of quarks in order to have an anomaly free theory (as will be explained below). Fermilab's 400 GeV proton–nucleus collider saw a strong dimuon excess at 9.5 GeV in 1977 [33]. This was soon shown to result from two mass peaks at 9.44 GeV and 10.17 GeV [34], given the names  $\Upsilon$  and  $\Upsilon'$  and attributed quark–anti-quark mesons formed from bottom quarks. It would be almost 20 years before the top, its weak-isospin partner quark would be found, but its existence was implied by theoretical considerations and indirect experimental evidence.

In order for the physics resulting from the complete Lagrangian to be anomaly free, the weak hypercharges of the fermions need to sum to zero. That is, without the total hypercharge of the particle content in the theory summing to zero, loop diagrams for electroweak processes like  $Z \rightarrow \gamma\gamma$  (with diagrams shown in figure 2.2) would lead to divergences. Now, the leptons have hypercharge  $-2$ , whereas the quarks have hypercharge  $+2/3$ . So, if the number of leptons and quarks is the same, then the hypercharges cancel (recalling that each flavour of quark has three fields, one for each colour of the strong force). Thus, knowing that there are six leptons, the top quark is necessary for a consistent theory unless the  $b$  is a EW singlet.

Experimentally, a singlet  $b$  would lead to diagrams for  $b \rightarrow s\ell^+\ell^-$  at very large levels [35], which was excluded in 1983 by the SLAC-LBL Mark II detector on the PEP storage ring searching for electron–positron collisions producing an  $\Upsilon$  and the  $\Upsilon$  subsequently decaying to a lepton pair [36]. These diagrams are suppressed when the  $b$  is in a doublet through a third generation GIM mechanism, equivalent to the GIM mechanism which led to the prediction of the charm quark by the non-observation of  $K \rightarrow \mu\mu$  decays in the 1970s. The GIM mechanism works by having the box diagrams (shown in figure 2.3) for the relevant decays cancel out almost exactly (exactly only in the limit of no quark masses). Without the  $c$  quark, only the diagram on the left Feynman diagram in the figure contributes, leading to a large expected decay rate.

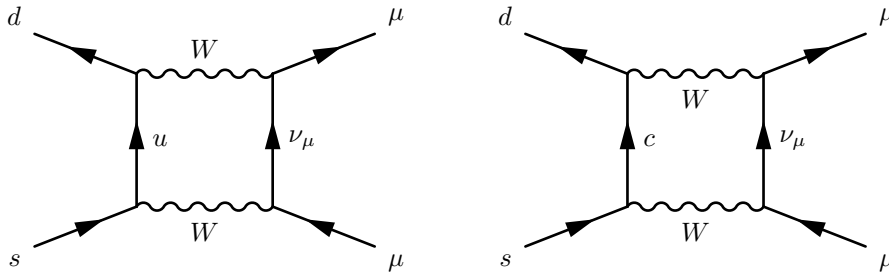


**Figure 2.3:** Feynman diagrams for the process  $K \rightarrow \mu\mu$  which illustrates the working of the GIM mechanism.

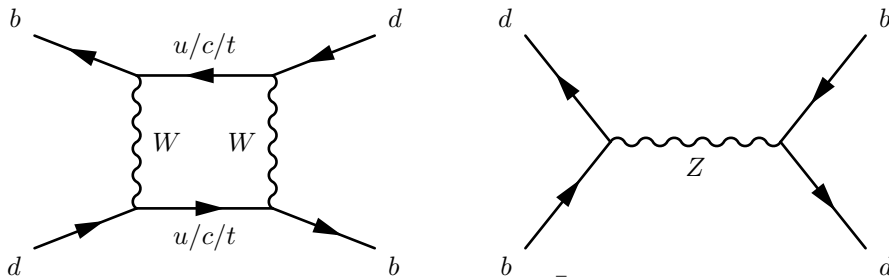


**Figure 2.4:** Feynman diagrams for the process  $B_d - \bar{B}_d$  mixing mediated by a  $W$  (left) or  $Z$  (right). In the Standard Model, the vertex in the right diagram does not exist.

A singlet  $b$  would also allow flavour changing neutral currents at tree level through  $Z^0$  exchange, which would lead to sizeable  $B_d^0 - \bar{B}_d^0$  mixing [37], whereas ARGUS measured small values for the mixing parameter [38]. The diagrams through which the mixing can occur are displayed in figure 2.4. Only the box diagram contributes in the SM.

### 2.2.1. The Top Quark Discovery

Knowing that the top quark should exist within the physics framework developed through the 1960s and 1970s, several experiments performed searches for the top. Since a priori, no top mass was preferred, a low mass (as low as 15 GeV) was assumed, allowing for resonant states to be produced. This is where the early experimental searches concentrated. The PETRA  $e^+e^-$  collider collected data between 1974 and 1984 and searched for the top quark as an increase in the ratio of collision events with final state hadrons and those with muons. Above twice the top mass, this ratio will increase due to the  $t\bar{t}$  production mode becoming available. They operated with centre of mass energies from 12 to 46.8 GeV without observing an excess, ruling out the top quark mass below 23.3 GeV [39, 40]. The TRISTAN  $e^+e^-$  collider at the KEK research facility in Japan (operating from 1987 to 1995) dedicated itself to similar searches for the top quark, searching up to 61.4 GeV, setting a 30.2 GeV limit without discovery by 1990 [41]. SLC and LEP, capable of collecting  $e^+e^-$  collision data at the  $Z$  boson mass, set a limit of half the  $Z^0$  mass of

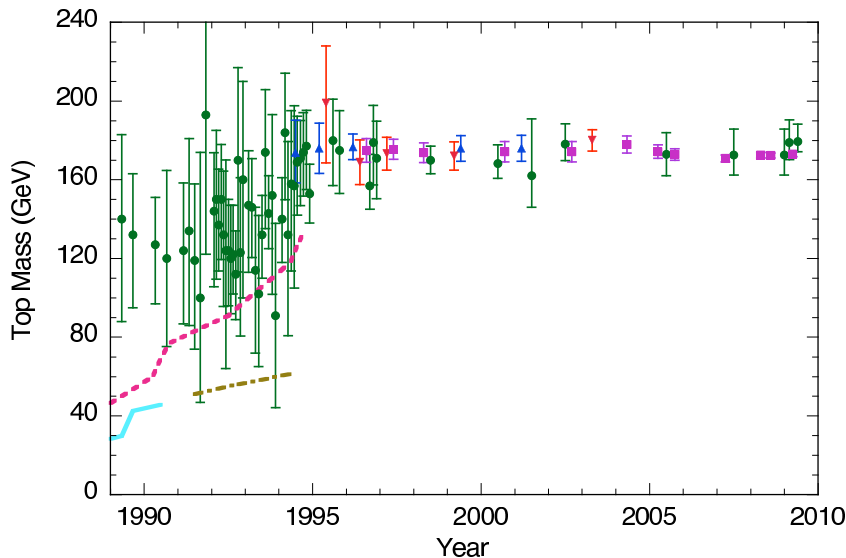


**Figure 2.5:** Evolution of the knowledge of the top quark mass with time. Includes fits to electroweak observables (green dots), 95% confidence limit lower bounds from  $e^+e^-$  annihilation (solid line) and  $p\bar{p}$  collisions (broken line), indirect lower bounds from the  $W$  boson width (dot-dash line) and direct measurements from CDF (blue triangles) and D0 (red triangles). The Tevatron average is shown in magenta. Taken from [50].

45 GeV from their 1989-90 runs [42–45]. The UA1 experiment on the hadronic  $Spp\bar{S}$  collider had early hints of a low mass top quark at around 40 GeV in 1984 [46, 47]. This, however, was unconfirmed from the competing UA2 experiment on the same ring and the excess was shown later to be due to mismodelling of the background [48]. Subsequent bounds on the top quark mass were placed at around 69 GeV in the 1988/9 running of the  $Spp\bar{S}$  [49].

Precision electroweak measurements later became available that gave indirect measurements of the top quark mass. Both the top quark and Higgs enter into the  $W$  mass through radiative corrections. The Higgs mass, however, only enters logarithmically, whereas the top enters as  $m_t^2$  (see section 2.6). So, a reasonable assumption on the Higgs mass combined with a precision measurement of the  $W$  boson mass allowed an indirect estimate of the top quark mass of 180 GeV by 1994, the year the top quark was discovered at the Tevatron collider. Figure 2.5 shows the evolution of the knowledge of the top quark mass both before and after the discovery.

The Tevatron Collider at Fermilab was a proton–anti-proton synchrotron collider conceived in the 1970s with the goal of colliding  $p\bar{p}$  with a centre of mass energy at or above 1 TeV [51]. It achieved this goal through the pioneering use of superconducting

magnets throughout the accelerator ring. Beam commissioning began in 1983 with first collisions in 1985 and a preliminary physics data collection (the so-called “Run 0”) from 1988 to 1989. “Run 1”, with a proton–anti-proton collision energy of  $\sqrt{s} = 1.8$  TeV, began in 1992, running until 1996 and delivering an integrated luminosity of  $160 \text{ pb}^{-1}$ , with two fully commissioned operational detectors, CDF [52] and DØ [53]. In 1994, CDF published the first evidence for the observation of the top quark [54], which was discovered in 1995 jointly by the CDF [55] and DØ [56] experiments. To understand how the top was produced and detected using a hadron collider, we must first understand the physics involved in hadron–hadron collisions.

### 2.3. Hadron Collider Physics

The proton is a composite object; simplistically, it is three valence quarks held together through soft gluon exchange. The exchanges are soft because of the asymptotic freedom of QCD: for soft emissions,  $\alpha_S$  is of order one, but as the scale of the emission,  $Q^2$  (where  $Q$  is the four-momentum transfer of the scattering process), increases  $\alpha_S$  drops dramatically, and so for a bound state object, these emissions are suppressed. Intuitively then, from the point of view of a hard probe (one far above the QCD confinement scale,  $\Lambda_{QCD} \approx 200$  MeV, approximately the scale at which QCD becomes non-perturbative), the partons that constitute the protons act like free objects, since the time-scale for interactions between partons within the proton ( $\Delta t \approx 1/\Lambda_{QCD}$ ) is much greater than the time-scale that a hard probe acts over ( $\Delta t \approx 1/Q$ ). Proton scattering can therefore be factored into two components: the Parton Distribution Function (PDF) characterises the momentum distribution of the partons inside the proton, and is a function of the momentum fraction  $x$  of the parton to the proton and the  $Q^2$  scale, and is independent of the nature of the hard probe; and the partonic cross-section  $\hat{\sigma}$  which is a perturbative expansion of the hard probe scattering from a free parton inside the proton (in the perturbative QCD (pQCD) framework). The factorisation theorem of QCD allows us to treat these two processes independently.

In high energy proton–proton collisions, hard interactions are the result of a hard parton in both protons, with parton energies taken from the relevant PDFs, scattering with each other independently of either proton. The partons can be the valence quarks, the gluons holding the proton together, or sea quarks, produced from gluon splitting. The production rate for a given final state  $F$  is then given by [58]:

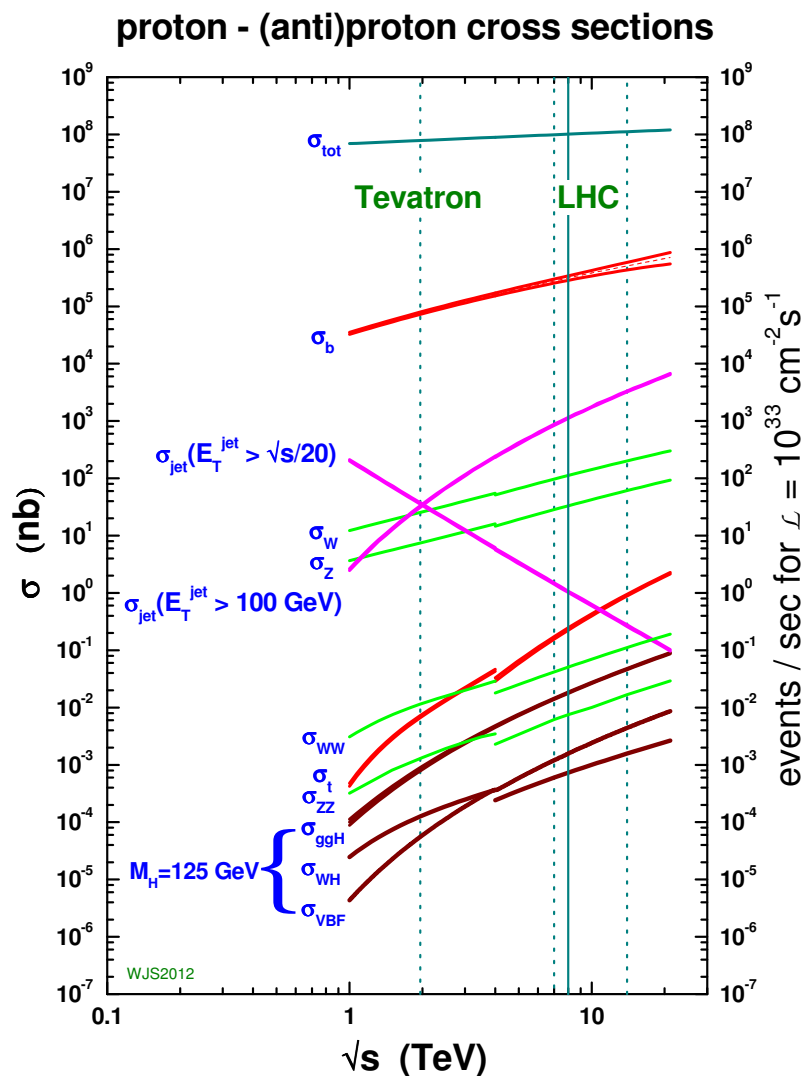


**Figure 2.6:** Summary of the cross-sections of various physics processes at the Tevatron and the LHC. The cross-sections are plotted with respect to the centre of mass energy of the hadron collision and are shown for  $p\bar{p}$  collisions below 3 TeV and for  $pp$  collisions above 3 TeV. Also shown are the energies at which the Tevatron and LHC have taken data, and the expected 13 TeV LHC run in 2015, as dashed and solid (for the current data under analysis at the LHC) blue lines. Taken from [57].

$$d\sigma(pp \rightarrow F + X) = \int dx_1 dx_2 \sum_{i,j} f_i(x_1, Q) f_j(x_2, Q) d\hat{\sigma}(ij \rightarrow F) \quad (2.6)$$

where the parton density functions  $f_i$  are summed over the parton types and are evaluated at a scale  $Q$  for the hard process under consideration. The cross-sections of typical processes of interest in proton–proton collisions are shown in figure 2.6. Since the PDFs represent long-distance processes which are non-calculable, they cannot be derived from first principles. However, since they are independent of the nature of the hard probe, they can be determined by one process and then used for any other process of interest by evolving the measured  $f(x, Q^2)$  to the  $Q^2$  scale of interest using the DGLAP equations [59–61]. Several groups provide fits for the PDFs using various parametrisations, with the inputs coming from electron-proton scattering measurements at HERA [62], and inputs from previous hadron collider machines such as dijet production at the Tevatron [63–66].

The PDF fits are performed by choosing a parameterisation of the proton PDFs at some starting scale  $Q_0^2$  (here we will follow the description in reference [67]). Typically, the generic form for the PDF for a given parton  $i$  is  $xf(x, Q^2) = A_i x^{B_i} (1-x)^{C_i}$ , where intuitively,  $A_i$  gives an overall normalisation,  $B_i$  describes the small  $x$  behaviour of the PDF, and  $C$  gives the  $x \rightarrow 1$  behaviour. Extra terms may be multiplied on for fine corrections, or to keep the gluon PDF from going negative. For example, the HERA PDF fits use  $xf(x) = Ax^B(1-x)^C(1+Ex^2)$  [67] while the MSTW PDFs use  $xf(x) = Ax^B(1-x)^C(1+D\sqrt{x}+Ex)$  for the valence up and down type quarks [68]. Given the parameterisations at the  $Q_0^2$  reference scale, and a choice for the free parameters  $A$ ,  $B$ ,  $C$ , etc., the PDFs can be evolved to the necessary  $Q^2$  scales using the DGLAP equations and compared with data. For jet measurements from the Tevatron and LHC, this is done using equation 2.6 and taking  $\hat{\sigma}_{ij}$  from perturbative QCD calculations. Similarly, for deep inelastic scattering measurements there are equivalent equations relating the cross-section measurements to an integral over a product of the PDFs and calculable hard processes. Once the above is set, scans over the free parameters are performed, using a  $\chi^2$  or similar measure to compare the theory and data distributions, from which best values and associated uncertainties can be obtained.

Higher-order corrections lead to including gluon emission and absorption processes in the hard scattering cross-section, which modify the incoming parton momentum

distributions from the non-perturbative part of the the factorisation. Therefore, the PDFs need to be modified to match a calculation at a given order of perturbation theory to take into account these contributions being done at the hard-scale. Thus, for a calculation performed at a given order, a PDF determined for that order must be used. For example, the MSTW PDFs fits discussed above are performed at leading order (LO), next-to-leading order (NLO), and next-to-next-to-leading order (NNLO) in the strong coupling constant  $\alpha_s$ . Typically, calculations are available at NLO, with NNLO calculations for top production having only recently been performed and differential distributions are not yet available.

Separating up the long and short range contributions requires the introduction of a factorisation scale  $\mu_F$ . This is an arbitrary parameter that must be set when performing the calculations. There is also an arbitrary renormalisation scale  $\mu_R$  which is relevant when renormalising the loop diagrams which are ultra-violet divergent. In an all-orders calculation, the final cross-section is independent of these scales, however cutting off the perturbation at finite order introduces a dependence on these scales to the cross-section results. Typically, this dependence is taken as an uncertainty on the final calculation, setting  $\mu = \mu_R = \mu_F = m_{top}$  for the top cross-section calculations, and taking the cross-section at  $\mu = m_{top}/2$  and  $\mu = m_{top}$  to be the uncertainty due to the scale, although this procedure is arbitrary. Going to higher orders in perturbation theory reduces this uncertainty, and for the NNLO calculations, its size is around 3% [69].

Finally, near the production threshold, soft gluon effects can lead to large logarithmic corrections of the cross-section; these logarithms can be resummed in an expansion valid for all orders of perturbation theory [70]. The current best theoretical cross-section for the production of  $t\bar{t}$  pairs (given below) is calculated at the complete next-to-next-to-leading order (NNLO) including next-to-next-leading-logarithmic soft gluon resummation (NNLL) [71].

## 2.4. Production of Top Quarks at Hadron Colliders

The dominant production mode of tops at hadron colliders is into top–anti-top pairs. At leading order, the QCD processes contributing to  $t\bar{t}$  production are gluon fusion and quark–anti-quark annihilation, illustrated in the Feynman diagrams of figure 2.8. At the Tevatron, the primary production mode was a valence quark from the proton annihilating with a valence anti-quark from the anti-proton. At the LHC, quark–anti-

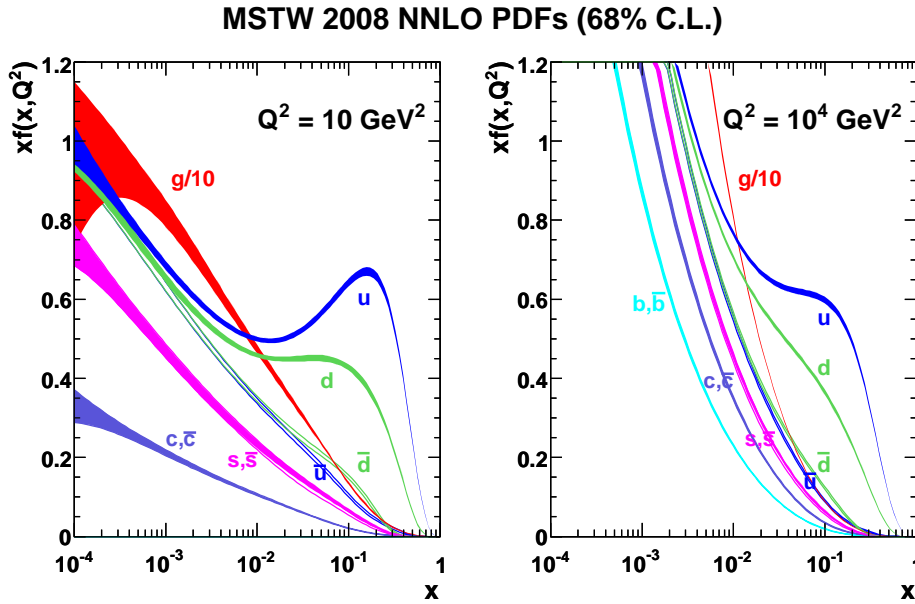


**Figure 2.7:** Figure showing parton distribution function  $xf(x, Q^2)$  against  $x$  for the various partons using the MSTW2008 NNLO PDF set [68, 72]. The left figure shows the PDF for  $Q^2 = 10 \text{ GeV}^2$ , and the right figure shows the PDF for  $Q^2 = 10^4 \text{ GeV}^2$ , an energy scale typical for LHC collisions. The error bands represent the 68% CL uncertainties of the fits. Figures from [73].

quark annihilation is suppressed since it is a proton–proton collider; also, the higher energies allow top production to probe lower  $x$  values of the PDF, which implies a larger gluon fusion cross-section (noting figure 2.7). At the threshold of top pair production, we have  $x = 2m_{top}/\sqrt{s}$ , which gives a minimum  $x = 0.05$  for the LHC, well into the range where the gluon PDF is dominant, but  $x = 0.18$  is the minimum value for the Tevatron, which is well within the valence quark regime, as can be seen in figure 2.7. Considering only leading order, the  $gg \rightarrow t\bar{t}$  process accounts for 80% of the cross-section at the LHC with the rest from quark annihilation, whereas the reverse was true at the Tevatron.

The total inclusive cross-section assumed in this thesis (which is the ATLAS Top Working Group’s recommended value) is  $\sigma_{t\bar{t}} = 177_{-11}^{+10} \text{ pb}$ , which was calculated with the Top++ program at full NNLO+NNLL [71]. For this value, the PDF and  $\alpha_S$  uncertainties were calculated using the PDF4LHC prescription [74] with the MSTW2008 68% CL NNLO [68, 72], CT10 NNLO [75, 76] and NNPDF2.3 5f FFN [77] PDF sets, added in quadrature to the scale uncertainty for the final uncertainties. The kinematic distributions used for simulation studies are not available at full NNLO+NNLL, but only at NLO. Therefore, when modelling kinematic dependent quantities, the NLO distributions are used and reweighted to the NNLO+NNLL cross sections. More details on the simulation

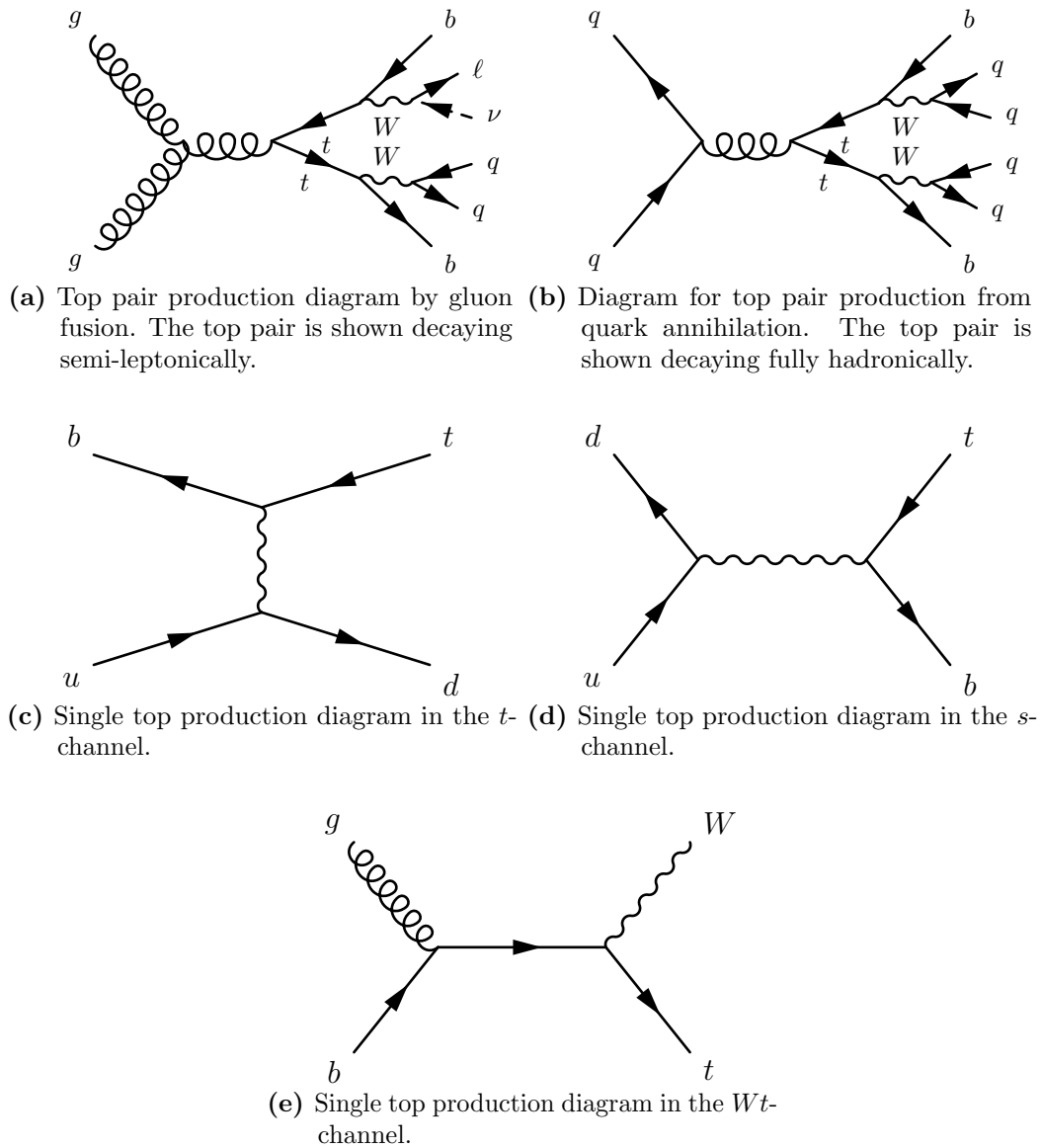


**Figure 2.8:** Feynman diagrams for the production and decay of the top quark at hadron colliders. The top rows show the top pair production and include the decay of the top into  $W$  and  $b$  in various configurations as indicated. The bottom rows show the single top production modes.

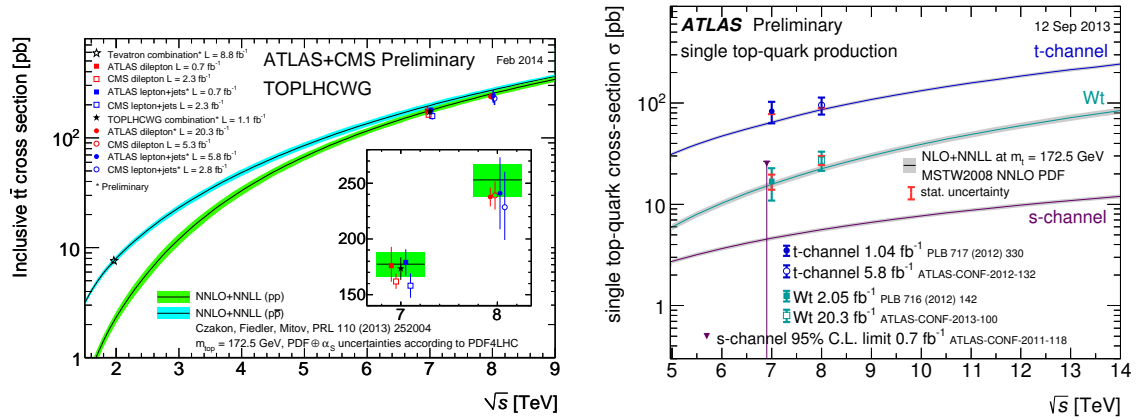


**Figure 2.9:** Summary of the measurements of the top cross-section. Results given for top pair production from the Tevatron and the LHC (left) and single top production in the various sub-channels which are measured independently at ATLAS (right). Taken from [78].

samples are given in section 4.2. The inclusive cross-sections measured at the Tevatron and LHC are currently in good agreement with the theory, as shown in figure 2.9.

One can also produce single top, which is suppressed relative to pair production as it requires the weak force. Single top production can proceed through an  $s$ -channel  $W$  production in  $qq' \rightarrow tb$ , a  $t$ -channel  $W$  exchange, or  $Wt$  production by excitation of a  $b$  sea quark. These processes are also shown in figure 2.8. For 7 TeV proton–proton collisions, the theoretical calculations for the cross-sections give 64.6 pb for  $t$ -channel production [79], 4.6 pb for  $s$ -channel production [80] and 15.7 pb for  $Wt$  production [81].

Since single top production proceeds via a weak process, the cross-section depends on the value of the CKM matrix element  $V_{tb}$ .  $V_{tb}$  is tightly constrained only under the assumption of the unitarity of the CKM matrix. Therefore, measurements of the single top cross-section provide a test of the unitarity of the CKM matrix. The current measurements agree well with theory, as can be seen in figure 2.9.

## 2.5. The decay of the top quark

The top quark decays via the electroweak process  $t \rightarrow Wb$  nearly 100% of the time in the SM. The other electroweak decays are highly suppressed by the CKM matrix elements,  $|V_{ts}|$  and  $|V_{td}|$ , which are needed for the top quark to decay into a  $s$  or  $d$  respectively. The decays of the top to  $s$  or  $d$ -quarks has yet to be experimentally observed.

The width of the top quark  $\Gamma_t$  at NLO level has been calculated to be [82]

$$\Gamma_t = \frac{G_F m_t^3}{8\pi\sqrt{2}} |V_{tb}|^2 \left(1 - \frac{m_W^2}{m_t^2}\right)^2 \left(1 + 2\frac{m_W^2}{m_t^2}\right) \left(1 - \frac{2\alpha_s}{3\pi} \left(\frac{2\pi^2}{3} - \frac{5}{2}\right)\right) \quad (2.7)$$

where  $\alpha_s$  is the strong force coupling constant,  $G_F$  the Fermi coupling of the weak force,  $\theta_W$  the Weinberg angle,  $m_t$  the mass of the top quark, and  $m_W$  the mass of the  $W$  boson. The evaluation of the equation gives a width of 1.3 GeV for  $m_t = 170$  GeV, well above the QCD hadronisation scale  $\lambda_{QCD} \approx 200$  MeV. The top quark width is known to NNLO [83], and leads to an improvement of theoretical accuracy for the top width to better than 1% [4]. The large mass of the top implies that it decays very quickly. Unlike every other quark, the top quark will decay before hadronisation and is in a regime that should be well described by perturbative QCD. This means that the top quark is very important in testing our understanding of QCD physics.

The  $W$  boson produced in the top decay will itself decay, into either a lepton-neutrino pair, or a quark–anti-quark pair, which leads to final state hadrons. The  $W$  decays leptonically in 32.4% of events and hadronically in 67.6% of events [4]. This is because there are 3 lepton channels available ( $e, \mu$ , and  $\tau$ ) and two quark channels ( $ud$  and  $sc$ ) and, ignoring masses, there is no preference for one decay channel over any other. In top pair events, this thus leads to the classification of dileptonic events (when both  $W$ s decay leptonically), semileptonic events (when one  $W$  decays leptonically and one decays hadronically), and hadronic decays (when both  $W$ s decay hadronically into jets). This is important for hadron colliders because the extremely large jet production cross-sections makes purely hadronic events difficult to extract from the background (though still achievable [84, 85]), but the cleanest dileptonic channel has a relatively small branching fraction of 10.5% [4]. The analysis in this thesis, therefore, uses the semileptonic channel, which has a lepton in the final state that provides clean triggering, and a larger branching fraction of 43.8% [4].

## 2.6. Other Properties of the Top Quark

The results of a recent top mass measurement from ATLAS are shown in figure 2.10. The mass of the top quark is an extremely important parameter of the Standard Model. The top mass enters into corrections of the  $W$  boson and Higgs masses in higher-order calculations and so alters the theoretically calculated value. The value of the  $W$  boson

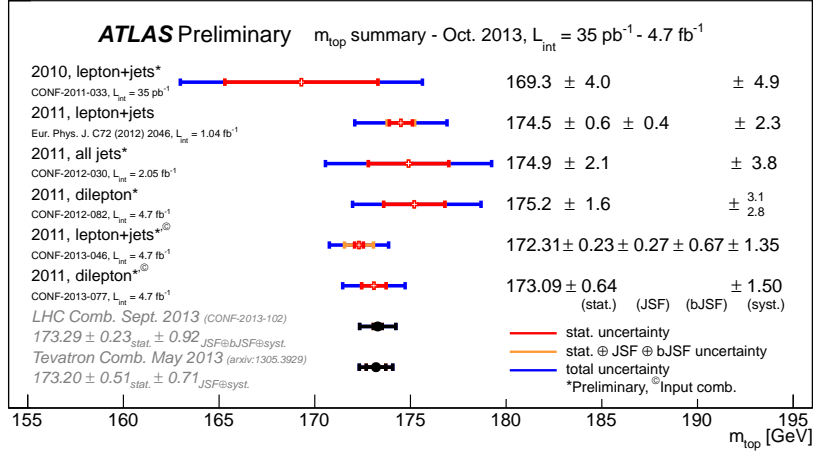


**Figure 2.10:** Top mass measurements from ATLAS, also including a comparison of the combination of the results from CMS and the Tevatron. Taken from [78].

mass,  $M_W$ , can be written as

$$M_W^2 = \frac{\pi\alpha}{\sqrt{2}G_F \sin^2 \theta_W (1 - \delta_r)} \quad (2.8)$$

where  $\alpha$  is the EM coupling constant,  $G_F$  the Fermi coupling of the weak force,  $\theta_W$  the Weinberg angle and  $\delta_r$  is the sum of corrections from loop processes. The contribution to the corrections due to the top quark is quadratic in the top mass

$$\delta_{r,top} = \frac{3G_F}{8\sqrt{2}\pi^2 \tan^2 \theta_W} m_t^2 \quad (2.9)$$

where  $m_t$  is the mass of the top quark, whereas the corrections due to the Higgs boson are only logarithmic in the Higgs mass,

$$\delta_{r,Higgs} = \frac{3G_F m_W^2}{8\sqrt{2}\pi^2} \left( \ln \frac{m_H^2}{m_Z^2} - \frac{5}{6} \right) \quad (2.10)$$

where  $m_H$  is the mass of the Higgs boson and  $m_Z$  the mass of the  $Z^0$  boson.

A global fit of the SM gives a top quark mass consistent with the measured value. Figure 2.11 compares the measured mass range of the  $W$  and top with the preferred Higgs mass, showing that the measured Higgs mass is compatible with electroweak expectations. The cross-section of the top also strongly depends on the top mass since the larger the mass, the larger the  $x$  needs to be for production to take place, cutting out more of the lower gluon  $x$  PDF as a source of production, and the available phase space get smaller,

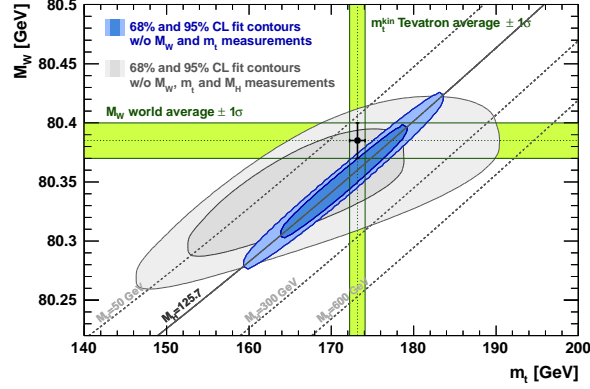


**Figure 2.11:**  $W$  mass plotted versus top mass with blue (grey) contours showing the allowed mass regions at the 68% and 95% confidence level based on global fit to electroweak observables when including (excluding) the Higgs mass in the fit. The direct top and  $W$  mass measurements are always excluded from the fit. The vertical and horizontal bands (green) indicate the  $1\sigma$  regions of the direct measurements. Taken from [86]

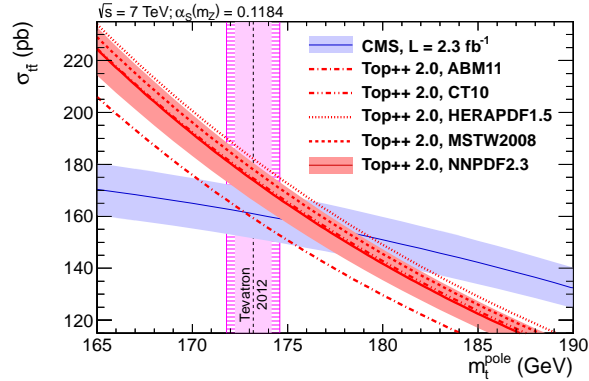


**Figure 2.12:** Top cross-section plotted versus top mass with predictions at NNLO with various PDFs with the CMS cross-section measurement shown as well as the Tevatron combined, direct pole mass measurement [87].

further reducing the cross-section. A cross-section measurement can therefore also serve as a top mass measurement, as shown in figure 2.12.

Since in the SM, the  $t$ -quark is the up-type quark of the third generation, it follows from the anomaly cancellation argument previously presented that the top quark must have charge  $+2/3$ . However, certain exotic models allow for a top quark with charge  $-4/3$ . This possibility, however, was recently disfavoured using ATLAS data at the  $8\sigma$  level [88].

Because the top quark decays before hadronisation, it affords a unique chance to study a bare quark. In particular, the polarisation of the top quark can be measured, as usually the gluon exchange required for hadronisation destroys the spin state of produced

quarks. In the Standard Model, the parity-conserving strong force production of the quark implies that the top quarks in pair production should be unpolarised. If the top is produced through some beyond the Standard Model physics process, some polarisation may be induced. ATLAS has released a measurement of the top quark polarisation showing good agreement with the Standard Model expectations [89].

Similarly, in the Standard Model the top quarks are expected to be produced with their spins correlated. When looking at the spin along a particular axis, the correlation  $A$  is defined as

$$A = \frac{N(\uparrow\uparrow) + N(\downarrow\downarrow) - N(\uparrow\downarrow) - N(\downarrow\uparrow)}{N(\uparrow\uparrow) + N(\downarrow\downarrow) + N(\uparrow\downarrow) + N(\downarrow\uparrow)} \quad (2.11)$$

where  $\uparrow$  ( $\downarrow$ ) represents the spin projection along (opposite) the given axis. Along the axis with maximal correlation, this is calculated in the Standard Model to be  $A = 0.44$  for top pair production. ATLAS has produced a result showing the first observation of spin correlation in the top pair production in agreement with the Standard Model and excluding uncorrelated production by  $5.1\sigma$  [90].

In this thesis, we are interested in measuring the kinematic properties characterising the production mechanism. That is, we are measuring the  $t\bar{t}$  pair production cross-section as a function of the production kinematics. A full discussion of these distributions is best done in the context of the ATLAS experiment and so is deferred until section 5.1, after it has been introduced.

# Chapter 3.

## The ATLAS Detector

The construction of the Large Hadron Collider (LHC) [91], and the experiments designed to take advantage of the high energy proton collisions it provides, represent one of mankind's largest scientific undertakings. This chapter gives a brief overview of the LHC and the ATLAS (A Toroidal LHC ApparatuS) detector [92]. The data collected by the ATLAS detector through 2011 was used for the top cross-section analysis presented in this thesis.

### 3.1. The LHC

The LHC machine is a two-ring superconducting hadron collider providing proton–proton collisions of up to 14 TeV centre of mass energy [91]. It is installed in the 26.7 km Large Electron-Positron (LEP) collider tunnel on the Swiss-French border outside Geneva at CERN. The LEP collider shut down in 2000 to free the tunnel for the construction of the LHC. The LHC uses twin bore magnets consisting of two sets of coils and beam channels in the same mechanical structure and cryostat.

The protons from the LHC are obtained by ionising hydrogen atoms in a duoplasmatron [93]. The protons are then passed successively through a series of pre-accelerators: the Radio Frequency Quadrupole (which accelerates the protons to 750 keV each and performs beam focusing), the 30 m long LINAC2 (which accelerates the protons to 50 MeV each) linear accelerator, the Proton Synchrotron Booster (PSB) (1.4 GeV), the Proton Synchrotron (PS) (25 GeV), the Super Proton Synchrotron (SPS) (450 GeV), and finally they are passed into the LHC. Each of these synchrotrons gradually increase the

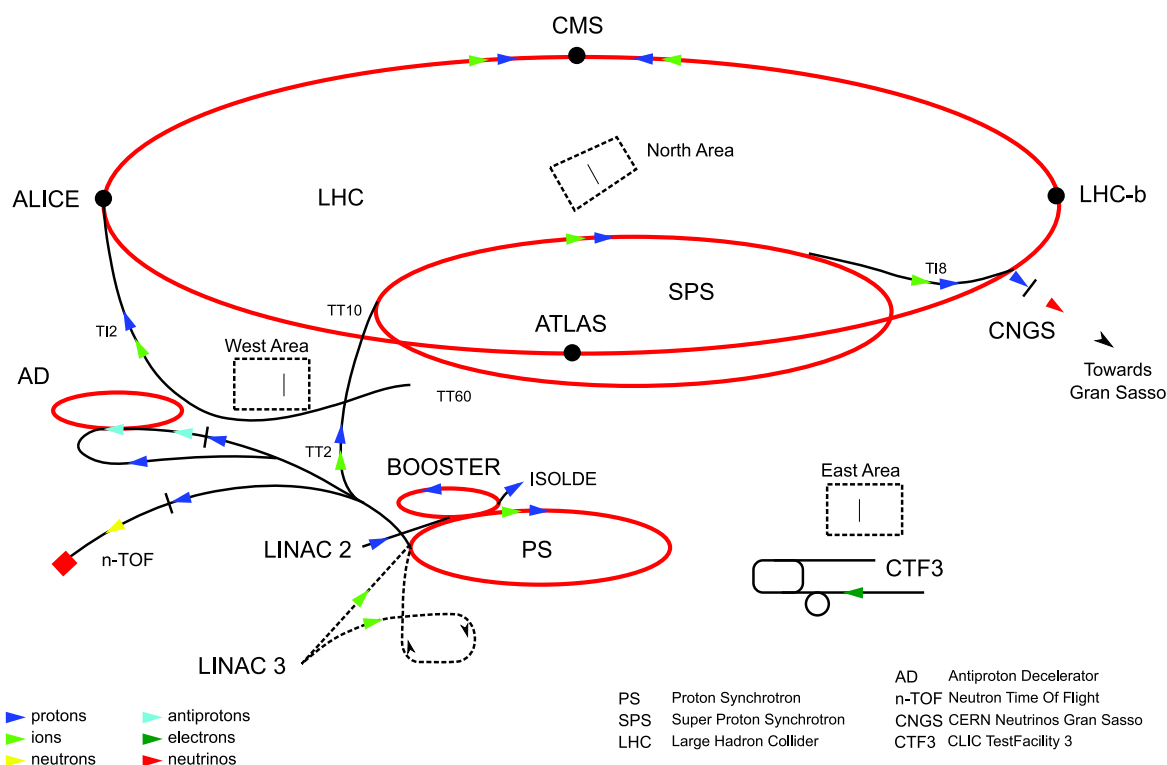


**Figure 3.1:** Schematic drawing of the CERN accelerator complex. The protons beams are passed through the LINAC2, PSB, PS, and SPS accelerators before being injected into the LHC. Taken from [94].

energy of the beam using RF cavities on the rings to accelerate the protons. Figure 3.1 shows the layout of the accelerator complex at CERN.

The PSB consists of four rings stacked on top of one another. At the beginning of the chain, the four rings are filled from beams through LINAC2 and then accelerated in the PSB and injected into the PS. This fill occurs again with another two beams injected through LINAC2 to PSB to the PS. This gives a total of six “bunches” in the PS. These bunches are a single group of protons which will be accelerated together through the RF systems of the accelerators. As the bunches are accelerated through the PS, three RF cavities operating independently at different phases further split each of the the bunches successively into three bunches, then each of these into a further two, then again in two. There is thus a total of 72 bunches orbiting the PS which are injected into the SPS, accelerated and then injected into the LHC. These bunches then constitute a single “bunch train” in the LHC. Several bunch trains are injected into the LHC with various gaps between them, for a total of 2808 bunches circulating in either direction when the ring is filled to its capacity. Once the LHC has been filled, the protons are accelerated to their maximum energy at which point they are put into collision mode, which stably

circulates the beams without acceleration and colliders them at the interaction points the detectors surround, while the experiments collect data from these collisions.

The number of events  $N$  for a given process with cross-section,  $\sigma$ , is:

$$N = \sigma L \quad (3.1)$$

which is written in terms of the integrated luminosity  $L$  which is a process-independent measure of the intensity of the beams integrated over the data collection period. The instantaneous luminosity  $\mathcal{L}$  is given by:

$$\mathcal{L} = \frac{N_b^2 n_b f_{rev} \gamma_r}{4\pi \epsilon_n \beta^*} F \quad (3.2)$$

where  $N_b$  is the number of particles per bunch,  $n_b$  is the number of bunches,  $f_{rev}$  is the revolution frequency,  $\gamma_r$  is the relativistic gamma factor,  $\epsilon_n$  the normalised transverse beam emittance, and  $\beta^*$  the beta function at the collision point. The  $F$  term is a geometrical correction factor which depends on the angle the beams cross each other  $\theta_c$  the RMS of the bunch length  $\sigma_z$  and the transverse RMS beam size  $\sigma^*$  (all taken at the interaction point):

$$F = \left( 1 + \left( \frac{\theta_c \sigma_z}{2\sigma^*} \right)^2 \right)^{-\frac{1}{2}} \quad (3.3)$$

The total luminosity  $L$  delivered by the machine is then the integral over time of the instantaneous luminosity  $\mathcal{L}$ . The design parameters of the LHC allow for a maximum instantaneous luminosity of  $\mathcal{L} = 10^{34} \text{ cm}^{-2}\text{s}^{-1}$ . Typical machine parameters for the 2011 and 2012 runs are given in figure 3.1. The machine delivered an integrated luminosity of  $L = 5.46 \text{ fb}^{-1}$  of  $\sqrt{s} = 7 \text{ TeV}$  collisions to ATLAS. It has also provided  $L = 22.8 \text{ fb}^{-1}$  of 8 TeV collisions in 2012. The analysis of this thesis uses the 2011 dataset with requirements on the quality of the data. This reduces the amount of usable collision data to  $4.59 \text{ fb}^{-1}$ .

The LHC provides 8 points for collision that are labelled, clockwise, Point 1 to 8 starting with ATLAS at point 1. At four of these points, particle detectors have been installed to record and measure the collisions. These experiments are:

**ATLAS** The general-purpose, nearly  $4\pi$  hermetic ATLAS detector is installed at Point 1. ATLAS is further described in the remainder of this chapter, and a complete description may be found in [92].

	2010	2011	2012	Nominal
Beam Energy [TeV]	3.5	3.5	4	7
$N_b$ [ $10^{11}$ ]	1.2	1.5	1.6	1.15
$n_b$	348	1380	1380	2808
$\epsilon_n$ [ $\mu\text{m}$ ]	2.4-4	1.9-2.4	2.2-2.5	3.75
$\beta^*$ [m]	3.5	1.5 $\rightarrow$ 1	0.6	0.55
$\theta_c$ [ $\mu\text{rad}$ ]	200	240	290	285
Bunch spacing [ns]	150	75 $\rightarrow$ 50	50	25
$\mu$	4	19	35	23
$L_{\text{max}}$ [ $10^{34} \text{ cm}^{-2} \text{ s}^{-1}$ ]	0.02	0.4	0.76	1

**Table 3.1:** Typical beamline parameters for the LHC during the 2010, 2011 and 2012 data-taking compared with the nominal design parameters.

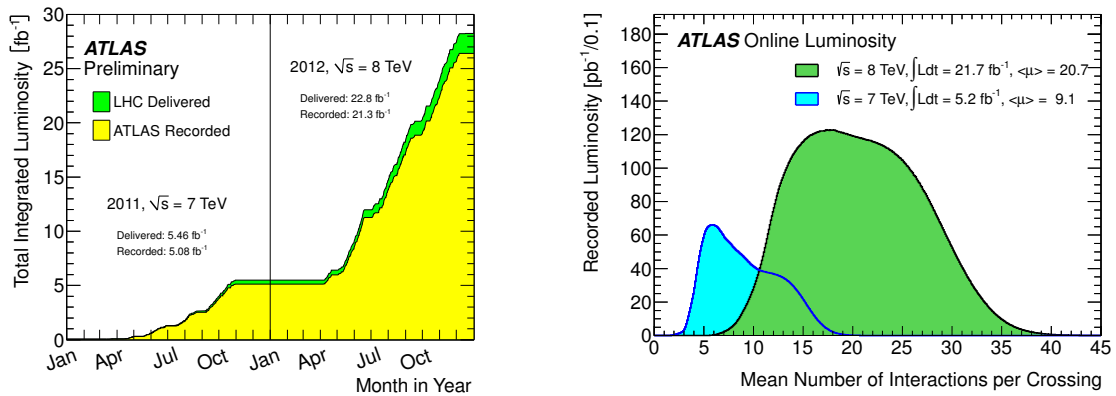


**Figure 3.2:** Integrated luminosity delivered and collected by ATLAS for the 2011 and 2012 runs (left) and the distribution of the average number of proton–proton interactions occurring per bunch crossing (right). Taken from [95].

**CMS** CMS at Point 5 is the other nearly-hermetic, general-purpose detector on the LHC [96]. The primary features of the CMS experiment include its large 4T solenoid magnet which encloses a 10-layer fully silicon charged-particle tracker, as well as the EM calorimeter and partially the Hadronic calorimeter. The iron yoke of the solenoid’s flux-return is instrumented with four layers of tracking to provide further muon detection and momentum measurement.

**LHCb** LHCb at Point 8 is designed for detecting and making precision measurements of the rare decays of  $B$  mesons, which can be used as indirect probes of possible physics beyond the SM [97]. It is designed as a single-arm forward spectrometer, with its inner-most tracking layer (the VELO (VERTex LOcator)) operating within the LHC beam vacuum<sup>1</sup> to provide high-precision vertex measurements of the  $B$  meson displacement.

**ALICE** Finally, ALICE at Point 2 is designed as a heavy-ion detector, addressing the physics questions of strongly interacting matter and the quark-gluon plasma [98]. ALICE contains several tracking and particle identification detectors allowing for good operation in the huge particle multiplicities of heavy-ion events. It also includes a muon spectrometer at  $-4 < \eta < -2.5$  to provide identification and separation of charmonium and bottomonium mesons.

## 3.2. ATLAS Overview

ATLAS is designed for the general purpose analysis of proton–proton collisions. Therefore, it was designed to provide nearly  $4\pi$  angular coverage around the collision point with systems to determine the kinematics of the collision products. The detector has been designed in such a way as to be able to observe, as much as possible, the potential new phenomena that may appear at the TeV scale. These considerations are outlined below.

The physics case for the general-purpose LHC experiments, ATLAS and CMS, was primarily to find and study the SM Higgs boson, if it existed. Confirming that a new resonance is the Higgs, and not some other particle, requires the discovery and precise measurement of several of the Higgs’ production and decay mechanisms. The study of these mechanisms provided benchmarks for the performance of all of the detector sub-systems. For example, the decay mode  $H \rightarrow \gamma\gamma$ , while expected to be small for a

---

<sup>1</sup>The VELO is retracted out when the beam is initially filled and needs to be focused, and in once beams have been declared stable.

SM Higgs, is one of the golden modes for Higgs discovery because of the extreme rarity of photons in proton–proton collisions. To identify and measure the photons, however, requires excellent particle tracking and highly performant calorimetry. The discovery of this channel is also helped by the longitudinal segmentation of the EM calorimeter, which allows the direction of the photon to be (roughly) measured and matched to the hard collision process. Similarly, the decay channel  $H \rightarrow ZZ^* \rightarrow \ell^- \ell^+ \ell^- \ell^+$  requires excellent muon and electron identification and charge determination over a large  $p_T$  range and  $H \rightarrow bb$  requires excellent jet and secondary vertex reconstruction to identify  $b$  decays from the predominantly light quark backgrounds. The  $H \rightarrow WW$  channel has large missing transverse momentum from the neutrinos from the  $W$  decay. Measurements in this channel therefore require good transverse momentum reconstruction, which implies hermetic electromagnetic and hadronic calorimetry with high resolution. The large luminosity requires that the detector components have fast, radiation-hard electronics and sensors with high granularity to handle the particle flux and reduce the influence of overlapping events. All of these requirements come into play in top pair reconstruction, which requires lepton identification, jet and missing transverse momentum reconstruction, and good tracking for the identification of  $b$ -jets from their secondary vertices.

The ATLAS detector is designed as a series of coaxial cylindrical subdetectors enclosing the proton–proton interaction point (the barrel), with a forward-backward symmetric series of disc-shaped subdetectors to complete the  $4\pi$  coverage (the end-caps). From inside out, the detector contains: a tracking system designed to detect and track charged, high energy particles coming from the central collision point, a calorimeter designed to measure the direction and energy of the outgoing particles, and a muon spectrometer designed to explicitly detect and identify muons from the collision event. The detector also has a three level, configurable triggering system, which works to identify and then store to disk the events of physics interest out of the massive number of collisions. Figure 3.3 shows a computer-generated image of the ATLAS detector in cut-away view, displaying all the detector sub-systems. Figure 3.4 shows an example of a dileptonic top pair event, illustrating the response of the ATLAS detector to these events. In particular, it illustrates the way the different sub-systems respond differently to the various particles produced in these events. The general performance goals of the detector are listed in table 3.2.

ATLAS uses a standard coordinate system and notation to describe the particles emerging from the interaction. The nominal interaction point, which is the centre of

**Table 3.2:** General performance goals of the ATLAS detector. Note that, for high- $p_T$  muons, the muon-spectrometer performance is independent of the inner-detector system. The units for  $E$  and  $p_T$  are in GeV.

Detector component	Required resolution	$\eta$ coverage	
		Measurement	Trigger
Tracking	$\sigma_{p_T}/p_T = 0.05\%p_T \oplus 1\%$	$\pm 2.5$	
EM calorimetry	$\sigma_E/E = 10\%/\sqrt{E} \oplus 0.7\%$	$\pm 3.2$	$\pm 2.5$
Hadronic calorimetry barrel and end-cap forward	$\sigma_E/E = 50\%/\sqrt{E} \oplus 3\%$ $\sigma_E/E = 100\%/\sqrt{E} \oplus 10\%$	$\pm 3.2$ $3.1 <  \eta  < 4.9$	$\pm 3.2$ $3.1 <  \eta  < 4.9$
Muon Spectrometer	$\sigma_{p_T}/p_T = 10\%$ at $p_T = 1$ TeV	$\pm 2.7$	$\pm 2.4$

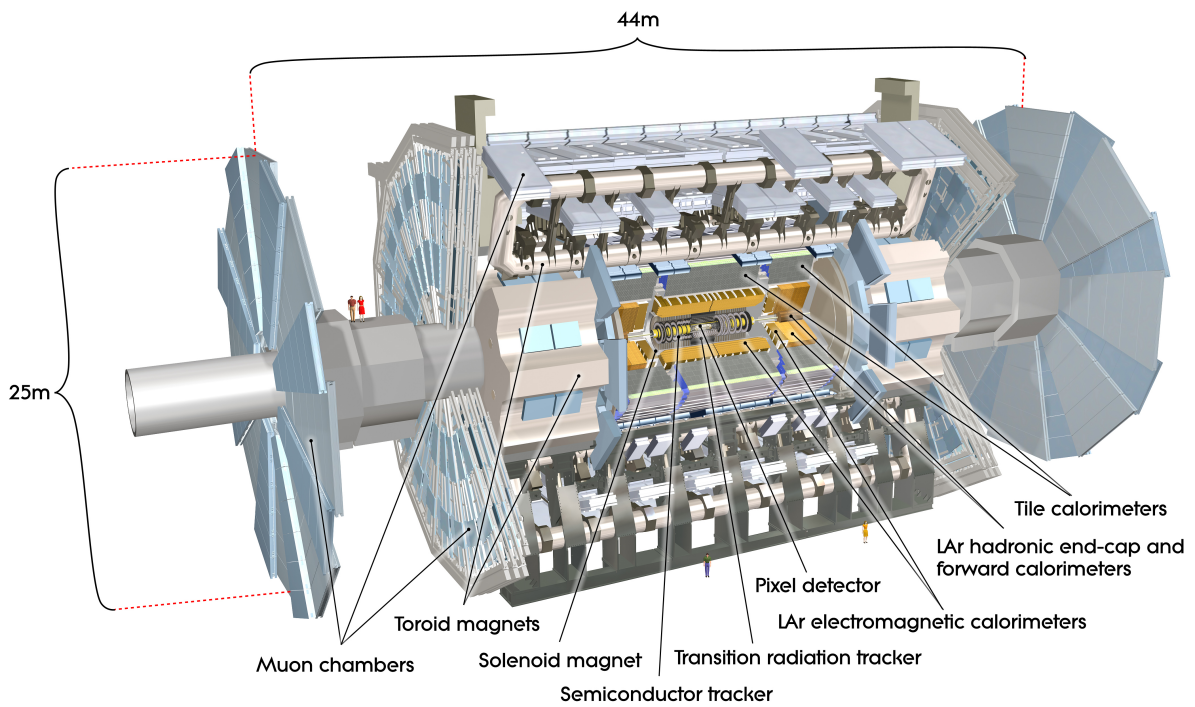


**Figure 3.3:** Overview of the ATLAS detector, including most of its subsystems shown in a cut-away view. From [92]

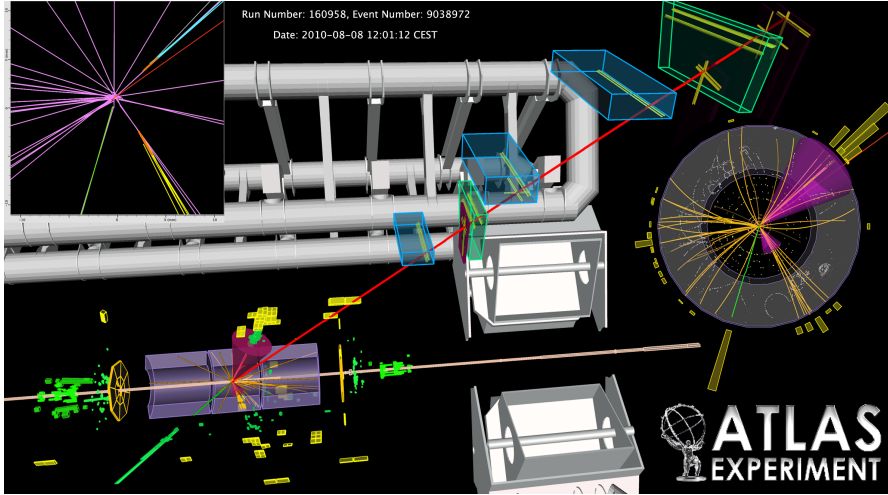


**Figure 3.4:** Event display of a top pair  $e\text{-}\mu$  dilepton candidate with two  $b$ -tagged jets. The electron is shown by the green track and calorimeter cluster in the 3D view, and the muon by the long red track intersecting the muon chambers. The two  $b$ -tagged jets are shown by the purple cones, whose sizes are proportional to the jet energies. The inset shows the XY view of the vertex region, with the secondary vertices of the two  $b$ -tagged jets indicated by the orange ellipses. Taken from [99]

the detector, defines the origin of the coordinate system. The  $z$ -axis is defined to be in the direction of the beam at the origin, with the positive side in the counter-clockwise direction of the LHC ring. The  $x$ - $y$  plane is defined so that the coordinate system is right-handed, with the  $y$ -axis pointing upward and the  $x$ -axis pointing to the centre of the LHC ring. The  $x - y$  plane is commonly referred to as the transverse plane, as it is transverse with respect to the beamline. Typically, rather than using the polar angle from the  $z$ -axis  $\theta$ , the pseudo-rapidity  $\eta = -\ln \tan \frac{\theta}{2}$  is used. This is because in the limit of a massless particle, the pseudo-rapidity is equivalent to the rapidity  $y = \frac{1}{2} \ln \frac{E+p_z}{E-p_z}$ , which is a quantity invariant with respect to Lorentz boosts along the  $z$ -axis. Solid angle distances  $\Delta R$  are then measured using the difference in pseudorapidity and the azimuthal angle  $\phi$  giving  $\Delta R = \sqrt{\Delta\phi^2 + \Delta\eta^2}$ .

Another important concept is the “fiducial volume” of the detector. This is defined as the kinematic acceptance of the detector for the various objects that are reconstructed. Since ATLAS is (approximately) cylindrically symmetric (so has complete azimuthal acceptance) and final state objects are approximately massless compared to their momenta, this usually refers to the  $\eta$  and  $p_T$  acceptances. This is analysis dependent and the ranges of the objects considered in the analysis of this thesis are presented in section 4.1.

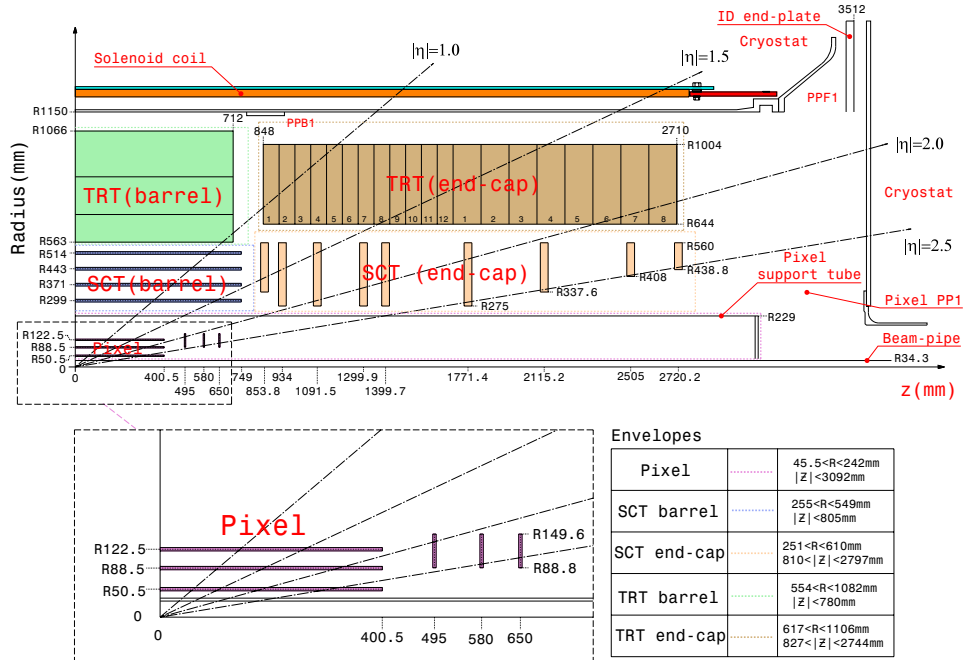


**Figure 3.5:** Schematic view of the ATLAS Inner Detector (ID). The diagram shows a  $r - z$  slice of the cylindrical barrel, disc endcaps along with the support tubes and solenoid providing charged particle bending inside the ID. Lines of constant  $\eta$  are indicated. Taken from [92].

### 3.3. The Inner Tracking Detector

The Inner Detector (ID) is a series of detectors designed to detect individual charged particles passing through them. The entire ID is encased in a 2T solenoid to bend the charged particles as they traverse through detector layers, thereby allowing momentum measurements. The innermost layers are 3 layers of Si pixel detectors which accurately measure the position of charged particles passing through them in all spatial dimensions. Then there are 4 layers of double-sided Si strip modules (SCT) which give accurate  $r - \phi$  and are double sided to provide stereo information in the  $z$  direction. Finally, there is the Transition Radiation Tracker (TRT) which consists of straw detection tubes filled with Xe gas operating in a proportional mode, with transition radiation layers interleaved to distinguish between electrons and hadrons through detecting the transition radiation produced by the electrons. Figure 3.5 shows the schematic outline of the inner detector.

The pixel detector [100] uses an n-type bulk 250  $\mu\text{m}$  thick sensors with  $n^+$  implants for readout. The pixel size is  $50 \times 400 \mu\text{m}^2$  with each pixel bump-bonded to the front-end electronics. The pixel sensors come in identical rectangular modules of dimension

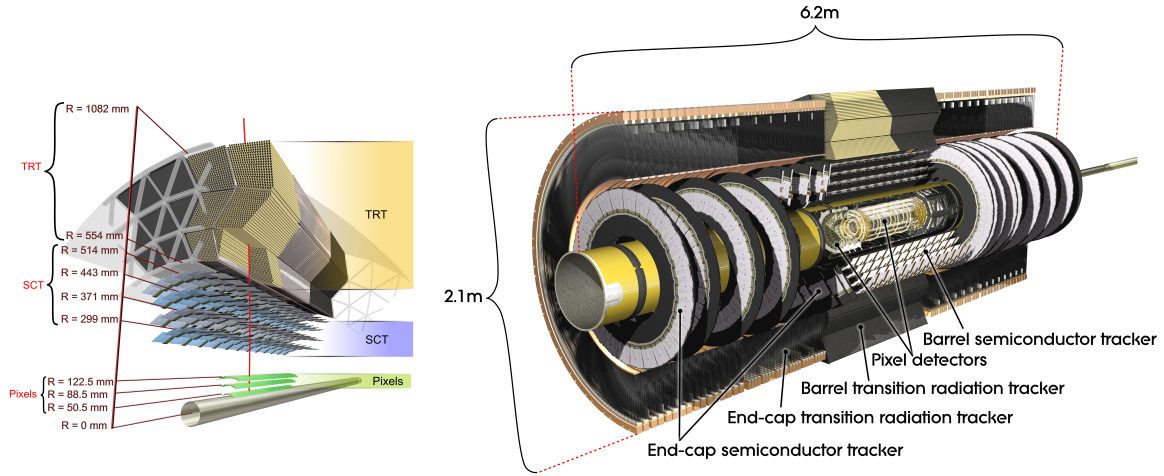


**Figure 3.6:** Cut-away view of the ATLAS Inner Detector in the barrel region (left) and of the entire Inner Detector (right). Taken from [92].

$19 \times 63 \text{ mm}^2$  which include the silicon sensor and the front-end electronics. There are 46080 read-out channels per module, and with a total of 1744 modules this gives around 80 million channels for the pixel detector system. This allows the pixel detector, whose innermost layer is only 50 mm radially from the interaction point, to deliver excellent spatial separation and identification of individual tracks even during high luminosity conditions. The layout for the positive  $z$  half of the detector (the negative  $z$  is a mirror image) is shown in figure 3.5 with a perspective representation in figure 3.6, where you can see the three concentric cylindrical barrel modules surrounding the interaction point, and three radial end-cap wheels on either end of the detector to provide precision tracking at high  $\eta$ . In the barrel, the modules are tilted at  $20^\circ$  with respect to the radial direction and overlapped to provide full azimuthal coverage, while in the endcaps, the modules are overlapped by alternating the placement of the sensors on the front and back of the wheel. This arrangements implies that a track produced at the origin within the  $|\eta| < 2.5$  acceptance of the pixel detector will pass through at least three pixel sensors.

The SCT [101] uses a more traditional single-sided p-in-n sensors with readout strips. The sensor thickness is  $285 \mu\text{m}$ , with a pitch between readout channels of  $80 \mu\text{m}$  in the rectangular barrel sensors, and radial strips in the trapezoidal end-cap sensors with mean pitch of  $80 \mu\text{m}$ . Each module consists of four sensors elements, 6cm in length. They are placed in daisy-chained couples glued on either side of a support board at a stereo angles of  $\pm 20 \text{ mrad}$ , which allows a single module to measure a 3D space-point of a charged particle traversing through the front and back modules. The modules are placed at a tilt angle typically of  $11^\circ$  in the four barrel layers to provide full coverage at

each layer. The tilt is in the opposite direction of the pixels due to the holes being the read-out charges in the SCT sensors whereas the electron cloud is read in the pixels. The trapezoidal end-cap modules can be attached to the end-cap wheels in a gap-less manner, with 9 end-cap wheels on either  $z$  side of the barrel. The placement of the end-cap wheels is such that a charged particle traverses at least 8 sensors (four double-sided modules) over the full  $|\eta| < 2.5$  coverage of the SCT. There are a total of 2112 barrel modules which have intrinsic resolutions of  $17 \mu\text{m}(r - \phi) \times 580 \mu\text{m}(z)$ , and 1976 end-cap modules with  $17 \mu\text{m}(r - \phi) \times 580 \mu\text{m}(r)$  resolution.

The Transition Radiation Tracker (TRT) [102, 103], the outermost detector in the ID, is built with 4 mm diameter straws filled with a Xe-based gas mixture and a gold-plated tungsten wire at the centre of the straw. Charged particles traversing the straw ionise the gas inside. The electric field set up between the straw tube and the interior wire creates a ionisation cascade, read out at the wire with a signal proportional to the energy of the original particle.

In the barrel, the 144 cm long straws are placed parallel to the beamline and the wires are split in half to allow separate measurements in positive and negative  $z$ . In the endcaps the straws are placed radially and have 37 cm length. There are a total of 351,000 straw tubes making up the TRT. A charged particle traversing through the TRT passes through, on average, 36 straws except in the barrel–end-cap transition region  $0.8 < |\eta| < 1.0$ , where the expected number of hits is 22. Between the straws, there is a polypropylene-polyethylene fibre mat. As charged particles pass through this material, transition radiation may be produced. The low energy photons produced are absorbed by the Xe-based gas mixture in the straws, creating an ionisation cascade. This then produces a much larger signal than minimum-ionising particles. The TRT straws thus have two signal thresholds with the higher one set to detect these “high-threshold hits”. Because the amount of radiation produced is a function of the particle energy divided by the mass, an electron will produce more transition-radiation on average than a pion, which is shown in figure 3.7. Typically, seven to ten high-threshold hits will be produced by electrons passing through the TRT.

### 3.3.1. Track Reconstruction

Tracks in ATLAS get reconstructed by an inside-out algorithm [105]. First, a pattern recognition is performed on the hits in the pixel detector to build three-point track candidates. Then, a combinatorial Kalman Filter algorithm is run to add hits in the

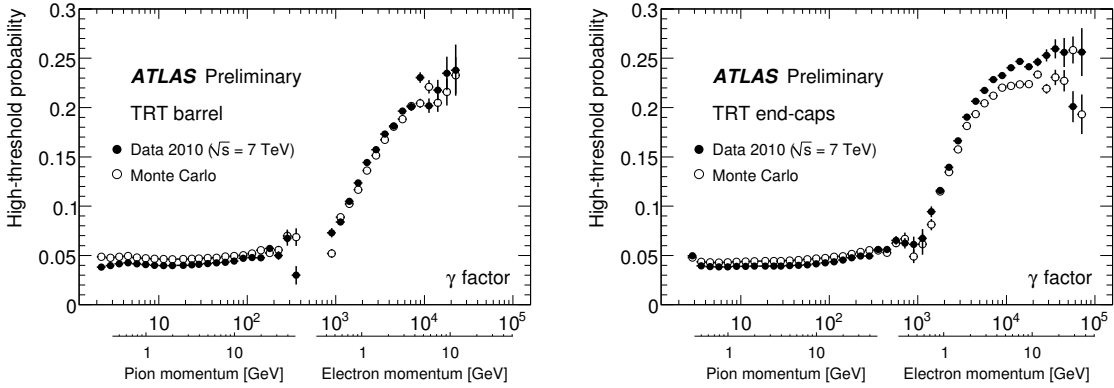


**Figure 3.7:** The probability for a charged particle producing a high-threshold hit as a function of the particle’s  $p_T$  in the barrel (left) and end-cap (right), illustrating the electron/pion discrimination capabilities of the TRT. Taken from [104].

successive detector radially outward through the silicon detectors. Ambiguities (shared hits, missing hits, etc.) in the track candidates thus built are then resolved and the tracks are extended into the TRT. Tracks reconstructed from this algorithm are required to have  $p_T > 400$  MeV.

A second outside-in algorithm is then run. It starts from track segments built from the TRT, and tries to match them to hits in the silicon detectors. The hits considered are those that haven’t been used in the inside-out step. The primary purpose of the algorithm is to reconstruct secondary tracks, that is tracks made from the decay of particles coming from the interaction point, for example the conversion of a photon into a pair of electrons within the tracking detector.

The standard Kalman Filter track fitter makes the assumption that the errors in the track position are Gaussian, which in general is a good assumption for particles whose momentum error are due to multiple scattering as they traverse through the detector material. However, depending on the  $\eta$  the charged particle passes through, the inner detector contains a few radiation lengths of material (figure 3.8), which can induce significant, large non-Gaussian changes in the momentum due to bremsstrahlung radiation. In particular, most electrons traversing through the detector will emit bremsstrahlung radiation. For this reason, electron track candidates are refitted using a Gaussian Sum Filter algorithm [106], which can use a sum of Gaussians of varying widths to model the detector tracking resolution, and allow electron track reconstruction to be improved by taking the larger error components into account.

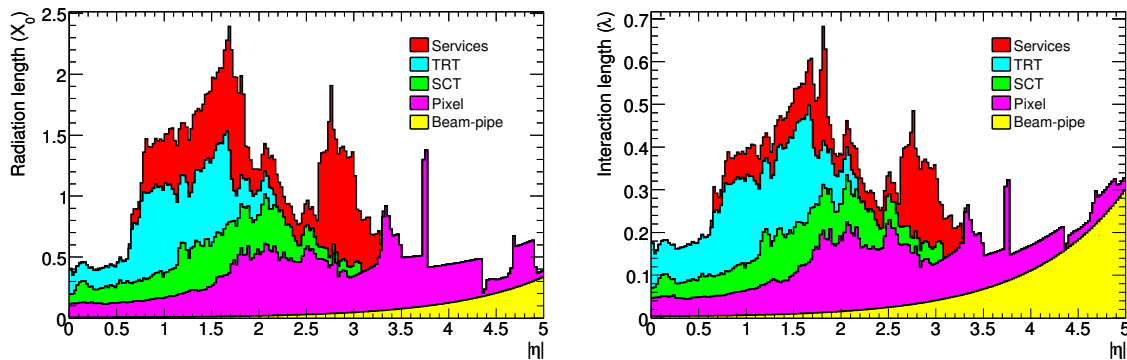


**Figure 3.8:** Amount of material in the inner detector as a function of  $\eta$  in terms of the radiation length (left) and interaction length (right). Taken from [92].

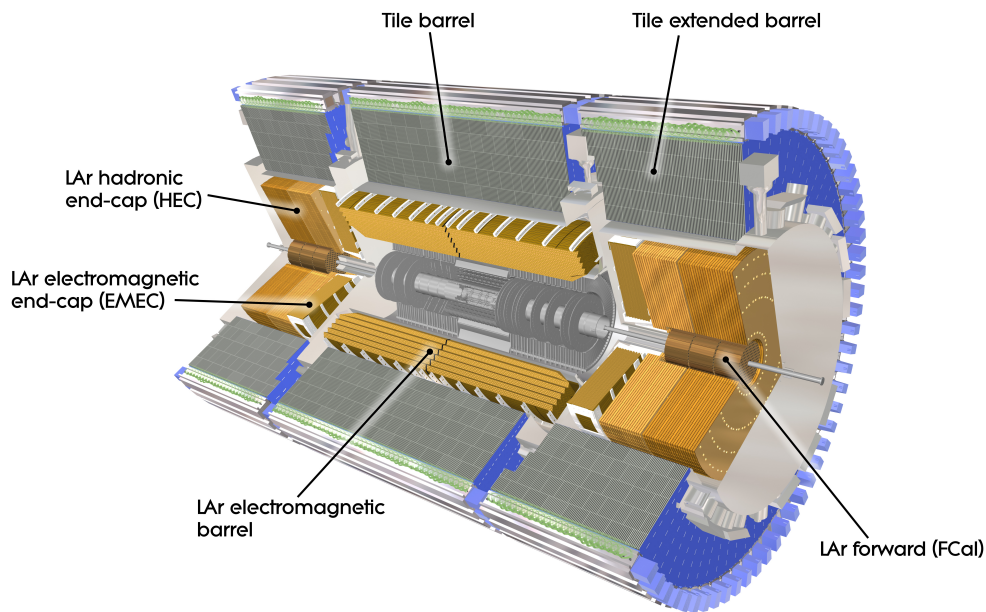


**Figure 3.9:** Cut-away view of the ATLAS calorimeter system. Taken from [92].

### 3.4. The Calorimeters

The ATLAS calorimeters are sampling calorimeters which provide destructive energy and direction measurements of electrons, photons and jets over a range  $|\eta| < 4.9$  with full  $\phi$  coverage. This is achieved by separate electromagnetic (for photons and electrons) and hadronic (for jets) calorimeters both with barrel and end-cap systems, and a combined forward calorimeter to provide the high  $\eta$  measurements. The various calorimeter systems are depicted in figure 3.9.

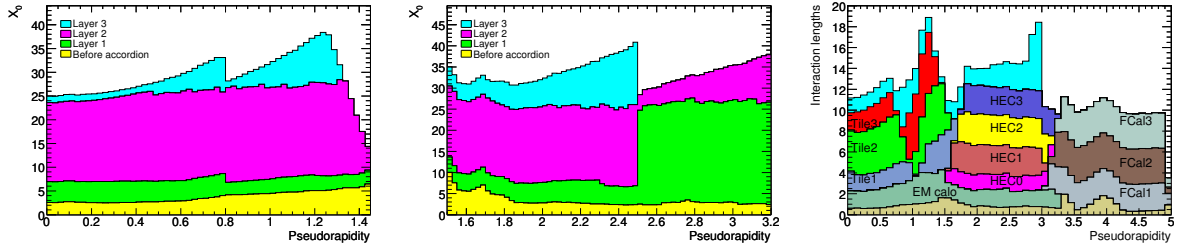


**Figure 3.10:** Cumulative amount of material in the EM and hadronic calorimeters. The left figures show the number of radiation lengths of material before the accordions, and for each accordion layer for the barrel (leftmost) and endcap (right). The rightmost figure shows the number of interaction lengths of material before the calorimeters, for the EM calorimeter as a whole, and for the various sections of the hadronic calorimeters. Taken from [92].

## Electromagnetic Calorimeters

The purpose of the electromagnetic (EM) calorimeters is to measure the energy contained by a photon or electron emanating from the collision. The mechanism is that a high-energy particle travelling through the calorimeter material will interact with the material, with electrons emitting photons and photons converting into electron-positron pairs, and each emission thereby reduces the energy of each particle in the cascade. The resultant electromagnetic shower will continue until the particles are below the ionisation or excitation thresholds at around an MeV. The ionisation or photon emissions can then be collected by a sensitive detector volume and thus measuring the energy of the initial particle producing the cascade. The size of an EM calorimeter is given in radiation lengths  $X_0$ , the mean distance over which an electron loses all but  $1/e$  of its initial energy due to bremsstrahlung. The material distribution in the EM calorimeter is shown in figure 3.10.

The EM calorimeter of ATLAS is a LAr sampling calorimeter folded into an accordion geometry which allows for full  $\phi$  coverage. The basic principle of a sampling calorimeter is to alternate absorber and read-out sections. The absorber material is very high density and so most of the cascade occurs in these sections. The active layer therefore only reads out a portion of the energy deposited and the full energy of the shower is estimated based on this read-out along with knowledge of the geometry and composition of the calorimeter to reconstruct the complete electromagnetic shower.

The EM calorimeter consists of lead absorbers alternated with active LAr layers with read-out electrodes situated in the middle of each pair of absorbers. Segmentation of the

electrodes is achieved by etching patterns on the different layers. The EM calorimeter is divided into a barrel section covering the range  $|\eta| < 1.47$ , and two end-caps on either side in the range  $1.475 < |\eta| < 2.5$  for the outer end-cap and  $2.5 < |\eta| < 3.2$  for the inner wheel, with each housed in its own cryostat. The section of the EM calorimeter matching to the ID range of  $|\eta| < 2.5$  has been optimised in granularity and is segmented into three radial sections of decreasing granularity to provide precision measurements of electrons and photons both in energy and direction. This segmentation is shown in figure 3.11. The inner wheel is segmented into two sections in depth and has a coarser granularity. Since EM showers will generally start before the calorimeters due to the few radiation lengths of the detectors and services radially closer than the EM calorimeter, a presampler is also included in the region  $|\eta| < 1.8$ . However, the EM calorimeter's barrel–end-cap transition region contains a large amount of passive material and so there is a reduction of measurement precision. Therefore, most physics analyses exclude electrons and photons within  $1.37 < |\eta| < 1.52$ , which is commonly referred to as the “the crack”. The total amount of material in the EM calorimeter is about 25 radiation lengths, which is sufficient to contain almost all showers of electromagnetic origin.

The performance goals of the EM calorimeter in terms of the energy resolution are given in table 3.2. From measurements of the  $Z \rightarrow ee$  mass peak, the effective constant term of the energy resolution has been extracted from 2010 data (the statistics were too small to determine the energy dependence), and were found to be 0.5% to 1.5% in the barrel region, and around 3% in the end-cap [107].

## Hadronic Calorimeters

Hadrons passing through the calorimeters initiate hadron showers, which are a succession of inelastic nuclear interactions with the detector material. A portion of the energy will develop into electromagnetic showers due to the production of neutral pions, which decay into photons. Typically, about a third of the energy goes into this electromagnetic component, though with large stochastic variations in this fraction. Also, some energy will be invisible to the detector, being lost either as the binding energy needed to release nucleons from the target nuclei, or low energy neutrons which do not ionise the detection material. The response of the electromagnetic component of the shower is therefore typically higher than the response to the hadronic component, due to this invisible energy. Since the production of neutral pions is a stochastic process, in any given event the fraction of the energy in the electromagnetic component is unknown, and therefore

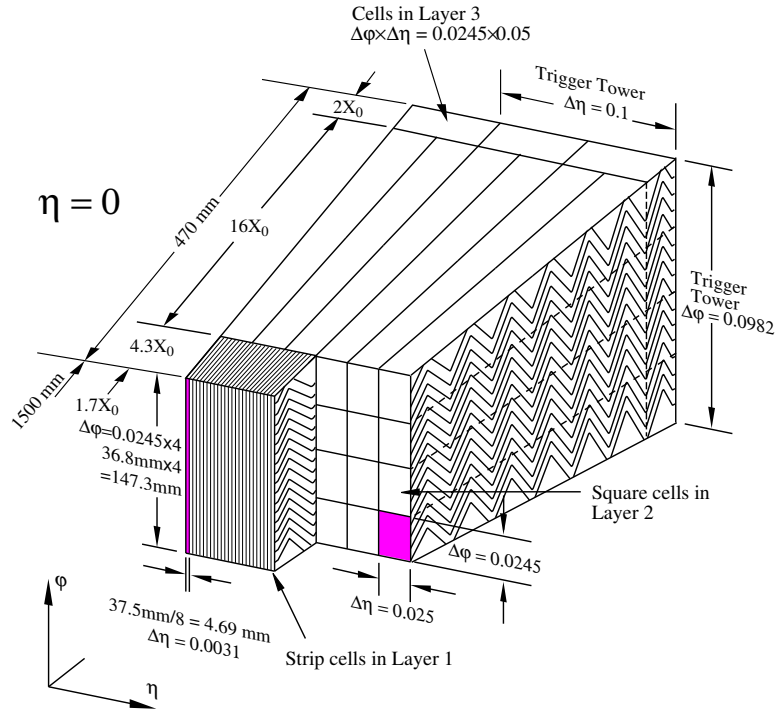


**Figure 3.11:** Figure showing the segmentation and accordion structure of the EM calorimeters. Taken from [92].

the response difference must be compensated. In ATLAS, this is done through offline calibration, discussed further in section 4.1.4.

The typical size of the showers is characterised by the nuclear interaction length,  $\lambda$ , which is the mean free path between interactions. The total material in terms of interaction length is shown for the ATLAS calorimeters in in figure 3.10, where it can be seen to be much larger than for the radiation length. To contain the shower in a reasonable volume, ATLAS also uses sampling calorimeters for the hadronic calorimeters, as already mentioned for the EM calorimeters.

The hadronic calorimeter is provided by two separate technologies. For  $0 < |\eta| < 1.7$ , the calorimeter is a central barrel and extended barrel made of scintillator interleaved with plates of steel absorbers. The hadronic end-caps, which cover  $1.5 < |\eta| < 3.2$  are copper/liquid-argon detectors with a flat-plate geometry rather than the accordion geometry of the EM calorimeters. Finally, the forward calorimeters, which are housed in the same cryostat as the end-cap calorimeters, cover  $3.1 < |\eta| < 4.9$  using LAr as the active material and are in three layers: the first layer is an electromagnetic module with copper absorber, and then two hadronic layers with tungsten absorbers. Another important function of the hadronic calorimeters is to eliminate the “punch-through” to the

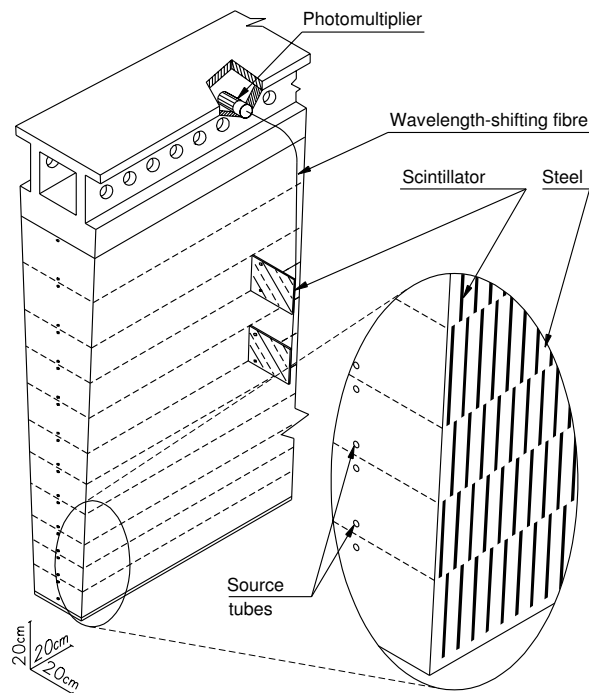


**Figure 3.12:** Illustration of the tile calorimeter absorber/scintillator layout and the readout. Taken from [92].

muon systems. That is, all the energy produced through hadronic and electromagnetic decays, other than muons, should be absorbed before the muon spectrometer. The calorimeters have material contributing 7-10 interaction lengths, which is sufficient to reduce punch-through to an acceptable level.

The tile calorimeter layout is depicted in figure 3.12. The active scintillators are embedded between steel plates whose short interaction length is sufficient to keep the barrel compact and inexpensive, and provide sufficient material to limit the punch-through. The light produced from the scintillation is collected by wavelength shifters at one edge of the scintillators, grouped radially, and guided to readout photomultiplier tubes on the outside of the calorimeters.

The performance goals of the hadronic calorimeters are given in table 3.2. The calorimeter response to single hadrons has been measured in  $\sqrt{s} = 900$  GeV and 7 TeV data collisions from 2009 and 2010 by reconstructing  $K_S$  and  $\Lambda$  particle decays [108]. The response uncertainty is 2–5% for central isolated hadrons.

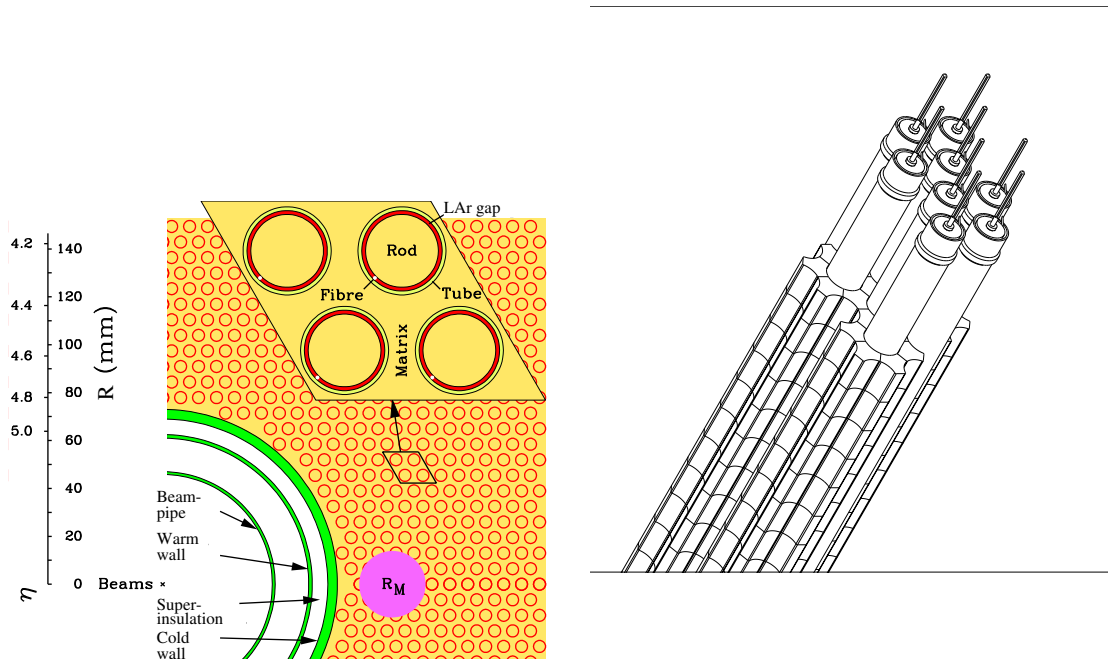


**Figure 3.13:** Illustration of the structure of the forward calorimeter. The EM calorimeter electrode in copper matrix is shown on the left, the hadronic tungsten electrodes surrounded by tungsten slugs is shown left. Taken from [92].

## Forward Calorimeter

The forward region is exposed to the highest particle flux (since most of the proton collisions result in only small transverse deviations). The detectors in this region therefore need to be extremely radiation hard and fast to cope with the high intensity. This region is provided for at ATLAS by the Forward Calorimeter (FCal). The FCal occupies the same cryostat as the end-cap calorimeters and covers  $3.1 < |\eta| < 4.9$ . It is split into three modules: an electromagnetic module (FCal1), followed by two hadronic modules (FCal2 and FCal3). Each module is 45 cm deep. Figure 3.13 shows an illustration of the structures contained in the forward calorimeter. FCal1 is made of a stack of copper plates with holes drilled through them. Through the holes, an electrode structure is inserted which consists of a copper tube encasing a copper rod, separated by a plastic fibre wound around the rod. FCal2 and FCal3 are each made using two copper plates between which are spanned by a similar electrode structure to FCal1, except tungsten rods are used instead of copper rods. The electrodes are surrounded by tungsten slugs. Tungsten is chosen to provide the short absorption length required for the calorimeter.

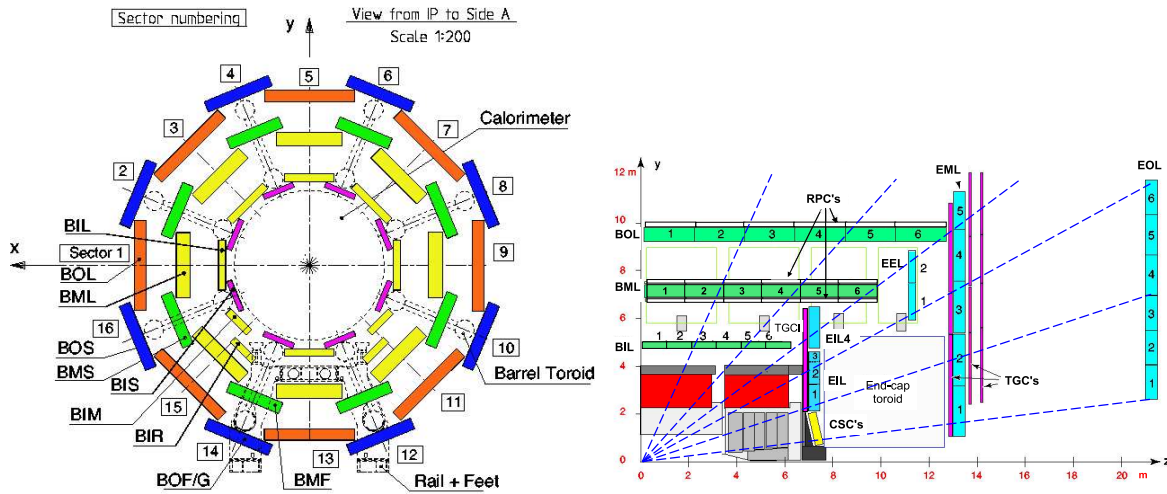


Figure 3.14:  $r - \phi$  (left) and  $r - z$  cross-sections of the muon detection system.

### 3.5. The Muon Spectrometer

Muons are the only known charged particles which can pass through the calorimeters. They are also the by-products of several important rare physics processes, including the top pair decays considered in this thesis. Muons are thus an exceptionally clean object for signalling the presence of interesting physics events. Therefore, after the layers of calorimetry, a large, dedicated muon detection system is in place. The muon detector consists of an air-core toroidal magnet system, with several types of charge particle tracking stations inside, illustrated in figure 3.14.

The magnetic field, which provides the bending needed for charge assignment and momentum measurement in the muon spectrometer, is provided by three sets of large air-core toroids. The toroid system consists of eight coils assembled symmetrically around the beam to provide a toroidal magnetic field around the outside of the main barrel components. The central barrel toroid covers  $0 < |\eta| < 1.4$ , while the two end-cap toroids cover  $1.6 < |\eta| < 2.7$ . The non-toroid region  $1.4 < |\eta| < 1.6$  provides much less bending power and so there is a corresponding degradation in the momentum resolution in this region.

The muon system provides tracking for muons in the range  $|\eta| < 2.7$ , with triggering capabilities for muons in the range  $|\eta| < 2.4$ . Over the full range  $|\eta| < 2.7$ , precision measurements of the track coordinates in the bending direction of the magnetic field are provided by Monitored Drift Tubes (MDTs). There are 1088 chambers of MDTs installed in ATLAS, covering the range  $0 < |\eta| < 2$  with three layers of chambers and

$2.0 < |\eta| < 2.7$  with 2 outer layers, with the inner layer replaced by the Cathode Strip Chambers (CSCs) in this region. Each chamber consists of three to eight layers of drift tubes. The drift tubes are directed in the  $r - \phi$  plane to provide high precision  $\eta$  reconstruction, because the geometry of the toroid field means that muons bend in the  $\eta$  direction in the muon spectrometer. The MDT chambers then provide a resolution of  $80 \mu\text{m}$  per tube which is about  $35 \mu\text{m}$  per chamber in the  $z$  axis.

At larger pseudorapidities,  $2 < |\eta| < 2.7$ , Cathode Strip Chambers (CSCs) – multiwire proportional chambers with cathodes segmented into strips – with higher granularity than the MDTs are used for the inner-most tracking layer, rather than MDTs, due to their higher rate capabilities and time-resolution capabilities and as they are able to withstand the higher background conditions. The CSCs provide a resolution of  $40 \mu\text{m}$  per chamber in the bending plane and 5 mm transverse to the bending.

Separate detectors are used for triggering high momentum muon events. In the barrel, Resistive Plate Chambers (RPCs) are used, while Thin Gap Chambers (TGCs) are used in the end-cap regions, allowing coverage of the range  $|\eta| < 2.4$ .

The performance goals of the muon detector in terms of muon momentum resolution is given in table 3.2. A study of the 2012 collision data of the  $Z \rightarrow \mu\mu$  mass peak has shown that the muon momentum resolution modelled in the ATLAS detector simulation is in good agreement with the data [109].

### 3.6. The Trigger System

At full luminosity during the 2011 data taking run, every bunch crossing contained up to 19 proton–proton collisions, with an average of 5 collisions. Figure 3.2 shows the exact distribution. Most of these collisions were soft scattering, producing only soft inelastic proton–proton interactions, events known as “minimum bias” (see also section 4.2.1). In general, the processes of interest are “hard” events, meaning that significant fractions of energy were involved in the collisions, with much of the energy in the event going into perturbatively calculable processes where the partons involved in the collision can be treated as acting freely, as discussed in section 2.3. These events occur at a much lower rate than the soft, minimum bias events. For example, the total inelastic proton–proton cross section is  $73 \text{ mb}$  [110], while the predicted top pair production cross-section at 7 TeV is  $177 \text{ fb}$  at the complete NNLO+NNLL [69]. In the 2011 data collection period, bunch

crossings occurred every 50 ns, and each crossing requires approximately 1 MB of data to be stored as an event for later analysis. Therefore, we need to be able to distinguish hard events from soft events in real time and store only those events of interest, in order to keep the data rate manageable. This is accomplished using a sophisticated, multi-levelled triggering system to find the events of interest and only store data for those events.

The trigger system consists of three stages which progressively refine the decision to accept or reject events for storage. These are the Level 1 (L1), Level 2 (L2) and the event filter (EF).

The hardware-based L1 trigger uses a subset of the detectors to perform an initial search for high-transverse momentum electrons, photons, muons, taus, and jets, as well as large missing and total transverse energy. Results from the L1 trigger are processed by a central trigger processor (CTP). The CTP allows for “menus”, or combinations of trigger selections, to be defined and pre-scaled, that is randomly accept only a specified fraction of events that pass a particular trigger menu. The L1 trigger defines a region-of-interest (RoI, an  $(\eta, \phi)$  area of the detector) where the selection process identifies interesting features (high  $p_T$  muons or high  $p_T$  electrons in our case). The design parameters for the L1 trigger reduces the event rate to about 75 kHz, from the starting rate of up to 40 MHz at 25 ns bunch crossings. L2 and the EF are both software-based and collectively form the High Level Trigger (HLT). The L2 uses the full granularity information of the detector in the L1 RoI (about 2% of the detector) to make a further refined selection; it is designed to reduce the rate to 3.5 kHz. The final stage is the event filter, which uses the full detector information and the offline reconstruction algorithms to make a final event selection. During the 2011 data-taking period, the L1 rate was kept below 60 kHz, the L2 below 5 kHz and the EF rate was 400 Hz averaged over the LHC fills [111], and so the trigger system was operating beyond design parameters.

The data output is separated into periods, designated with a letter. Each period represents a period of data taking when the LHC machine conditions were approximately the same and the trigger menu was stable. In 2011, the periods of interest for our data are from B to M; table 3.3 shows the luminosities collected in each of these periods.

Semi-leptonic top pair events can be most easily identified from the single, high transverse momentum lepton produced. Thus, single lepton triggers were used to select events for analysis. The remainder of this chapter will describe the electron trigger

Period	Luminosity ( $\text{pb}^{-1}$ )
B-D	173.798
E-H	924.67
I	328.61
J	220.38
K	575.156
L-M	2368.38

**Table 3.3:** Amount of data collected in each run period in 2011 by the ATLAS detector, determined to be of good quality and used in this thesis. Periods are merged together when there is no change in the conditions for the triggers collected in this thesis.

system and the muon trigger system, and the actual triggers used in the semi-leptonic top pair analysis.

### 3.6.1. Single Electron Trigger

The electron and photon triggers used in 2011 are described fully in [111]. At L1, the Cluster Processor (CP) module is used to identify  $e/\gamma$  leptons. The calorimeters are split into  $0.1 \times 0.1$  towers and the CP searches each  $2 \times 2$  combination of these towers for an energy sum above a certain (programmable) threshold. The  $e/\gamma$  algorithm uses the EM calorimeter only for this threshold, while the  $\tau$  algorithm uses the energy sum of the EM and HAD calorimeters. For each window that meets the threshold requirement, the  $4 \times 4$  cell, including both the EM and HAD calorimeters, enclosing the selected window can be processed for isolation requirements, that is, requiring the 12-cell window surrounding the chosen core to have lower cluster energy than a given threshold, which will in general depend on the energy required of the core. When a region that satisfies the trigger requirements is found, the event is accepted and the coordinates of its  $2 \times 2$  core are sent to the L2 trigger as the Region of Interest (RoI) for further processing.

At L2, the electron trigger uses the data from the full suite of detectors in the  $0.4 \times 0.4$  region around the L1 RoI. Track reconstruction is performed using a speed-optimised algorithm inside the RoI to determine whether a good, matched track can be found, which would be expected if the cluster was made by an electron, but no tracks in the case of an unconverted photon. For clustering, the L2 algorithm finds the cell with the largest energy deposit in the RoI, and takes the cluster energy as the sum of the cells in a

$\Delta\eta \times \Delta\phi = 0.075 \times 0.175$  region in the barrel and a  $0.125 \times 0.125$  region in the end-caps. The position is given as the energy-weighted average of the cluster. The EF uses offline tracking algorithms to reconstruct the electron track and offline algorithms to find the electron cluster in the calorimeter with a sliding window algorithm and then apply offline corrections (see section 4.1.2). At both L2 and the EF, electron candidates are selected if they pass selection criteria based on quantities constructed from the calorimeter cluster and track. These include the lateral width of the shower (small for real electrons), the amount of energy in the hadronic calorimeter (small for real electrons), requiring tracks whose position extrapolates to the within a defined region of the calorimeter cluster centre, and requiring the inner pixel detector to be hit. There are options for applying these cuts at the loose, medium or tight level, with the requirements becoming more and more stringent; for example, no track cuts are applied at loose, and a certain number of TRT hits were only required at tight. The unprescaled triggers in 2011 operated at the medium level.

The electron triggers used were always the lowest unprescaled  $p_T$  threshold single electron triggers. For periods B-H, and I-K, `EF_e20_medium` and `EF_e22_medium` were used respectively. These EF triggers were seeded from the `EM14` and `EM16` L1 triggers respectively. These simply required the energy in the EM calorimeter to be above the number given after `EM`, with no hadronic calorimeter requirements. To cope with the increasing luminosity in the runs later in the year, the electron triggers needed to add hadronic leakage requirements. The triggers used were `EF_e22vh_medium1` and `EF_e45_medium1` for periods L-M. The `EM16VH` L1 trigger which seeded `EF_e22vh_medium1` had the additional requirement that no more than 1 GeV in a  $0.2 \times 0.2$  window in the hadronic calorimeter behind the EM cluster was allowed. The transition from `medium` to `medium1` involved tightening the shower shape variables to be closer to the offline definitions and adding extra track quality cuts, including requirements on the fraction of high-threshold TRT hits and requiring the inner-most pixel layer to be hit (previously this was only required at tight). This was done to avoid raising the  $p_T$  threshold but have negligible effect on the final offline efficiency. The trigger rates from the EF algorithms can be seen in figure 3.15. The transition from `EM14` to `EM16` to `EM16VH` reduced the L1 trigger rate from 7.3 kHz to 5.7 kHz to 3.6 kHz at the reference luminosity  $L = 1.0 \times 10^{33} \text{ cm}^{-2}\text{s}^{-1}$ .

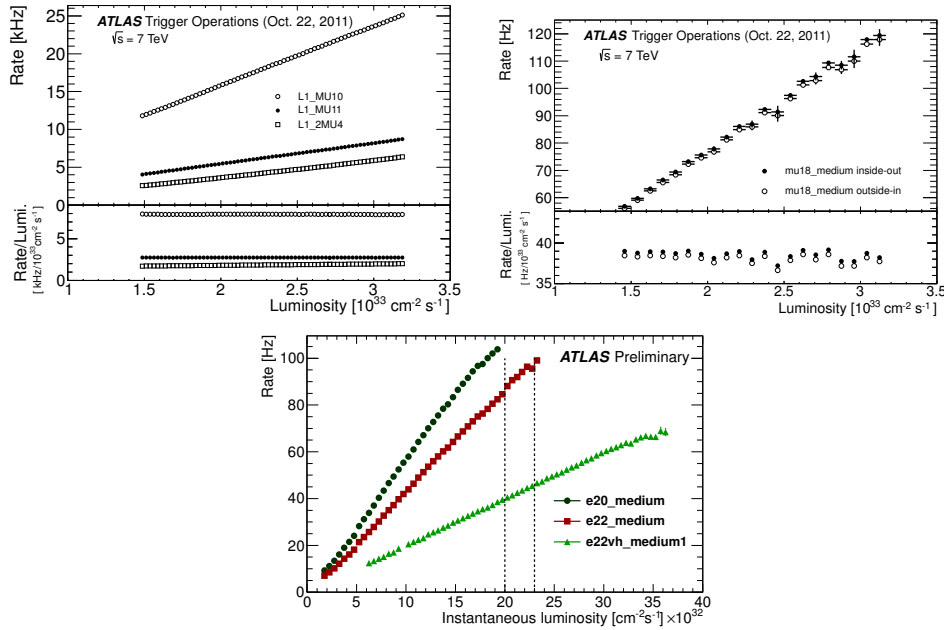


**Figure 3.15:** Muon (top) and electron (bottom) trigger rates for the 2011 data periods versus luminosity. For the muons, displayed is the L1 trigger rates for different  $p_T$  thresholds (left) and the trigger rate for the EF mu18\_medium stream (right) versus luminosity. For electrons, the event rates for the various EF triggers are shown versus luminosity. Taken from [111] for electrons and [112] for muons.

### 3.6.2. Single Muon Trigger

The 2011 muon triggers are fully described in [112]. The muon trigger uses information from dedicated RPC detectors in the barrel region  $|\eta| < 1.05$ , and TGCs in the outer regions  $1.05 < |\eta| < 2.4$ . In the barrel, the trigger looks for a signal in RPC2 (see figure 3.14 for the geometry of the detectors), and then interpolates an infinite momentum path between the interaction point and searches for a coincidental hit in RPC1, with the width of the search region determined by a  $p_T$  threshold in the trigger. For low momentum muon triggers, this is the only requirement. For high-momentum tracks, the trigger does the same extrapolation to RPC3 and looks for another coincidence hit. The end-cap similarly looks for hits on an outer plane (see figure 3.14 for the geometry), and interpolates an infinite momentum track from the IP to the M2 plane, looking for a coincidence hit in a  $p_T$  defined window. This information is combined with information from the inner end-cap layers to make the final trigger decision. For both low and high momentum triggers, if a hit pattern matching the requirements is found and the trigger gets accepted, the  $\eta$  and  $\phi$  information is combined and sent as an RoI to the L2 trigger.

For the muons, the L2 seeded by the muon L1 uses the high-granularity MDT and CSC data from the RoI and the initial L1 rough momentum measurement to construct higher quality muon tracks. The reconstructed muon track is first reconstructed using only the muon spectrometer information, and then further refined by combining with a track from the ID using a fast track combination algorithm. The calorimeter information can also be used at this level to define isolated muons, by looking at the energy deposited in the calorimeters along the muon track, and require the muon candidate to be isolated from large deposits. For the 2011 triggers used here, however, isolation was not required.

In the top pair analysis, the `mu18` and `mu18_medium` EF level triggers are used for periods B-I and J-K, respectively. These are seeded by the L1MU10 and L1MU11 respectively [112]. The rates for both the L1 and EF triggers versus the luminosity are shown in figure 3.15.



# Chapter 4.

## Object and Event Selection

This section details the objects, events, and samples that will be studied in chapter 6. Physics objects that correspond to the objects produced in the hard process are reconstructed from the detector output. This is the subject of section 4.1. In order to understand the distortion of the objects by the detector, Monte Carlo (MC) techniques are used to generate simulated samples of the physics processes which will be used in the analysis. The use and production of these MC samples are discussed in section 4.2. For several of the processes which form a background to the top pair production, we use data-driven methods to estimate the size and distribution. Section 4.3 describes these techniques. Finally, given that we can find the true objects and their kinematics produced by the MC, we can use this information to produce objects equivalent to the reconstructed objects, but before the measurement and influence of the detector. These “particle-level” objects built from the MC are described in section 4.4. For convenience, table 4.6 summarises the selections at both reconstruction and particle-level.

The work presented in this chapter summarises the the work of the top reconstruction and top background groups at ATLAS, for the 2011 data analysis. These groups are responsible for producing the results needed to go from the detector output to top quark events, including producing simulation versus data corrections and background estimations. The author played a role in this as a developer of software which takes the various selections, corrections, and background estimations and applies them to the detector data to produce the final reconstructed distributions of section 4.3.4. This software has become the standard resource in the ATLAS top group for performing these selections and corrections.

## 4.1. Object Reconstruction and Selection

From the detector outputs detailed in Chapter 3, physics objects may be created. The detectors are used to identify the type of object that was detected and then corrections based on the object type are applied to produce a 4-vector describing the object’s momentum. Further corrections and calibrations can be applied to the simulated samples so that the simulation may better match the performance of the detector seen in data. This section lists the major physics objects and describes how they are identified and calibrated. Then, the event selection used to identify proton–proton collisions that are likely to be from top pair production events, based on the output of the object reconstruction, is described.

### 4.1.1. Primary Vertex

The primary vertex (PV) is the vertex reconstructed from charged particle tracks that originated from the hard collision event. Since several proton–proton collisions will occur each bunch crossing (for the 2011 running period of interest, from six to eleven on average, see figure 3.2), some of the calorimeter deposits and tracks reconstructed will be from pileup events unrelated to the primary, hard interaction which is being studied. Also, several of the objects will have their momenta corrected based on the assumption of the position of the primary vertex being the origin of the hard collision. Therefore, reconstructing and associating physics objects to this primary vertex is of particular importance.

The vertices reconstructed in a beam-crossing are found using an iterative vertex fitting procedure [113]. An initial vertex seed is obtained by finding the global maximum in the distribution of the  $z$  coordinates of the tracks. Then, the position of the vertex is found using an adaptive vertex fitting algorithm [114]. This algorithm fits the vertex with a  $\chi^2$ -based algorithm, and iteratively down-weights tracks incompatible with the vertex using a deterministic annealing scheme.<sup>1</sup> Tracks which are incompatible with the primary by more than about  $7\sigma$  (determined from the  $\chi^2$ ) are used to seed a new vertex.

---

<sup>1</sup>In deterministic annealing, a measurement with  $\chi^2$  is reweighted by a temperature  $T$  to  $e^{\chi^2/2T}$  and a likelihood function based on these weights is minimised to find the track parameters. The “deterministic” part is that a fixed set of temperatures is tried one after the other (an example schedule giving good results in the study in [114] is the geometric series  $T = 32, 16, 8, 4, 2, 1$ ), going from large temperatures to  $T = 1$  using the track parameters found in the last temperature step as a seed. Intuitively, using higher temperatures “flattens out” the likelihood function, and the minimisation routine is therefore less likely to fall into a local minima, allowing the phase space to

This procedure is repeated until all the tracks are associated with a vertex, or no new vertices are produced.

The primary vertex of the event is to be distinguished from the pileup vertices, which are the vertices from proton–proton collisions in the bunch crossing that are not associated with the hard interaction, and secondary vertices, which are formed from particles in the hard collision which travel a measurable distance away from the primary vertex before decaying.

For our analysis, we require that the primary vertex have at least 4 tracks with  $p_T > 400$  MeV associated to it.

#### 4.1.2. Electrons

Electrons are reconstructed [107] from energy deposits in the EM calorimeter using a sliding window algorithm [115]: the EM calorimeter is divided into  $\Delta\eta \times \Delta\phi = 0.025 \times 0.025$  segments (corresponding to the granularity of the middle layer of the calorimeter), and any  $3 \times 5$  window of these segments which has a combined energy greater than 2.5 GeV is selected as an electron seed cluster. To select a cluster as an electron, a reconstructed track must be found where the track extrapolation is within  $\Delta\eta < 0.05$  and  $\Delta\phi < 0.1$  of the barycentre of the cluster on the side toward which the track bends and  $\Delta\phi < 0.05$  on the other side. In the case of multiple tracks matching to a cluster, the tracks are further required to have hits in the silicon detectors and then the closest in  $\Delta R$  is selected to be the matching track. For each selected electron, the cluster energy is then recalculated in  $3 \times 7$  ( $3 \times 5$ ) towers of cells in the barrel (endcaps). The cluster energy is now corrected for estimated energy deposits in front of and leaked behind the EM calorimeter and energy estimated to be leaked outside the cluster. These corrections are derived from simulation of the detector. The final 4-momenta of electrons is then taken using the matched track for the  $\eta$  and  $\phi$  parameters at the vertex, and the energy given by the cluster energy.

From the electron candidates that are built by the above procedure, further selection requirements are imposed to reject cases where jets fake the electron. These requirements are collectively called “tight++”. These include allowing only a certain fraction of energy in the hadronic calorimeter, a well collimated energy deposition found by comparing

---

be fully explored initially. Taking a temperature of 1 is equivalent to not weighting the likelihood, so the best minima is better explored as the temperature is lowered to 1.

the cluster energy to the energy in a larger tower area, requiring hits in the  $b$ -layer (the innermost pixel subdetector) and a minimum number of hits in the rest of the silicon, requiring a minimum number of high-threshold hits in the TRT and restrictions on the ratio of cluster energy to the track momentum. The cluster is also required to be isolated from hadronic activity in the rest of the event. A 90% isolation efficiency cut is made on the energy sum around the direction of each selected electron calculated within a cone of radius  $\Delta R = \sqrt{\Delta\eta^2 + \Delta\phi^2} = 0.2$ , after the exclusion of the cells associated with the electron cluster, and correction for leakage from the electron cluster. A 90% isolation efficiency cut was also made on the sum of the  $p_T$  of the tracks around the electron in a cone of radius  $\Delta R = 0.3$ .

Because jets are reconstructed independently of electrons, for each electron there will be a corresponding jet reconstructed. Therefore, an overlap removal is performed, such that the jet closest to an identified electron and within  $|\Delta R| < 0.4$  (approximately the size of reconstructed jets) is removed.

Figure 4.1 shows the efficiencies for reconstructing an electron cluster with the above algorithm and also subsequently identifying it as an electron. The figures show that the efficiency of an electron to pass the above criteria is not exactly modelled by the MC. Therefore, scale factors correcting for this efficiency difference have been measured to improve the simulation quality. The scale factor is defined as the ratio of the data efficiency to the MC efficiency. These scale factors are measured from a  $Z \rightarrow ee$  sample, using the “tag and probe” method [107]. In the tag and probe method, a “tag” electron is identified with stringent electron identification requirements. From the events with a tag electron, a “probe” electron is searched for, using very loose identification requirements, and requiring the invariant mass of the two electrons to be consistent with a  $Z$  boson. Because of the tight requirements on the first electron, there are almost no background events, and so the electrons are real electrons from a  $Z \rightarrow ee$  decay and so can be applied to both data and MC. The probe electron can then be tested against the tight identification requirements, and the fraction of probe electrons passing the requirements then gives the efficiency of electron identification.

The  $Z \rightarrow ee$  sample, along with  $J/\psi \rightarrow ee$  and  $W \rightarrow e\nu$  samples were also used to derive electron energy scale and resolution corrections to the simulation [116].

Electrons used in the thesis were required to be in the pseudorapidity range  $|\eta| < 2.47$ , excluding the barrel/end-cap transition region of  $1.37 < |\eta| < 1.52$ . The reconstructed

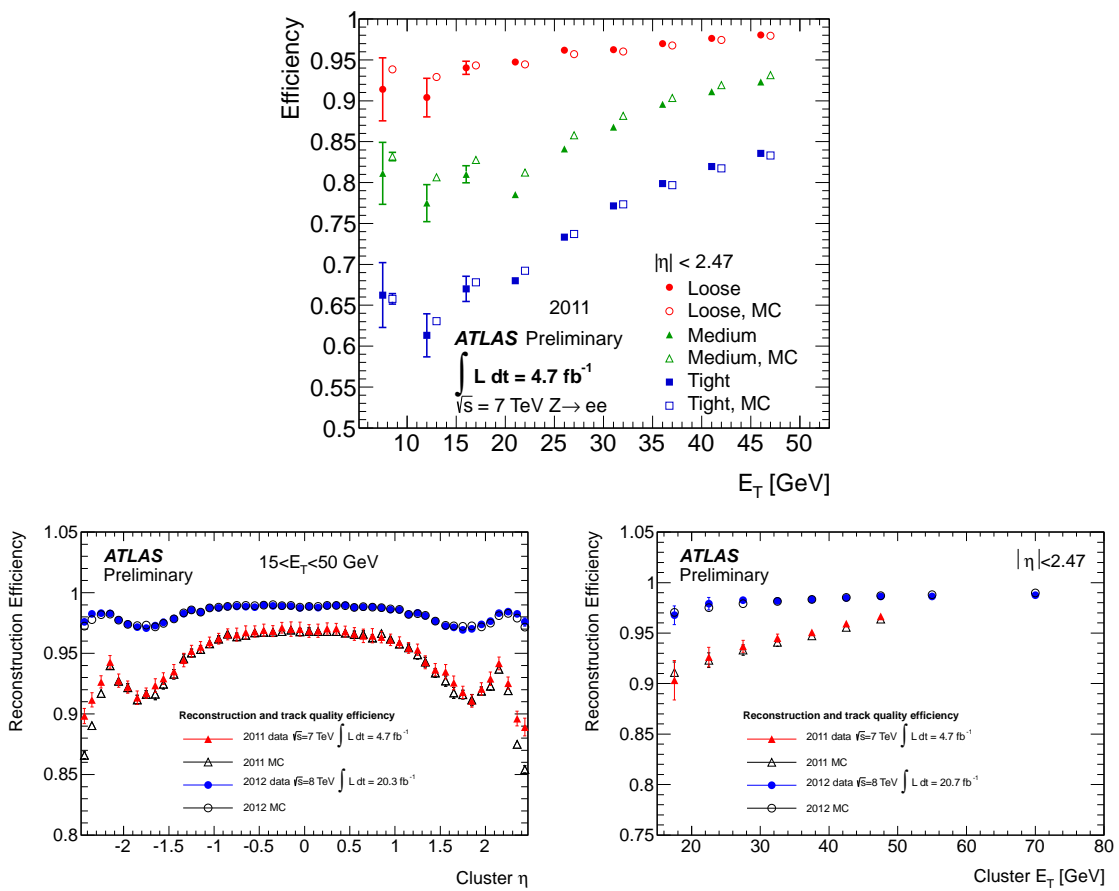


**Figure 4.1:** Electron reconstruction (top) and identification efficiencies with respect to the  $\eta$  (bottom left) and  $E_T$ (bottom right) of the electron. Note that this thesis only uses electrons satisfying the tight criteria. Taken from [117].

$p_T$  of electrons used in the event selection are required to be greater than 25 GeV, but electrons with  $p_T > 15$  GeV are used for the overlap removal and additional lepton veto.

### 4.1.3. Muons

A muon is identified as a charged particle leaving a track through the Muon Spectrometer (MS) [118]. To reconstruct muon candidates, particle tracks are first reconstructed separately in the Inner Detector (ID) and the MS. The MS tracks are then back extrapolated to the interaction point and a compatible ID track is searched for. This is done by forming a  $\chi^2$  difference between the tracking parameters of the ID and MS tracks, and requiring a  $\chi^2$  probability greater than 0.001. When a compatible ID track is found, the track parameters are then refit using the hits in both the ID and MS and the energy deposits in the calorimeter along the muon path to obtain the “combined” muon. If more than one ID track satisfies the  $\chi^2$  requirement, then all such tracks are refit, and the one with the best match after the refit is taken to as the muon candidate for a given MS track.

To ensure only well reconstructed muons are used, muon tracks are required to have a hit in the innermost pixel layer if expected from the reconstructed-track trajectory, at least one pixel hit if expected, at least six SCT hits if expected and no more than two missing hits along the track trajectory within the pixel and SCT detector subsystems. Muons crossing the TRT are required to have a hit pattern consistent with a well-reconstructed track. Muons are selected by requiring a reconstructed  $p_T$  greater than 25 GeV (lowered to 15 GeV for overlap removal and additional lepton veto) and a pseudorapidity  $|\eta| < 2.5$ . They are required to be isolated via the constraint that the calorimeter energy within a cone of  $\Delta R = 0.2$  around the direction of the muon is less than 4 GeV and the track transverse momentum sum within a cone of  $\Delta R = 0.3$  around the direction of the muon is less than 2.5 GeV. The efficiency of the requirements to reconstruct a true muon are shown in figure 4.2.

### 4.1.4. Jets

High energy partons from the hard interaction process, as calculated in perturbative QCD (as discussed in section 2.3), fragment into hadrons (collectively a “jet”) whose combined momenta will recover the parton’s momentum. At the detector reconstruction level, these particles leave energy deposits, or “clusters”, in the hadronic calorimeter

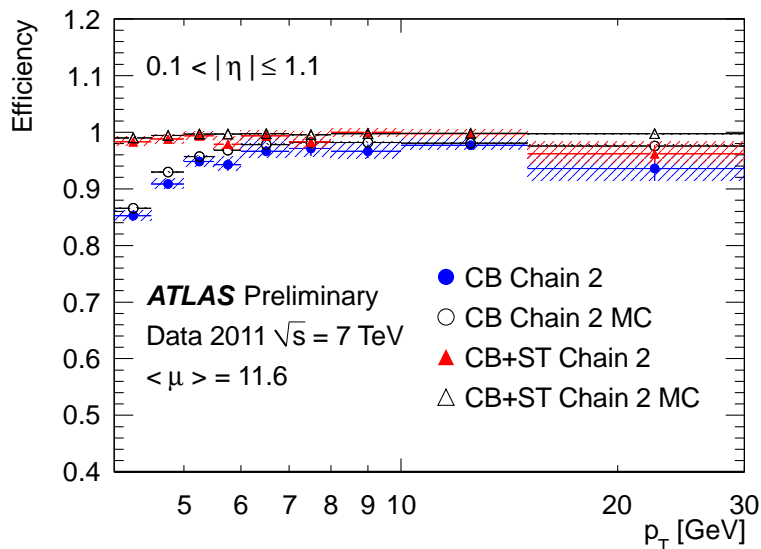


**Figure 4.2:** Muon reconstruction efficiencies as a function of  $p_T$ . “Chain 2” refers to the refit ID and MS muons that are used in this analysis (other reconstructions used at ATLAS are not considered here). CB are combined muons that are used here; ST are “segment tagged” muons, where a ID track was not found, or the refit failed. ST muons are not used for this analysis. Taken from [119].

which are grouped together according to a jet algorithm. Early jet algorithms simply placed a cone of a fixed radius  $R$  around the hardest single cluster found, and then removed all the clusters in that cone from consideration and repeated the procedure until all clusters above a fixed threshold are formed into a jet. This procedure, however, led to theoretical instabilities in the algorithm. A gluon splitting into two collinear gluons will mean that a previously hard particle can become arbitrarily soft and will therefore lead to different jet grouping. This is particularly a problem when comparing to theoretical predictions based on a fixed-order perturbative expansion, since at each order, more radiation effects are allowed and so applying these algorithms to the theoretical predictions is unstable. These considerations led to the requirement for jet algorithms to be “collinear safe”. This can be avoided if instead of looking at cones based on  $p_T$ , one uses every particle or cluster in the event to build a cone and then uses a “split-merge” procedure when deciding on how to form final stable cones. This leads to a new “infra-red” instability: a soft emission between two hard particles gives the algorithm a new cone seed which can merge the two particles, where before the algorithm would have assigned them to separate jets. This infra-red problem again leads to theoretical problems, since the emission of soft radiation is a non-perturbative effect and cannot be modelled precisely.

Further discussion of jet algorithms (including the one described below) can be found in [120].

The now widely-used method which avoids this is a “sequential recombination” algorithm, which builds jets step-by-step by repeatedly merging together nearby clusters of energy. The algorithm that the LHC experiments use is the anti- $k_T$  algorithm [121]. In this algorithm, a distance is calculated between all the clusters  $i$  and  $j$  in the event  $d_{ij}$ , and a “beamline” distance  $d_{iB}$  is also calculated for each particle  $i$ :

$$\begin{aligned} d_{ij} &= \min(k_{T,i}^{-2}, k_{T,j}^{-2}) \frac{\Delta_{ij}^2}{R^2} \\ d_{iB} &= k_{T,i}^{-2} \end{aligned} \tag{4.1}$$

where  $R$  is a free parameter of the algorithm (0.4 for this analysis),  $\Delta_{ij}^2 = (y_i - y_j)^2 + (\phi_i - \phi_j)^2$ , and  $k_{T,i}$ ,  $y_i$  and  $\phi_i$  are, respectively, the transverse momentum (with respect to the beam axis), the rapidity, and the azimuth of the cluster. The algorithm proceeds by either combining together the pair with the minimum distance and recalculating the distances using this new object in place of the old pair, or calling the object  $i$  a jet if the minimum distance is  $d_{iB}$ , removing it from the list. The algorithm continues this procedure until all the clusters have been removed from the list into jets.

Conceptually, the anti- $k_T$  algorithm merges nearby objects first and works out from a hard core, “growing” the jet until it reaches the size of the distance parameter of the algorithm  $R$ . For an isolated hard particle, this means that the algorithm will output a circular jet of size  $R$ , as one would have from the cone algorithms. But because the algorithm works by merging nearby objects first and then building outward, the infra-red and collinear problems of the cone algorithms are avoided, since soft emissions will not impact hard jet growth, and collinear emissions are quickly merged together. These properties also imply that the anti- $k_T$  algorithm is resilient against pileup and the description of the underlying event since the particles or energy deposits from these processes operate in a manner similar to the soft radiation. Thus, the jet area defined by the algorithm will be stable against pileup, which can easily be dealt with by applying an event-by-event correction based on, for example, the number of pile up vertices, which acts as a measure of the amount of extra pileup radiation expected.

The input energy deposits for ATLAS reconstructed jets are “topoclusters” (topological clusters) defined from the detector output [122]. At ATLAS, the fine segmentation of the calorimeter means that a single high-energy particle can deposit its energy in several

neighbouring cells. A topocluster is a set of neighbouring cells that have been grouped together as a way of approximating the energy deposition of a single such particle. Topoclusters are formed by finding all calorimeter cells with an energy deposition with signal-to-noise ratio greater than 4.<sup>2</sup> The seed cells are then ordered in descending signal-to-noise ratio, and then for each cell, all its neighbouring cells with signal-to-noise greater than 2 are added to the seed to form a proto-cluster. If a potential neighbour could be added to two of these proto-clusters, then the two clusters are merged along with the neighbour into a single proto-cluster. Each neighbour is also added to a neighbour-seed list. If a neighbouring cell does not have a signal-to-noise greater than 2, then it is still added to the proto-cluster, but it does not get added to the neighbour-seed list. Once all the seed clusters have been processed, then the neighbour cell list is processed in the same way (i.e. by looking at its neighbours that have not already been accounted for), with the new neighbours being added to the parent proto-cluster. This process continues until there are no more seed clusters in the list. Once the merging process is finished, each proto-cluster is searched in turn for “local maxima”. These are defined as cells which are minimum energy 500 MeV and of greater energy than any of its surrounding cells. If more than one such local maxima, then the clustering procedure is repeated with these local maxima as seeds, with the difference that only cells in the parent cluster are considered and no cluster merging occurs. This splits up topoclusters being formed from several close-by high energy particles, when it is possible to distinguish them. The topoclusters after splitting are then each assigned a 4-vector, such that the energy is the energy sum of the cells in the cluster, the mass is zero, and the direction is in the energy-weighted average of the direction of all the cells in the cluster.

The energy of the cells in the topoclusters are measured at the EM scale. The EM scale is the detector response corrected assuming that the total energy response is due to electromagnetic showers. Since the jet algorithm is applied to the topoclusters, the jets will also be measured at the EM scale. The jet energy that is needed is the energy of the constituent hadrons forming the jets, since this is the in-principle measurable energy that can be compared to theory (and not the parton energy, since this is theoretically ill-defined non-perturbatively). Therefore the “EM jets” need to be corrected to the particle-level; that is, corrected for the ratio of the reconstructed jet  $p_T$  with respect to the  $p_T$  found from the truth stable particles as determined from simulation. This is done using the “EM+JES” (Jet Energy Scale) calibration scheme [123].

---

<sup>2</sup> The average noise is determined by averaging events triggered on at random and measuring the energy. Since high-energy events are rare, this will mostly be due entirely to detector noise but still correspond to the real running detector rather than simulation.

The EM+JES scheme consists of three steps: subtract the energy estimated to be due to pileup, correct the jet direction so that the jet originates from the primary vertex of the interaction instead of the geometrical detector centre, and correct the energy and direction by calibration constants derived from simulation comparisons to truth jets, that is, jets formed using the same algorithm constructed from the underlying hadrons before detector interaction.

Jets in this thesis are also required to pass quality criteria designed to reject events from pileup. Each bunch crossing has several soft collision events, which lead to a number of low momentum hadrons from pileup collisions entering the detector. If these hadrons happen to bunch in a particular region, a jet can be reconstructed which is unrelated to the hard collision event. At ATLAS, the Jet Vertex Fraction (JVF) has been developed as a method to reject these pileup jets [124]. The JVF algorithm first associates reconstructed tracks to a jet by matching tracks within  $\Delta R < 0.4$  of the jet centre. The JVF is then calculated as the sum of the  $p_T$  of the selected tracks originating from the selected primary over the sum of the  $p_T$  from all the selected tracks. That is, the JVF is essentially the fraction of the constituent tracks' transverse momentum coming from the primary vertex. A value of the JVF close to 1 means that all the tracks in the jet can be associated to the primary vertex, while a value near 0 means that none of the tracks in the jet can be associated with the primary vertex and the jet was therefore likely to have come from pileup. If no tracks can be associated to the jet, then it is assigned the value -1. For this analysis, we require  $|JVF| > 0.75$  which provides good rejection of pileup jets as can be seen in figure 4.3. The figure shows that without the cut, the average number of reconstructed jets in conjunction with a  $Z$  boson production increases as a function of the number of reconstructed vertices, meaning that jets uncorrelated with the hard scatter are being reconstructed, and increasing with the level of pileup. On the other hand, using the chosen rejection point, the number of jets reconstructed is constant with respect to the number of pileup vertices, showing that the JVF requirement is efficient in rejecting pileup jets.

Another quality criteria required is that events with a jet which are classified as “bad” are rejected. A “bad” jet is one where the jet has not been produced by real energy deposits in the calorimeter, but instead from noise bursts in the calorimeter, LHC beam-gas interactions, or cosmic-rays inducing showers. Jets from hardware noise are identified by using: the difference between expected versus actual pulse shape (the time-dependent calorimeter cell profile) to find poor quality calorimeter cells; the fraction of energy in the LAr calorimeter with poor pulse shape; and the fraction of energy in

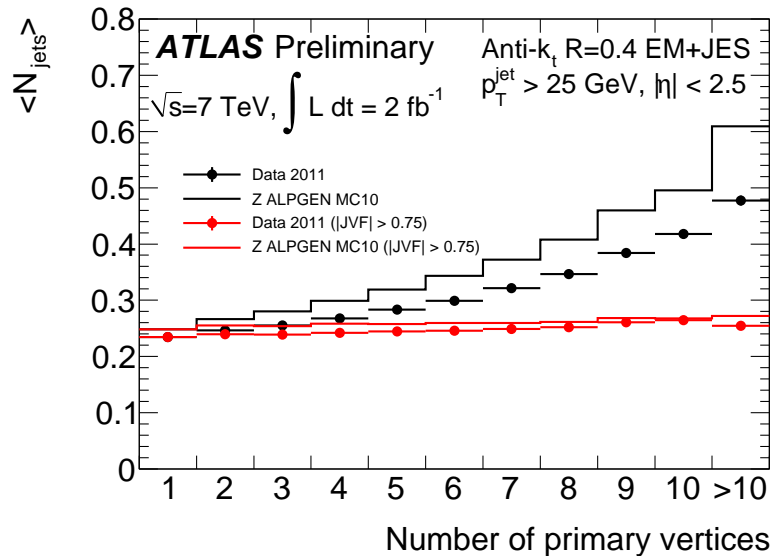


**Figure 4.3:** Average number of jets in  $Z \rightarrow \ell\ell$  ( $\ell = \mu, e$ ) for data and simulation, before and after a  $|JVF| > 0.75$  requirement. Taken from [125].

the HEC calorimeter with poor pulse shape. Cosmic and beam-induced backgrounds will, in general, have no particles trackable to the proton collision point at the centre of the detector associated with them. Therefore, to discriminate these sources, the ratio of the sum of the  $p_T$  of the charged particles associated to the jet to the sum of the energy deposits calorimeter cells is used. They are also not likely to occur in time with the collision and so the jet time, defined as the energy weighted sum over all cells in the jet of the time difference between the collision and the energy deposition in a calorimeter cell, is used to reject out of time jets. The actual values used in this analysis to reject events with bad jets are defined from the “loose” selection in [126].

#### 4.1.5. $b$ -jet Identification

In particle colliders, jets containing  $b$ -quarks can be discriminated against light quark jets. This is mostly due to the long lifetime of the  $B$ -hadrons, which when combined with the large momenta of the objects produced at the LHC, and therefore a large time dilation, results in a flight path of the  $B$ -hadrons long enough to be identified from a reconstructed secondary vertex or the large impact parameters (the distance of closest approach of the track to the primary vertex) of its decay products.  $B$ -hadrons may also be identified from the large hadron mass and the large branching ratio into leptons. The top pair decay studied in this analysis contains (at least) two  $b$ -jets and the relative rarity

of events with  $b$ -jets in proton–proton collisions means that requiring the identification of  $b$ -jets in an event leads to a significant background reduction. There are several  $b$ -tagging algorithms used for this analysis, each of which will be described in turn [127].

IP3D is an impact parameter based algorithm, that works on the level of individual tracks associated with a jet. The tracks used are required to pass quality cuts. They must have at least 7 silicon hits (hits in the pixel or SCT detectors) with at least 2 pixel hits, one of which must be from the innermost layer. They must have impact parameters  $|d_0| < 1$  mm and  $|z_0| < 1.5$  mm.  $d_0$  is the impact parameter in the  $r - \phi$  plane,  $z_0$  along the beam axis, and both are signed with respect to the direction of the jet (positive if in front of the primary vertex w.r.t. the jet direction, negative if behind). This requirement rejects most tracks which originate from the decays of long-lived mesons, such as  $K_S^0$ ,  $\Lambda$  and the hyperons, and tracks produced by photon conversion after interaction with the beamline or detector, which would otherwise produce spurious tagging. Finally, they must have a  $p_T > 1$  GeV. Tracks are associated to the jet with a jet  $p_T$  dependent  $\Delta R$ . The tracks are required to be closer to the jet at higher  $p_T$ , since harder jets are more collimated, and so we can reduce the number of tracks produced in pileup events and the underlying event without missing any tracks actually produced by the jet by placing tighter cuts at higher  $p_T$ . For example at 20 GeV jet  $p_T$ , they must have  $\Delta R < 0.45$ , whereas at 150 GeV they must have  $\Delta R < 0.25$ .

From these tracks, the IP3D algorithm calculates the impact parameter significances  $d_0/\sigma_{d_0}$  and  $z_0/\sigma_{z_0}$ , and finds a likelihood for the tracks to have originated from a  $b$ -jet,  $\mathcal{L}_b$ , and a likelihood for the track to have come from a light jet,  $\mathcal{L}_l$ . These likelihoods are produced from a likelihood distribution derived from simulation. The output of the IP3D algorithm is then  $\sum_i \ln \frac{\mathcal{L}_b}{\mathcal{L}_l}$  where  $i$  indexes the tracks associated with the jet.

The SV1 algorithm is a secondary vertex-based algorithm. It takes the tracks associated to the jet and tries to fit a secondary vertex away from the primary vertex. It uses tracks similar to IP3D but with looser cuts since it will reject tracks during the secondary vertex fit. It requires a track as for IP3D except it only requires track  $p_T > 400$  MeV, only 1 pixel hit which need not be on the innermost layer  $d_0 < 3.5$  mm and does not require the  $z_0$  cut, but tracks are required to have an impact parameter significantly far from the vertex. From the tracks, it forms two-track vertices using every pair of tracks. If any of these two-track vertices have a mass compatible with a long lived particle ( $K_S^0$ ,  $\Lambda$ , hyperons) it removes both of them from the list of tracks associated to the jet. It then combines the remaining two-track vertices into a single vertex, and then removes the worst fit track. It repeats this procedure until the overall  $\chi^2$  of the track

errors to the vertex is below a quality threshold. The output is a likelihood ratio (of  $b$  to light jets) combination of the 2D likelihood of the invariant mass of tracks associated with the vertex and the ratio of the sum of energy of the tracks associated with the vertex to the energy of all the tracks in the jet, and the 1D likelihood of the number of two-track vertices, and the  $\Delta R$  distance between the jet axis and the line joining the primary and secondary vertices.

The final algorithm used is the JetFitter algorithm [128]. The JetFitter algorithm uses the same tracks as IP3D. The idea of JetFitter is to find an axis along which the  $B$ -hadron decayed, possibly with an extra vertex due to a  $D$ -decay, and constrain the  $B$ -vertex position along this “flight” axis. It starts with the position of the primary vertex and the flight axis in the form of the PV in the direction of the jet momentum, with an associated uncertainty based on simulation as to the average displacement of the  $B$ -vertex from the jet momentum axis. Then, for the  $i$ th track associated with the jet, it defines a distance  $d_i$  along the flight axis that corresponds to a vertex for the track along this axis. This vertex position  $d_i$  is found from the position of closest approach of the track to the axis. The algorithm proceeds by updating the flight axis direction and the  $d_i$ s, by applying a Kalman filter update of the input parameters, one track at a time. Then, each two-vertex combination is checked for the compatibility of each distance parameter (technically by implementing a constraint such that  $d_i = d_j$  for each  $i, j$  in turn), and each vertex with the primary vertex (by testing with  $d_j = 0$ ) and finding the combination with the highest probability using a  $\chi^2$  of the tracks to the fitted vertices. It then merges these two distances thereby reducing the number of vertices by one and then repeats Kalman filter procedure. The process is iterated until the probability for the most probable two-vertex combination falls below a threshold. The position and uncertainties of the decay length significance  $d_0/\sigma_{d_0}$  is then taken as a momentum-weighted average of the remaining  $d_i$ s along the flight axis divided by the associated uncertainty. It uses this along with the invariant mass of all charged particle tracks attached to the decay chain (i.e. not merged with the primary vertex) and the energy fraction of the decay chain tracks to the total energy to form a likelihood ratio for a heavy flavour to light flavour jet which is the output of the algorithm.

In our analysis,  $b$ -jets are identified using the MV1  $b$ -tagger [129], which combines the results of IP3D, SV1, and JetFitter into a single discriminant using a neural network. We compare the output value of MV1 with a value which has been calibrated to be 70% efficient at identifying  $b$ -jets with  $p_T > 15$  GeV in simulated  $t\bar{t}$  events. This

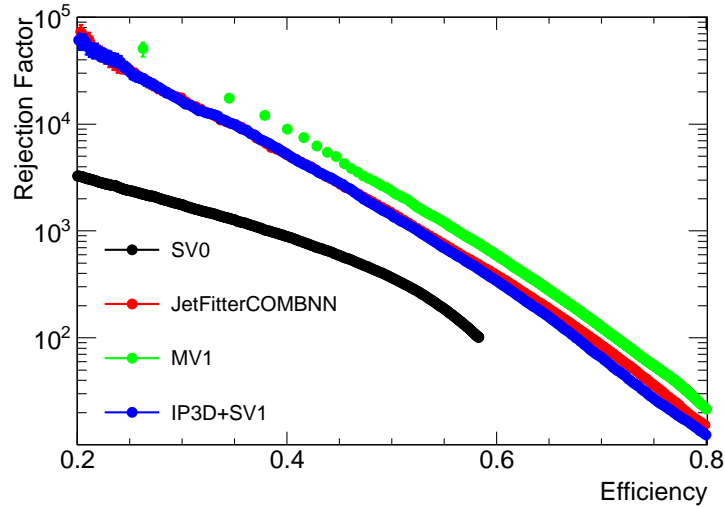


**Figure 4.4:** Light jet rejection factor (inverse of the probability to tag a light jet as a  $b$ -jet) against  $b$ -jet efficiency for the MV1 tagger used in the thesis and the component taggers. Taken from [116].

corresponds to a light jet rejection of 150. The light jet rejection for different working points for MV1 and the constituent algorithms is shown in figure 4.4.

#### 4.1.6. Missing Transverse Momentum

The hard processes that are being considered in LHC analyses are described by the interactions of partons within the protons, as outlined in section 2.3. These partons will contain some unknown fraction of the proton energy, so that the centre of mass momenta of the hard collision process is unknown and cannot be used as a constraint, even though the total proton energy is fixed to 7 TeV. The protons, however, travel directly along the beam axis, which is defined to be the  $z$ -axis, and so, to a good approximation, the partons contained in the proton will have insignificant transverse momentum. Therefore, a momentum imbalance in the transverse plane can be interpreted as being due to one or more particles that are transparent to the detector. Within the SM, this can only be neutrinos or instrumental effects (including the finite fiducial volume), but in new physics models, new particles can be produced which have small or no interactions with standard matter and so also contribute to missing transverse momentum. Typically, these particles are introduced to explain dark matter or at least may become potential dark matter candidates. Thus, missing transverse momentum is an important quantity when searching for new physics. The symbol  $E_T^{miss}$  is used for the magnitude of the missing

transverse momentum. The symbol is chosen as the transverse energy  $E_T = E \sin \theta$  is equivalent to the transverse momentum for massless particles or in the limit of high energy processes compared to the masses of the particles involved.

From an experimental point of view, missing transverse momentum is also an important quantity, since to calculate the momentum imbalance, one must use all the detector subsystems together in concert to build a complete picture of the event. Miscalibrations of any of the objects reconstructed by the detector can lead to mismeasurements of the missing transverse momentum. Calorimeter topoclusters are important for this, since the way they are formed naturally suppresses noise, as any energy deposition must pass a severe noise suppression threshold in order to be included in a topocluster, or be directly adjacent to such a deposition.

The present analysis uses an object-based missing transverse momentum (the method as presented in [130] but using slightly different object calibrations), where each topocluster in the event is associated with an object category. Each object category has an associated term added into the total missing transverse momentum (given in equation 4.2) with its own calibration scheme. The electron term,  $E_{x,y}^{RefEle}$ , uses electrons satisfying the tight++ criteria as outlined in section 4.1.2. The topoclusters associated with electrons are calibrated using the full electron energy scale excluding out-of-cluster corrections. The jet term  $E_{x,y}^{RefJet}$  uses jet objects constructed as in section 4.1.4 which have  $p_T > 20$  GeV, while the soft jet term  $E_{x,y}^{RefSoftJet}$  uses jets with  $7 < p_T < 20$  GeV. Jets are calibrated with the full EM+JES corrections described in section 4.1.4, while soft jets are calibrated only to the EM scale. The muon term  $E_{x,y}^{RefMuon}$  includes muons as described in section 4.1.3 without requiring any isolation from other activity in the event. The term adds the  $p_T$  as determined from track momentum, rather than the calorimeter topocluster (since high- $p_T$  muons are minimum ionising, so will not deposit their full energy in the calorimeter unlike the other objects considered). If the muon is isolated from a jet by at least  $\Delta R = 0.3$ , then the calorimeter energy is added to the muon term. Otherwise, this topocluster's energy is added to the jet term, since it is assumed in this case that this muon was produced as part of a jet. In order of preference, each calorimeter topocluster is attempted to be associated with: an electron, a jet, a soft jet, or a muon. If no associated object is found, the topocluster gets added to a separate term  $E_{x,y}^{CellOut}$  called "Cell Out". These Cell Out topoclusters are calibrated to the EM scale.

The missing transverse momentum is then given in each direction by:

$$-E_{x,y}^{miss} = E_{x,y}^{RefEle} + E_{x,y}^{RefJet} + E_{x,y}^{RefSoftJet} + E_{x,y}^{RefMuon} + E_{x,y}^{CellOut} \quad (4.2)$$

from which the scalar quantity  $E_T^{miss}$  can be derived:

$$E_T^{miss} = \sqrt{(E_x^{miss})^2 + (E_y^{miss})^2} \quad (4.3)$$

Another useful related quantity which can be derived from the  $E_T^{miss}$  is the transverse  $W$  mass  $m_T^W$  [4]:

$$m_T^W = \sqrt{2p_T^l E_T^{miss} (1 - \cos(\phi^l - \phi_T^{miss}))} \quad (4.4)$$

where  $p_T^l$  and  $\phi^l$  refer to the lepton kinematic quantities (the event selection will explicitly require there to be exactly one lepton in the event) and  $\phi_T^{miss}$  is the azimuthal angle formed from the  $E_{x,y}^{miss}$  values. This quantity is useful since it acts as a proxy for measuring the leptonically decaying  $W$  mass, since it decays into a lepton and a neutrino, and it is assumed that  $E_T^{miss}$  is due to the neutrino. This quantity is used because the full  $W$  mass cannot be calculated since the neutrino  $p_z$  is unmeasurable.

#### 4.1.7. Event-level selection

In this section we go through the object selections that we require for events to enter into our analysis. Unless otherwise noted, these requirements will apply equally to our study of both the reconstructed-level events, and the particle-level MC studies.

As mentioned, one of the major challenges at the LHC is to reject the overwhelming amount of QCD multijet backgrounds which are orders of magnitude more likely to occur than our top pair production processes. We already said that one of the primary ways of doing this is to select events which have a high- $p_T$  lepton and this motivated our choice for reconstructing the top-pair in a semi-leptonic topology. Therefore, the first requirement we place on events is that it was accepted one of the high- $p_T$  lepton triggers. Because the luminosity changed over the course of the run, the threshold on lepton  $p_T$  allowed by the triggers increased to keep the data inflow from the detector at a manageable level. This means that the exact triggers used changed across the course of the 2011 run. For electron events, the `EF_e_20_medium`, `EF_e22_medium` and `EF_e22vh_medium` for periods

B-H, I-K and L-M respectively. The event filter muon trigger was `mu_18` for periods B-I, and `mu_18_medium` for periods J-M. The muons allowed a lower  $p_T$  threshold because muons are more difficult for QCD to fake. In our particle-level selection, there is no equivalent requirement that we can place at this level of preselection.

We require exactly one high- $p_T$  lepton to have been reconstructed. This means exactly one electron or muon with  $p_T > 25$  GeV. We further require that there be no second well-reconstructed lepton in the event with  $p_T > 15$  GeV. This cut was optimised by the  $t\bar{t}$  + jets analysis to reduce the contribution from dileptonic  $t\bar{t}$  events [131]. In both channels at reconstruction-level, to avoid biasing our sample with non-triggered events, the selected lepton was required to match the lepton reconstructed by the high-level trigger, by requiring the trigger object to be within a cone of  $\Delta R = 0.15$  around the direction of the lepton.

We require that  $E_T^{miss} > 35$  GeV and  $m_T^W > 30$  GeV. These cuts greatly reduce the QCD multijet background, where we expect no  $E_T^{miss}$ , and allow us to use the opposite direction  $E_T^{miss}$  cuts to define a control region separate from our signal analysis region to use to extract a data-driven estimate for the QCD background expectation (of section 4.3.3).

We wish to reconstruct the complete  $t\bar{t}$  decay topology. Thus, we will require that at least four jets are reconstructed and pass our quality criteria, with  $p_T > 25$  GeV. We further require that at least two of these jets be  $b$ -tagged using the MV1 tagging algorithm in the case of reconstructed events, or the  $B$ -hadron jet clustering for particle level events.

## 4.2. Monte Carlo Simulation Samples

### 4.2.1. Overview

Monte Carlo (MC) simulation of the proton–proton collision and subsequent passage of outgoing particles through the detector is used extensively in ATLAS physics analyses. From the inception of the LHC, MC studies were used to optimise the design of the detector for the physics program and to perform feasibility studies for various specific physics processes.<sup>3</sup> In this analysis, simulated data were used to develop and compare various analysis strategies, and to provide detector smearing and acceptance correction factors for the particle level analysis and extrapolations of our results to the full top pair production phase space from the fiducial volume of the detector. Simulation consists of event generation and detector simulation. In event generation, the collision is simulated and partons are decayed to hadrons, which defines the “particle-level”. The detector simulation simulates the passage of particles through the detector and records the energy depositions in the sensitive detector volumes. After this, the ATLAS reconstruction software can be applied, which reconstructs the physics objects to be used in analysis from the detector output in the same manner as for real collisions.

### Event Generation

Simulated data samples are produced through several stages, each one of which requires a separate, dedicated computer program [133]. The first step is that the analyser chooses a physics process of interest, for example, top pair production. A program then generates the hard partonic interaction which produces this event, sampling from the allowed matrix element and PDF weighted phase space. In LHC interactions, this is typically performed by a dedicated hard process calculator working in a fixed order perturbative QCD scheme. In the generation of this hard process, short lived but on-shell particles are usually decayed as part of the process.

The hard event is then passed to a general purpose generator which can take the output partons and produces a parton shower (usually using an angle or energy ordered description of the shower) to a pre-defined cut-off point. In addition to the hard process, the “underlying event”, the interactions undergone by the partons in the proton which are

---

<sup>3</sup>For example, the expected performance paper published in 2008 before first collisions was an extensive review of the expected performance in key LHC physics areas based on simulation [132].

not actively involved in the hard interaction, is simulated. The program then hadronises the outgoing partons, which are then the final state description of the proton–proton collision. Example programs are ALPGEN [134], POWHEG [135], AcerMC [136] and MC@NLO [137] for the hard process simulation, which are coupled to PYTHIA [138] or HERWIG [139] for the parton showering and hadronisation. For HERWIG, the default description of the underlying event is inadequately described and JIMMY [140] is used for the underlying event instead.

At the LHC, each bunch crossing usually produces multiple proton–proton collisions. These are generally “minimum bias” collisions, that is, they do not have a hard, perturbatively calculable collision, but only soft inelastic interactions. Therefore, to the proton–proton collision producing the hard event are also added minimum bias collisions before the event is passed to the detector simulation. These extra collisions are referred to as “pileup”. The number of pileup collisions added in the simulation is generated such that the overall distribution is the same as measured in the 2011 data.

## Detector Simulation

After the generation to the final state hadrons, these particles are then passed into the detector simulation [141]. At ATLAS, GEANT4 [142] is used as the standard detector simulator. GEANT4 represents the detector as a series of material volumes. The description is as detailed as possible, so it is continually updated as the detector is understood in better detail. Effects like detectors being misaligned from their nominal position or sagging under their weight are accounted for as the slightest mismodelling can affect the final physics results.

GEANT4 takes the event generation output and propagates them through the detector volumes, using small steps to simulate the various material interactions. These effects include: multiple Coloumb scattering, the photoelectric effect, Compton scattering, ionisation, bremsstrahlung, conversion, annihilation, hadronic decays, and hadronic interactions. These processes are cut-off at a pre-determined energy scale, at which point the energy is considered to have been deposited in the current detector volume.

Energy deposition in instrumented detector volumes are recorded in HITS file, which stores the location and magnitude of the deposition. To this HITS file generated for a single collision, energy depositions generated from cavern background and detector noise are added to form the full description of the energy deposited in sensitive volumes of

the detector. This file is then passed to the ATLAS digitisation software, which reads the file in and converts it into Raw Data Object (RDO): software objects which are the same as those used to store the actual detector output.

These RDOs are then passed through the full reconstruction algorithm chain, as a collision data event would, and so a simulated event equivalent to a real detector event is produced. In addition to the standard reconstruction output, information from the underlying event generator is stored, so that the “truth” (that is, the generator record before particles pass through the detector) may be analysed to derive corrections based on detector smearing and reconstruction efficiencies.

## Fast Simulation

In addition to the standard GEANT4 simulation, a fast simulator, ATLFAST-II [143], can be used. Rather than performing the detailed physics simulation and digitisation of the standard detector simulation, ATLFAST-II directly produces the RDO files that can then be passed to the reconstruction software.

For the inner detector, the full suite of tracking simulation and reconstruction algorithms are used in the samples of this analysis, as the calorimetry takes the most simulation time. However, there is also an option to use the FATRAS program, which performs the tracking extrapolation algorithm in reverse to pass a particle through each element of the inner detector in turn and produce the RDO that would have been read in from the detector.

In the calorimeters, FastCaloSim is used [144]. FastCaloSim uses a calorimeter response parameterisation for each of the individual electrons, photons and hadrons reaching the calorimetry. Millions of single particle GEANT4 simulated particles are used to generate a parameterisation of the longitudinal and lateral shower shape, with separate parameterisations based on the particle’s energy and  $|eta|$ . Given the shower shape, the particle’s energy is deposited into the calorimeter cells (that is, the output RDOs) in a single step, without simulating the detailed interactions with the calorimeter, but still allows the full reconstruction software to be run on the output. Using FastCaloSim reduces the simulation time by an order of magnitude.

## 4.2.2. Simulated Samples

### Signal Samples

Several simulated top pair production samples have been generated to study the predicted properties of these events. These samples differ by: the matrix element calculator used for the hard process, the parton showering program used to generate the final particle level particles, and the tuning of the programs used in the generation. The matrix element calculators differ in respect to the underlying physics processes included in them. The ALPGEN generator performs calculations at tree level. However, it calculates the tree level diagrams for top pairs produced in association with  $n$  additional partons, for  $n$  up to 5. This should give a better description of the additional jet spectrum produced in top pair events, which is shown to be the case in an ATLAS analysis of the jet multiplicity spectrum in top pair events [131]. The MC@NLO+HERWIG and POWHEG generators, on the other hand, run their calculations including loop corrections up to order  $\alpha_s^2$ . This should give a more precise description of the top pair production observables, but means that they only calculate the parton spectrum up to one additional parton in the final state, and rely on the parton showering to produce additional jets.

Table 4.1 gives an overview of the signal samples used. The nominal  $t\bar{t}$  sample was generated using POWHEG [135] generator. The POWHEG sample was produced with the CTEQ6.6 PDF set and showered with the Perugia 2011C PYTHIA tune [145, 146].

A POWHEG +PYTHIA sample was generated with a sample with a retuning of the MC where the colour reconnection term was disabled and the other parameters retuned. This sample is used to estimate the size of the systematic uncertainties due to colour reconnection.

Additional  $t\bar{t}$  samples were generated was generated using the ALPGEN [134] v2.13 generator and the CTEQ6L1 [147] PDF. The processes corresponding to the leading order matrix elements for  $t\bar{t}$  with zero to four exclusive and five inclusive associated partons and  $t\bar{t} + b\bar{b}$  and  $t\bar{t} + c\bar{c}$  were individually generated. Parton showering and fragmentation was performed using HERWIG [139] v6.520. The MLM parton-jet matching scheme [134] was applied to avoid double counting of configurations generated by both the parton shower and the matrix-element calculation. The exclusive heavy flavour samples were combined with the inclusive samples, after the removal of overlapping events. The overlapping events were rejected by using angular matching for  $b$ - and  $c$ -quarks within a cone of  $\Delta R < 0.4$  and  $p_T > 25$  GeV.

To assess the effect of different fragmentation and parton shower models, a sample was generated using ALPGEN v2.14 with the PYTHIA [138] parton shower and CTEQ5L PDF [148].

Initial State Radiation (ISR) and Final State Radiation (FSR) variations were produced by varying the ALPGEN renormalisation scale associated with  $\alpha_S$  at each local vertex in the matrix element and parton shower calculation by a factor of two relative to the original scale  $k_T$  between two partons [149]. This variation was obtained by `ktfac` values of 0.5 and 2.0, resulting in additional ALPGEN +PYTHIA samples. These ISR/FSR up and down variations are referred to as the  $\alpha_S$ -up and  $\alpha_S$ -down variations. The central and shifted ALPGEN +PYTHIA samples were made with the PYTHIA Perugia 2011 tune [145][146]. These settings were shown to give variations which enclose the uncertainty band of the  $t\bar{t}$  gap fraction measurement of [150], which will be presented in section 5.1.

Another  $t\bar{t}$  sample was generated using the the MC@NLO [137] generator. The MC@NLO sample was produced with the CT10 PDF set [75], interfaced to the HERWIG parton shower. This sample compared with the ALPGEN +HERWIG sample were used to evaluate the size of the systematic uncertainties due to the matrix element calculation.

As discussed in section 2.4, the predicted SM  $t\bar{t}$  cross section for  $pp$  collisions at a centre-of-mass energy of  $\sqrt{s} = 7$  TeV is  $\sigma_{t\bar{t}} = 177_{-11}^{+10}$  pb for a top mass of 172.5 GeV as obtained from the NNLO QCD calculations [69]. All  $t\bar{t}$  MC samples were generated with a top-quark mass of 172.5 GeV and were normalised to this cross section.

## Background Samples

Samples of  $W$  and  $Z$  bosons with zero to four exclusive and five inclusive associated partons were generated with ALPGEN v2.13, CTEQ6L1 PDF and the HERWIG shower. Since this analysis makes requirements based on whether jets are identified as  $b$ -quark jets, separate samples of  $W + b\bar{b}$ ,  $W + c$ ,  $W + c\bar{c}$ , and  $Z + b\bar{b}$  events were generated. The overlap between these samples and the respective inclusive jet flavour samples was removed using the Heavy Flavour Overlap Removal (HFOR) tool to perform angular matching within  $\Delta R < 0.4$ . In the case of  $W$  + jets, the normalisation was taken from a data-driven method, whereas the MC simulation was used to provide the shape description.

The  $t$ -channel single top-quark sample was generated with the AcerMC generator [136], whereas MC@NLO was used to generate  $Wt$ - and  $s$ -channels. The single top-quark

	ID	Process	Generator	PDF	$\sigma$ [pb]	$k$ -factor
	105200	$t\bar{t}$ no full-had	MC@NLO+HERWIG/ JIMMY	CT10	80.11	1.12
	117050	$t\bar{t}$ no full-had	POWHEG+PYTHIA	P2011C tune w/CTEQ6L1	80.07	1.202
	117001	$t\bar{t}$ no full-had	POWHEG+PYTHIA	P2011C tune w/HERAPDF15	73.10	1.317
	117430	$t\bar{t}$ no full had	POWHEG+PYTHIA	P2011 tune w/CTEQ6L1, no CR	80.07	1.202
ALPGEN+HERWIG	105894	$t\bar{t}l nqq + 0$	ALPGEN+HERWIG/ JIMMY	CTEQ6L1	13.86	1.755
	105895	$t\bar{t}l nqq + 1$	ALPGEN+HERWIG/ JIMMY	CTEQ6L1	13.69	1.755
	105896	$t\bar{t}l nqq + 2$	ALPGEN+HERWIG/ JIMMY	CTEQ6L1	8.47	1.755
	105887	$t\bar{t}l nqq + 3$	ALPGEN+HERWIG/ JIMMY	CTEQ6L1	3.78	1.755
	105888	$t\bar{t}l nqq + 4$	ALPGEN+HERWIG/ JIMMY	CTEQ6L1	1.34	1.755
	105889	$t\bar{t}l nqq + 5+$	ALPGEN+HERWIG/ JIMMY	CTEQ6L1	0.50	1.755
	105890	$t\bar{t}l nln + 0$	ALPGEN+HERWIG/ JIMMY	CTEQ6L1	3.47	1.687
	105891	$t\bar{t}l nln + 1$	ALPGEN+HERWIG/ JIMMY	CTEQ6L1	3.40	1.687
	105892	$t\bar{t}l nln + 2$	ALPGEN+HERWIG/ JIMMY	CTEQ6L1	2.11	1.687
	117897	$t\bar{t}l nln + 3$	ALPGEN+HERWIG/ JIMMY	CTEQ6L1	0.94	1.687
	117898	$t\bar{t}l nln + 4$	ALPGEN+HERWIG/ JIMMY	CTEQ6L1	0.33	1.687
117899	$t\bar{t}l nln + 5+$	ALPGEN+HERWIG/ JIMMY	CTEQ6L1	0.13	1.687	
ALPGEN+PYTHIA	117083	$t\bar{t}l nqq + 0$	ALPGEN+PYTHIA	CTEQ5L	11.44	2.258
	117084	$t\bar{t}l nqq + 1$	ALPGEN+PYTHIA	CTEQ5L	11.10	2.258
	117085	$t\bar{t}l nqq + 2$	ALPGEN+PYTHIA	CTEQ5L	7.01	2.258
	117086	$t\bar{t}l nqq + 3$	ALPGEN+PYTHIA	CTEQ5L	3.19	2.258
	117087	$t\bar{t}l nqq + 4$	ALPGEN+PYTHIA	CTEQ5L	1.15	2.258
	117088	$t\bar{t}l nqq + 5+$	ALPGEN+PYTHIA	CTEQ5L	0.51	2.258
	117113	$t\bar{t}l nln + 0$	ALPGEN+PYTHIA	CTEQ5L	2.86	2.165
	117114	$t\bar{t}l nln + 1$	ALPGEN+PYTHIA	CTEQ5L	2.77	2.165
	117115	$t\bar{t}l nln + 2$	ALPGEN+PYTHIA	CTEQ5L	1.75	2.165
	117116	$t\bar{t}l nln + 3$	ALPGEN+PYTHIA	CTEQ5L	0.80	2.165
	117117	$t\bar{t}l nln + 4$	ALPGEN+PYTHIA	CTEQ5L	0.29	2.165
117118	$t\bar{t}l nln + 5+$	ALPGEN+PYTHIA	CTEQ5L	0.12	2.165	
ALPGEN+PYTHIA up	117520	$t\bar{t}l nqq + 0$	ALPGEN+PYTHIA	radHi KTFac0.5 CTEQ5L	9.97	2.215
	117521	$t\bar{t}l nqq + 1$	ALPGEN+PYTHIA	radHi KTFac0.5 CTEQ5L	10.83	2.215
	117522	$t\bar{t}l nqq + 2$	ALPGEN+PYTHIA	radHi KTFac0.5 CTEQ5L	7.72	2.215
	117523	$t\bar{t}l nqq + 3$	ALPGEN+PYTHIA	radHi KTFac0.5 CTEQ5L	3.95	2.215
	117524	$t\bar{t}l nqq + 4$	ALPGEN+PYTHIA	radHi KTFac0.5 CTEQ5L	2.58	2.215
	117525	$t\bar{t}l nln + 0$	ALPGEN+PYTHIA	radHi KTFac0.5 CTEQ5L	2.50	2.120
	117526	$t\bar{t}l nln + 1$	ALPGEN+PYTHIA	radHi KTFac0.5 CTEQ5L	2.71	2.120
	117527	$t\bar{t}l nln + 2$	ALPGEN+PYTHIA	radHi KTFac0.5 CTEQ5L	1.93	2.120
	117528	$t\bar{t}l nln + 3$	ALPGEN+PYTHIA	radHi KTFac0.5 CTEQ5L	0.99	2.120
	117529	$t\bar{t}l nln + 4+$	ALPGEN+PYTHIA	radHi KTFac0.5 CTEQ5L	0.65	2.120
ALPGEN+PYTHIA down	117530	$t\bar{t}l nqq + 0$	ALPGEN+PYTHIA	radLo KTFac2 CTEQ5L	12.65	2.284
	117531	$t\bar{t}l nqq + 1$	ALPGEN+PYTHIA	radLo KTFac2 CTEQ5L	11.17	2.284
	117532	$t\bar{t}l nqq + 2$	ALPGEN+PYTHIA	radLo KTFac2 CTEQ5L	6.35	2.284
	117533	$t\bar{t}l nqq + 3$	ALPGEN+PYTHIA	radLo KTFac2 CTEQ5L	2.60	2.284
	117534	$t\bar{t}l nqq + 4+$	ALPGEN+PYTHIA	radLo KTFac2 CTEQ5L	1.24	2.284
	117535	$t\bar{t}l nln + 0$	ALPGEN+PYTHIA	radLo KTFac2 CTEQ5L	3.16	2.190
	117536	$t\bar{t}l nln + 1$	ALPGEN+PYTHIA	radLo KTFac2 CTEQ5L	2.79	2.190
	117537	$t\bar{t}l nln + 2$	ALPGEN+PYTHIA	radLo KTFac2 CTEQ5L	1.58	2.190
	117538	$t\bar{t}l nln + 3$	ALPGEN+PYTHIA	radLo KTFac2 CTEQ5L	0.65	2.190
	117539	$t\bar{t}l nln + 4+$	ALPGEN+PYTHIA	radLo KTFac2 CTEQ5L	0.31	2.190

**Table 4.1:** Summary of the dataset number, process, generator, PDF, cross-section, and  $k$ -factor for each signal Monte Carlo sample used.

samples were each normalised according to next to an approximate NNLO calculation for the  $t$ - [151],  $s$ - [152] and  $Wt$ -channels [153]. Diboson events (events producing  $WW$ ,  $WZ$ , or  $ZZ$ ) were produced using HERWIG normalised to an approximate NNLO calculation [154].

	ID	Process	Generator	PDF	$\sigma[pb]$	$k$ -factor
Single Top	117360	Single top ( $t$ -chan) $\rightarrow e\nu$	ACERMC+Pythia	MRSTMCa1	8.06	0.865
	117361	Single top ( $t$ -chan) $\rightarrow \mu\nu$	ACERMC+Pythia	MRSTMCa1	8.06	0.865
	117362	Single top ( $t$ -chan) $\rightarrow \tau\nu$	ACERMC+Pythia	MRSTMCa1	8.05	0.866
	108343	Single top ( $s$ -chan) $\rightarrow e\nu$	MC@NLO+HERWIG/ JIMMY	CT10	0.47	1.064
	108344	Single top ( $s$ -chan) $\rightarrow \mu\nu$	MC@NLO+HERWIG/ JIMMY	CT10	0.47	1.064
	108345	Single top ( $s$ -chan) $\rightarrow \tau\nu$	MC@NLO+HERWIG/ JIMMY	CT10	0.47	1.064
	108346	Single top ( $Wt$ -chan) inclusive	MC@NLO+HERWIG/ JIMMY	CT10	14.59	1.079
W + jets	107680	$W \rightarrow e\nu + 0$	ALPGEN+HERWIG/ JIMMY	CTEQ6L1	6930.50	1.196
	107681	$W \rightarrow e\nu + 1$	ALPGEN+HERWIG/ JIMMY	CTEQ6L1	1305.30	1.196
	107682	$W \rightarrow e\nu + 2$	ALPGEN+HERWIG/ JIMMY	CTEQ6L1	378.13	1.196
	107683	$W \rightarrow e\nu + 3$	ALPGEN+HERWIG/ JIMMY	CTEQ6L1	101.86	1.196
	107684	$W \rightarrow e\nu + 4$	ALPGEN+HERWIG/ JIMMY	CTEQ6L1	25.68	1.196
	107685	$W \rightarrow e\nu + 5$	ALPGEN+HERWIG/ JIMMY	CTEQ6L1	6.99	1.196
	107690	$W \rightarrow \mu\nu + 0$	ALPGEN+HERWIG/ JIMMY	CTEQ6L1	6932.40	1.195
	107691	$W \rightarrow \mu\nu + 1$	ALPGEN+HERWIG/ JIMMY	CTEQ6L1	1305.90	1.195
	107692	$W \rightarrow \mu\nu + 2$	ALPGEN+HERWIG/ JIMMY	CTEQ6L1	378.07	1.195
	107693	$W \rightarrow \mu\nu + 3$	ALPGEN+HERWIG/ JIMMY	CTEQ6L1	101.85	1.195
	107694	$W \rightarrow \mu\nu + 4$	ALPGEN+HERWIG/ JIMMY	CTEQ6L1	25.72	1.195
	107695	$W \rightarrow \mu\nu + 5$	ALPGEN+HERWIG/ JIMMY	CTEQ6L1	7.00	1.195
	107700	$W \rightarrow \tau\nu + 0$	ALPGEN+HERWIG/ JIMMY	CTEQ6L1	6931.80	1.195
	107701	$W \rightarrow \tau\nu + 1$	ALPGEN+HERWIG/ JIMMY	CTEQ6L1	1304.90	1.195
	107702	$W \rightarrow \tau\nu + 2$	ALPGEN+HERWIG/ JIMMY	CTEQ6L1	377.93	1.195
	107703	$W \rightarrow \tau\nu + 3$	ALPGEN+HERWIG/ JIMMY	CTEQ6L1	101.96	1.195
	107704	$W \rightarrow \tau\nu + 4$	ALPGEN+HERWIG/ JIMMY	CTEQ6L1	25.71	1.195
	107705	$W \rightarrow \tau\nu + 5$	ALPGEN+HERWIG/ JIMMY	CTEQ6L1	7.00	1.195
	117293	$W \rightarrow l\nu + c + 0p$	ALPGEN+HERWIG/ JIMMY	CTEQ6L1	644.4	1.20
	117294	$W \rightarrow l\nu + c + 1p$	ALPGEN+HERWIG/ JIMMY	CTEQ6L1	205.0	1.20
	117295	$W \rightarrow l\nu + c + 2p$	ALPGEN+HERWIG/ JIMMY	CTEQ6L1	50.8	1.20
	117296	$W \rightarrow l\nu + c + 3p$	ALPGEN+HERWIG/ JIMMY	CTEQ6L1	11.4	1.20
	117297	$W \rightarrow l\nu + c + 5p$	ALPGEN+HERWIG/ JIMMY	CTEQ6L1	2.8	1.20
	117284	$W \rightarrow l\nu + cc + 0p$	ALPGEN+HERWIG/ JIMMY	CTEQ6L1	127.53	1.20
	117285	$W \rightarrow l\nu + cc + 1p$	ALPGEN+HERWIG/ JIMMY	CTEQ6L1	104.68	1.20
	117286	$W \rightarrow l\nu + cc + 2p$	ALPGEN+HERWIG/ JIMMY	CTEQ6L1	52.08	1.20
	117287	$W \rightarrow l\nu + cc + 3p$	ALPGEN+HERWIG/ JIMMY	CTEQ6L1	16.96	1.20
	107280	$W \rightarrow l\nu + bb + 0p$	ALPGEN+HERWIG/ JIMMY	CTEQ6L1	47.35	1.200
	107281	$W \rightarrow l\nu + bb + 1p$	ALPGEN+HERWIG/ JIMMY	CTEQ6L1	35.76	1.200
	107282	$W \rightarrow l\nu + bb + 2p$	ALPGEN+HERWIG/ JIMMY	CTEQ6L1	17.33	1.200
	107283	$W \rightarrow l\nu + bb + 3p$	ALPGEN+HERWIG/ JIMMY	CTEQ6L1	7.61	1.200
Z + jets	116250/107650	$Z(\rightarrow ee) + 0p$	ALPGEN+HERWIG/ JIMMY	CTEQ6L1	3055.2 / 668.3	1.25
	116251/107651	$Z(\rightarrow ee) + 1p$	ALPGEN+HERWIG/ JIMMY	CTEQ6L1	84.9 / 134.4	1.25
	116252/107652	$Z(\rightarrow ee) + 2p$	ALPGEN+HERWIG/ JIMMY	CTEQ6L1	41.4 / 40.5	1.25
	116253/107653	$Z(\rightarrow ee) + 3p$	ALPGEN+HERWIG/ JIMMY	CTEQ6L1	8.4 / 11.2	1.25
	116254/107654	$Z(\rightarrow ee) + 4p$	ALPGEN+HERWIG/ JIMMY	CTEQ6L1	1.9 / 2.9	1.25
	116255/107655	$Z(\rightarrow ee) + 5p$	ALPGEN+HERWIG/ JIMMY	CTEQ6L1	0.5/0.8	1.25
	116260/107660	$Z(\rightarrow \mu\mu) + 0p$	ALPGEN+HERWIG/ JIMMY	CTEQ6L1	3054.9 / 668.7	1.25
	116261/107661	$Z(\rightarrow \mu\mu) + 1p$	ALPGEN+HERWIG/ JIMMY	CTEQ6L1	84.9 / 134.1	1.25
	116262/107662	$Z(\rightarrow \mu\mu) + 2p$	ALPGEN+HERWIG/ JIMMY	CTEQ6L1	41.5 / 40.3	1.25
	116263/107663	$Z(\rightarrow \mu\mu) + 3p$	ALPGEN+HERWIG/ JIMMY	CTEQ6L1	8.4 / 11.2	1.25
	116264/107664	$Z(\rightarrow \mu\mu) + 4p$	ALPGEN+HERWIG/ JIMMY	CTEQ6L1	1.9 / 2.8	1.25
	116265/107665	$Z(\rightarrow \mu\mu) + 5p$	ALPGEN+HERWIG/ JIMMY	CTEQ6L1	0.5 / 0.8	1.25
	116270/107670	$Z(\rightarrow \tau\tau) + 0p$	ALPGEN+HERWIG/ JIMMY	CTEQ6L1	3055.1 / 668.4	1.25
	116271/107671	$Z(\rightarrow \tau\tau) + 1p$	ALPGEN+HERWIG/ JIMMY	CTEQ6L1	84.9 / 134.8	1.25
	116272/107672	$Z(\rightarrow \tau\tau) + 2p$	ALPGEN+HERWIG/ JIMMY	CTEQ6L1	41.4 / 40.4	1.25
	116273/107673	$Z(\rightarrow \tau\tau) + 3p$	ALPGEN+HERWIG/ JIMMY	CTEQ6L1	8.4 / 11.3	1.25
116274/107674	$Z(\rightarrow \tau\tau) + 4p$	ALPGEN+HERWIG/ JIMMY	CTEQ6L1	1.9 / 2.8	1.25	
116270/107670	$Z(\rightarrow \tau\tau) + 5p$	ALPGEN+HERWIG/ JIMMY	CTEQ6L1	0.5 / 0.8	1.25	
Dib.	105985	WW	HERWIG/ JIMMY	MRST	11.5003	1.48
	105986	ZZ	HERWIG/ JIMMY	MRST	0.9722	1.30
	105987	WZ	HERWIG/ JIMMY	MRST	3.4641	1.60

**Table 4.2:** Summary of the dataset number, process, generator, PDF, cross-section, and  $k$ -factor for each background Monte Carlo sample used.

## The Underlying Event and Pileup

The underlying event was modelled using JIMMY [140] and the AUET1 tune [155] for HERWIG showered events and the PYTHIA UET2 tune [156] for PYTHIA showered events.

Additional in-time and out-of-time inelastic  $pp$  interactions were generated with the PYTHIA AMBT1 tune [157] and then overlaid on each hard processes generated. The distribution of secondary interactions was re-weighted to match the distribution of the average number of additional interactions per bunch crossing measured in the data sample. The pileup particles were added for the detector simulation, but were then excluded from the generator record.

MC samples were passed through a GEANT4 [142] simulation of the ATLAS detector [141]. The samples (described below) used to study the effects of Initial State Radiation (ISR) and Final State Radiation (FSR) and colour reconnection, together with nominal samples were passed through the ATLFASST-II [141] simulation of the ATLAS detector. The POWHEG +HERWIG sample was also passed through the ATLFASST-II simulation.

## 4.3. Background Estimation

### 4.3.1. Backgrounds from MC

Signal events are considered to be only semi-leptonic  $t\bar{t}$ . This means that any contribution to the data from dileptonic  $t\bar{t}$  decays will be considered background in our analysis. For our purposes, a top is leptonically decaying if the  $W$  boson from the top decays into an electron, a muon, or a tau which subsequently decays into an electron or muon. Hadronically decaying taus are considered to give hadronically top decays. Therefore, in the analysis, the contribution from dileptonic events, where dileptonic is defined as above, will be accounted for in the data by an estimate of the size of this background obtained from the nominal  $t\bar{t}$  sample, POWHEG +PYTHIA, and then dealt with as for the remaining backgrounds.

Fully hadronically decaying top events are unlikely to enter the analysis and are anyway indistinguishable (for our purposes) from multijet background, and will therefore

automatically be included as part of the data-driven estimate of this background, which is discussed below.

Contributions from single top,  $Z$ +jets and diboson production were evaluated using corresponding Monte Carlo samples and theoretical cross-sections for these processes as listed in table 4.2.

### 4.3.2. $W$ +Jets Normalisation

#### Overall $W$ +jets Normalisation

The theoretical cross-sections for the production of a  $W$  boson in association with jets (given in table 4.2) has a large theoretical uncertainty. Since it is also a large background for semi-leptonic top pair analyses, a standard method has been developed for a data-driven estimate of the normalisation and the heavy-flavour fraction of these  $W$ +jets events.

The method is based on the charge asymmetry of  $W$  production at a proton–proton collider. A  $W^+$  boson can be produced from, for example,  $u\bar{d} \rightarrow W^+$  whose rate will depend on the  $u(x_1)\bar{d}(x_2)$  proton PDFs (in equation 2.6), while  $W^-$  may proceed through  $d\bar{u} \rightarrow W^-$  and so depend  $d(x_1)\bar{u}(x_2)$ . Since the  $u$  and  $d$  PDFs in a proton are different (recalling that a proton has 2 valence  $u$ -quarks, and only 1 valence  $d$ -quark while the anti-quarks must be from the sea and so we should have  $\bar{u}(x) = \bar{d}(x)$ ), the overall rate for the two processes will be different. The theoretical value for the ratio of these processes:

$$r = \frac{\sigma(pp \rightarrow W^+)}{\sigma(pp \rightarrow W^-)} \quad (4.5)$$

is well understood, having only a few percent uncertainty. Since the other processes that are important in the signal region (QCD multijet production, top pair production,  $Z$  associated with jets) are charge symmetric, a measurement of the charge asymmetry in the signal region can be used to estimate the overall  $W$ +jets production rate. Note that the single top production process will have a small asymmetry. However, since the overall cross-section for single-top production is much smaller than for  $W$ +jets, its contribution is simply estimated from simulation rather than being data-driven.

The charge asymmetry is measured by counting the lepton charges  $N_+$  ( $N_-$ ) for the number of positively (negatively) charged leptons observed in data. For the  $W$ +jets

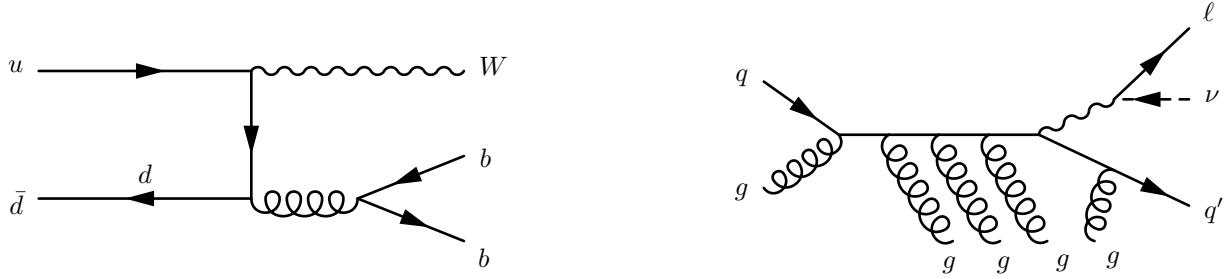


**Figure 4.5:** Example Feynman diagrams of  $W$ +jets processes which have similar topology to our  $t\bar{t}$  signal. The diagram on the left shows the  $W$  being produced in association with  $b$  quarks; the diagram on the right shows a  $W$ +jets event.

channel, this is equivalent to the number of  $W^+$  or  $W^-$  events since to enter our signal region, the  $W$  must decay leptonically, which, when its produced in association with several additional jets, will have the same object composition as our signal top pair events. The method then proceeds by rewriting the total number of expected  $W$ +jets events in terms of the theoretical charge asymmetry ratio  $r = \frac{N_{W^+}}{N_{W^-}}$  and the observed charge asymmetry  $\Delta = N_+ - N_-$ . The number of events of either charge can be rewritten as:

$$\begin{aligned} N_{W^-} &= \frac{\Delta}{1-r} \\ N_{W^+} &= \frac{r\Delta}{1-r} \end{aligned} \quad (4.6)$$

and so the overall number of  $W$ +jets events

$$N_W = N_{W^+} + N_{W^-} = \frac{1+r}{1-r}\Delta \quad (4.7)$$

if we estimate  $r$  from simulation  $r = r_{MC} = \frac{N_{W^+}^{MC}}{N_{W^-}^{MC}}$ , and measure the charge asymmetry in data  $\Delta = \Delta^{data} = D_+ - D_-$  (with the aforementioned single top asymmetry subtracted based on simulation), then the total number of  $W$ +jets events expected in data  $N^{exp}$  is

$$N^{exp} = \left( \frac{N_{W^+}^{MC}}{N_{W^-}^{MC}} \right) (D_+ - D_-) \quad (4.8)$$

Since the jet multiplicity is strongly correlated with the  $x$  value of the PDF that is being probed (a larger  $x$  tending to produce more jets, since the outgoing parton will have a larger momentum and therefore be more likely to split into larger momentum daughters which can then each form individual jets), the expected number of  $W$ +jets events is obtained independently for each jet bin, as at higher  $x$  there is a larger difference

# jets	Muon		Electron	
	Pretag	Tagged	Pretag	Tagged
1 jet	$1.05^{+0.09}_{-0.07}$	$1.05^{+0.26}_{-0.23}$	$0.98^{+0.09}_{-0.08}$	$0.98^{+0.28}_{-0.27}$
2 jet	$0.97^{+0.07}_{-0.06}$	$0.97^{+0.13}_{-0.12}$	$0.88^{+0.09}_{-0.06}$	$0.88^{+0.16}_{-0.15}$
3 jet Exclu	$0.89^{+0.07}_{-0.06}$	$0.89^{+0.12}_{-0.11}$	$0.81^{+0.10}_{-0.08}$	$0.81 \pm 0.14$
4 jet Exclu	$0.95^{+0.11}_{-0.10}$	$0.95^{+0.17}_{-0.15}$	$0.83 \pm 0.10$	$0.83^{+0.14}_{-0.16}$
3 jet Inclu	$0.90^{+0.08}_{-0.06}$	$0.90^{+0.12}_{-0.11}$	$0.81^{+0.09}_{-0.07}$	$0.81 \pm 0.14$
4 jet Inclu	$0.94^{+0.10}_{-0.09}$	$0.94^{+0.16}_{-0.14}$	$0.83^{+0.11}_{-0.09}$	$0.83 \pm 0.14$
5 jet Inclu	$0.90^{+0.16}_{-0.14}$	$0.90^{+0.22}_{-0.20}$	$0.82^{+0.21}_{-0.15}$	$0.82^{+0.24}_{-0.20}$

**Table 4.3:** Table of scaling factors for the  $W$  in association with  $n$  jets MC samples based on the CA method. Pretag refers to the analysis selection without the requirement of any  $b$ -tagged jets, tagged means the analysis selection requires at least 1 jet to be  $b$ -tagged.

between the  $u$  and  $d$  PDFs (see figure 2.7). This is done by applying the formula with the extra requirement that the event contain exactly  $n$  jets for the  $n$  jet bin, up to four jets, or contain at least 5 jets for a final 5+ jet bin, to obtain a  $N_{n-jets}^{exp}$  normalisation expectation.

Finally, when estimating the distribution of  $W$ +jets in some kinematic distribution that we are interested in, the shape of the distribution is taken from the MC simulation, while the overall normalisation factor is set to the  $N_{jets}^{exp}$  from this charge asymmetry method, separately for each jet bin. The scaling factors, which is the ratio of the data-driven method to the MC estimate, derived from this procedure are shown in table 4.3. The scale factors are compatible between the electron and muon channels, within the uncertainty of the analysis, but predict value for the scale factors below 1 in both channel. They are compatible to 1 within the  $1\sigma$  uncertainties of the muon analysis only.

## Heavy Flavour Normalisation

As well as the overall cross-section, the fraction of  $W$  boson events produced in association with heavy quarks ( $c$  or  $b$ ) has been estimated from data. We assume that the MC correctly describes the kinematics and simulation of events where heavy flavour jets are produced in association with a  $W$  boson correctly, but that the flavour composition of the MC sample is not necessary correctly described, due to the theoretical uncertainties in

calculating these compositions. For example, the production of a charm jet in association with  $W$  requires knowledge of the proton's strange quark PDF, which is uncertain in the literature, with some PDF fits favouring a  $s$ -quark sea distribution consistent with the  $\bar{d}$  distribution [158], while others prefer a strange suppressed PDF of  $\bar{s}/\bar{d} \approx 0.5$  [68].

The total number of  $W$ +jets events can be expressed in terms of the total number of  $W$ +jets events and the fractions of events that a particular jet type is produced in association with the  $W$ . The fractions considered are  $F_{bb}$ , the fraction of events where a  $b\bar{b}$  pair is produced in association with the  $W$  (which we shall refer to as  $W$ +jets + $b\bar{b}$ ),  $F_{cc}$  where a  $c\bar{c}$  pair is produced ( $W$ +jets + $c\bar{c}$ ),  $F_c$  where a  $c$  and light jet are produced ( $W$ +jets + $c$ ), and  $F_l$  where only light jets are produced. Since heavy quarks are produced far less often than light jets, the case where more than one or two heavy quarks are produced in association with the  $W$  are not considered. We wish to determine these fractions from data.

We thus have

$$\begin{aligned} N_{pre}^{W^\pm} &= N_{pre}^{W^\pm} (F_{bb} + F_{cc} + F_c + F_l) \\ N_{tag}^{W^\pm} &= N_{pre}^{W^\pm} (F_{bb}P_{bb} + F_{cc}P_{cc} + F_cP_c + F_lP_l) \end{aligned} \quad (4.9)$$

where  $N_{pre}^{W^\pm}$  are the number of  $W$ +jets events reconstructed in the sample without any  $b$ -tagged jets requirements (the pretag sample),  $N_{tag}^{W^\pm}$  the number of events in a sample where at least one jet is required to be  $b$ -tagged (the tagged sample), and  $P_{bb}$ ,  $P_{cc}$ ,  $P_c$ , and  $P_l$  is the probability for, respectively, a  $W$ +jets + $b\bar{b}$  event,  $W$ +jets + $c\bar{c}$  event,  $W$ +jets + $c$  event or  $W$ +jets with light jets only event to contain a  $b$ -tagged jet. The  $P_i$  probabilities are determined from MC simulation, and we have considered the positive and negative leptons separately (i.e. both lines represent two equations).

The first line simply gives us that the fractions need to add to one. The second gives us two equations (one for positive and negative leptons separately). We thus have three equations and four unknowns, so we arbitrarily set  $F_{cc} = k_{cc}^{bb}F_{bb}$  where  $k_{cc}^{bb}$  is the amount of  $W + cc$  relative to  $W + bb$  determined from MC simulation.

Since the heavy flavour composition of the  $W$ +jets sample will change the expected charge asymmetry, i.e. the  $r_{MC}$  value used, the  $N_{pre}$  and  $N_{tag}$  values are rederived and the heavy flavour normalisation procedure are iterated until the values are stable.

The heavy flavour fractions are determined using just the 2-jet bin. The fractions in the other jets are taken by using the MC simulation ratio of heavy flavour events in the

	$K_{bb}$	$K_c$	$K_{light}$
Muon	$1.24^{+0.34}_{-0.34}$	$0.98^{+0.37}_{-0.31}$	$0.97^{+0.07}_{-0.08}$
Electron	$1.41^{+0.31}_{-0.39}$	$0.73^{+0.39}_{-0.35}$	$1.00 \pm 0.09$

**Table 4.4:** Heavy flavour fraction scaling factors for the 2-jet bin. The scaling factors are applied to each category separately, then an additional scaling factor to all the samples so that the pretag number of events is the same as the value obtained by the charge asymmetry method.

$n$ -jet bin to the 2-jet bin and then doing an overall normalisation to preserve the number of events in pretag, found by the charge asymmetry method above. Table 4.4 shows the heavy flavour fractions derived in the 2-jet bin. The scale factor is found separately in the muon and electron channels. The values are compatible with 1 in both channels, though with some tension in the  $bb$  component, preferring a value above 1.

### 4.3.3. QCD Multijet Estimation

Multijet production from standard QCD processes is an important class of background. In these events, either one of the jets is incorrectly reconstructed as a lepton and so can pass the lepton selection or a lepton from a heavy flavour decay (recalling the  $B$ -hadrons have large leptonic branching ratios) takes the majority of the jet's energy and so it passes the lepton isolation requirements. To then pass the full event selection requires also a large amount of missing transverse momentum. Since there will be no actual missing transverse momentum in the event, this means that it only occurs in this process for very poorly reconstructed  $E_T^{miss}$ . Thus, these events will only occur rarely in the total QCD multijet sample, but because the multijet cross-section is orders of magnitude higher than the top cross-section (see figure 2.6) there will still be a non-trivial number of multijet events passing the event selection. Since orders of magnitude less multijet simulation can be produced than will actually occur in the detector, the simulation will not produce enough events to be able to model these events accurately. Therefore, a data-driven method has been developed to estimate the size and kinematics of this background: the matrix method.

In the matrix method, two categories of events are reconstructed, one with a loose selection, the other a tight. Using an independent measurement of the efficiency for either events with a jet faking a lepton (fake events) or events with a real lepton (real

events) to pass the tight selection given the loose selection, an estimate of the number of fake events in the tight selection can be obtained [116].

$$\begin{aligned} N^{loose} &= N_{real}^{loose} + N_{fake}^{loose} \\ N^{tight} &= \epsilon_{real} N_{real}^{loose} + \epsilon_{tight} N_{fake}^{loose} \end{aligned} \quad (4.10)$$

where

$$\begin{aligned} \epsilon_{real} &= N_{real}^{tight} / N_{real}^{loose} \\ \epsilon_{fake} &= N_{fake}^{tight} / N_{fake}^{loose} \end{aligned} \quad (4.11)$$

then

$$N_{fake}^{tight} = \frac{\epsilon_{real}}{\epsilon_{real} - \epsilon_{fake}} (\epsilon_{real} N^{loose} - N^{tight}) \quad (4.12)$$

From the expression, one sees that a robust estimate of the background requires loose and tight selections with significantly different efficiencies. Since in general, an estimate is needed for a kinematic distribution rather than simply the number of events, the previous equation can be used as an per-event reweighting  $w$  [159]:

$$w = \frac{\epsilon_{real}}{\epsilon_{real} - \epsilon_{fake}} (\epsilon_{real} isLoose - isTight) \quad (4.13)$$

where  $isLoose$  ( $isTight$ ) is 1 if the event passes the loose (tight) selection and 0 otherwise. By running over all events in the loose and tight selection (avoiding overlap for events passing both selections), and weighting each event by  $w$ , an estimation for any kinematic distribution may be obtained. This weighting method also allows the efficiencies to be parametrised in terms of the kinematic variables that may affect the efficiency, for example the  $p_T$  and  $\eta$  of the lepton or the distance to the nearest jet.

For  $\mu + \text{jets}$ , two sets of efficiency factors, which differ in the control region used to estimate fake efficiencies, are used and then the weight used for a given event is the average of the weights of the two methods.

In the first method, method A, the real efficiency term is measured using a tag and probe method with  $Z \rightarrow \mu\mu$  boson decays in data. In this method a high-quality, tight, “tag” muon is found in conjunction with a loose, “probe” muon, and it is required that the muon momenta add to give an invariant mass in a window around the  $Z$  peak. Since

this is a very clean decay channel, the hard physics process is almost certainly  $Z$  boson production, and so both reconstructed muons are real, prompt muons. The efficiency is then the ratio of the loose probe muons that also pass the tight criteria. A study of the real efficiencies as a function of the muon  $\eta$  and  $p_T$  show that they are essentially independent of these variables.

To extract the fake efficiency, method A uses a low  $E_T^{miss}$  and  $m_T^W$  control region. It requires the standard  $t\bar{t}$  selection of section 4.1.7, except that the  $E_T^{miss}$  and  $m_T^W$  cuts are replaced by:

$$m_T^W < 20 \text{ GeV}, E_T^{miss} + m_T^W < 60 \text{ GeV} \quad (4.14)$$

With this selection a large proportion of the events are QCD multijet, since these events have no real missing transverse momentum. Therefore, the majority of the events will be fakes, that is, the muons will be non-prompt. A small contribution from  $W$ +jets and  $Z$ +jets will still be in the selection, so this is estimated from MC simulation and subtracted before the fake efficiencies are obtained. In this method, the loose muons are identified as for the tight muons described in section 4.1.3, except that the muon calorimeter and track isolation requirements are dropped. Comparing the fraction of tight events in this selection after the background subtraction then gives the fake efficiency. Figure 4.6 shows the efficiencies derived from these procedures, which is binned based on the  $\eta$  of the muon and the  $p_T$  of the highest  $p_T$  jet in the event. These figures show that the real and fake efficiencies are sufficiently different, as was need from equation 4.12, to provide a robust estimate of the multijet background contribution. It also shows that the real efficiency is essentially 1 for all muon rapidities and independent of the jet activity in the event. The fake efficiency shows a slight  $\eta$  dependence and a definite leading jet  $p_T$  dependence. This can be understood as lower  $p_T$  jets being less collimated and so muons produced from hadronic decays inside the jet are more likely to be ejected outside of the jet cone.

The second method, method B, uses signal MC to determine the real event efficiency. For the fake efficiency, Method B uses the fact that most of the fake muons in the final analysis will be muons originating from heavy flavour decays and so will generally be non-prompt (i.e. not coming from the primary vertex). The efficiency is then studied as a function of the transverse impact parameter  $d_0$ :

$$\epsilon(x) = N_{d_0 > x}^{tight} / N_{d_0 > x}^{loose} \quad (4.15)$$

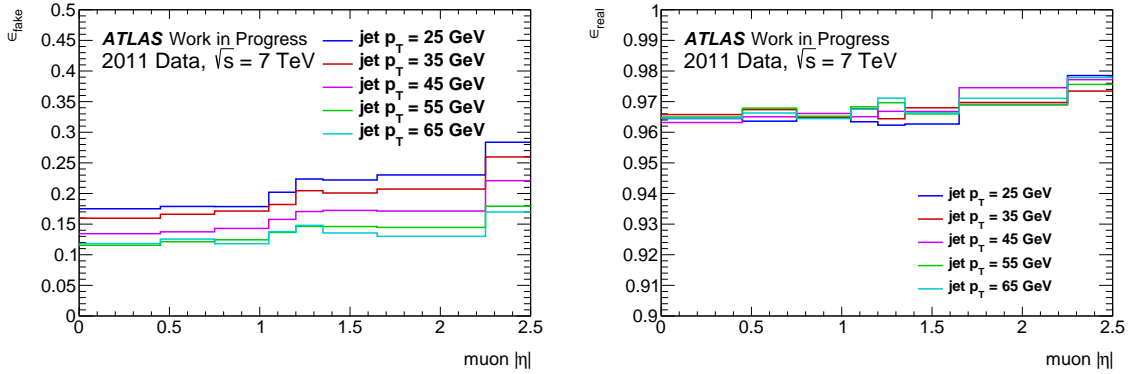


**Figure 4.6:** The fake (left) and real (right) efficiencies with respect to the muon  $|\eta|$  for the multijet matrix method in the muon channel, method A. The different curves show the efficiency for different leading jet  $p_T$  ranges.

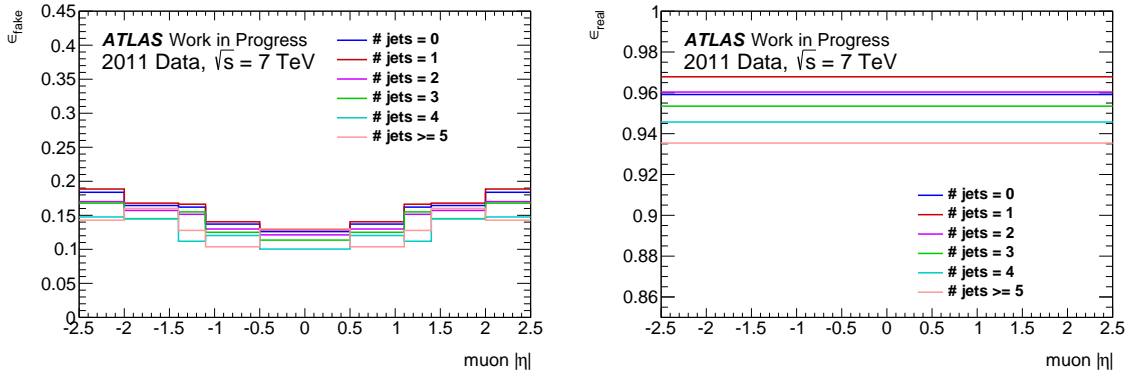


**Figure 4.7:** The fake (left) and real (right) efficiencies with respect to the muon  $|\eta|$  for the multijet matrix method in the muon channel, method B. The different curves show the efficiency for different number of jets in the event.

For small values of  $x$ , the efficiency will contain contributions from both the real prompt leptons, and the fake non-prompt leptons. MC simulation studies show, however, that for large values of  $x$ ,  $\epsilon(x)$  approaches the QCD only value of  $\epsilon$ . Therefore,  $\epsilon_{\text{fake}}$  is extracted by fitting the data measurement of  $\epsilon(x)$  with prompt and non-prompt components, and taking the non-prompt component at  $x = 0$  to be the fake efficiency. This method bins the efficiencies by muon  $\eta$  and the number of jets in the event. Figure 4.7 shows the efficiencies derived from these procedures. Again, the real efficiency is found to be close to 1 across all selections, while the fake efficiency is slightly  $\eta$  dependent.

For electrons, the loose electrons are selected in the same way as for our electron selection of section 4.1.2, except that all the isolation requirements are dropped. The real efficiency is estimated using a tag and probe with a  $Z \rightarrow ee$  sample. The fake efficiency is extracted from events with  $E_T^{\text{miss}} < 20$  GeV. The efficiency is obtained by the ratio of

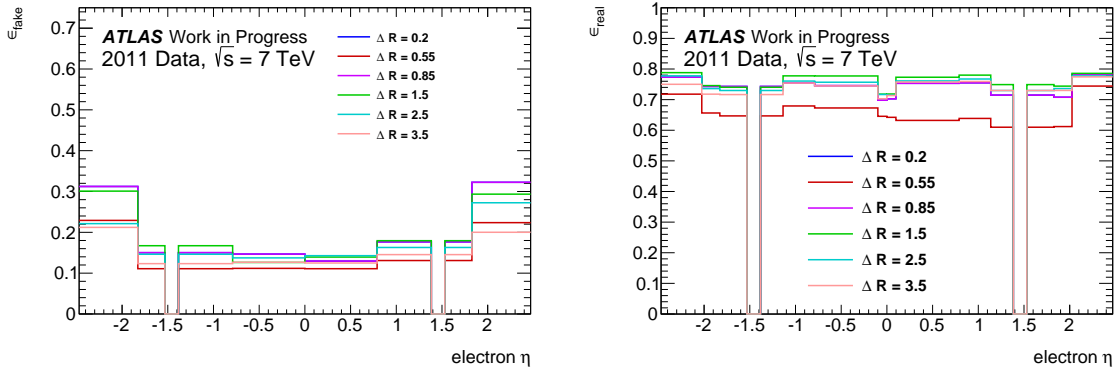


**Figure 4.8:** The fake (left) and real (right) efficiencies for the multijet matrix method in the electron channel. The efficiencies are calculated for different values of the electron’s  $\eta$  and by the  $\Delta R$  between the electron and the nearest jet.

tight events in the loose electron sample, after subtracting the non-multijet background, predicted by the MC, from the data sample. The efficiency is binned in terms of the  $\eta$  of the electron and the smallest  $\Delta R$  between the electron and any jet in the event. Figure 4.8 shows the real and fake efficiencies obtained from the method. Note that efficiencies around  $\eta = 1.5$  are zero since no electrons are reconstructed in this crack region. Since it is more likely for a jet to fake an electron (as a calorimeter deposit) than a muon (which requires a muon being produced in the jet decay), the tight selection requirements needed give a real efficiency of around 0.8, and lower when there is a nearby jet. The fake efficiencies are small (around 0.1), except at large  $\eta$ , where the efficiency reaches 0.3 for fakes far from any other jet activity. This difference is again large enough that we can expect a robust estimate for the background contribution.

#### 4.3.4. Data/Monte Carlo Comparisons

Having established background estimates and presented the signal sample, we can now look at the object kinematics for the given event selection in data and compare with the total of these estimates. In all the following figures, the  $t\bar{t}$  signal sample used is POWHEG+PYTHIA as this was found to give the best match to the data. Table 4.5 shows the expected background, signal and data yields with our event selection outlined above. Figure 4.9 shows the distribution of the reconstructed lepton kinematics. Figure 4.10 shows the reconstructed  $E_T^{\text{miss}}$  and the associated  $m_T^W$ . Figure 4.11 show the kinematic distributions of the jet in the event with the highest  $p_T$  (the leading jet). From the

figures, generally good agreement is seen between the data and the estimation within the systematic uncertainties (which will be discussed in section 6.2).

Source	Yields	
	$e + \text{jets}$ ( $\pm \text{stat.} \pm \text{syst.}$ )	$\mu + \text{jets}$ ( $\pm \text{stat.} \pm \text{syst.}$ )
$t\bar{t}$ (single-lepton)	$7806 \pm 20 \pm 628$	$9409 \pm 22 \pm 699$
$t\bar{t}$ (dilepton)	$572 \pm 5 \pm 55$	$672 \pm 6 \pm 62$
Single top-quark	$434 \pm 6 \pm 50$	$517 \pm 7 \pm 50$
$W + \text{jets}$	$263 \pm 15 \pm 109$	$363 \pm 18 \pm 126$
Multijet	$134 \pm 16 \pm 65$	$56 \pm 4 \pm 11$
$Z + \text{jets}$	$52 \pm 4 \pm 13$	$28 \pm 3 \pm 7$
Diboson	$7 \pm 1 \pm 1$	$7 \pm 1 \pm 1$
Expectation	9269	11053
Data	$8791 \pm 94$	$10690 \pm 103$

**Table 4.5:** Event yields for data, MC simulation and data driven background estimates, in the electron and muon channels. The expected background yields include statistical and systematic uncertainties for each channel, while the data yield shows the statistical uncertainty. The  $t\bar{t}$  prediction is from the POWHEG+PYTHIA P2011C sample and all MC samples are normalised to  $4591.01 \text{ pb}^{-1}$ .

## 4.4. Particle-object selection

Particle objects were constructed by studying the particles output by the event generators before they were passed through detector simulation. They were used to construct a particle event with objects equivalent to the reconstructed objects just described, so that the truth properties, as defined by the event generator, could be compared with the reconstruction. The particle objects were run through the same requirements as the reconstruction to build our final distributions, and these were used to obtain corrections which account for the distortion of the physics distributions by the detector. The correction procedure is covered in section 6.1.

Leptons and jets were defined using particles with a mean lifetime  $\tau > 0.3 \times 10^{-10} \text{ s}$ , directly produced in proton–proton interactions or from subsequent decays of particles with a shorter lifetime. Electrons, muons and neutrinos were selected by requiring the particles to have a non-quark or hadron parent, either directly or via a tau decay. This

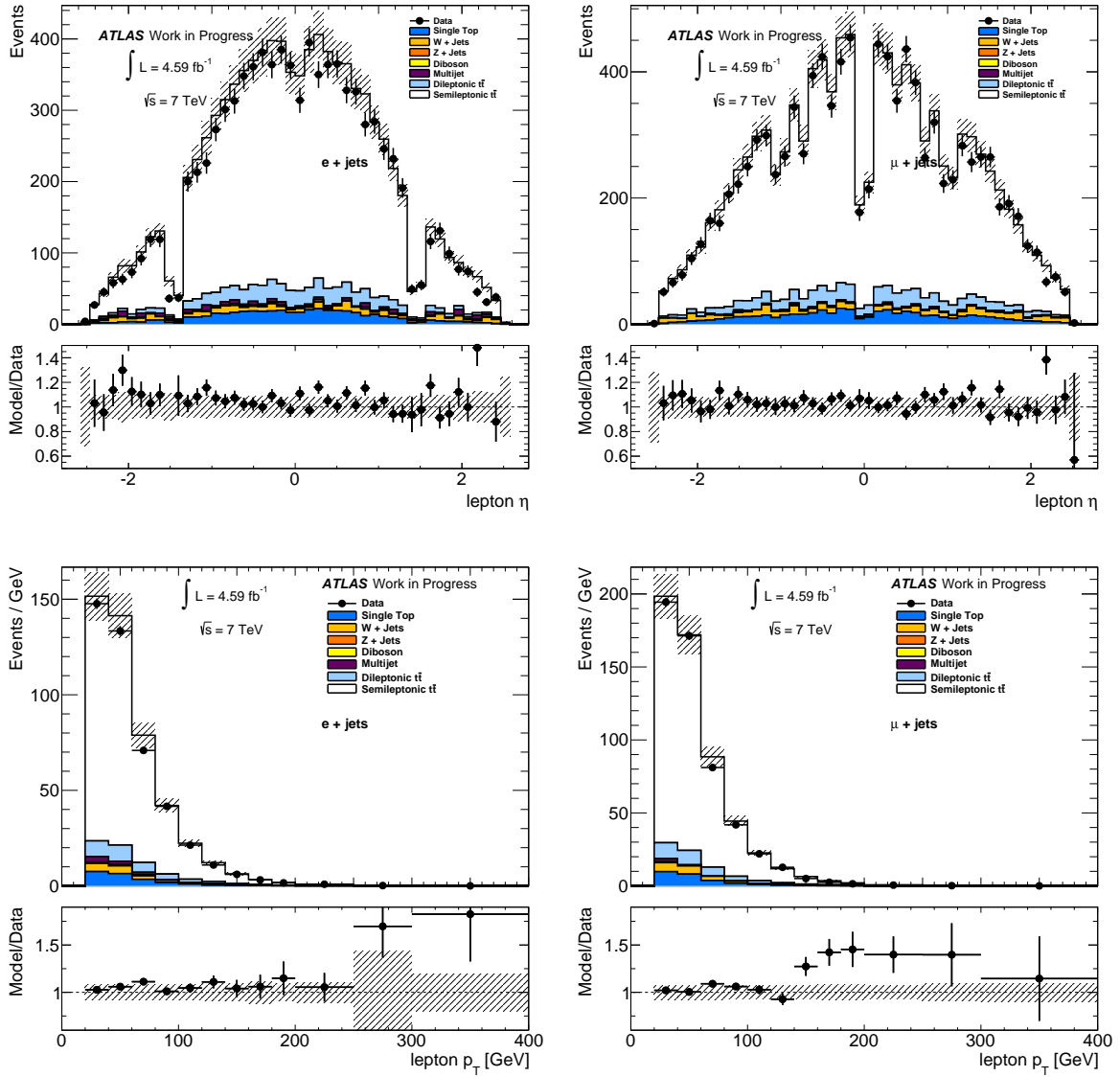


**Figure 4.9:** Data and MC distributions for leptonic quantities which include the lepton  $\eta$  (top) and  $p_T$  (bottom) for the electron (left) and muon (right) channels. The shown uncertainties are statistical on the data, and from the systematics as the hashed band on the Monte Carlo stack. POWHEG+PYTHIA MC is used for the signal expectation. At least two  $b$ -tags are required in the event.

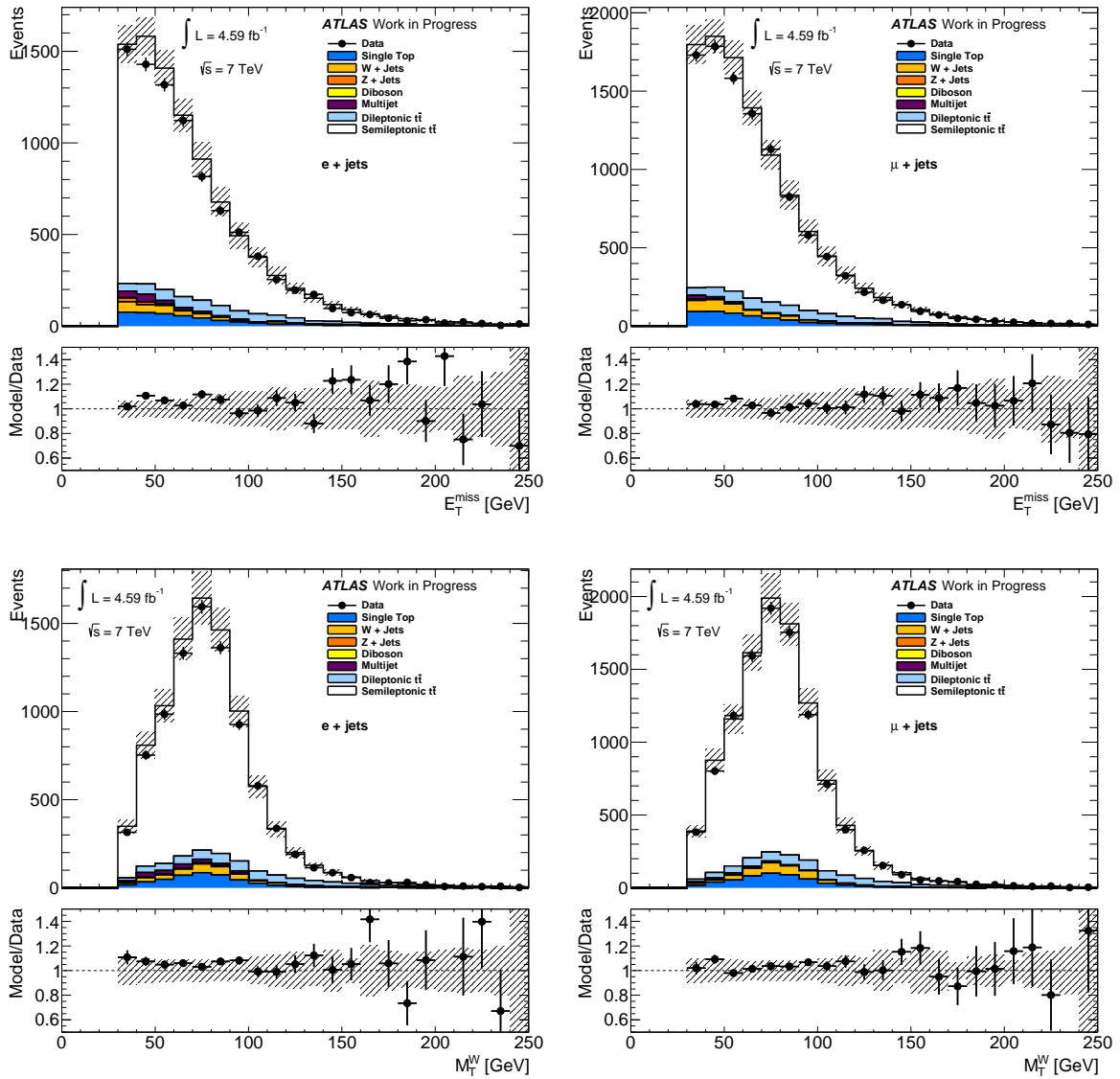


**Figure 4.10:** Data and MC distributions for missing transverse energy quantities which include the  $E_T^{miss}$  (top) and  $m_T^W$  (bottom) for the electron (left) and muon (right) channels. The uncertainties are statistical on the data, and from the systematics as the hashed band on the Monte Carlo stack. POWHEG+PYTHIA MC is used for the signal expectation. At least two  $b$ -tags are required in the event.

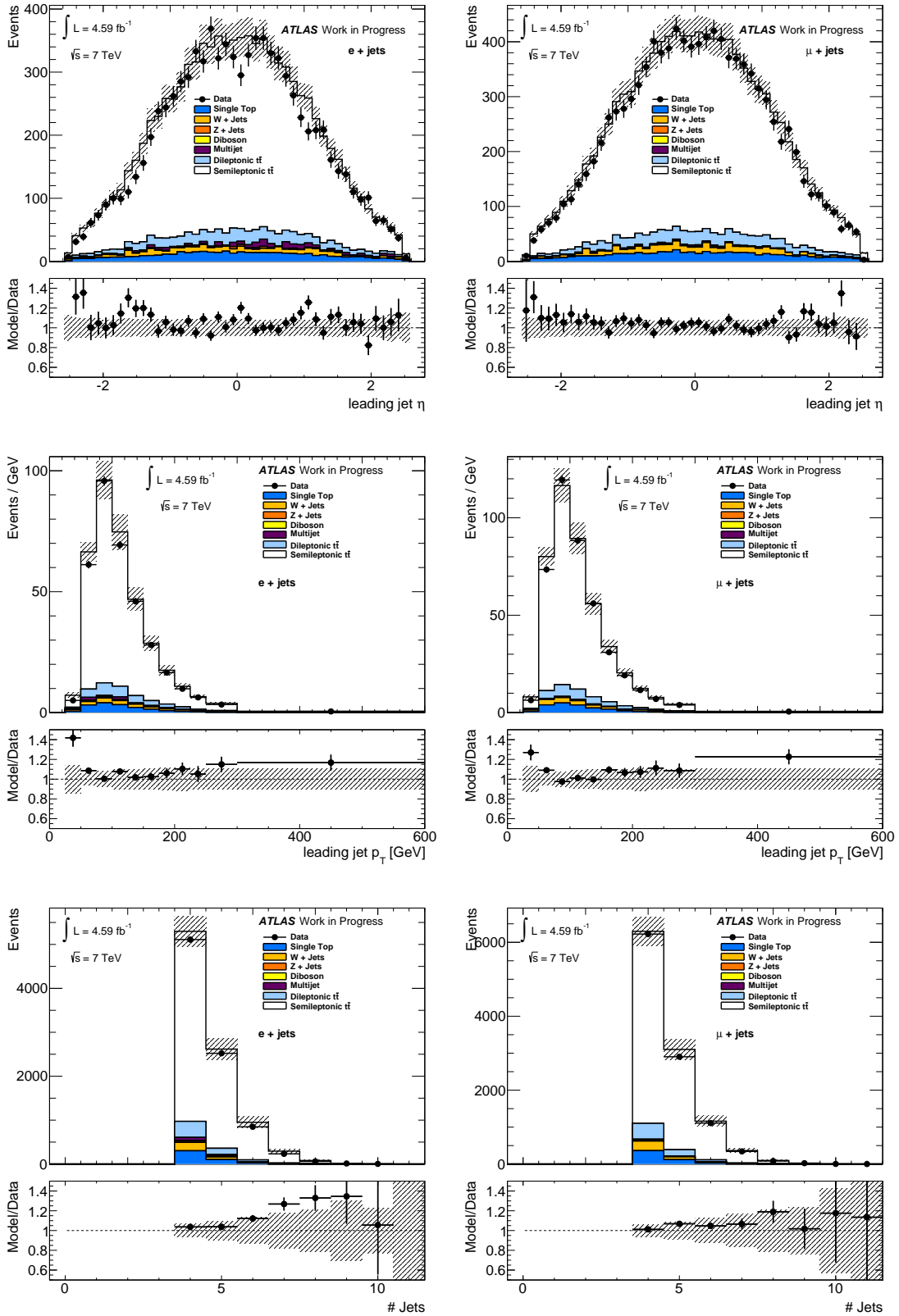


**Figure 4.11:** Data and MC distributions for jet quantities which include the leading jet  $\eta$  (top),  $p_T$  (middle) and the number of jets (bottom) for the electron (left) and muon (right) channels. The uncertainties are statistical on the data, and from the systematics as the hashed band on the Monte Carlo stack. POWHEG+PYTHIA MC is used for the signal expectation. At least two  $b$ -tags are required in the event.

requirement was made to indirectly select leptons from  $W$  or  $Z$  boson decays. The indirect lepton selection was found to match the  $W$  boson via generator record tracing in all cases except for orphaned leptons, that is, leptons without any parent particles in the generator record. Orphaned leptons were excluded as background. The non-quark requirement was needed in the indirect lepton selection due to the manner in which  $b$ -fragmentation is stored within some event records.

Electron and muon four vectors were calculated after the addition of photons within a  $\Delta R = \sqrt{(\Delta\phi)^2 + (\Delta\eta)^2}$  cone of 0.1 of their original directions. The four vector sum of the selected neutrinos was taken to be the missing transverse energy  $E_T^{miss}$ . Jets were clustered using the anti- $k_t$  algorithm (described in section 4.1.4) with radius parameter  $R = 0.4$ . All particles were considered for jet clustering, except for electrons, muons and neutrinos indirectly matched to  $W/Z$  boson decays and any photons associated with the electrons or muons.  $B$  hadrons were normalised to a small energy value and clustered within the particle jets. The presence of one or more  $B$  hadron within the list of jet constituents was taken as the  $b$ -tagging result.

These object selections were developed to allow Rivet analysis of the final distributions after correcting back to the particle level. Rivet is a tool for automatically performing data to event generator comparisons and will be discussed further in section 5.2. These selections were agreed upon in discussion with the Rivet authors as part of a wider effort to develop particle level analyses for the top quark at hadron colliders.

A summary of the selections made at both reconstruction and particle level is shown in table 4.6.

**Table 4.6:** Table summarising the event selections used for the analysis of this thesis.

Object	Reconstruction	Particle
<b>Jet</b>	From calo cells $ JVF  > 0.75$	Stable particles
	$p_T > 25$ GeV At least four jets passing above $ \eta  < 2.5$	
<b>B-tagging</b>	MV1 > 0.601713	B hadron clustered in jet
<b>Lepton</b>	Exactly 1 $e$ or $\mu$ (trig.+rec.)	Exactly 1 $e$ or $\mu$ (from top)
	$p_T > 25$ GeV (no other $e/\mu$ with $p_T > 15$ GeV) $ \eta  < 2.5$ ( $e^{rec}$ : $ \eta  < 2.47$ excluding $1.37 <  \eta  < 1.52$ )	
	$\Delta R(jet, lepton) > .25$ for all selected jets	
<b><math>E_T^{miss}</math></b>	Transverse calorimeter energy imbalance $E_T^{miss} > 35$ GeV	$\sum \nu$ at particle-level $\sum p_T > 35$ GeV
	$m_T^W > 30$ GeV	

# Chapter 5.

## Pseudo-Top Definition

In this chapter, we investigate the construction of a differential observable which measures the kinematics of top pair production. We begin in section 5.1 with a discussion of the top kinematic observables we are interested in measuring and their theoretical interpretation. Section 5.2 describes the previous measurements of the differential distributions of these variables and the problems in their theoretical interpretation. Section 5.3 introduces a new object, the “pseudo-top”, which we propose to measure to alleviate those problems. This section studies various possible definitions and their properties, concluding with a pseudo-top definition which will be analysed with ATLAS data in the next chapter.

### 5.1. Differential Distributions

The inclusive cross-section gives a general indication of whether QCD can account for the cross-section production. In order to truly test pQCD and the assumptions in the models that are used in the theory of top pair production in hadron colliders, more refined measurements are needed. Reconstructing the kinematics of the top pair and measuring the distributions of these kinematics provides a more stringent test of the theory. Measuring the mass of the top pair system, for instance, gives at leading order the total energy of the production process. This is strongly correlated with the description of the gluon PDF, since gluon fusion the high- $x$  regime is the dominant production process. Since the measurement of PDFs typically involves either probes sensitive to only the electric charge distribution of the proton in the case of deep inelastic scattering (and so only sensitive to the gluon PDF indirectly through scaling violations), or the low- $x$  gluon PDF in the case of jet production measurements, the high- $x$  gluon PDFs (above about

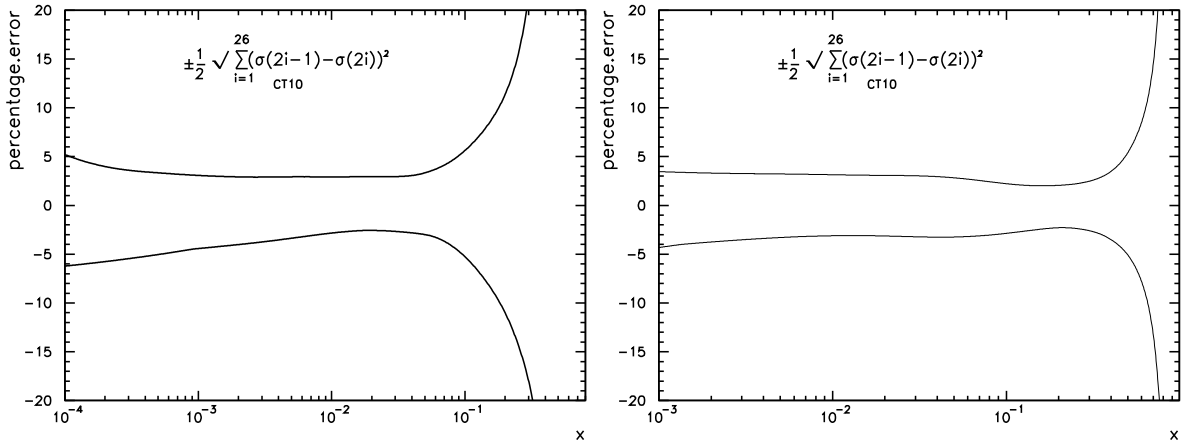


**Figure 5.1:** Gluon (left) and up quark (right) proton PDF uncertainty bands for  $Q^2 = 172.5 \text{ GeV}^2$  from the CT10 PDF fit [75]. Produced using [163].

$x = 0.1\text{--}0.2$ ) are comparatively poorly constrained. This is shown in figure 5.1 which shows the uncertainties on the gluon and up quark PDF distributions with  $Q^2 = m_t^2$ . The figures show that the large  $x$  gluon PDF diverges (due to extrapolation uncertainties) at smaller  $x$  than the up PDF, with 25% uncertainty in the gluon PDF by  $x = 0.3$  where the up PDF uncertainty is not 25% until around  $x = 0.8$ . References [160–162] show that the inclusive cross-section measurement alone can improve the uncertainty in the large- $x$  gluon PDF, and that further studies of the differential cross-sections (in particular the top pair mass and rapidity) will be able to further improve the result. It has also been noted that the top production is the only process which has been calculated to NNLO and sensitive to the gluon, and so the only such process that can be consistently included in an NNLO PDF fit approximations [162].

As an example of the impact that these types of studies can have, consider the so-called gap fraction analysis [150]. In this analysis,  $t\bar{t}$  events are selected and the properties of the additional jets in the event are probed. The analysis looks for dileptonic decays and requires two identified  $b$ -jets, which are assumed to be from the decay of the top. Events are vetoed if they contain an additional jet above a  $p_T$  threshold in a specified rapidity range, and the fraction of the surviving events to the total number of events is measured. This is done for several rapidity ranges, with a varying  $p_T$  threshold. Examples of the results of the measurements from ATLAS are shown in figure 5.2. This gap fraction is a sensitive probe to the initial state radiation produced in the parton showering, and allows the parameters of the phenomenological radiation models used in producing  $t\bar{t}$  event simulations to be constrained. Samples derived from the allowed extremes in the parameters based on a fit to the gap fraction measurement are used in

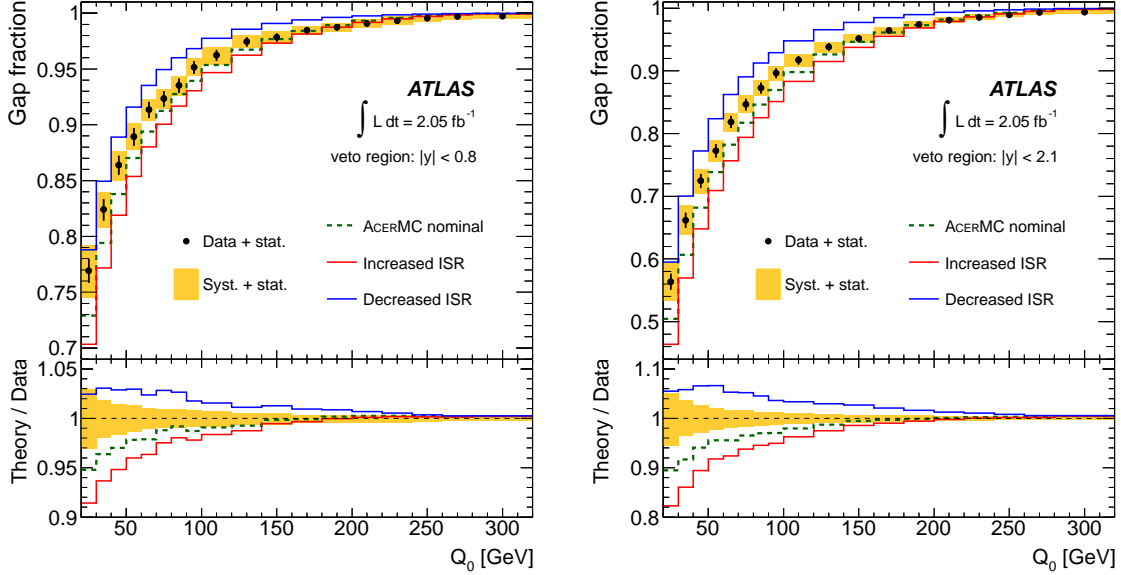


**Figure 5.2:** The measured gap fraction as a function of  $Q_0$ , the jet  $p_T$  threshold for additional jet activity, for  $|y| < 0.8$  (left) and  $|y| < 2.1$  (right). The measurement is compared to the ACERMC generator, where different settings of the PYTHIA parton shower parameters are used to produce samples with nominal, increased and decreased initial state radiation. From [150].

this analysis to estimate the uncertainties due to initial state radiation. This gives better estimates of the amount of ISR/FSR in  $t\bar{t}$  events than were previously available.

For hadron collisions, incoming partons can be analysed in terms of the PDF values probed and their rapidity (following [164]). For massless partons, their momenta can be written  $p_1^\mu = \frac{\sqrt{s}}{2}(0, 0, x_1, x_1)$ ,  $p_2^\mu = \frac{\sqrt{s}}{2}(0, 0, -x_2, x_2)$  where  $x_1, x_2$  are the fraction of the protons momentum that they carry, and  $s$  is the centre of mass energy squared. Then, the centre of mass energy squared of the partonic collision can be written  $\hat{s} = x_1 x_2 s$ . The rapidity of the pair is given by  $y = \frac{1}{2} \log \frac{x_1}{x_2}$  and we thus have

$$x_1 = \sqrt{\frac{\hat{s}}{s}} e^y, \quad x_2 = \sqrt{\frac{\hat{s}}{s}} e^{-y} \quad (5.1)$$

At leading order, the top pair is the only product of the collision and so the 4-momentum of the  $t\bar{t}$  system will be equivalent to the 4-momentum of the parton system. Thus the rapidity of the system  $y = |y^{t\bar{t}}|$  and the mass of the  $t\bar{t}$  system  $\hat{s} = m^{t\bar{t}}$  can be simply related to the values of the parton PDF being probed for a given collision (if we consider only the leading order processes to contribute). Figures 5.3 and 5.4 show the  $m^{t\bar{t}}$  and  $|y^{t\bar{t}}|$  distributions respectively with different PDFs used with the

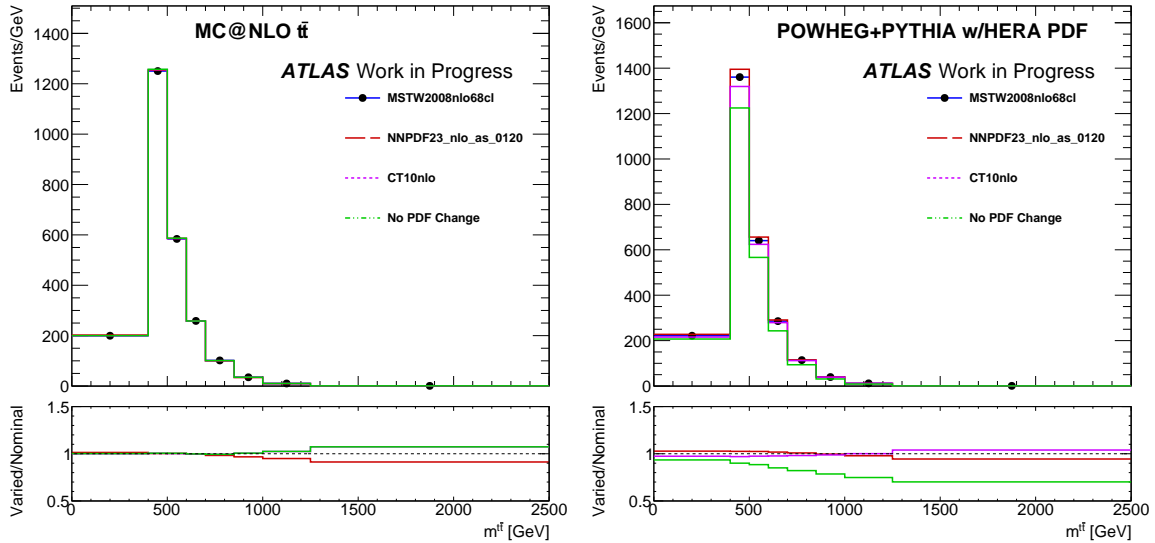


**Figure 5.3:** The  $m^{t\bar{t}}$  parton-level distribution for the ALPGEN+HERWIG (left) and POWHEG+PYTHIA (right)  $t\bar{t}$  signal samples, reweighted using various PDFs. The bottom of the figures show the ratio of the varied PDFs to the MSTW2008 NLO PDF.

ALPGEN+HERWIG  $t\bar{t}$  signal MC. A substantial difference can be seen particularly with the HERAPDF, which is softer (has lower average  $m^{t\bar{t}}$ ) than the other PDF fits.

The values of the PDF probed in a given  $t\bar{t}$  collision,  $x_1$  and  $x_2$ , can also be related to the kinematics of the outgoing top partons (again following [164]). When considering the leading order production without extra jets, as in figure 2.8, it can be shown that the PDF values are given by:

$$x_1 = \frac{m_T}{\sqrt{s}}(e^{y_t} + e^{y_{\bar{t}}}), \quad x_2 = \frac{m_T}{\sqrt{s}}(e^{-y_t} + e^{-y_{\bar{t}}}) \quad (5.2)$$

where  $m_T$  is a transverse mass given by  $m_T = \sqrt{m_t^2 + p_T^2}$ ,  $p_T$  is the transverse momentum of the quarks, and  $y_t$  and  $y_{\bar{t}}$  are the quark and anti-quark rapidities respectively. Figure 5.5 shows the top  $p_T$  parton-level distribution for ALPGEN+HERWIG  $t\bar{t}$  with various PDFs, and for the additional radiation settings with ALPGEN+PYTHIA  $t\bar{t}$ . Sensitivity to the additional radiation settings is seen at high  $p_T$ . Figure 5.6 similarly shows the top  $|y^t|$  distribution.

Of course, beyond leading order, extra radiation can be produced which means the relationships presented above will no longer be valid. The top pair recoiling off the extra radiation is then given non-zero  $p_T$ . The  $p_T^{t\bar{t}}$  variable, measuring the  $p_T$  of the top pair

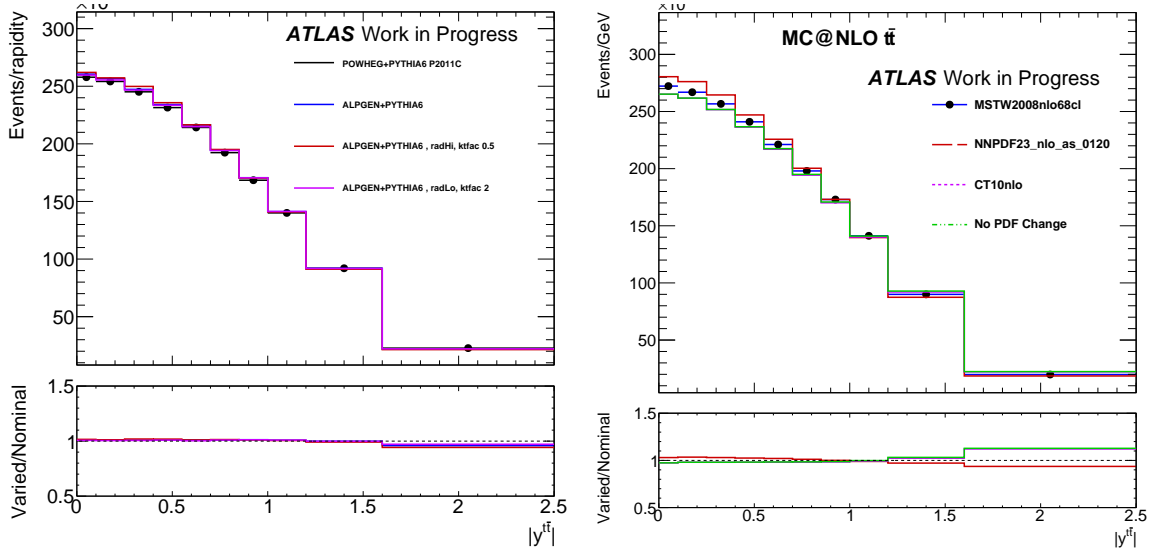


**Figure 5.4:** The  $|y^{t\bar{t}}|$  parton-level distribution for the ALPGEN+HERWIG, ALPGEN+PYTHIA, and ALPGEN+PYTHIA  $t\bar{t}$  generated with extra gluon radiation fitted to the gap analysis, both for the high radiation (radHi) and low radiation (radLo) limits. The right figure shows the various PDF distributions in ALPGEN+HERWIG  $t\bar{t}$  as for figure 5.3. The “nominal” sample used as denominator of the ratio in the lower half of the figures the is indicated by dots on the histogram in the upper half of the figures.

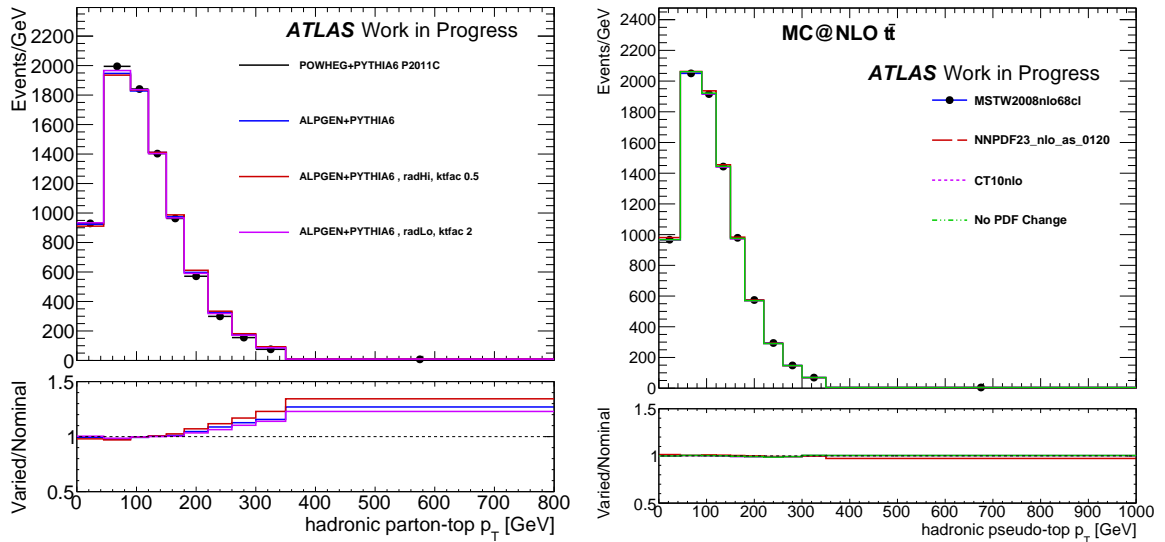


**Figure 5.5:** The top  $p_T$  parton-level distribution for the ALPGEN+HERWIG, ALPGEN+PYTHIA, and ALPGEN+PYTHIA  $t\bar{t}$  generated with extra gluon radiation fitted to the gap analysis, both for the high radiation (radHi) and low radiation (radLo) limits. The right figure shows the various PDF distributions in ALPGEN+HERWIG  $t\bar{t}$  as for figure 5.3.

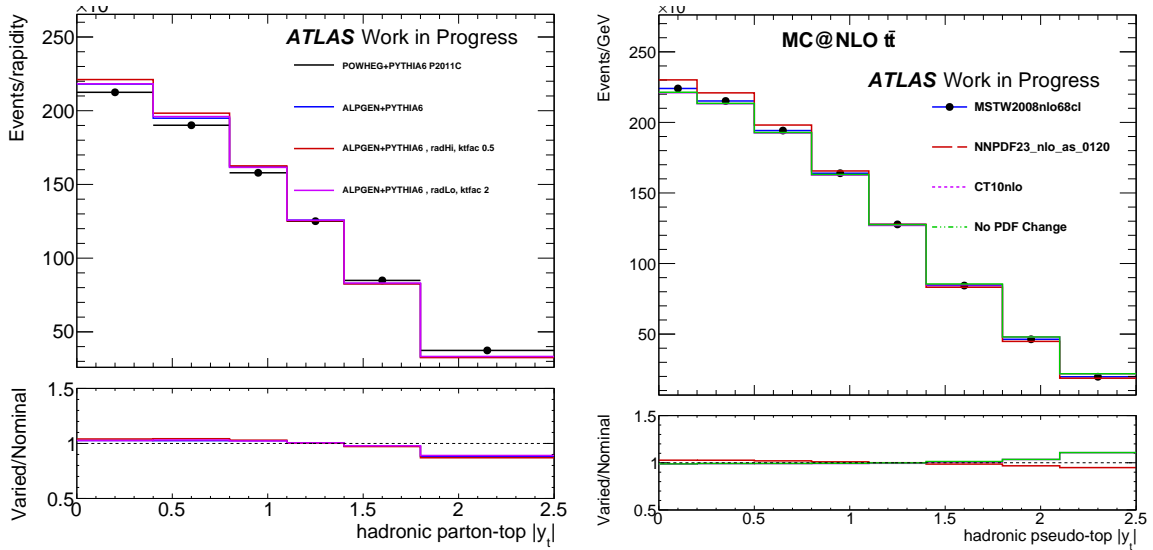


**Figure 5.6:** The  $|y^t|$  top parton-level distribution for the ALPGEN+HERWIG, ALPGEN+PYTHIA, and ALPGEN+PYTHIA  $t\bar{t}$  generated with extra gluon radiation fitted to the gap analysis, both for the high radiation (radHi) and low radiation (radLo) limits. The right figure shows the various PDF distributions in ALPGEN+HERWIG  $t\bar{t}$  as for figure 5.3. The “nominal” sample used as denominator of the ratio in the lower half of the figures the is indicated by dots on the histogram in the upper half of the figures.

system, is therefore a probe of the extra radiation in the event, regardless of the source of the radiation. It will therefore be useful in constraining phenomenological parameters associated with the radiation from the initial state partons, which is calculated in the parton showering step of the MCs. It is also interesting to compare the NLO matrix element calculators matched to a shower MC with the LO multi-leg generators, which have explicit calculations for extra radiation. As an example, figure 5.7 shows the parton level  $p_T^{t\bar{t}}$  distribution for the ALPGEN+PYTHIA  $t\bar{t}$  sample with different PDFs and different settings for the phenomenological model used to generate additional radiation in PYTHIA. It should also be remarked that the extra radiation has thus only been calculated to leading order (either by up to a single extra parton in NLO calculation, or by up to several extra partons at tree level only in the LO multileg generators), and that loop effects, which has a sizeable contribution in determining, for example, the top  $p_T$  distribution, are currently not included in any predictions.

Thus, fully constraining the PDF requires knowledge of the complete kinematics of the system as far as experimentally possible. In this thesis, we consider the  $y$ ,  $p_T$  and mass of the  $t\bar{t}$  system as well as the individual tops, splitting them into the hadronic

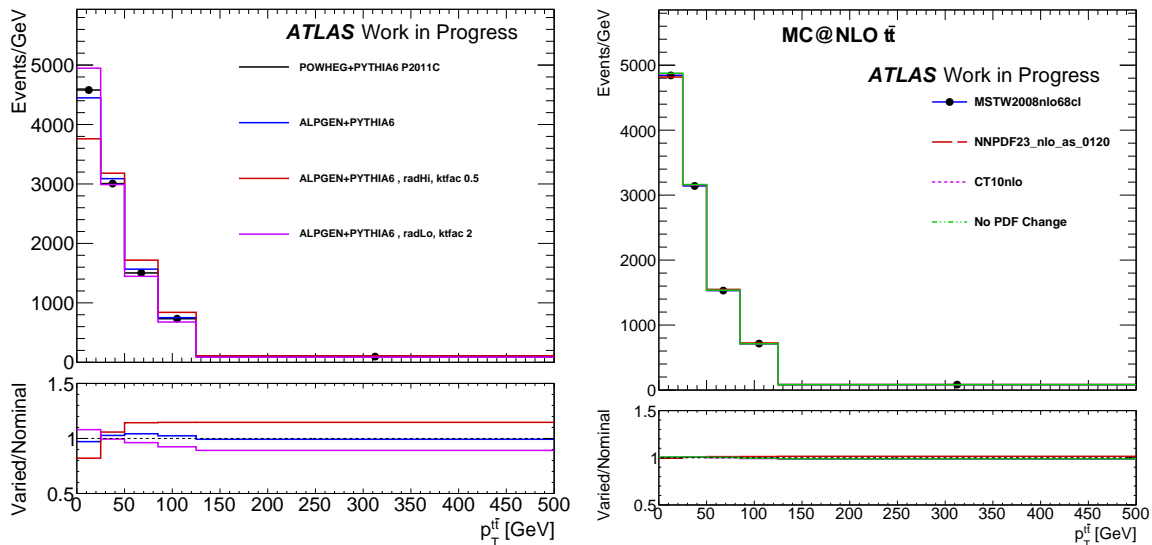


**Figure 5.7:** The  $p_T^{t\bar{t}}$  parton-level distribution for the ALPGEN+HERWIG, ALPGEN+PYTHIA, and ALPGEN+PYTHIA  $t\bar{t}$  generated with extra gluon radiation fitted to the gap analysis, both for the high radiation (radHi) and low radiation (radLo) limits. The right figure shows the various PDF distributions in MC@NLO+HERWIG  $t\bar{t}$  as for figure 5.3. The “nominal” sample used as denominator of the ratio in the lower half of the figures the is indicated by dots on the histogram in the upper half of the figures.

and leptonic sides. From the expressions for the relation between the PDFs and the kinematics, this is enough information to provide constraints to the PDF at high  $x$ .

Further motivation for measuring the kinematics of top pair production is that hints for physics beyond the standard model may show up in these distributions. A high-mass resonance decaying to top quarks would produce an enhancement of the top cross-section at high  $m^{t\bar{t}}$ , and further probes of the angular distributions of the top pair would distinguish the spin of the resonances [165]. Similarly the  $p_T$  distributions of the individual top quarks has been shown to be sensitive to new physics effects [166].

New physics can also affect the dynamics of the production. For example, the cause of the Tevatron’s measured enhancement in the forward-backward asymmetry of the top pair system is still an open question (as of early 2014). In this analysis, the top quark pair is reconstructed in the semi-leptonic decay channel using a kinematic fitter for object assignment, and the variable  $\Delta y = y_t - y_{\bar{t}}$  measured. The asymmetry  $A^{t\bar{t}} = \frac{N(\Delta y > 0) - N(\Delta y < 0)}{N(\Delta y > 0) + N(\Delta y < 0)}$  is then obtained. This variable measures the fraction of events where the top travels in the same direction as the proton beam (or conversely, the anti-top travels in the direction of the anti-proton beam). At leading order, no asymmetry is

expected, while higher-order diagrams connect the incoming and outgoing partons and generate a small asymmetry. The experiments measure a much higher than expected asymmetry that appears to be  $t\bar{t}$  mass dependent [167, 168].

While this asymmetry is not directly measurable at the LHC, related asymmetries have been introduced and measured without significant deviations being found, such as the asymmetry using top and anti-top production in absolute rapidity  $\Delta y = |y_t| - |y_{\bar{t}}|$  [169]. These asymmetry measurements serves to illustrate that new physics can show up more subtly than simple cross-section enhancements and resonances in mass distributions. The top pair system is regarded as particularly fruitful for these effects, since its high mass and the large centre-of-mass energy required to produce top quarks would likely lead to top quarks having the largest deviations due to any new physics that may be present at high energies.

Finally, as well as being interesting in terms of testing our understanding of QCD and possible direct couplings to new physics, the top quark is generically an important background to most new physics searches. For example, searches for supersymmetry (SUSY) typically concentrate on finding final states produced from the production of SUSY particles which decay through a chain of new particle states and produce a high  $p_T$  lepton [170]. The lightest SUSY particle is stable (and therefore a candidate for being the dark matter particle) and therefore escapes the detector unobserved. The final experimentally observable decay products are then several high  $p_T$  jets, lepton(s) and  $E_T^{miss}$ , which is of course the same as the final state produced by top production. Since SUSY particles are typically expected to be heavier than the top (since they have yet to be observed), the searches for these particles need to explore the high  $p_T$  tails of, for example, the lepton  $p_T$  spectrum. In this regime, there are large extrapolation uncertainties, which constraining the top pair modelling would reduce.

Thus, understanding and modelling the top quark system is important on several fronts, and producing better models of its production can be attained through the measurement of the kinematic distributions and comparing them with theory.

## 5.2. Issues with Current Top Analyses

Until now, measurements of the top pair system have been produced by requiring events with final state objects consistent with top pair decays. The final state objects are

run through a likelihood function which can be used to discriminate the best object assignment. In this procedure, a likelihood is constructed with terms for the top quark mass, and  $W$  masses from the objects, and a minimisation is performed, (by allowing the reconstructed objects energies to vary within detector resolution functions) which map the reconstructed objects to the underlying parton level objects. Each jet to top object assignment is tried in turn, and the combination with the lowest likelihood is taken as the top pair observables for the event. For example, a recent ATLAS differential measurement was produced in this manner [171]. The measurements were performed for the top pair mass,  $p_T$  and rapidity, and the individual top  $p_T$ . Example results of this analysis, shown in figure 5.8, show that the predictions for the top pair mass are discriminating against various PDF sets.

There are, however, several problems with this method that prevent it from being used as a generic test of theory and for tuning the phenomenological MC parameters, as would be useful from the discussion above.

Only a small fraction of top pair events make it to the final analysis. Firstly, our analysis is looking for semi-leptonic  $t\bar{t}$  events, which have a branching fraction of 37.8% of total top pair decays,<sup>1</sup> so only this fraction may be looked at in our analysis. Even given a semi-leptonic event, not all events will get included in the final analysis. To understand this, consider the fiducial volume of an experiment. This is the region of phase space, with respect to the  $p_T$  and angular requirements on the hadronised objects making up the event, that is accessible to the experiment. For example, in our setup the fiducial range of leptons is  $p_T > 25$  GeV (required for good triggering and lepton identification), and  $|\eta| < 2.5$  (which is the coverage of the detector). If a lepton is produced outside this range then it will not enter into any analysis that we may perform. This leads to an acceptance fraction for our events, which is the fraction of events passing the fiducial requirements. For our analysis, this acceptance is as small as a few percent. This is illustrated in figure 5.9 which shows the selection efficiency for the parton-level ATLAS analysis described earlier. Not only is the efficiency only a few percent, but it is also changes across the distribution. This can lead to several models that differ at the parton level leading to equivalent reconstruction level distributions. When these reconstructed distributions are corrected back to the parton level, they therefore implicitly assume the out of fiducial volume distribution, and so are highly dependent on the theoretical models used to estimate the acceptance correction factors (figure 6.2 shows a 20%

---

<sup>1</sup>This number includes the fact that only  $\tau$  leptons decaying to an electron or muon are considered as “leptonic” decays.

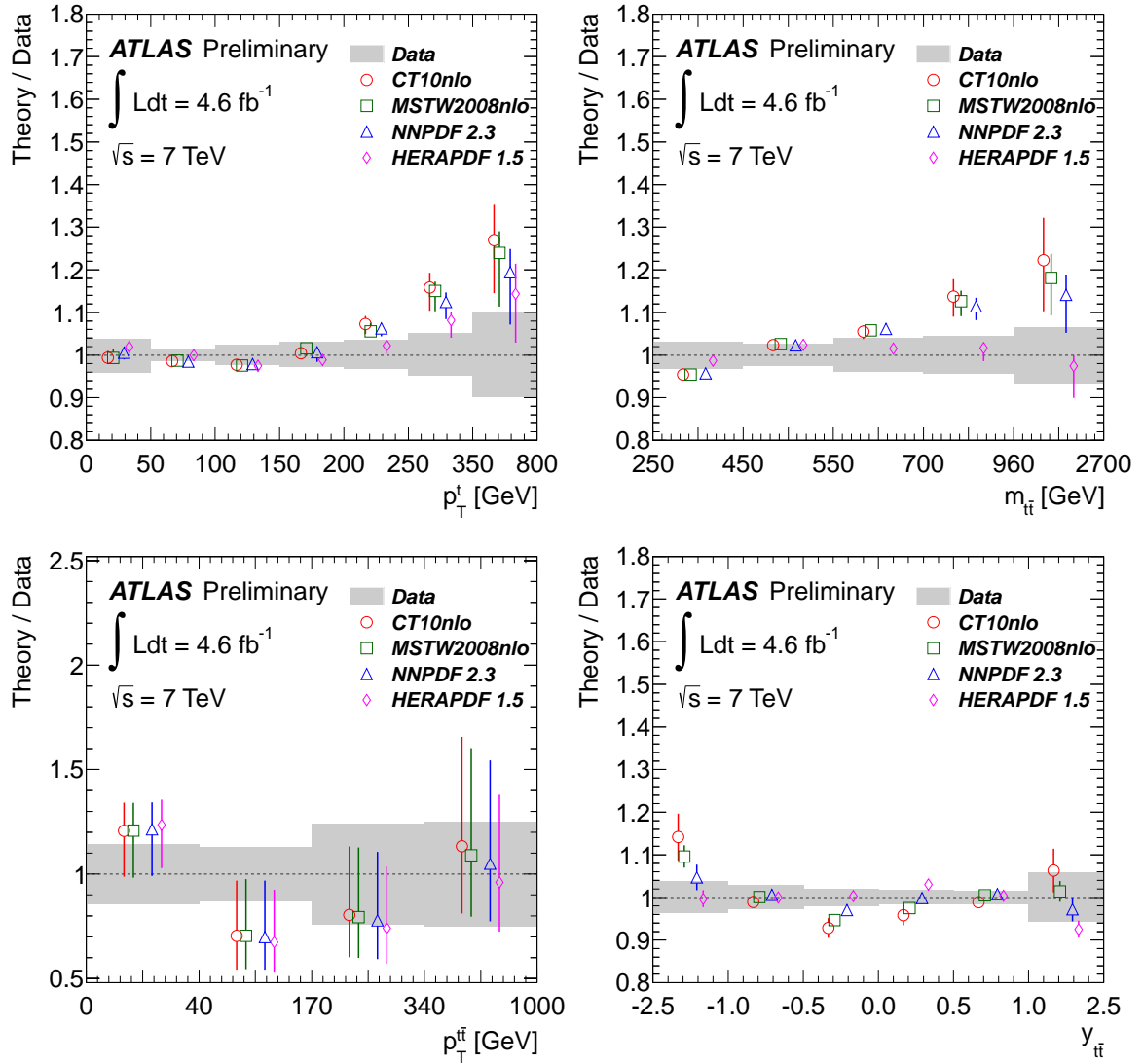


**Figure 5.8:** Results from the ATLAS top parton analysis, showing ratios of the NLO QCD predictions to the measured normalised differential cross-sections for different PDF sets (CT10, MSTW2008NLO, NNPDF2.3 and HERAPDF1.5) (points) for  $p_T^t$  (top left),  $m_{t\bar{t}}$  (top right),  $p_T^{t\bar{t}}$  (bottom left), and  $|y_{t\bar{t}}|$  (bottom right). The points are slightly offset in each bin to allow for better visibility. The gray bands show the total statistical and systematic uncertainty on the unfolded distributions, while the error bars denote the uncertainties on the PDFs which include the internal PDF set variations and also fixed scale uncertainties. From [171].

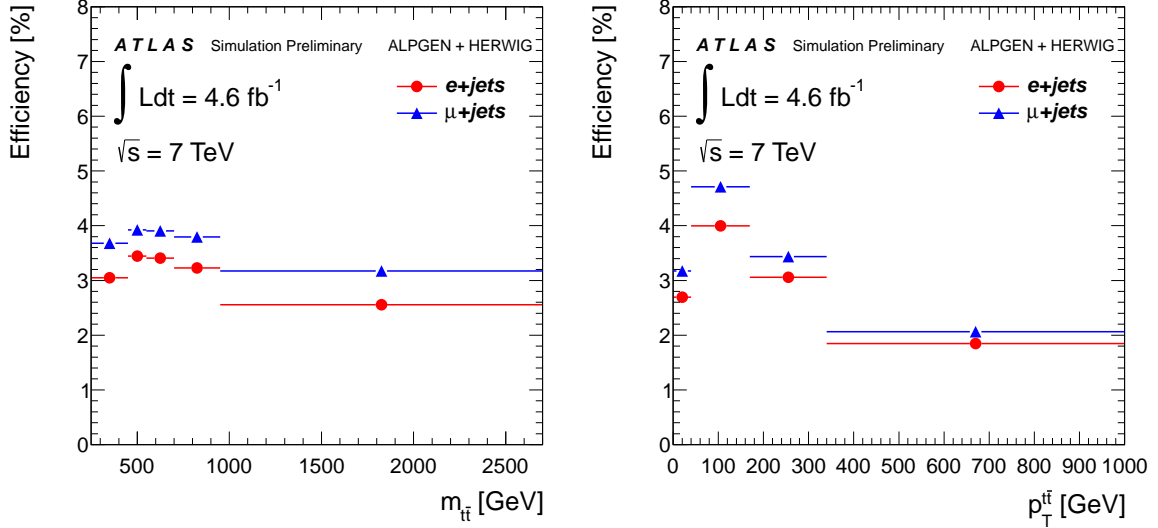


**Figure 5.9:** Selection efficiencies for the parton-level ATLAS analysis for the top pair mass (left) and transverse momentum (right) obtained using ALPGEN +HERWIG MC. From [171].

difference between the parton to particle-level acceptance between ALPGEN +HERWIG and POWHEG +PYTHIA at low top pair  $p_T$  for instance). The uncertainty in this extrapolation can be estimated by comparing different MCs, but nonetheless locks the analysis into the current best description, and means the measurement is unable to be used when future improvements of the description become available.

For example, we already introduced the I/FSR parton showering MC parameters which were constrained through a differential jet measurement. The extra radiation affects acceptance corrections when calculating cross-sections from the data, even though in the context of a parton shower MC it is a purely phenomenological parameter. Therefore, any measurement in the top sector is affected by this parameter, even those that correct back to the parton level descriptions of the top, which assume a particular model of the jet distributions when making the parton-level extrapolations.

Reconstructing the parton level top thus means that the unfolding procedure (taking the reconstructed distribution and porting it to the parton level based on the Monte Carlo corrections) is unfolding through the description of the shower, the underlying event, the colour reconnection and the hadronisation. This ties the analysis to this particular description of these non-perturbative processes, so the analysis can only be compared fairly with this single model, since the model is assumed when constructing the final result. In order for the analysis to have utility in constraining the parameters

and discriminating against the different models, it therefore should be constructed in a manner independent of these descriptions, or as independent as possible.

Thus, new methods of reconstructing and studying the top quark system are desirable. This thesis presents the first definition of a “pseudo-top”, an object created from either the fully hadronised objects at the end of the Monte Carlo chain, or from the reconstructed objects delivered by the detector. Since these object definitions are independent of the parton level description of the event, many of the problems with the current set of analyses are avoided, at the expense of dropping the requirement that we try to access the true top quarks underlying these events.

We start from the assumption that the event selection process which needs to be performed to find top events at colliders like the LHC will be defined by conditions on the final-state objects: the leptons, neutrinos, jets, and b-jets. From these objects, a “pseudo-top” is then constructed. This pseudo-top is a mapping of the final-state objects onto the  $t\bar{t}$  pair. This mapping can then be used to extract properties of the pseudo-top objects. If then desired, from the pseudo-top distributions one may use a particular MC to correct the well-defined pseudo-top definition to a model-dependent parton-level top. This distribution can then be further extrapolated to the full phase-space of the top pair production, reintroducing the model dependencies which we were trying to avoid when making the pseudo-top construction.

As part of the definition for the mapping, it should be definable as a Rivet routine [172]. Rivet is a tool used in phenomenology studies, whereby MC generator authors can automatically hook their generator up to compare with experimental data. It can also then be used to tune the phenomenological parameters that are needed to describe the non-perturbative shower evolution and other effects.

The pseudo-top thus defined then provides a more “future-proof” measurement of the distributions of interest, since it requires only knowledge of the particle-level. That is, it is mostly independent of the renormalisation scheme or perturbative order used when calculating the distributions and it does not rely on any assumptions about the hadronisation, or colour reconnection models used to describe the top pair event. Finally, the definition of the pseudo-top measurement does not extrapolate into experimentally inaccessible regions of phase-space, where we have no experimental input with which to construct our correction factors. If necessary, these factors can be provided by the theorist who is interested in using the measurement for their studies. Be it tuning a

generator based on the measurement, or using the measurement to constrain parton distribution functions, or new physics models.

### 5.3. Pseudo-Top definition

Several definitions of the pseudo-top have been considered. The aim is to use a definition where the objects at particle and reconstruction level are as close as possible. It is also desirable, where possible and such a comparison is sensible, for the pseudo-top to also be close to the partonic variables. An example where this is impossible is for the Sherpa generator [173], which does not allow access to intermediate parton states, such as the  $W$  or top, generated during the calculations.

We first define some matching conditions in section 5.3.1 which we will use to test the pseudo-top constructions for good reconstruction and particle level agreement, as well as a parton level match which is only used to give an idea of the correlation to parton level, and not as part of the analysis definition. Section 5.3.2 presents the various pseudo-top construction methods that we have considered, and compares them primarily based on the reconstruction and particle level matching. Finally, section 5.3.3 presents the pseudo-top construction that we have chosen to analyse in the next chapter, and shows various observables reconstructed from the data sample of section 4.3.4, which is used for the rest of the analysis.

#### 5.3.1. Matching

##### Particle-Reconstruction Matching

In studying the pseudo-top observables, it will be useful to know how often the objects selected at the particle and reconstruction level coincide. We call the procedure that we use to determine if the objects are equivalent particle-reconstruction matching. A particle and reconstructed jet match if they are within  $\Delta R$  of 0.35 of each (recalling that the anti- $k_T$  jet algorithm used for these studies has size parameter 0.40, so jets are approximately  $\Delta R = 0.40$ ). Events in the signal MC are classified as matching if the corresponding jets are matched at particle and reconstruction level. That is, the jet associated with the hadronically decaying top at the reconstruction level matches the hadronically decaying top  $b$ -jet at the particle level and so on for all the objects in

the pseudo-top definition. Lepton association was also looked at, but we found that in all but 4 or 5 out of a 5 million event sample the leptons selected at particle and reconstruction level were within  $\Delta R = 0.02$  and so the lepton is always considered to match. The “matching efficiency” is then defined as the fraction of events that match all the jets between the reconstruction and particle level, considering only those events where a pseudo-top is reconstructed at both levels.

### Parton Matching

It is also useful to match the observables to the parton level observables. The algorithm for matching a particle jet to the parton-level top decay product runs as follows:

- Loop over the generator level objects, and call the objects identified as quarks, gluons, photons and taus and having a  $p_T$  of at least 5 GeV “good”
- Select the “good” generator object with the highest  $p_T$  that is within  $\Delta R$  of 0.40 of the particle level jet, identify this as the parton matched to the jet
- Follow the parent links of the matched parton until either a top quark is found, or we reach the top of the record
- If a top quark is found, call the particle jet a top match and record the charge of the direct top decay product (i.e. either the  $W$  or the quark in the  $t \rightarrow qW$  decay) it matches to, otherwise declare the particle jet to be unmatched to a top decay

The generator 4-vectors of the tops are also stored and studied in comparison with the pseudo-top construction. The generators used output many copies of the same object into the event record. In the case of the parton top-quark, this will be due to the generator storing the top-parton before and after it radiates. We use the generator top parton right before it decays. When comparing distributions involving parton-tops, it is these parton-tops that we are referring to.

Following the matching, we select a “Parton-Matched” pseudo-top which is considered to be the best possible pseudo-top for the event. This partonically-defined construction is used only to judge the performance of the various pseudo-top observables, but it should be emphasised parton-level information is not utilised in the actual construction or analysis of pseudo-top observables. The hadronic  $W$  is selected by requiring both jets be matched to the  $W$  decaying from a top. We select the hadronic top by combining this  $W$  with a particle jet that matches to the correct signed  $b$  decay parton. The leptonic

$W$  is formed by combining the lepton with the  $E_T^{miss}$  and solving for the  $p_z$  component (dropping the imaginary component, if it exists, and using only the real component or taking the smaller value to resolve the two-fold ambiguity if it does not) We form the leptonic top by taking the leptonic  $W$ , and combining it with a particle jet matching to a parton coming from a top b quark decay with the correct sign. In all cases, if there is more than one candidate (for example if more than two jets match to partons from the hadronic  $W$ ), we choose the candidate whose mass is closest to the known  $W$  mass or top mass. As will be seen, this construction gives clean peaks around the  $W$  and top masses better than any of our particle-level only constructions, and therefore is taken to be representative of those events where the top decays cleanly in the fiducial volume. No further attempt has been made to quantify this association as the construction is only used as a rough baseline for comparison.

This construction is used as a point of reference for the constructions, where we build pseudo-tops without reference to the parton level. The parton-matched candidate is used purely as a guide in the development of the pseudo-top observables.

### 5.3.2. Construction of the Pseudo-Top Observable

In the event selection of section 4.1.7, we stated that we require events in our analysis to have at least two jets identified as  $b$ -jets. To motivate the double-tag selection and to give the flavour of the pseudo-top constructions, consider first an observable constructed from a no-tag analysis. That is, start with an event selection containing exactly one lepton, the missing transverse momentum and  $m_T^W$  requirements, and at least four jets, but without any tagging requirements.

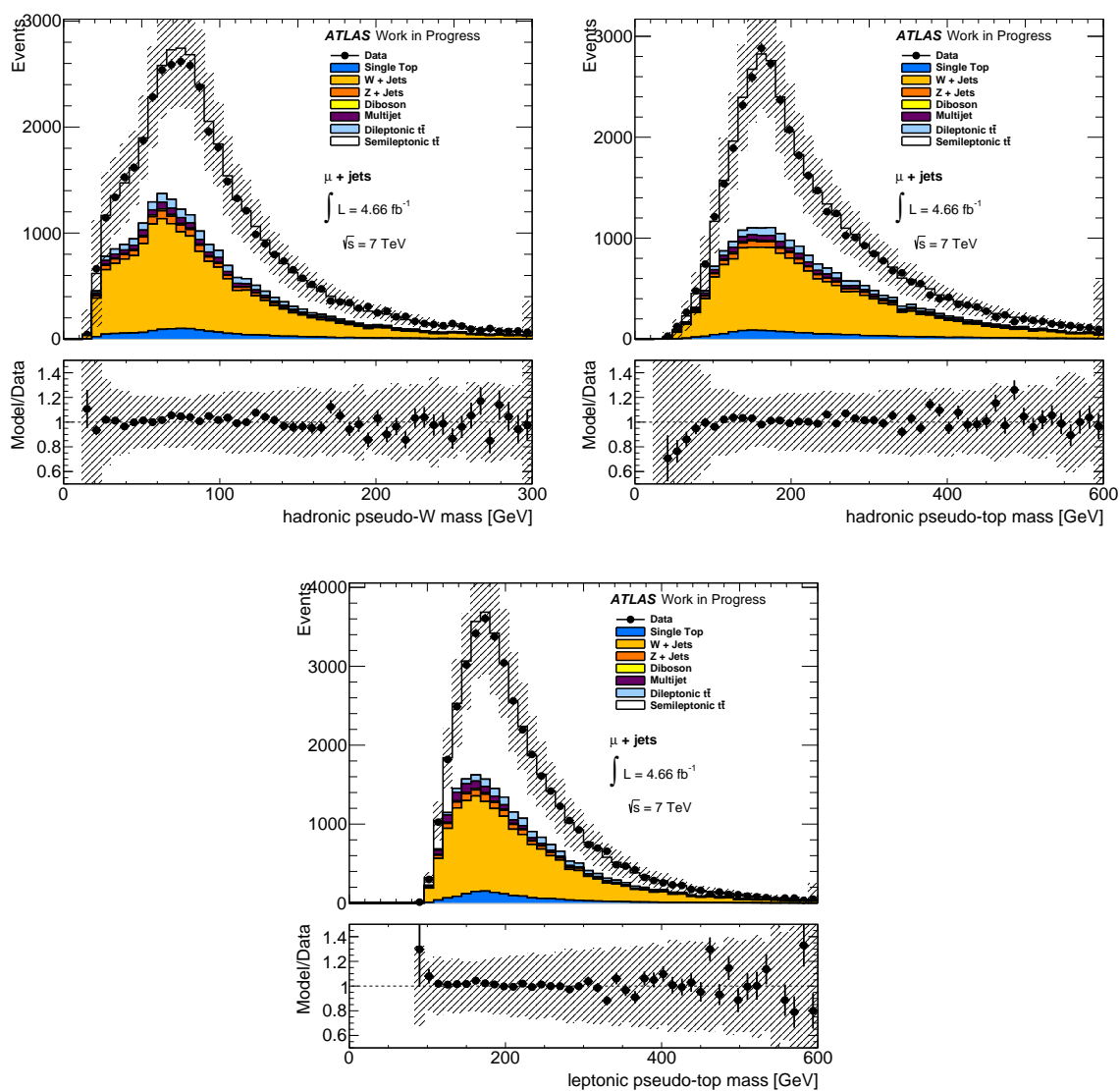
The leptonic  $W$  is constructed in the same way for all the constructions: take the the lepton, and the  $E_T^{miss}$ , and then solving for the  $p_z$  by requiring the invariant mass of the combination of lepton plus  $E_T^{miss}$  plus  $p_z$  combine to be the  $W$  mass (with  $E_T^{miss}$  plus  $p_z$  4-vector having no mass since it should form a neutrino). In general, this gives a two-fold ambiguity which can be resolved by taking either the higher or the lower solution. In the case of an imaginary component in the solution, we simply drop this part and take only the real part of the solution, which is then unique. The solutions with imaginary components will then have mass slightly higher than the  $W$  mass. This procedure will be explored further later in the chapter.

Turning to the jets, for the pre-tag construction, take the two highest  $p_T$  jets to be associated with the  $b$ -jets from the top decay. The motivation is that the jets from the top are further up the decay chain and from the most massive objects in the event, so will tend to have more energy than the other objects. Of these, associate to the leptonically decaying top the jet closest in  $\Delta R$  to the lepton, and associate the other jet with the hadronically decaying top. Finally, the hadronically decaying  $W$  decays into two quarks, so, from the remaining jets, take the two jets with the highest  $p_T$  and associate them with the hadronically decaying  $W$ . This then completes the construction of the top pairs for the pre-tag selection.

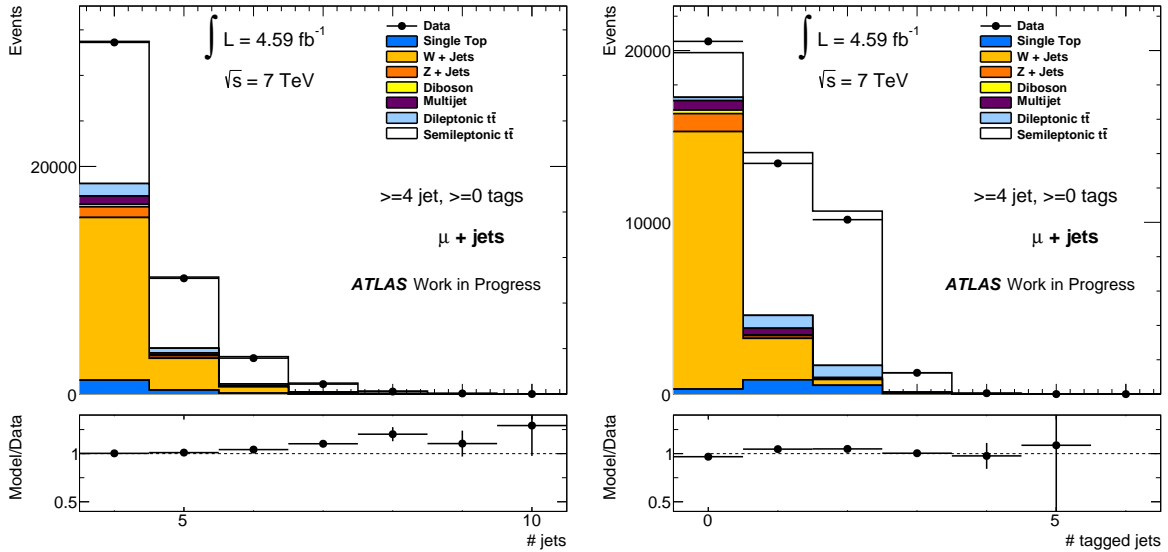
Figure 5.10 shows data and MC distributions for the pseudo-top and pseudo- $W$  masses made using this construction. From the figure, it can first be seen that the top sample forms peaks in the hadronic  $W$  mass spectrum and the top mass spectrum at the masses of the  $W$  and top respectively. This implies that, at least for a fraction of the events, the simple algorithm is correctly reconstructing the  $W$  and top from the final state objects. Also, the  $W$  with jets background is substantial in the pre-tag selection, with roughly the same order of magnitude of events as the signal top pair events. At pre-tag, the  $W$ +jets background has essentially the same topology as top pair production, which also means that estimating the exact size of the background is difficult, leading to very large background uncertainties, which in turns dilutes the power of the analysis to distinguish signal models. However, the fraction of events where a  $W$  is produced with heavy flavour is small, while top pair events always have two  $b$ -jets. So, at least a single  $b$  tag should be required in the event selection, to reduce the background levels and the associated uncertainties.

Figure 5.11 shows the distributions of the number of tagged jets, before any tagging requirements are applied. The  $b$ -tag algorithm we use is tuned to tag  $\epsilon = 75\%$  of real  $b$ -jets, so given that there are at least two  $b$ -jets in the top sample, we would expect  $2\epsilon - \epsilon^2 = .94$  to contain at least one tagged jet, while  $\epsilon^2 = 0.56$  events to contain two  $b$ -tags. There is therefore a substantial reduction of signal events between requiring one or two tagged jets. On the other hand, the  $W$  background is almost negligible, even at the one-tag level. Therefore, finding a suitable algorithm at the one tag level would be desirable.

The problem at the one-tag level is that the particle-level  $b$ -tagging is essentially 100% efficient, so the  $b$ -jets from the top always get tagged at particle level. Therefore, any construction using the tagging information ends up with large off-diagonal terms from the exclusive one-tag events, where the algorithm will differ at reconstruction and



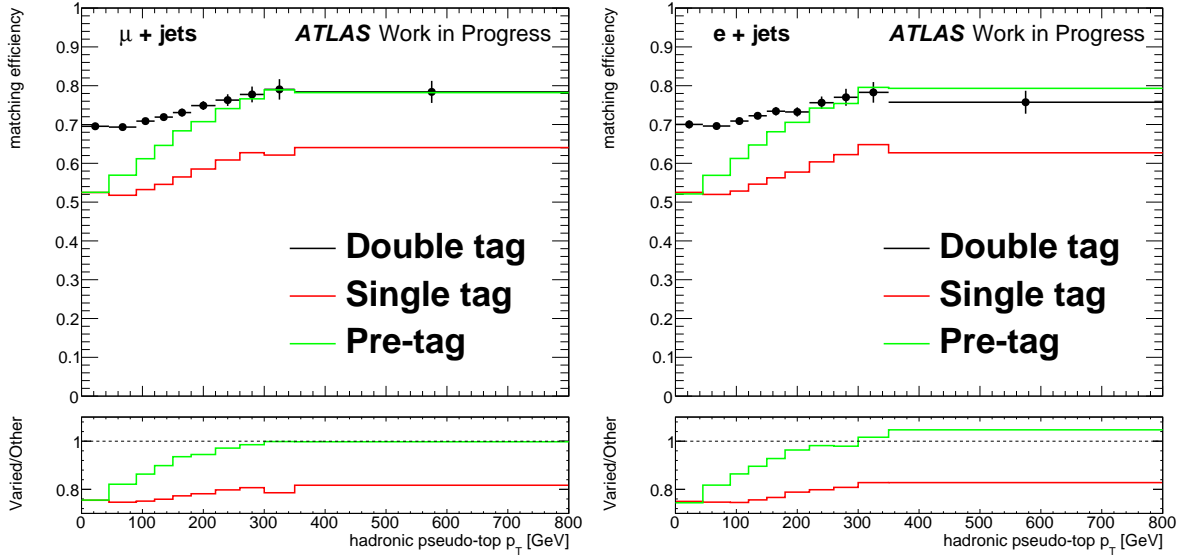
**Figure 5.10:** The pre-tag construction in data compared with Monte Carlo predictions in the muon channel. Shown are the hadronic pseudo- $W$  mass (top, left), the hadronic pseudo-top mass (top, right) and the leptonic pseudo-top mass (bottom). POWHEG+PYTHIA is used as the top pair signal MC. The uncertainty bands show the total systematic uncertainty on the combined signal and background estimation.



**Figure 5.11:** The number of jets (left) and the number of tagged jets (right) in the muon channel after all  $t\bar{t}$  event selection requirements except  $b$ -tagging.

particle-level. For example, a algorithm we tried was to do the same as for pre-tag, except the jets associated with the top quarks are: 1) the  $b$ -jet and the highest  $p_T$  non- $b$ -jet for exactly one  $b$ -tagged jet in the event, and 2) the two highest  $p_T$  tagged jets for two or more tags. This then leads to poor matching performance between reconstruction and particle as shown in figure 5.12, where the matching efficiency (defined above) is shown as a function of the hadronic top  $p_T$ . For low  $p_T$  tops (constituting the bulk of the events), the efficiency is around 50%. Any similar construction leads to similar difficulties. For example, taking just the single highest  $p_T$   $b$ -jet in multiply tagged events, and treating the remaining jets in the same way as for a single tag event will lead to the exact same problem, since the reconstruction level still has a large fraction of events with only a single tag, and the jet tagged will be independent of the  $p_T$  to first approximation, so randomly distributed between the real  $b$ -jets. Therefore, the matching to particle level, which almost always tags the  $b$ -jets, will still be low. A pretag-like assignment, where the tags are only required to accept the event, and not used in the construction, also leads to a smaller matching efficiency.

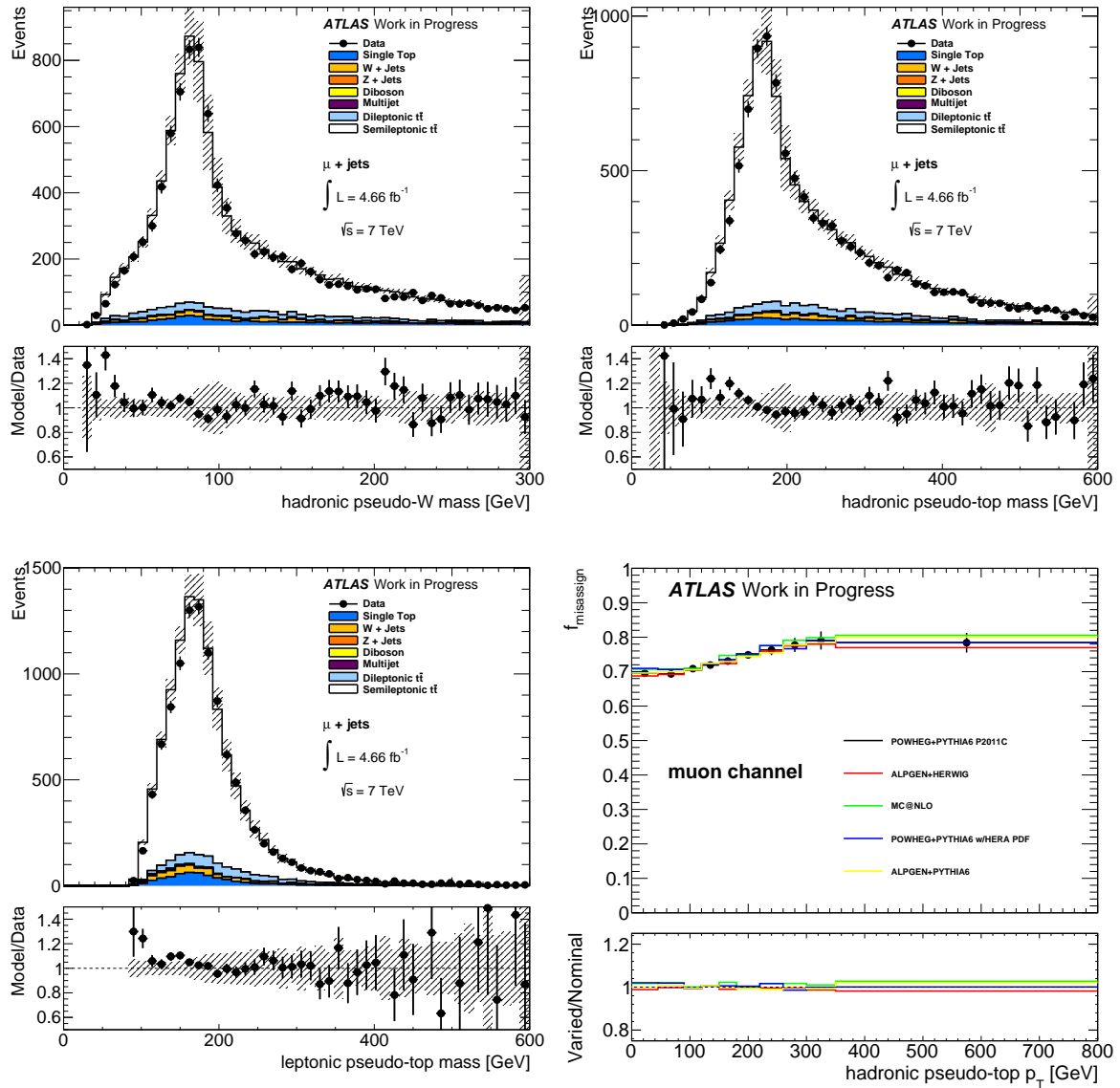
Thus, we are led to requiring two tags in the event. Taking again the pre-tag construction as the base, this time associating the two highest  $p_T$   $b$ -tagged jets with the top  $b$ -quarks. Figure 5.13 shows the reconstructed mass distributions and the matching efficiency in the muon channel. The requirement of two tagged jets in the events reduces the background to an almost imperceptible level, while the matching efficiency is above



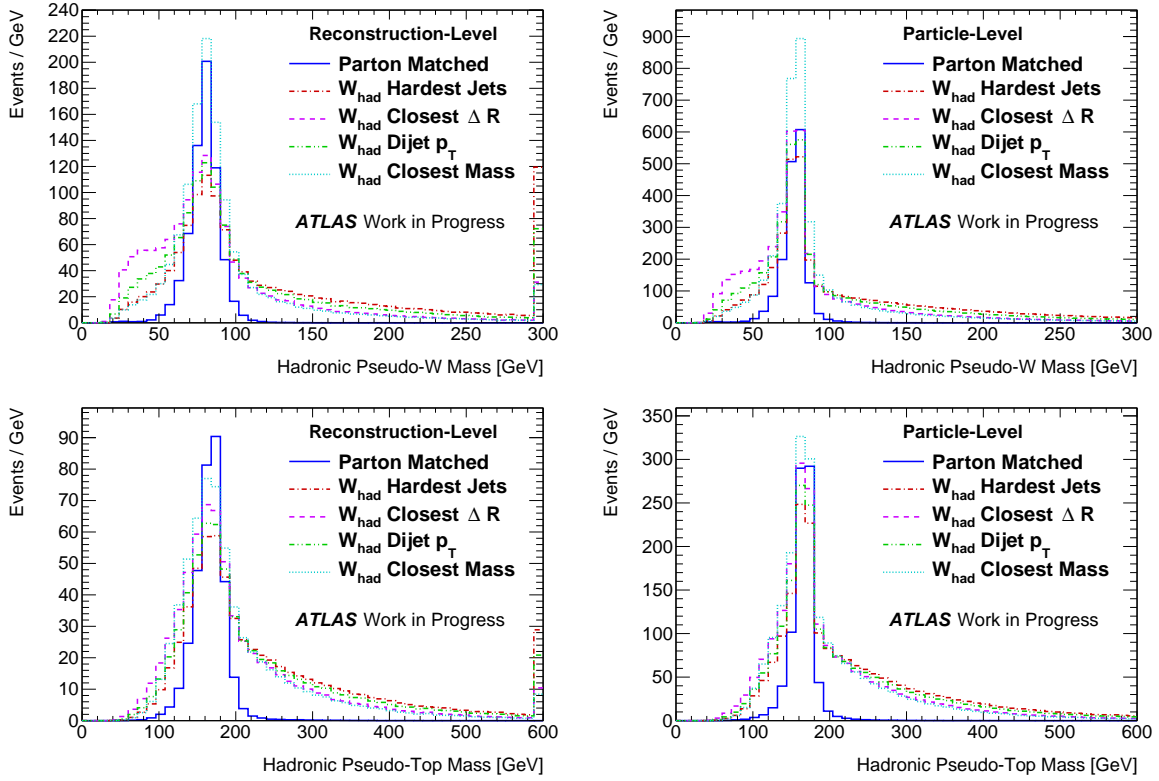
**Figure 5.12:** Efficiency to completely match the pseudo-tops constructed at reconstruction and particle level as a function of the hadronic top  $p_T$  in the muon (left) and electron (right) channels. POWHEG+PYTHIA MC is used and pre-tag, single-tag and double-tag constructions are compared.

the 70% level across the entire hadronic pseudo-top  $p_T$  spectrum, independent of the MC used to derive this quantity.

Having settled on trying to find a two tag construction, we adjusted the algorithm and see if it can be improved. To begin, an obvious point of inquiry is the hadronic  $W$  construction. Several methods of identifying the hadronic  $W$  jets were considered and are compared in the hadronic  $W$  mass distributions for the reconstruction and particle level (both of which are also independent of the top  $b$ -jet association method) and the hadronic top mass distributions (which uses the lepton  $\Delta R$  method as before) in figure 5.14. The constructions that were looked at are: the two highest  $p_T$  jets, the two jets closest in  $\Delta R$ , the two jets which form the highest  $p_T$  dijet, and the two jets whose combined invariant mass is closest to the known  $W$  mass of 80.4 GeV [4]. The parton matched distribution is also shown as a comparison point. The figures show that the closest mass construction gives the best peak, with the other constructions giving shorter and fatter mass peaks. It also shows that the parton-matched events form only a small subset of the events, with long tails of events seen in all the constructions, and in particular, the  $\Delta R$  construction has a secondary mass peak below the  $W$  mass. This indicates that in many of the events, the  $W$  to two jet description of the decay is unsatisfactory, with one of the the jets going out of the fiducial volume, or the jets merging together into a single jet, or the one or



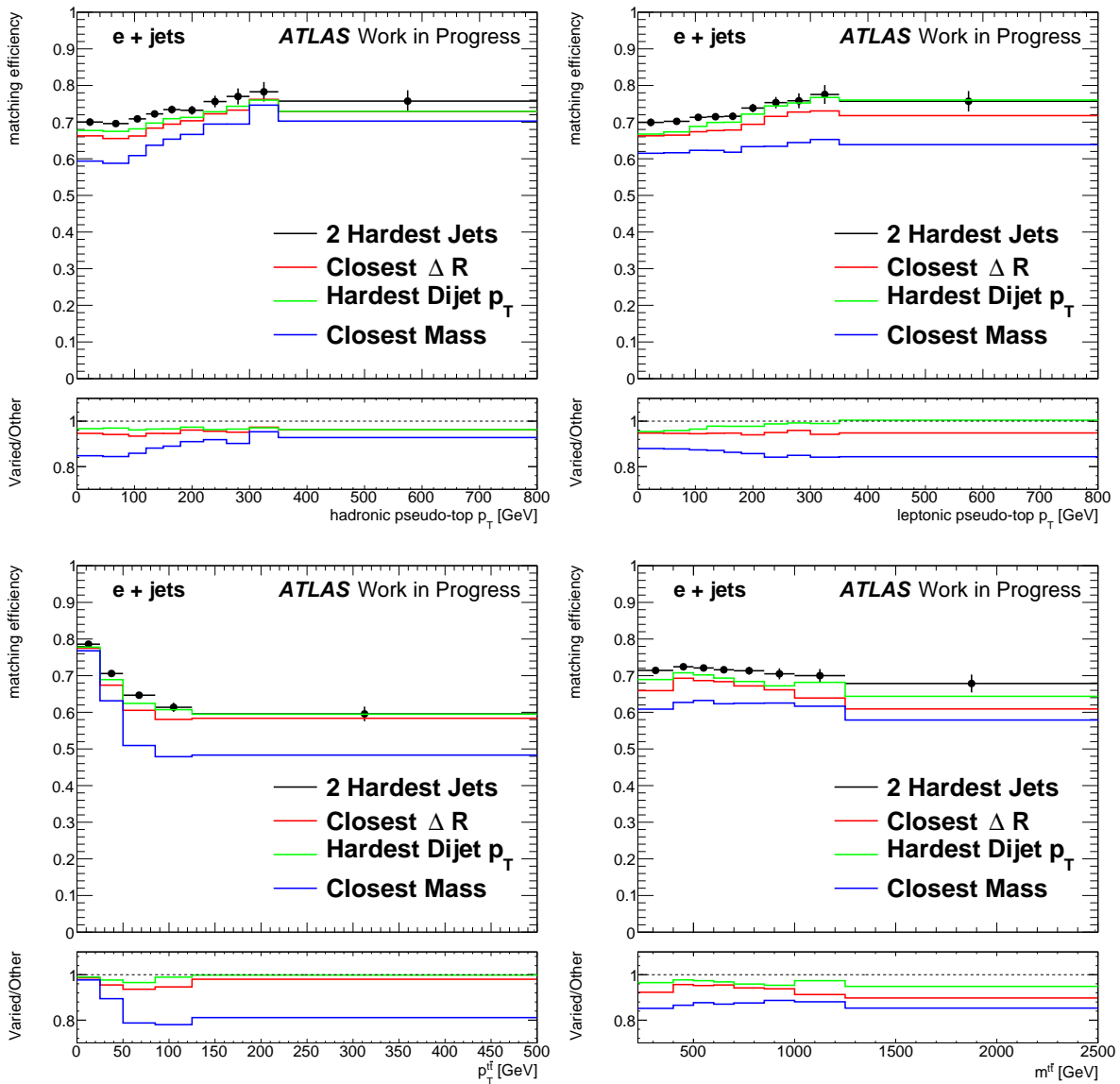
**Figure 5.13:** The two tag construction based on the pre-tag construction in data compared with Monte Carlo predictions in the muon channel showing the hadronic pseudo- $W$  mass (top left) and pseudo-top mass (top right) and leptonic pseudo-top mass (bottom left). POWHEG+PYTHIA is used as the signal sample. The lower right figure shows the matching efficiency between reconstruction and particle level for the semi-leptonic top pair signal for various MCs with respect to the hadronic top  $p_T$ .



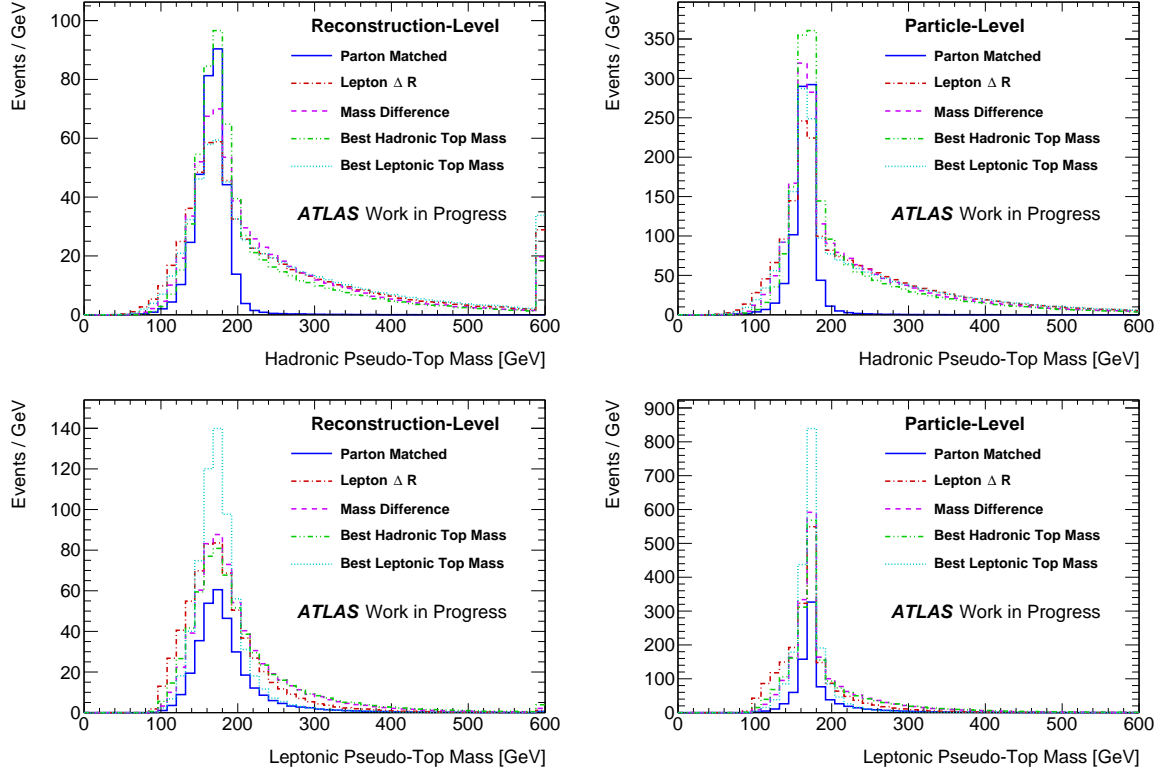
**Figure 5.14:** Comparison of the various  $W$  hadronic mass construction techniques using the POWHEG+PYTHIA signal sample in the electron channel. The left figure shows the reconstructed mass distributions, and the right figure shows the particle-level mass distributions for the hadronic pseudo- $W$  (top) and pseudo-top (bottom).

both of the partons splitting into multiple jets. The parton matched distribution gives those events where we can say that the two jet description is valid, and, again, we can see from the peaks that the closest mass construction is finding all of these events.

Parton-level matching, however, is only a secondary consideration. Figure 5.15 shows the matching efficiency for the constructions as a function of several of the variables of interest. From the figures, the closest mass, our front-runner based on the mass distributions, fails dismally in matching between particle and reconstruction level, while the hardest jets gives the best matching efficiency. This is explainable in terms of the complexity of the constructions: the hardest jets simply uses the  $p_T$  of the objects in isolation, while the mass boils down the complete di-object descriptions and compares it against a fixed number and is therefore more susceptible to combinatoric problems. Therefore, the closest mass is rejected on matching grounds, while the  $\Delta R$  construction is suspicious due to the second, low mass peak. The hardest jets is then the best based on matching.

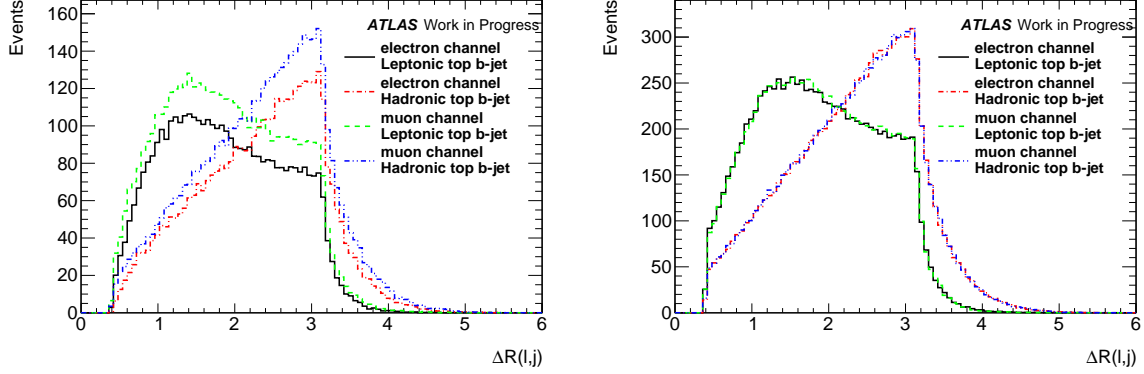


**Figure 5.15:** Comparison of the various  $W$  hadronic mass construction techniques using the POWHEG+PYTHIA signal sample in the electron channel. The figures show the matching efficiency for the various constructions between the reconstruction and particle levels for the hadronic pseudo-top  $p_T$  (top left), leptonic pseudo-top  $p_T$  (top right), pseudo-top pair  $p_T$  (bottom left) and mass (bottom right).



**Figure 5.16:** Comparison of the various top association techniques using the POWHEG+PYTHIA signal sample in the electron channel. For all the methods, the two hardest remaining jets are associated to the hadronic  $W$ .

Several methods of how to assign the jets to the hadronic and leptonic tops were also considered. There are two jets set aside for this purpose, so its a matter of trying to assign at least one, then the other is fixed. As for the hadronic  $W$ , two methods are to either: assign the jet that gives the mass closest to the top mass for the leptonic top side, or assign the jet giving the closer mass to the hadronic top. Figure 5.16 shows that this improves the mass peak for the top that we compare with the true mass, at the expense of a worse resolution for the other top. This implies that we are sculpting the peaks with these methods, without necessarily selecting the best matches. Along the same line of thought, we can try assigning the tops based on the assignment which gives the smaller difference between the masses. This method treats both sides equivalently, and from the figures we can see that the resolutions are more similar. Another method is the one already used, which is to pick the jet closer to the lepton as the leptonic top jet. This method is justified by figure 5.17, which shows that for the parton matched distributions, the leptonic jet does tend to be closer to the lepton. This method gives similar mass resolution on both sides, similar to the resolution of the wrong-side top mass.



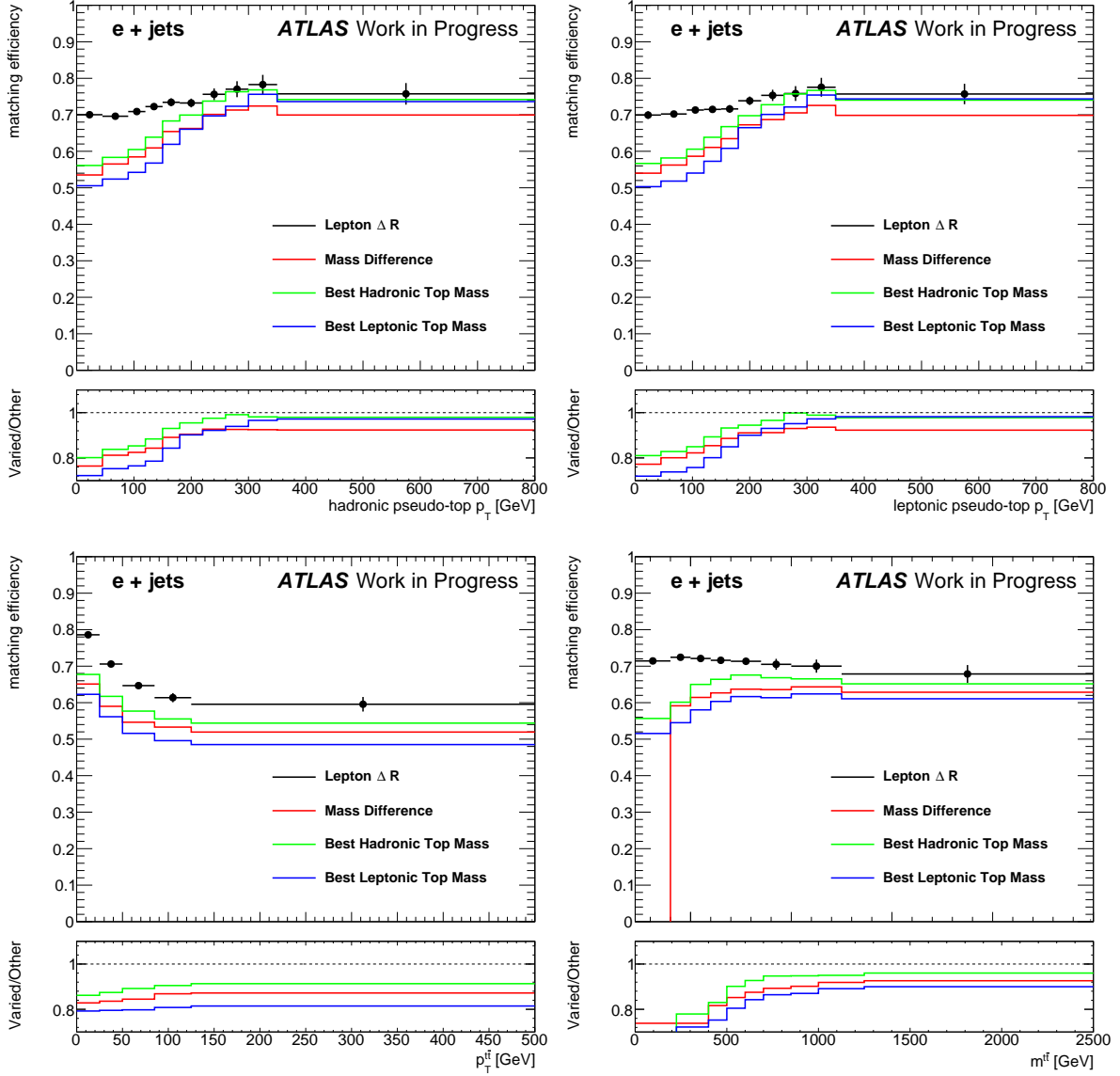
**Figure 5.17:**  $\Delta R$  between the top jet and the lepton for the parton matched top construction using the POWHEG+PYTHIA signal sample in reconstruction (left) and at particle level (right).

Figure 5.18 shows the matching efficiency for the top jet association methods. These figures show that the mass difference are worse in terms of matching than the lepton association method. As for the hadronic mass constructions, this is explainable in terms of the masses being more sensitive to fluctuations in the input 4-vectors, than the simple geometrical relationships (in this case) or simple, single variable kinematic information (in the  $W$  case).

### Neutrino $p_z$

When a  $W$  decays into a lepton and neutrino pair, the neutrino escapes as missing momentum, which can only be measured in the transverse plane, since the momentum along the  $z$ -axis of the hard interaction is unknown and in general for proton collisions non-zero. Since the neutrino is the only major source of missing transverse momentum, we assign the total reconstructed  $E_T^{miss}$  to the neutrino. This leaves the  $p_z$  of the neutrino unknown, however since we know that the lepton (which is fully measured by ATLAS) and the neutrino come from a  $W$  decay, the mass of their Lorentz vector sum must be that of the  $W$  boson.

$$\begin{aligned}
 M_W^2 &= (p_\nu + p_l)^2 \\
 &= (E_\nu + E_l)^2 - |\mathbf{p}_\nu + \mathbf{p}_l|^2 \\
 &= (E_\nu + E_l)^2 - (\mathbf{p}_{x,\nu} + \mathbf{p}_{x,\ell})^2 - (\mathbf{p}_{y,\nu} + \mathbf{p}_{y,\ell})^2 - (\mathbf{p}_{z,\nu} + \mathbf{p}_{z,\ell})^2
 \end{aligned} \tag{5.3}$$



**Figure 5.18:** Comparison of the various top jet association techniques using the POWHEG+PYTHIA signal sample in the electron channel. For all the methods, the two hardest remaining jets are associated to the hadronic  $W$ . The figures show the matching efficiency for the various constructions between the reconstruction and particle levels. The bottom part of the figure shows the ratio of the method to the nominal lepton  $\Delta R$  method, which is represented as the data points in the plots. The top row shows this as a function of the hadronic (left) and leptonic (right) pseudo-top  $p_T$ , the bottom row shows the top pair  $p_T^{t\bar{t}}$  (left) and  $m^{t\bar{t}}$  (right).

manipulating this equation and then solving for the neutrino  $z$  momentum gives

$$p_{z,\nu} = \frac{p_{z,\ell} \left( \frac{M_W^2 - M_l^2}{2} - p_{x,\nu} p_{x,\ell} - p_{y,\nu} p_{y,\ell} \right)}{E_l^2 - p_{z,\ell}^2} \pm \frac{E_l \sqrt{\left( \frac{M_W^2 - M_l^2}{2} - p_{x,\nu} p_{x,\ell} - p_{y,\nu} p_{y,\ell} \right)^2 - (p_{x,\nu}^2 + p_{y,\nu}^2) (E_l^2 - p_{z,\ell}^2)}}{E_l^2 - p_{z,\ell}^2} \quad (5.4)$$

The equation has two real solutions when

$$\left( \frac{M_W^2 - M_l^2}{2} - p_{x,\nu} p_{x,\ell} - p_{y,\nu} p_{y,\ell} \right)^2 - (p_{x,\nu}^2 + p_{y,\nu}^2) (E_l^2 - p_{z,\ell}^2) \geq 0 \quad (5.5)$$

Since the neutrino is known to have come from the  $W$  boson decay, and an imaginary momentum component has no physical meaning, this equation should always be satisfied and will be at the particle level, where we take the true value of the neutrino transverse momentum as  $E_T^{miss}$ . However, since the reconstructed  $E_T^{miss}$  will be smeared by detector effects, the solution can be pushed into the non-physical region with imaginary solutions. In this case, the default solution we have used is to simply drop the imaginary component and take the  $p_z$  as the real part of equation 5.4. One may also be more rigorous and scale the variables considered fixed to restore the equation to giving real solutions.

We consider first scaling the missing transverse energy. In general, this is the least well-measured quantity involved in forming the top pair system and so the most likely to have been mismeasured, causing the failure of equation 5.5. The minimal scaling needed to satisfy that equation will be such that the equation gives 0. So, if we equate the expression to 0 and replace  $E_T^{miss}$  with  $f E_T^{miss}$  for some scaling factor  $f$  (rewriting with the two-vectors  $\mathbf{p}_T^\nu = (p_x^\nu, p_y^\nu)$  and  $\mathbf{p}_T^\ell = (p_x^\ell, p_y^\ell)$ ), we have

$$\left( \frac{M_W^2 - M_l^2}{2} - f \mathbf{p}_T^\nu \cdot \mathbf{p}_T^\ell \right)^2 - f^2 |\mathbf{p}_T^\nu|^2 |\mathbf{p}_T^\ell|^2 = 0 \quad (5.6)$$

if we solve for  $f$  (ignoring the negative solution since this would give non-physical, negative  $E_T^{miss}$ ), we find that (taking  $m_\ell \approx 0$ )

$$f = \frac{M_W^2}{2 (|\mathbf{p}_T| |\mathbf{p}_\ell| - \mathbf{p}_T \cdot \mathbf{p}_\ell)} \quad (5.7)$$

If we rewrite the bottom term as  $2|\mathbf{p}_T||\mathbf{p}_\ell|(1 - \cos\theta)$ , it is easily recognisable as the missing transverse mass shown previously in equation 4.4. Applying the scale factor to

the  $E_T^{miss}$  and then re-evaluating equation 5.4 for the  $p_z$  gives a new momentum vector for the neutrino, satisfying equation 5.5 and summing with the lepton to the  $W$  mass, which is the output of this method.

Another option is to rescale the  $W$  mass to give a real value for the  $z$  momentum. The justification for this is that an off shell  $W$  boson would have mass  $M_W^2 + \delta m^2$  for some value of  $\delta m^2$ . This could then cause equation 5.4 to have an imaginary component. Choosing  $\delta m^2$  to give an invariant mass closest to the  $W$  pole and a real solution implies solving equation 5.5 equal to zero for the new  $W$  mass

$$M_W^2 \rightarrow M_W^2 + \delta m^2 = 2\sqrt{(p_{x,\nu}^2 + p_{y,\nu}^2)(E_l^2 - p_{z,\ell}^2)} + 2(p_{x,\nu}p_{x,\ell} + p_{y,\nu}p_{y,\ell}) + M_l^2 \quad (5.8)$$

Substituting this into equation 5.4 then gives

$$p_{z,\nu} = p_{z,\ell} \sqrt{\frac{p_{x,\nu}^2 + p_{y,\nu}^2}{E_l^2 - p_{z,\ell}^2}} \quad (5.9)$$

Considering now the case of a real solution, there will be two solutions to the quadratic equation, and we consider taking either the higher of the two solutions, or the lower, there being no other handle to choose from. We can also investigate the effect of the choice of the imaginary component by creating a new selection that requires the neutrino  $p_z$  fit to have only real solutions. It should also be noted in passing that the  $p_T$  distributions are unaffected by this concern.

Figure 5.19 shows the distribution of the relative difference between the particle-level pseudo-top and the parton top and the reconstruction-level and particle-level pseudo-top for the leptonic top rapidity in the POWHEG+PYTHIA sample. The figure compares the pseudo-top constructed choosing the smallest  $|p_z|$  neutrino and the largest magnitude  $|p_z|$  neutrino when simply dropping the imaginary component, as well as the two variable scaling methods presented above. The smallest  $|p_z|$  solution has both a larger peak at zero, and a smaller spread across the distribution. This implies that it is superior to the higher  $|p_z|$  in terms of matching to parton level. The difference between the two methods at reconstruction to particle level is similar. The two scaling methods are almost equivalent to the dropping the imaginary component method for the particle to parton distribution. This is to be expected since we are using the actual neutrino  $p_z$ , so there should not be smearing effects which cause equation 5.5 to be unsatisfied. Our definition of the  $E_T^{miss}$  at particle level, though, does include all neutrinos not from hadrons or quarks, of which there may occasionally be more than one in a given event. This explains

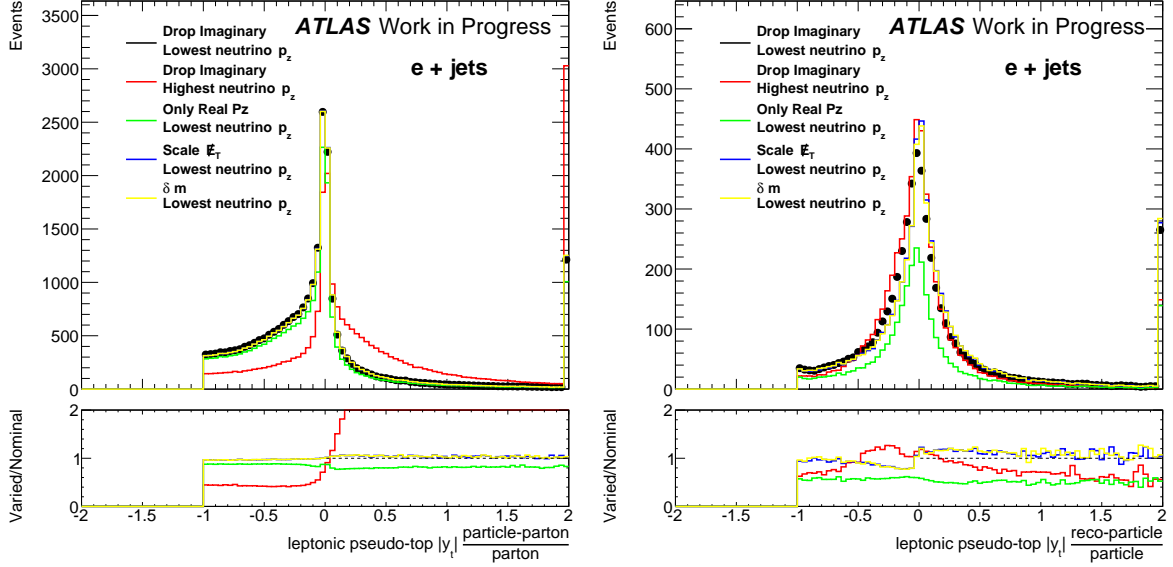


**Figure 5.19:** The distribution of the relative difference between the particle-level pseudo-top and the parton top (left) and between the reconstruction level and particle level pseudo-top (right, i.e.) for the leptonic top rapidity in the POWHEG+PYTHIA sample for several different methods of neutrino  $p_z$  reconstruction methods. For each event in the signal sample, the  $\frac{\text{particle-parton}}{\text{parton}}$  and  $\frac{\text{particle-parton}}{\text{parton}}$  is calculated and added into the respective distribution. The ratio of a given method is given compared with the nominal imaginary part dropped if a non-real solution is found, and take the lowest  $|p_z|$  for multiple solutions method.

the minor differences between the distributions. The reconstruction to particle level efficiency distributions show that the two scaling methods perform slightly better than the dropped imaginary component method, and similar to each other.

For simplicity, and since the distributions remain relatively unaffected, the method of simply dropping the imaginary component and taking only the real component as the  $p_z$  of the neutrino is used for the remainder of the thesis. The other methods have been tested and result in negligible changes to the final unfolded distributions presented in section 6.3.

### 5.3.3. Pseudo-Top Analysis Definition in Data

To summarise our findings, the final analysis uses the following definition of a pseudo-top. The pseudo-top is defined for hadronic-top and leptonic-top observables. The two highest  $p_T$   $b$ -jets were reserved for combination with  $W$ -bosons. The hadronic  $W$ -boson was constructed from the remaining two highest  $p_T$  jets. The  $\Delta R(\text{jet}, e/\mu)$  was calculated

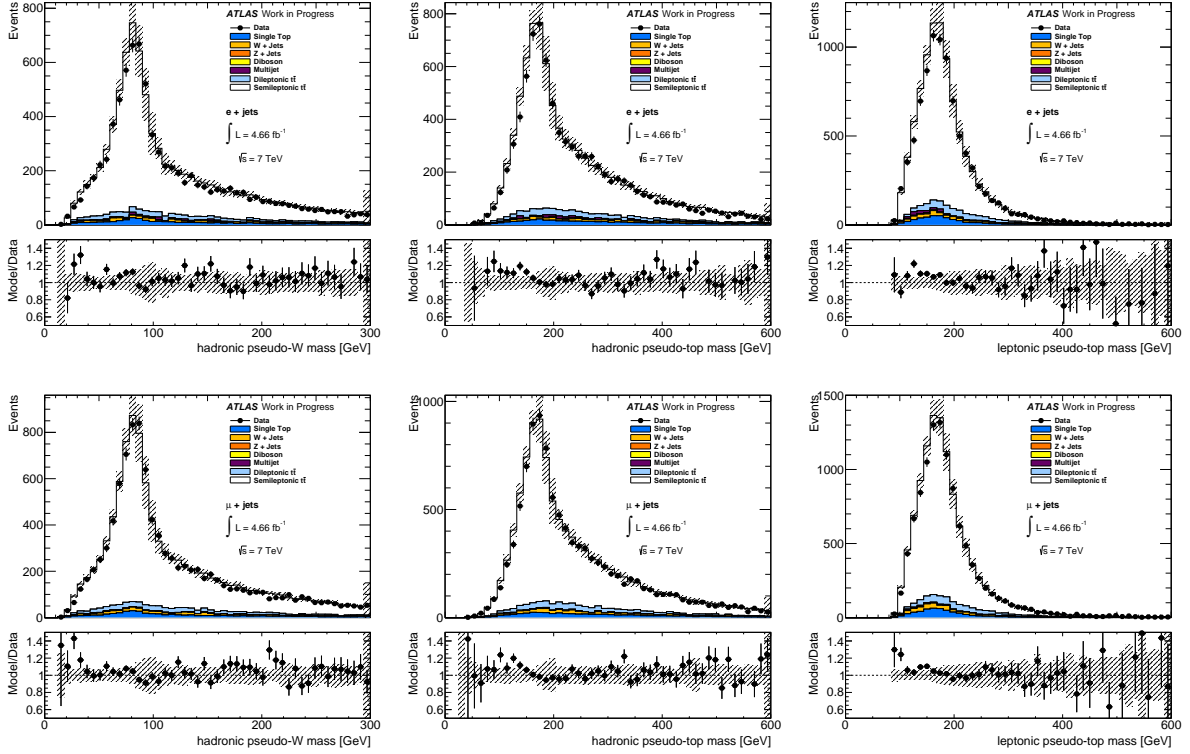


**Figure 5.20:** Reconstructed mass distributions for (left to right) the hadronic  $W$ , hadronic top, and leptonic top in the electron (top) and muon (bottom) channels.

for the two hardest  $b$ -jets and the electron or muon. The  $b$ -jet closest to the lepton was assigned as a decay product of the leptonic top-quark decay. The hadronic pseudo-top was then defined from the hadronic  $W$ -boson candidate and the larger  $\Delta R$   $b$ -jet. The leptonic  $W$  was constructed from the lepton and the  $E_T^{miss}$ , using the world average  $W$  mass of 80.4 GeV to constrain the  $p_z$  solution of the  $E_T^{miss}$ , taking the lower of the two values from the solution to the quadratic equation. Finally, the leptonic pseudo-top was formed from the combination of the leptonic  $W$  and the  $b$ -jet assigned from the minimum  $\Delta R(jet, e/\mu)$ .

Figure 5.20 shows the reconstructed mass distributions for the pseudo-objects, along with the overall Monte Carlo prediction. Agreement in line with the overall MC/data for the objects, discussed in section 4.3.4, is seen. From this, it is inferred that the background estimations are good and so the subtraction is justified. Also, the topology of the top decays are well-described, and so the correction factors derived from the samples should also give a good description, within caveats on signal shape differences, between samples to be estimated as a systematic uncertainty (see section 6.2).

Moving to the distributions we are interested in studying, the reconstructed distributions and Monte Carlo comparisons for the top pair system are presented in figure 5.21. Relatively good agreement is seen, though some discrepancies are now showing. These will be further commented upon after the analysis procedure and final particle-level measurement is presented, for now it is simply noting as interesting that the Monte Carlo overestimates the tails in all these distributions.

The final distributions are for the analysis of the  $|y^t|$  and  $p_T^t$  of the hadronic and leptonic tops, shown in figure 5.22 and figure 5.23. Good agreement between data and MC can be seen in these figures with again some disagreement in the high- $p_T$  tails of the  $p_T$  distributions.

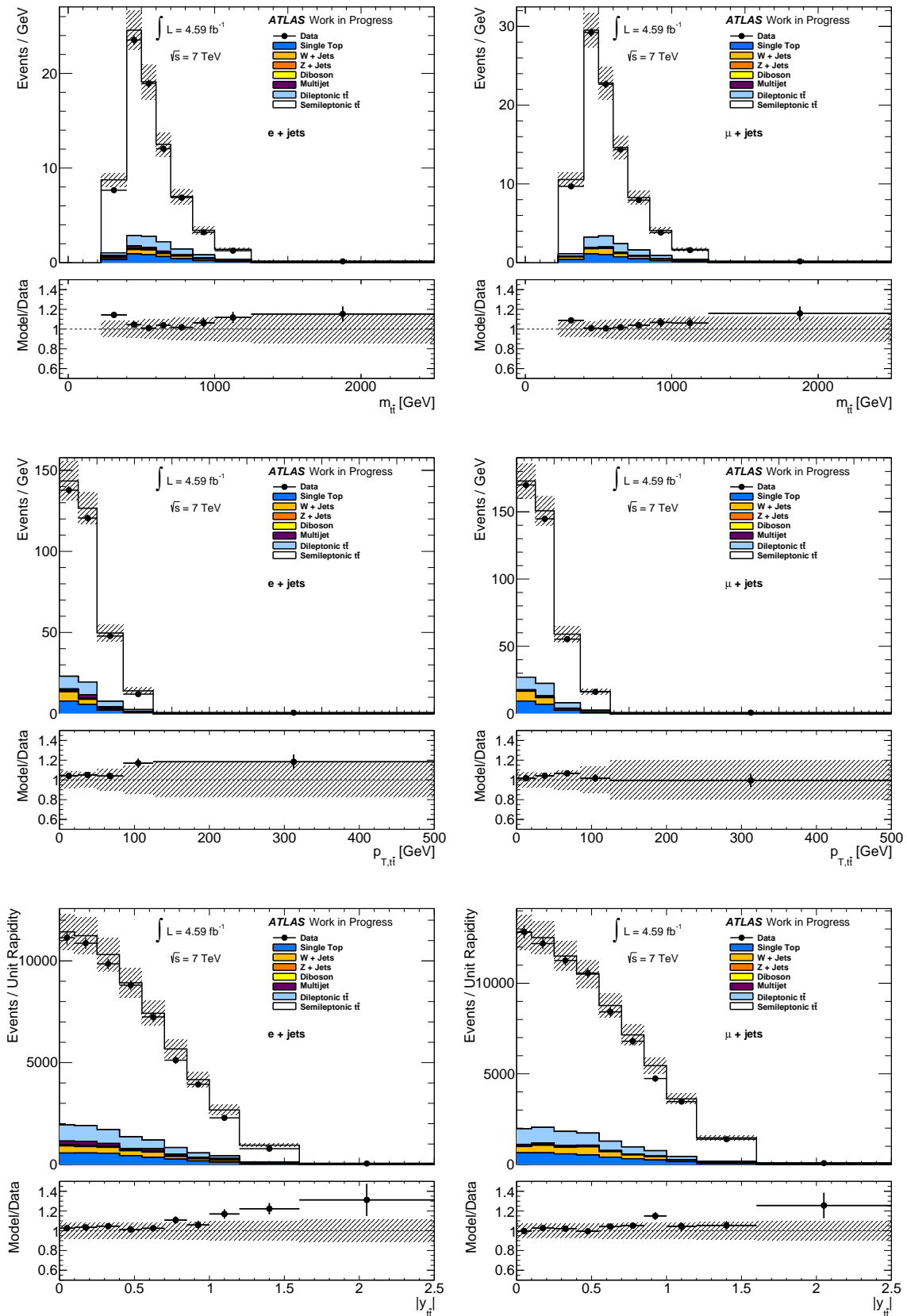
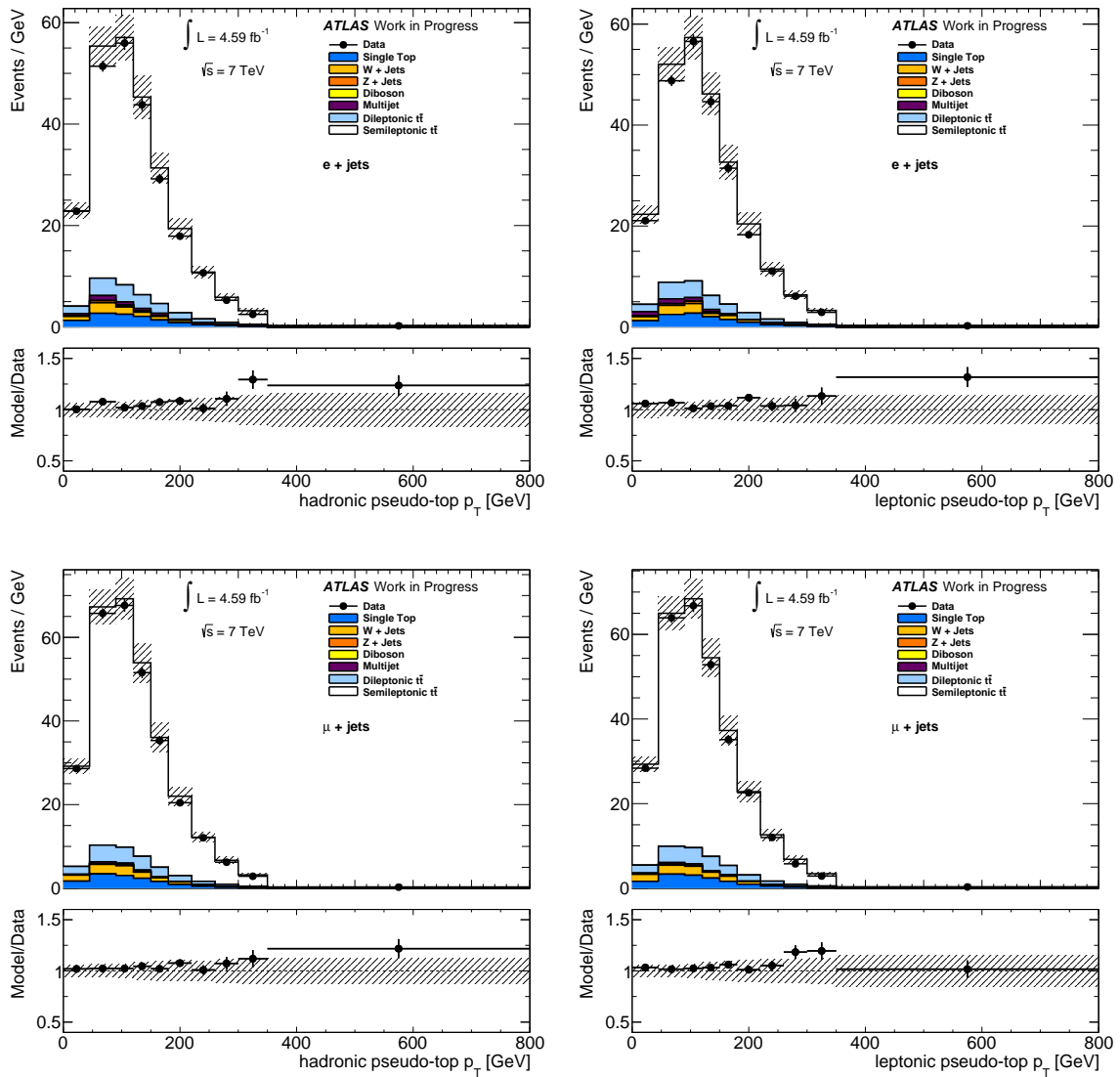
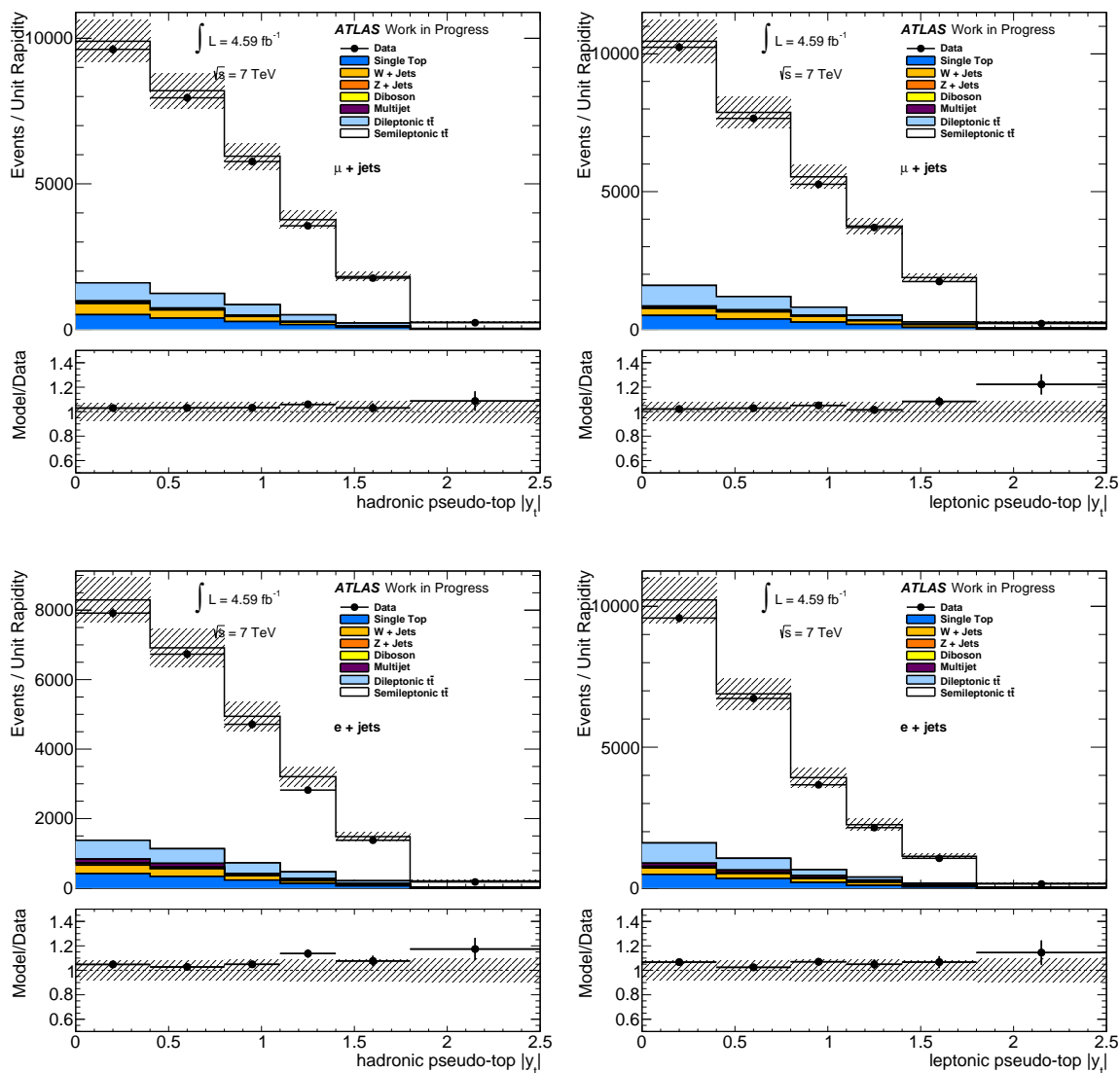


Figure 5.21: Reconstructed distributions for (top to bottom) the the  $m_{t\bar{t}}$ ,  $p_{T,t\bar{t}}$ ,  $|y_{t\bar{t}}|$  in the electron (left) and muon (right) channels.



**Figure 5.22:** Reconstructed distributions for (left to right) the hadronic and leptonic top  $p_T$  in the electron (top) and muon (bottom) channels.



**Figure 5.23:** Reconstructed distributions for (left to right) the hadronic and leptonic top  $|y^t|$  in the electron (top) and muon (bottom) channels.



# Chapter 6.

## Differential $t\bar{t}$ Cross-Section Analysis

Building on the definitions of the procedure arrived at in the previous chapter, this chapter presents the measurement of the kinematic distributions in semi-leptonic top pair events at ATLAS. Section 6.1 details the corrections applied, to account for detector effects and inefficiencies, to take the reconstructed data distributions, presented at the end of the previous chapter, to the unfolded distributions at particle level. Section 6.2 explains the source of, and the procedures used to estimate the size of, the systematic uncertainties. These systematics include uncertainties in modelling the detector response, the production and decay of the top, and the background composition and size. Section 6.3 presents the results of applying the correction procedures to the 2011 ATLAS dataset. Section 6.4 discusses these results in the context of the theory of top production and decay as presented in section 5.1. Finally, section 6.5 applies an additional correction to present the distributions at the parton level, and compares these results to the results of the dedicated ATLAS parton-level differential cross-section analysis [171].

### 6.1. Corrections and unfolding

Our goal in this analysis is to provide a selection of kinematic distributions related to the top quark which can be used to compare with theoretical and phenomenological models of top pair production at the LHC. As discussed in chapter 4, the detector will smear and distort the physical distribution, and we may misreconstruct the physics objects which go into the pseudo-top variables. The detector also rejects (accepts) some events

events which fall outside (inside) the fiducial range after reconstruction but were inside (outside) the range at particle level. To compare with theory, these detector effects must be taken into account.

One option is to provide the reconstructed data and smearing matrices, and for any given theory pass the generated distribution through the analysis chain to compare with the data. However, this requires extensive computing power which may not be available to all groups wishing to make comparisons and the results presented would not be directly comparable between different experiments. We will thus present, along with the untouched reconstructed distribution, a corrected distribution which accounts for these detector effects.

### 6.1.1. Basic Cross-Section Measurement

First, let us consider performing an inclusive cross-section measurement. The starting point is to relate the number of events produced to the delivered integrated luminosity of the machine:

$$N_p = L\sigma_p \tag{6.1}$$

where  $N_p$  is the number of events produced due to a process  $p$  (e.g.  $pp \rightarrow t\bar{t} + X$ ),  $L$  is the integrated luminosity, and  $\sigma_p$  is the cross-section of the process  $p$ . Due to detector inefficiencies, the selection criteria applied by the analysis, and a finite fiducial volume, the detector will not be able to reconstruct all the events of process  $p$ . Typically, these inefficiencies are accounted for in two separate factors. The first is  $\epsilon_p$  which is the fraction of  $p$  events that the analysis accepts at reconstruction compared with the number of events possible to reconstruct given the fiducial volume of the detector (that is, asking for the particle-level objects to be within the allowed angular ranges and the requirements on the energies of the objects). The efficiency then accounts for reconstruction inefficiencies. This gives a correction from the number of events at reconstruction level to the number of events that actually occurred in the fiducial volume. Secondly, the acceptance factor  $A$  is the fraction of the total number of events that fall within the fiducial volume. The acceptance factor is therefore a purely theoretical quantity since the detector, even in principle, does not have access to the events outside the fiducial volume. Also, the process in question may be a sub-process of the process to be measured (for example, semi-leptonic top events compared with all top pair events), so a branching fraction  $\mathcal{B}$

**Table 6.1:** Numbers entering the simple example calculation of the measured  $t\bar{t}$  cross-section.

$\epsilon$	$A$	$L$ (pb)	$N_{data}$	$N_{bkgd}$	$\sigma_{t\bar{t}}$ (pb)
0.3241	0.0783	4591.01	8791	1458	166.6

to this sub-process is also required. Finally, in any measurement there will be a certain number of background events  $N_{bkgd}$ . So  $N_{bkgd}$  must be estimated and then subtracted from the total data yield  $N_{data}$  to give the number of signal events in the data sample. Putting this together the cross-section is calculated as:

$$\sigma_p = \frac{1}{LBA\epsilon}(N_{data} - N_{bkgd}) \quad (6.2)$$

To illustrate, we apply this formula to the results from data and use the POWHEG+PYTHIA simulation to find  $A$  and  $\epsilon$ , and the background modelling from section 4.3 we have for the electron channel, an measurement of  $\sigma_{t\bar{t}} = 166.6$  pb for the overall cross-section. The factors used to derive this are shown in table 6.1.

This simple demonstration, where we have not attempted to calculate systematics, agrees well with the ATLAS measurement of  $165 \pm 2(\text{stat.}) \pm 17(\text{syst.}) \pm 3(\text{lumi.})$  pb [174]. The ATLAS measurement was made using this background subtraction procedure, and the same data and a signal region similar to ours, but requiring only one jet tagged as a  $b$ -jet with an algorithm that searches for a semi-leptonic  $B$  decay.

### 6.1.2. Unfolding to a Differential Cross-Section

Now we extend the previous section to obtain the differential distribution that we are trying to measure. We must take into account the distribution of events in our binning and the correlations of the bins when we move from reconstruction to particle level.

For a variable  $x$  that describes some portion of the kinematics of the events, there will be a true, underlying distribution that we are trying to measure  $\frac{d\sigma}{dx}$ . As before, there will be restrictions to the fiducial volume of the detector, and detector inefficiencies, but now these effects may be a function of the variable being measured. The distribution will therefore be distorted from the nominal by an acceptance function, an efficiency function, and a response matrix, to account for the detector resolution smearing out the measured variable. Therefore, we measure the variable in variable-width bins, where the

bin width is approximately the resolution of the detector over that region, to limit the smearing between the bin (more on the binning procedure is covered in section 6.1.4). As previously discussed, for our main measurements we also correct only to the fiducial volume, to avoid large corrections into detector-inaccessible regions. The goal is thus to go from the number of events in each bin  $i$  in the reconstructed data  $d_i$  to a cross-section measurement in the fiducial detector volume  $\frac{d\sigma_i^{fid}}{dx}$ .

The correction procedure then proceeds as follows. First, the estimate of the expected background events in each bin  $b_i$  is subtracted from the data. Then, a per-bin correction factor  $\rho_i$  is applied to account for the fraction of signal events that were reconstructed, but which are outside the fiducial volume at particle level. This can occur when the detector reconstructs a physics object with more transverse momentum than it really had, moving it into the fiducial region (for instance, there is a large  $E_T^{miss}$  resolution and so a small  $E_T^{miss}$  can easily be reconstructed larger), or if the object is misidentified (for example, a jet is reconstructed as an electron, where the true electron in the event falls outside the fiducial volume). This correction is obtained from signal Monte Carlo. Then, we use the per-bin matching efficiency  $m_i$  of section 5.3.1 to correct for events where the reconstructed pseudo-top objects do not correspond at particle and reconstruction level. This is done as we only want to unfold the distributions for detector smearing, whereas for non-matched events the objects are not the same and so the difference in the variable at particle and reconstruction is a pseudo-top construction error, not detector smearing. The resulting distribution is unfolded (a procedure described below) to particle level, using a response matrix  $U_{ij}$  which measures the probability for an fully-matched event in bin  $j$  at reconstruction level to be in bin  $i$  at particle level.  $U_{ij}$  is obtained from Monte Carlo. Finally, a per-bin particle-level efficiency factor  $\epsilon_i$  is applied to correct for events within the fiducial volume that are either not reconstructed or not matched. After this correction, the number of signal events at particle-level per bin is obtained. Finally, the overall luminosity  $L$  is applied to turn the number of events at particle level into a cross-section.

Putting the above together, the equation for correcting from the data distribution to the fiducial cross-section is given by:

$$\frac{d\sigma_i^{fid}}{dx} = \frac{1}{L\epsilon_i} \sum_j [U^{-1}]_{ij} [m_j \rho_j (d_j - b_j)] \quad (6.3)$$

The matrix  $U_{ij}$  is defined as taking the particle level distribution to the reconstruction level, because the effect of the detector is to take the particle level objects and give a smeared

reconstructed output. It is a well-known problem that simply inverting the response matrix and unfolding leads to severe numerical instabilities of the solution, where small changes in the input matrix lead to large differences in the output. So, we do the unfolding step (applying and summing the  $[U^{-1}]_{ij}$  response matrix to the matched, fiducial volume corrected, background subtracted distribution) using the iterative Bayesian unfolding technique [175] implemented in RooUnfold [176]. This procedure treats the problem in probabilistic terms, using the matrix and data to construct a likelihood and using Bayes' theorem with a prior distribution (usually the true MC) to obtain a new posterior and iteratively applying the posterior as a prior to converge on a smooth output distribution.

For brevity and consistency of notation between the factors, we often present the factors with a different notation. The purity  $\rho_j$  is  $f_{\text{reco!part}}$ , that is, the correction factor for reconstructed events without a pseudo-top at particle level. The matching efficiency is  $f_{\text{misassign}}$ , for the correction for misassigned events. And the inverse of the reconstructed to particle efficiency is  $f_{\text{part!reco}}$ , the correction factor (now applied as a multiplicative factor) for particle events which are not reconstructed. There is also an additional correction factor, not used for the analysis, which corrects the particle level distribution to the parton level  $f_{\text{truth!part}}$ . These factors for all the distributions are shown in appendix B.

The number of iterations is a free parameter in the Bayesian unfolding. There is a trade off in the number of steps, where fewer steps will give higher weighting to the initial prior (i.e. give higher weighting to the initial MC) while more iterations leads to larger uncertainties (similar to the numerical instabilities in the original inversion problem). The technique, however, converges in very few steps, so usually less than 10 is sufficient.

### 6.1.3. Unfolding configuration study

The reconstruction-level data distributions were corrected according to equation 6.3. The  $[U^{-1}]_{ij}$  term in this equation represents a Bayesian unfolding with two iterations. The number of iterations used for the Bayesian unfolding was selected by comparing the final statistical uncertainty and the closure of the measurement. Two iterations were found to ensure closure. As the number of iterations increases, the uncertainty from the MC statistical uncertainty in the response matrix and the statistical uncertainty in the input histogram is expected to become larger.

The leptonic pseudo-top  $p_T$  spectrum in the electron channel was used to study the performance of the unfolding. Other observables behaved in a similar manner. The

raw relative statistical uncertainty on the data before the corrections were applied is given in table 6.2. As described in section 6.2.1, the statistical uncertainty on the input distribution was propagated through the unfolding by using pseudo-experiments (ensemble tests), following a Poisson distribution according to the number of events in the given bin. The statistical uncertainty on the final distribution is tabulated in table 6.3, as a function of the number of iterations used for the unfolding. As expected, the statistical uncertainty increases as the number of iterations increases. The effect of the number of iterations on the final measurement and total systematic uncertainty was also studied and is shown in tables 6.4 and 6.5 respectively. The values converge quickly during the first iteration and then change by a relatively small fraction as the number of iterations increase.

	Bin range (GeV)									
	[0, 45]	[45, 90]	[90, 120]	[120, 150]	[150, 180]	[180, 220]	[220, 260]	[260, 300]	[300, 350]	[350, 1000]
Stat	0.035	0.023	0.026	0.029	0.034	0.038	0.050	0.067	0.085	0.094

**Table 6.2:** The relative statistical uncertainty on the reconstruction-level leptonic pseudo-top  $p_T$  in the electron channel data.

	Bin range (GeV)									
	[0, 45]	[45, 90]	[90, 120]	[120, 150]	[150, 180]	[180, 220]	[220, 260]	[260, 300]	[300, 350]	[350, 1000]
1 Iter.	0.036	0.025	0.025	0.027	0.029	0.030	0.041	0.049	0.065	0.105
2 Iter.	0.047	0.029	0.030	0.029	0.036	0.039	0.051	0.067	0.087	0.144
3 Iter.	0.057	0.033	0.033	0.036	0.043	0.046	0.058	0.075	0.107	0.152
4 Iter.	0.058	0.037	0.036	0.038	0.042	0.051	0.059	0.089	0.119	0.179
5 Iter.	0.062	0.038	0.042	0.040	0.046	0.061	0.068	0.094	0.132	0.159
6 Iter.	0.062	0.039	0.043	0.041	0.048	0.057	0.074	0.100	0.146	0.183
7 Iter.	0.063	0.041	0.042	0.043	0.053	0.060	0.076	0.103	0.156	0.179

**Table 6.3:** The relative statistical uncertainty on the  $t\bar{t}$  production cross-section, as a function of the leptonic pseudo-top  $p_T$  in the electron channel and the number of iterations used for the Bayesian unfolding. The correction factors from the nominal POWHEG+PYTHIA MC sample are used in the pseudo-experiments to derive the statistical uncertainty on the unfolded distribution.

#### 6.1.4. Binning Procedure

In order to obtain the most information on the kinematic distributions being measured, we aim to set the binning as small as is reasonable, or conversely, to measure in as many

	Bin range (GeV)									
	[0, 45]	[45, 90]	[90, 120]	[120, 150]	[150, 180]	[180, 220]	[220, 260]	[260, 300]	[300, 350]	[350, 1000]
1 Iter.	11.747	27.761	32.009	25.901	17.101	10.100	5.880	3.234	1.539	0.085
2 Iter.	11.691	27.544	32.374	26.158	17.100	9.895	5.948	3.305	1.529	0.080
3 Iter.	11.693	27.385	32.597	26.276	17.099	9.738	6.001	3.355	1.528	0.078
4 Iter.	11.717	27.265	32.750	26.331	17.115	9.620	6.044	3.384	1.525	0.077
5 Iter.	11.746	27.170	32.862	26.349	17.147	9.530	6.080	3.401	1.521	0.077
6 Iter.	11.774	27.093	32.951	26.343	17.187	9.459	6.112	3.410	1.516	0.077
7 Iter.	11.798	27.031	33.025	26.322	17.234	9.401	6.139	3.414	1.511	0.077

**Table 6.4:** The fully corrected differential  $t\bar{t}$  production cross-section, as a function of the leptonic pseudo-top  $p_T$  in the electron channel and the number of iterations used for the Bayesian unfolding. The results were propagated to the final distribution using correction factors from the nominal POWHEG+PYTHIA MC sample.

	Bin range (GeV)									
	[0, 45]	[45, 90]	[90, 120]	[120, 150]	[150, 180]	[180, 220]	[220, 260]	[260, 300]	[300, 350]	[350, 1000]
1 Iter.	0.116	0.090	0.106	0.102	0.115	0.112	0.150	0.135	0.161	0.257
2 Iter.	0.129	0.092	0.108	0.104	0.120	0.117	0.156	0.146	0.174	0.279
3 Iter.	0.140	0.094	0.109	0.108	0.124	0.120	0.159	0.153	0.187	0.287
4 Iter.	0.143	0.097	0.111	0.109	0.125	0.122	0.161	0.162	0.194	0.301
5 Iter.	0.149	0.099	0.114	0.110	0.128	0.126	0.166	0.166	0.203	0.292
6 Iter.	0.148	0.100	0.115	0.112	0.129	0.125	0.169	0.171	0.214	0.307
7 Iter.	0.150	0.100	0.115	0.112	0.131	0.126	0.170	0.174	0.221	0.306

**Table 6.5:** The total (statistical  $\oplus$  systematic) relative uncertainty on the differential  $t\bar{t}$  production cross-section, as a function of the leptonic pseudo-top  $p_T$  in the electron channel and the number of iterations used for the Bayesian unfolding. The systematic uncertainties were propagated to the final distribution using correction factors from the nominal POWHEG+PYTHIA MC sample.

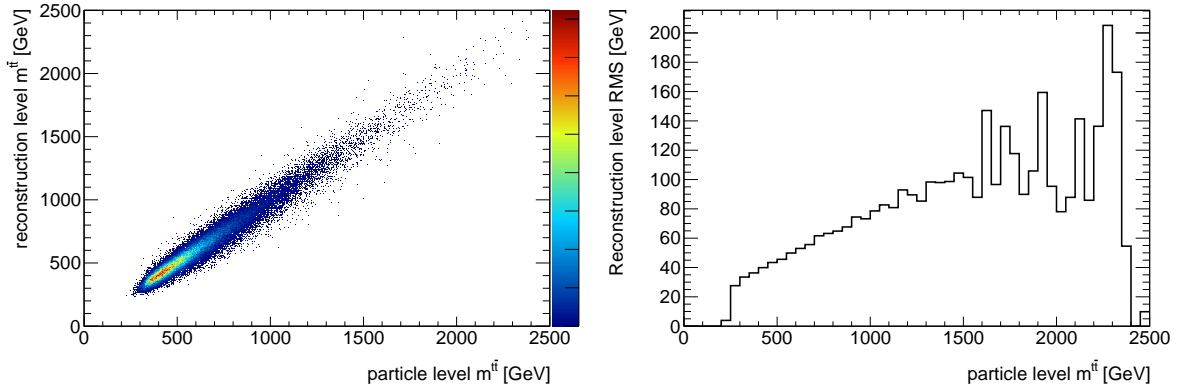


**Figure 6.1:** Response matrix (left) and RMS of the reconstructed pseudo-top  $m^{t\bar{t}}$  at a given particle level  $m^{t\bar{t}}$  based on the response matrix (right), for the POWHEG+PYTHIA signal in the electron channel.

bins as possible for a given distribution. The detector resolution sets the natural limit to the granularity that we can use for our measurements, since we are not sensitive to differences smaller than the resolution, as they get smeared out. The procedure we use to set the bin sizes is to start by taking from the signal MC a finely binned response matrix between reconstruction and particle level. Each column of the matrix represents the reconstruction distribution for a fixed (approximately) particle level value. The root-mean-square (RMS) of the column is then the detector resolution for that particular particle level value. As an example, figure 6.1 shows the response matrix and RMS distributions for the  $m^{t\bar{t}}$  distribution. The response matrices for all the distributions (after binning) are shown in section 6.1.5. The binning is set by starting from the edge of the distribution, and taking a bin size of twice the average RMS (to cover the full width of the resolution) of those particle level values being covered by the bin. At the edge of the first bin, this procedure is repeated until the entire distribution is covered with bins, taking the final bin to be the rest of the range once the RMS starts diverging, due to the low statistics in those bins.

In the tails of the distribution, some of the bins need to be merged together, as the low statistics in the tail lead to large systematic uncertainties from large fluctuations due to small statistics. This merging is done empirically after setting the binning based on the resolutions by checking the expected systematic sizes (to be discussed in section 6.2), and merging until the systematics in the bins that have large systematic fluctuations, due to the small statistics of the sample, reduce to approximately the level of the bulk distribution.

**Table 6.6:** Bin edges used in the analysis of the given kinematic distribution.

Distribution	Bin edges	No. of bins
top $y$	0.0, 0.4, 0.8, 1.1, 1.4, 1.8, 2.5	6
top $p_T$	0, 45, 90, 120, 150, 180, 220, 260, 300, 350, 800	10
$t\bar{t}$ $y$	0.0, 0.1, 0.25, 0.4, 0.55, 0.7, 0.85, 1.0, 1.2, 1.6, 2.5	10
$t\bar{t}$ mass	225.0, 400, 500, 600, 700, 850, 1000, 1250, 2500	8
$t\bar{t}$ $p_T$	0.0, 25, 50, 85, 125, 500	5

To enable the combination of the channels (discussed in section 6.3.1), the same binning is used for both the electron channel and the muon channel. The differences between the channel, however, are minimal enough that this has a negligible effect on the binning used. Also, to facilitate comparison, and for a final combination to parton level, the binning for the hadronic and leptonic sides use the same binning, taken from the distribution with the larger bin widths. For both the individual pseudo-top  $p_T$  and rapidity, this is the leptonic distribution. The bin edges found from this procedure for the kinematic distributions we will measure are tabulated in table 6.6.

### 6.1.5. Correction Factors and Response Matrices

Figures B.1 to B.7 in appendix B show the correction factors for the distributions to be measured, derived from the various signal samples (except the response matrix, which is exclusively derived from the POWHEG+PYTHIA sample). The correction factors that we use in the measurements are from the POWHEG+PYTHIA sample, since this has good agreement between Monte Carlo and data as well as a large number of generated events (5 million), which helps to reduce the size of the systematics due to low statistics in the tails of the distributions. Generally however, good agreement is seen between the various Monte Carlo samples for all of the correction factors used in the analysis. This should be compared with figure 6.2, which shows the efficiency for a generated top pair event to end in the fiducial volume (the parton acceptance). The figure shows that this correction is highly dependent on the sample being used to estimate it. That is, the correction to outside the fiducial volume, where we have no detector information, is highly dependent on the model being used to make the correction. This quantifies part of the argument we made previously, that parton level measurements are highly dependent on model-dependent correction factors whose effects are hard to disentangle and use for

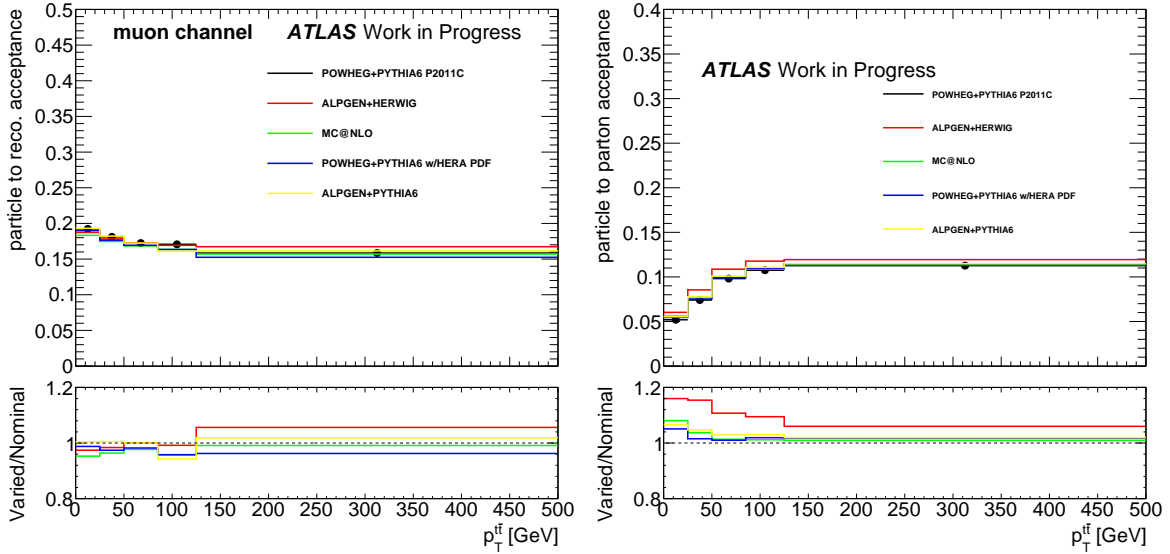


**Figure 6.2:** The fraction of  $t\bar{t}$  signal events at particle level that are accepted at reconstruction level (left), and similarly, the parton to particle level acceptance fraction (right). The acceptances are shown as a function of the top pair  $p_T$  in the muon channel. Several  $t\bar{t}$  MC model for these quantities are compared and shown in ratio to the nominal POWHEG+PYTHIA sample (shown with points) in the bottom of the figure.

constraining the models themselves. This is to be compared with the reconstruction to particle level efficiency, which is comparatively independent of the MC used.

Figure 6.3 (along with figure B.5) shows the analysis distribution after each of the correction factors has been applied and through the unfolding. Starting from the reconstructed distribution, it shows the effect of applying, in turn, the correction for reconstruction phase space, the misassigned reconstruction, the unfolding, and the correction to the full particle level. Also displayed is the parton level distribution for the events accepted in the particle level reconstruction. The figure shows that the the largest correction is for the particle level acceptance, that the unfolding has only a minimal impact on the distribution and also that the particle and parton level distributions have a shape difference in the  $t\bar{t}$  distributions. In particular, the shape of the  $t\bar{t}$   $p_T$  distribution is significantly softer in the pseudo-top particle level than the parton level, as the particle-level pseudo-top construction can pick up a jet which the  $t\bar{t}$  system is recoiling against, thereby reducing the  $p_T$  of the pseudo-top pair. We have also checked the alternative pseudo-top constructions and this is a generic feature of all of the constructions based on physics level objects. Comparing the electron and muon channels, the reconstructed distributions are slightly different between the two channels, due to the smaller  $\eta$  ranges

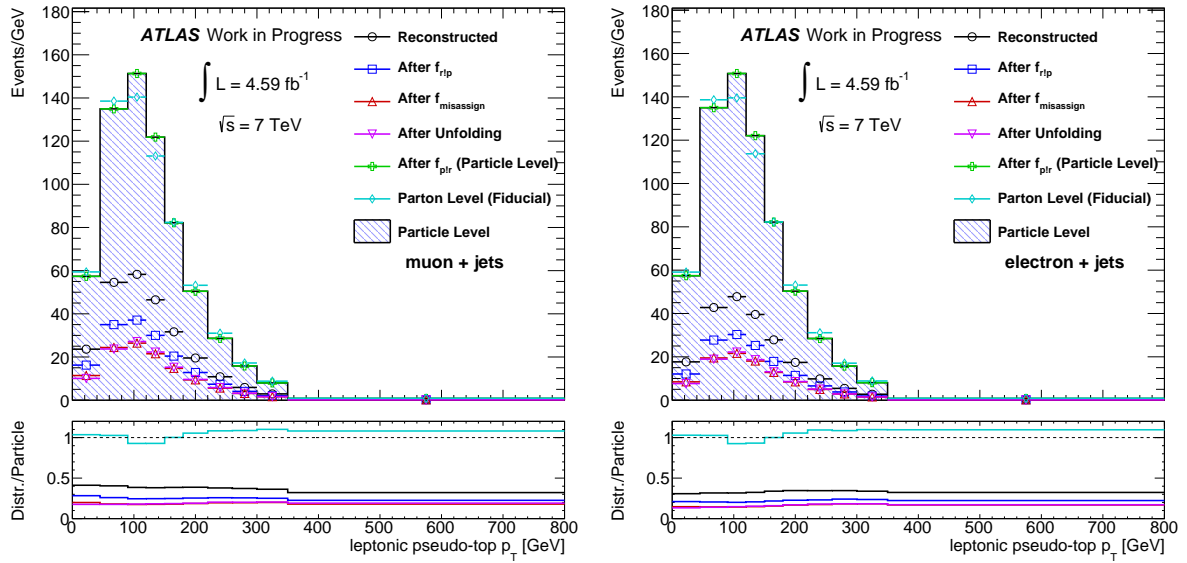


**Figure 6.3:** Distributions stepping through the analysis corrections with the leptonic pseudo-top  $p_T$  in the muon channel (left) and electron channel (right) using the POWHEG+PYTHIA signal sample. The bottom of the figure shows the ratio of the particle-level leptonic pseudo-top  $p_T$  restricted to the fiducial region to the given distribution.

accessible to the ATLAS detector for electrons and muons. This difference, however, does not propagate through to the final particle level distribution since the ranges have been defined to be the same for both leptons, and so the correction factors account for the reconstruction level differences.

## 6.2. Systematic Uncertainties

Systematic uncertainties represent our ignorance of the true underlying distributions relevant for our analysis. This may be uncertainty of the exact shape and normalisations used for both the background and signal modelling, uncertainties on the extraction of data to simulation scale factors, or uncertainties in the detector calibrations. This section describes the sources systematic uncertainty affecting our analysis, and how we estimate the size of these uncertainties. The final systematic uncertainty tables of the analysis are shown in appendix C, which show the size of the effect of each systematic for each bin of each distribution.

### 6.2.1. Propagation of Uncertainties

The correction factors ( $f_{\text{part!reco}}$ ,  $[U^{-1}]_{ij}$ ,  $f_{\text{misassign}}$ ,  $f_{\text{reco!part}}$  introduced in section 6.1.2) were determined from the nominal POWHEG+PYTHIA  $t\bar{t}$  MC sample. The statistical uncertainty on each correction factor was estimated by performing 1000 pseudo experiments following the statistical uncertainties on each term. Poisson and normal distributions were used for the  $[U^{-1}]_{ij}$  and ( $f_{\text{part!reco}}$ ,  $f_{\text{misassign}}$ ,  $f_{\text{reco!part}}$ ) correction factors respectively. The difference between the mean of all 1000 unfolded distributions and the true ALPGEN+HERWIG  $t\bar{t}$  distribution was taken to be the systematic uncertainty due to the statistical uncertainty on the correction factors.

The uncertainty on the background estimation was determined at the reconstruction-level. All of the systematic uncertainties were evaluated for the non- $W$  + jets MC samples. The total uncertainty on the non- $W$  + jets MC was then determined by adding the individual systematic uncertainties and statistical uncertainty in quadrature. The uncertainties on each of the  $W$  + jets data-driven normalisation factors and the statistical uncertainty of the MC sample were added together in quadrature. Finally, the shape and normalisation uncertainties on the data-driven estimate of the multijet background were added together in quadrature. The non- $W$  + jets MC,  $W$  + jets and multijet background templates were then added together with their combined uncertainties. The systematic uncertainty on the unfolded spectrum from the background was evaluated by performing 1000 pseudo-experiments, following a normal distribution with a width matching the total uncertainty band. The square root of the variance of the unfolded spectra of the pseudo-experiments was taken as the uncertainty on the background.

Systematic uncertainties affecting the  $t\bar{t}$  sample used to unfold the pseudo-top  $p_T$  spectrum were evaluated as relative bias. That is, the uncertainty attributed to a particular signal systematic,  $S$ , which is a systematic variation from some nominal sample  $N$  in the  $i$ th bin  $\Delta_i$  is obtained by first taking the reconstructed distribution and unfolding with our nominal unfolding procedure, producing  $S_i^{\text{unfolded}}$  and  $N_i^{\text{unfolded}}$  for the systematic and nominal samples respectively. Then the distributions at particle level from the MCs are produced for the systematic  $S_i^{\text{particle}}$  and nominal  $N_i^{\text{particle}}$  samples. The uncertainty is then calculated according to

$$\Delta_i = (S_i^{\text{unfolded}} - S_i^{\text{particle}}) - (N_i^{\text{unfolded}} - N_i^{\text{particle}}), \quad (6.4)$$

that is, the difference in the number of events at particle level between the unfolded distribution and the truth distribution for the systematic sample, the systematic bias, and subtracting off the bias from the nominal sample. The nominal sample bias is attributed to using a different sample generator for the systematic variation. This procedure is performed to avoid double counting the generator bias, which has its own systematic uncertainty. The modelling systematics are included in the list in the next section and are the parton shower uncertainty, the initial and final state radiation uncertainty, the colour reconnection uncertainty, and the generator uncertainty.

### 6.2.2. Sources of Systematic Uncertainty

This section enumerates the sources of systematic uncertainty that were considered in the analysis and details the procedure used to estimate their sizes in the final distributions.

**MC statistics of the correction factors** The samples used to make the correction factors,  $f_{reco!part}$ ,  $f_{part!reco}$ ,  $f_{misassign}$  and  $[U^{-1}]_{ij}$ , are of limited statistics. Particularly in the tails of the 2D unfolding matrices, there are only a few events. Therefore, there is some uncertainty in the value of these unfolding matrices due to the limited statistics. The size of the uncertainty is estimated by generating 1000 sets of unfolding correction factors and the unfolding matrix, where each set has been fluctuated according the statistical uncertainty of the distributions used to generate the correction factor. For example, for the unfolding matrix, each bin of the 2d matrix has been filled by weighted MC events. The statistical uncertainty of each bin is therefore the square root of sum of the weights square of the events filling that bin. Each sample set is filled with a value generated by picking a random value from a Gaussian distribution with mean the weighted value of the bin and width equal to the statistical uncertainty. The matrix is then normalised as required for the unfolding procedure. The other correction factors are constructed in a similar manner. The reconstructed data is the passed through all of the sets of fluctuated correction factors, and the uncertainty on each bin of the unfolded output is the root mean square of the distribution of values for the bin. In this way, correlations between the bins, which change due to the fluctuating unfolding matrix, are taken into account in the uncertainty.

**Muon Momentum** The muon momentum resolution is extracted from the  $Z$  width in  $Z \rightarrow \mu\mu$  events [177]. Uncertainties due to the momentum scale are estimated by smearing

the muon  $p_T$  in MC by the resolution. This smearing is applied separately to the Inner Detector and the Muon Spectrometer. The size of the uncertainty is taken as the shift with respect to the nominal unfolding using the smeared sample.

**Electron Energy** The energy scale for the electrons are obtained from studying dielectron peaks resulting from the decay of particles of well-known mass:  $Z \rightarrow ee$ ,  $J/\psi \rightarrow ee$ , and energy over momentum using isolated electrons from  $W \rightarrow e\nu$ . The energy scale is corrected as a function of  $\eta$ ,  $\phi$  and  $E_T$  and uncertainties from the measurements are taken as systematic uncertainties. An energy smearing term is also applied to MC samples so that the resolution of the MC samples match the energy resolutions in data. To obtain the uncertainty, we rerun the MC with the resolution smearing taken as the extremes of the uncertainty band on the resolution, and the uncertainty is the difference between these bands and the nominal.

**Lepton Efficiencies** For both the muons and electrons, there are uncertainties on the difference in efficiency between MC and data for a lepton to be (1) triggered on, (2) reconstructed offline and (3) identified as a good quality lepton. For the electrons this is done using the  $Z \rightarrow ee$  tag and probe method for the trigger and reconstruction efficiencies, and  $Z \rightarrow ee$  and  $W \rightarrow e\nu$  for the identification efficiency. The systematic uncertainty from these factors is mostly due to the uncertainty in subtracting the backgrounds from these analyses. The muon reconstruction efficiency is measured using the  $Z \rightarrow \mu\mu$  tag and probe method [178]. The muon identification and trigger efficiencies were also measured using tag and probe methods [179, 180]. The systematic uncertainty is obtained by rerunning the nominal sample with the extremes of the uncertainty of the measurements, and taking the difference between these samples and the nominal in the final unfolded distributions as the uncertainty.

**Jet Energy Scale** As discussed in section 4.1.4, reconstructed jets need to be energy corrected to the jet energy scale. The jet energy scale (JES) is a correction from the initial calorimeter calibrated energy based on electromagnetic response (EM scale) to the energy of the hadronic jets. The JES is derived initially from MC by constructing jets from stable particle level objects to the reconstructed EM scale jet energy. The jets used for this correction are isolated jets from an inclusive MC sample included pileup. Then, to account for residual differences between data and simulation, an in-situ correction method has been used and applied as a last step of jet reconstruction [181].

This correction is derived from dijet events, where it is known that the jets should be  $p_T$  balanced (up to parton radiation modelling effects, the size of which are estimated by comparing PYTHIA and HERWIG in MC). The pseudo-rapidity dependence for jets with  $|\eta| < 2.8$  is analysed by testing the transverse momentum balance in dijet events of the jet against a jet lying in a reference region  $|\eta| < 0.8$ . The reference region is used as jets in this region are seen to be well-modelled in simulation and require no extra calibration. At  $|\eta| = 2.8$  the uncertainties of this procedure become large, but as this analysis only uses jets with  $|\eta| < 2.5$ , we will not discuss this further. The energy scale for central jets ( $|\eta| < 1.2$ ) is tested by comparing the transverse momentum of events with a  $Z$  boson and a recoiling jet. Since the  $Z$  bosons are well-measured at the EM scale (as they decay to muons or electrons) with much less uncertainty than the JES, these provide a clean, robust test of the momentum calibration.

A large number of sources of uncertainty have been identified and the size of these estimated. These are broadly categorised into: statistical uncertainties (due to the statistical uncertainties of the jet-balance and photon-balance calibrations), model uncertainties (for example, the contribution of particles outside the jet cone to the jet  $p_T$ ), detector uncertainties (for example, photon purity uncertainties and electron or photon energy scales), mixed uncertainties (for example, the sensitivity of the calibrations to pileup interactions), the uncertainty of the jet-balance  $\eta$  intercalibration, pileup offset uncertainties, close-by jet uncertainties, single particle response uncertainties, high- $p_T$  jet uncertainties, uncertainties due to non-closure of the calibration and flavour composition and response uncertainties. The number of components is reduced by combining the parameters which are found to be highly correlated in terms of their uncertainty with respect to the  $\eta$  and  $p_T$  of the jet, leaving a total of 16 parameters which are independently varied in our analysis to give the JES uncertainty. We obtain the uncertainty by rerunning, once for each component of uncertainty, with a JES given by the extremes of the allowed JES for the particular component and comparing the final unfolded distributions to the nominal. Each component is considered as a separate uncertainty in the final analysis, and in the list of systematics (presented in Appendix C), shown as a JES with the component name listed next to it.

**Jet Energy Resolution** The MC description of the jet energy resolution (JER) was evaluated using the dijet balance measurement and the bi-sector technique on data [182]. Both measurements show that JER in the MC simulation agrees with the observed data distribution. Therefore, by default no extra smearing is applied to reconstructed MC jets,

and for the systematic uncertainty, the uncertainty of the JER measurement is added as an extra smearing to evaluate the effect on our measurement, by comparing the final unfolded distributions obtained with the extra smearing to the nominal.

**Jet Reconstruction Efficiency** The efficiency of the calorimeter to reconstruct jets was measured using data by reconstructing jets from tracks and searching for a matching calorimeter jet [183, 184]. The MC simulation efficiency agreed with the data within the uncertainty bands of the measurement. The extremes of the uncertainty bands of the relative efficiency between MC and data was taken as a systematic uncertainty. In order to estimate the effect of this uncertainty, the main signal sample was rerun discarding a random fraction of jets in the inefficient regime and the difference between this and the nominal unfolded distributions was taken as the jet reconstruction efficiency uncertainty.

**Jet Vertex Fraction** The systematic uncertainty due to the Jet Vertex Fraction (JVF) cut (described in section 4.1.4) was estimated by varying the scale factors for the hard-scatter jet selection efficiency (the fraction of hard-scatter jets that are classified as hard-scatter by the JVF selection) and for the pileup jet rejection efficiency (the fraction of jets from pile-up energy deposits classified as pile-up jets by the JVF selection).

The scale factors for the JVF are defined as the ratio of the data efficiency and the MC efficiency, and are applied to MC. The efficiencies are measured using a Tag and Probe method looking for a  $Z$  boson recoiling back-to-back against a single jet [116]. From this sample a hard-scatter enriched region is defined as having a  $Z$  boson with  $p_T > 30$  GeV and  $\Delta\phi(Z, \text{jet}) > 2.9$ . Very few of the events in this region have pile-up jets, since the  $p_T$  requirement implies the  $Z$  boson is recoiling off of QCD radiation. A pile-up enriched region is defined by requiring the  $Z$  boson has  $p_T < 10$  GeV, and the jet has  $p_T > 20$  GeV, without any requirements on the  $\Delta\phi(Z, \text{jet})$ . The low  $p_T$  requirement on the  $Z$ , along with the requirement that only one jet is reconstructed, implies that the  $Z$  boson was produced with negligible QCD radiation in this region, and the jet is being constructed from the energy due to pile-up interactions. From the corresponding regions, efficiencies for correct classification of hard-scatter or pile-up jets are measured in data and MC and a scale factor correcting the difference,  $K = \epsilon_{data}/\epsilon_{MC}$  is produced which is applied to the analysis of MC. The scale factor is parameterised with respect to the jet  $p_T$  by a falling exponential  $f(x) = ae^{bp_T^{jet}} + c$  where  $a, b$  and  $c$  are free parameters that are found by fitting to the distribution  $K(p_T^{jet})$ . The JVF systematic uncertainty is then found by using the  $K$  value given by the maximal difference when the parameters

are varied within the uncertainty allowed by the fit. This uncertainty is summed in quadrature given by taking the maximally varied  $K$  for different signal selection regions (for example, varying  $\Delta\phi$  in the definition of the hard-scatter region) and rerunning the  $K$  analysis. This is to account for the uncertainty in region selection purity, for example the contamination of hard-scatter events in the pile-up region. Further details on the scale factor derivation (in particular, how contamination of hard-scatter jets in the pile-up region is accounted for) is given in [116].

**$b$ -tagging Scale Factors**  $b$ -tagging scale factors were applied to correct for data and MC efficiency differences. The efficiencies are measured from samples of dileptonic  $t\bar{t}$  events [185, 186]. In these events, two  $b$ -tagged jets are expected, and any additional jets are light jets. 2 and 3 jet bins are used to fit a likelihood function which gives the  $b$ -tagging efficiency as a function of the jet  $p_T$ . From the efficiencies in data and MC, scale factors can be determined as a function of jet  $p_T$  for both the efficiency of a  $b$ -jet being tagged ( $b$ -jet efficiency) and the efficiency for a light jet to be tagged as a  $b$ -jet (mistag rate). The uncertainties on these rates, determined from the uncertainties on the likelihood minimisation, are the  $b$ -tagging systematics. As usual, the unfolded distributions with the systematic scale factors are compared with the nominal to obtain the uncertainty due to  $b$ -tagging scale factors.

**Missing Transverse Momentum** For all the systematics involving object energy recalibration, the missing transverse momentum term is also recalculated to take into account the object rescaling, which affects the  $E_T^{miss}$  according to equation 4.2. There are two further sources of uncertainty in the missing transverse momentum not taken into account: the cellout term (discussed in section 4.1.6, this term also includes the uncertainty on the soft jets described in that section), and the effect of pileup. The cellout uncertainty is estimated using samples of  $Z \rightarrow \ell\ell$  events [187], as these events have a well-measured  $Z$  boson, recoiling against soft energy deposits (i.e. no hard jets or other hard scale physics objects). The observed discrepancy between data and MC of the cellout  $E_T^{miss}$  term in scale and resolution (as a function of the total transverse energy of the events) is taken as the total uncertainty due to soft energy  $E_T^{miss}$  uncertainties. Samples with the soft terms varied up and down by the derived uncertainties are produced and compared with the nominal unfolded distributions to derive the uncertainty of this component on our analysis.

The uncertainty in the description of extra energy deposits due to pileup interactions is estimated by varying the jet, soft-jet and cellout components by 6.6%, as determined from studying the dependence of the MC to data ratio in  $Z \rightarrow \ell\ell$  events on the number of pileup interactions and taking the maximum difference as the uncertainty to be applied. Samples with the varied terms are compared to the nominal unfolded distributions to obtain these additional uncertainties.

**Background Subtraction** For the background samples which are completely determined from simulation, the above systematics are used to determine the uncertainty of the size of the background contribution, and therefore the uncertainty on the background subtraction. This comprises all samples except the  $W$ +jets and the QCD. For the QCD sample, the size of the uncertainty is estimated by running the QCD estimation procedure of section 4.3.3 with (separately) the fake rates and the real rates varied up and down within the uncertainties of their determination. For the  $W$ +jets samples, the overall uncertainty on the charge asymmetry normalisation method (see section 4.3.2) is run, as well as the uncertainty on the flavour fractions are run separately to determine the size of the uncertainty. In the final analysis, the square root of the sum of the squares combination of the size of all the background uncertainties are taken as a single, overall background subtraction uncertainty. The analysis was rerun with the background size increased and decreased based on this uncertainty, and the resultant distributions compared with the nominal distribution to obtain the background subtraction uncertainty.

**Parton Shower** Since parton showering is described phenomenologically by MCs, and there are various ways of modelling it, the effect of different models needs to be accounted for. The size of this uncertainty is estimated by taking the relative difference between the ALPGEN+HERWIG  $t\bar{t}$  and ALPGEN+PYTHIA  $t\bar{t}$  samples as the systematic uncertainty. Since neither of these samples is being used as the main analysis sample, both will give slightly different results from the main POWHEG+PYTHIA  $t\bar{t}$  sample. However, the relative offset from POWHEG+PYTHIA  $t\bar{t}$  is not considered as a systematic due to the parton showering, but instead attributed as coming from the difference between ALPGEN and POWHEG, only the relative offset between the samples per equation 6.4.

**Initial and Final State Radiation** The amount of initial and final state radiation produced in top events has been constrained by measurements of the jet gap fraction by ATLAS [150]. This measurement was presented in section 5.1. ATLAS tuned the ISR/FSR

parameters for two samples of ALPGEN+HERWIG  $t\bar{t}$  which provide an envelope of the uncertainty on the gap fraction measurement. The size of the ISR/FSR systematic uncertainty is then estimated for this analysis by taking the maximum difference between these two samples and the nominal ALPGEN+HERWIG  $t\bar{t}$  and taking this as a symmetric error.

**Colour Reconnection** Top quarks are coloured objects and so treating them decaying independently leaves a coloured parton and anti-coloured parton on opposite sides of the event. Since stable, coloured objects are not observed in nature, the event must reconnect the colour across the branches to produce colour-singlet states. This is implemented purely phenomenologically in MCs, and currently there are no observations that constrain the effect of this colour reconnection. The size of the uncertainty is estimated by rerunning a sample of POWHEG+PYTHIA  $t\bar{t}$  turning off the colour reconnection parameter and taking the relative difference of this result with the POWHEG+PYTHIA  $t\bar{t}$  sample with the colour reconnection parameter on as the systematic uncertainty.

**Generator** The nominal POWHEG+PYTHIA  $t\bar{t}$  sample used to describe the signal is made by an NLO generator, which produces diagrams up to the one loop level with no extra partons, or with an additional parton in the final state, relying on the parton shower for additional jets. We also have access to multileg LO generators, which account for only tree-level Feynman diagrams, but may produce several additional partons in the final state and so should in principle account for the jet distribution better. As noted, additional radiation effects can influence the analysis results, for example the top pair  $p_T$  spectra can be decreased from the analysis using a recoil jet in the pseudo-top construction. On the other hand, the NLO generators should better account for the top production kinematics. We account for uncertainty due to these potential differences with a generator uncertainty. The difference between the nominal POWHEG+PYTHIA  $t\bar{t}$ , an NLO generator, and the ALPGEN+HERWIG  $t\bar{t}$  sample, a multileg LO generator, was used to estimate the size of the generator uncertainty.

**Luminosity** The integrated luminosity of the total data sample was measured in ATLAS using van der Meer scans. The systematic uncertainty of this procedure was estimated to be 1.8% [188]. This is applied uniformly to all final distributions.

### 6.3. Results

The  $t\bar{t}$  cross-section is presented, as a function of pseudo-top  $p_T^t$  and after correction for all detector effects, in figures 6.4, 6.5 and 6.6. Overall statistical and systematic uncertainties are indicated in the figures. For a complete breakdown of the uncertainties discussed in the previous section, appendix C contains tables of the size of each source of systematic uncertainty for each of the distributions for all bins. Generically, the  $b$ -tagging, I/FSR, and generator uncertainties are the largest contributors to the total systematic uncertainty. In the high  $p_T$  and mass tails, the background subtraction uncertainty and some of the components of the JES uncertainty also become large.

The unfolded data are compared with several MC models, which have different matrix element calculations, matching schemes and fragmentation models. Most of the MC models are consistent with the measurements, although they appear to be systematically lower than the central values at lower values of pseudo-top  $p_T^t$ .

#### 6.3.1. Particle Level Combination

The corrected particle level pseudo-top distributions are independent of whether they are measured in the electron or muon channel, since we ensured that we defined the fiducial volume to be the same for both leptons, and there is no measurable difference in the  $W$  decay distribution to either lepton. Therefore the distributions for the two decay channels can be combined into a single result. This increases the statistics for the distribution and decreases their overall systematic uncertainty, since many of the systematics are correlated between the analyses. Thus, the combination of the results increases the overall discrimination power.

The measurements were combined by using the BLUE (Best Linear Unbiased Estimator) method [189]. The BLUE method takes a set of  $n$  measurements  $y_i$ , of the same observable  $y$  and creates the best fit for them, taking into account the correlations between correlated sources of systematic uncertainty as represented by a covariance matrix  $E$ . BLUE constructs an estimate of  $y$  from the measurements  $y_i$  by requiring that (1) the estimate  $\hat{y}$  is a linear combination of the individual estimates, (2) is an unbiased estimate, and (3) has the minimum possible variance  $\sigma^2$ . The first condition implies that

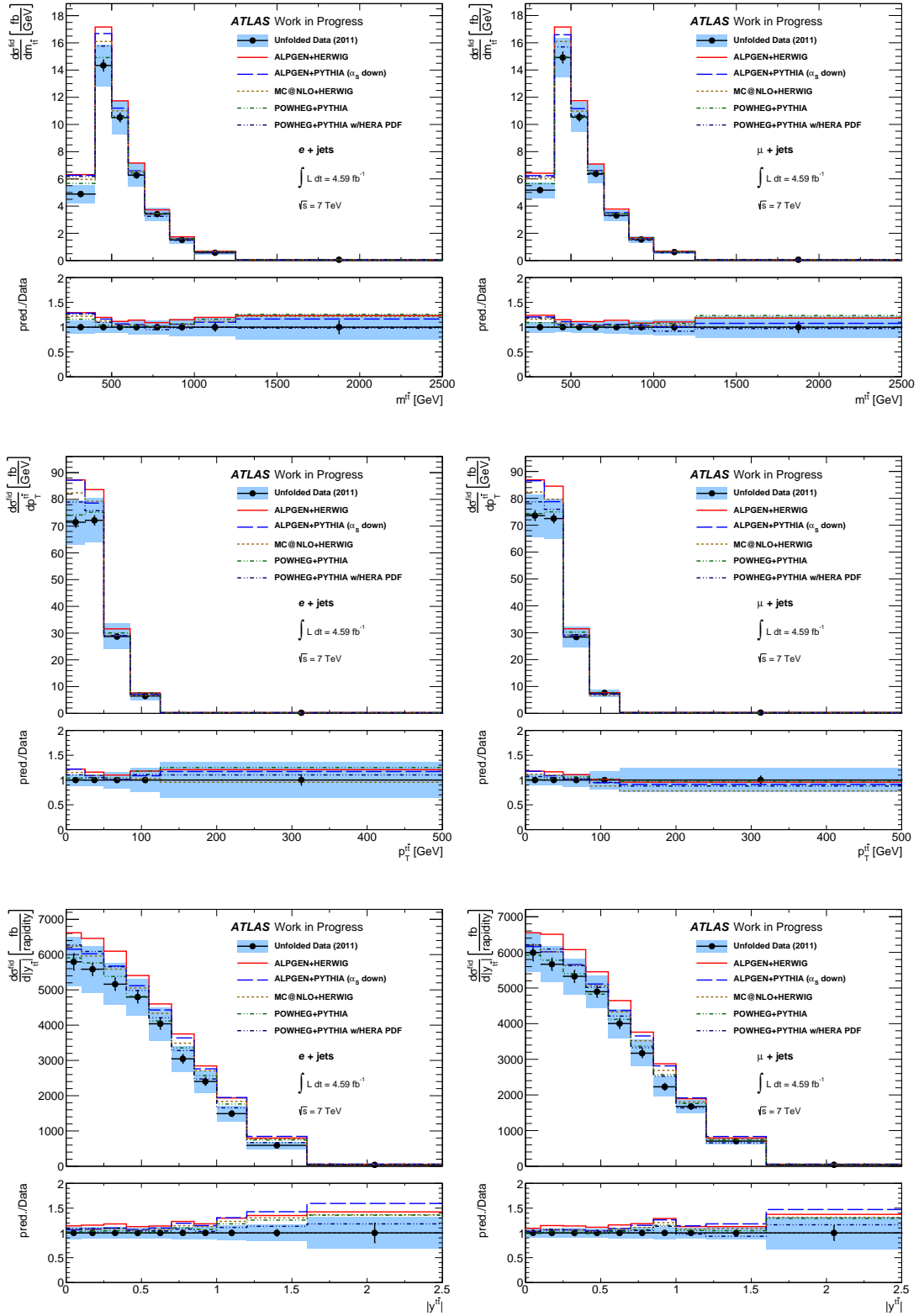


**Figure 6.4:** Unfolded and corrected distributions for (top to bottom) the the  $m^{t\bar{t}}$ ,  $p_T^{t\bar{t}}$ ,  $|y^{t\bar{t}}|$  in the electron (left) and muon (right) channels. The corrections used are derived from the POWHEG+PYTHIA  $t\bar{t}$  sample. Data points are shown with error bars for statistical uncertainties and error bands for total statistical and systematic uncertainties.

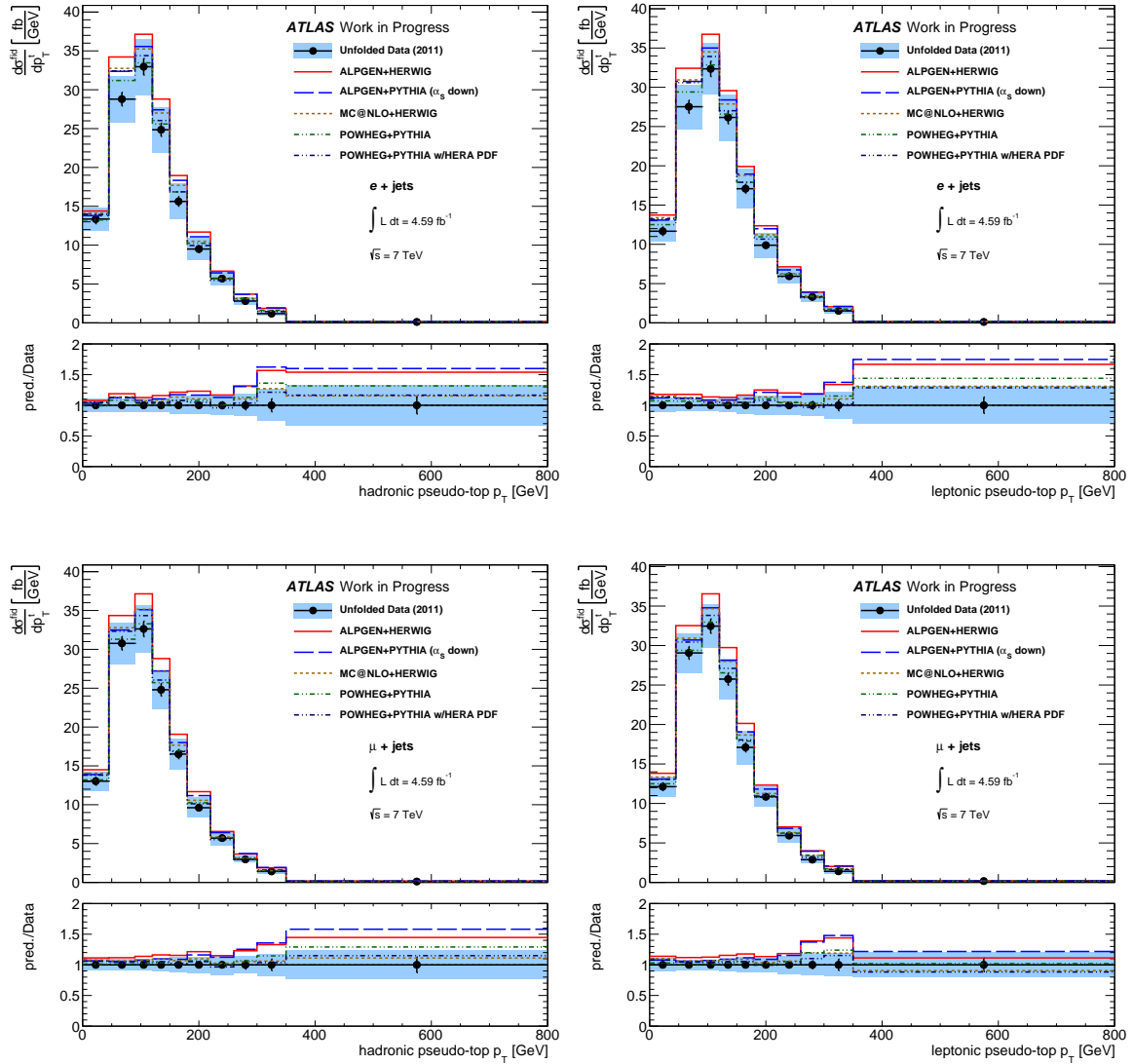


**Figure 6.5:** Unfolded and corrected distributions for (left to right) the hadronic and leptonic top distributions of top  $p_T^t$  in the electron (top) and muon (bottom) channels. The corrections used are derived from the POWHEG+PYTHIA  $t\bar{t}$  sample. Data points are shown with error bars for statistical uncertainties and error bands for total statistical and systematic uncertainties.

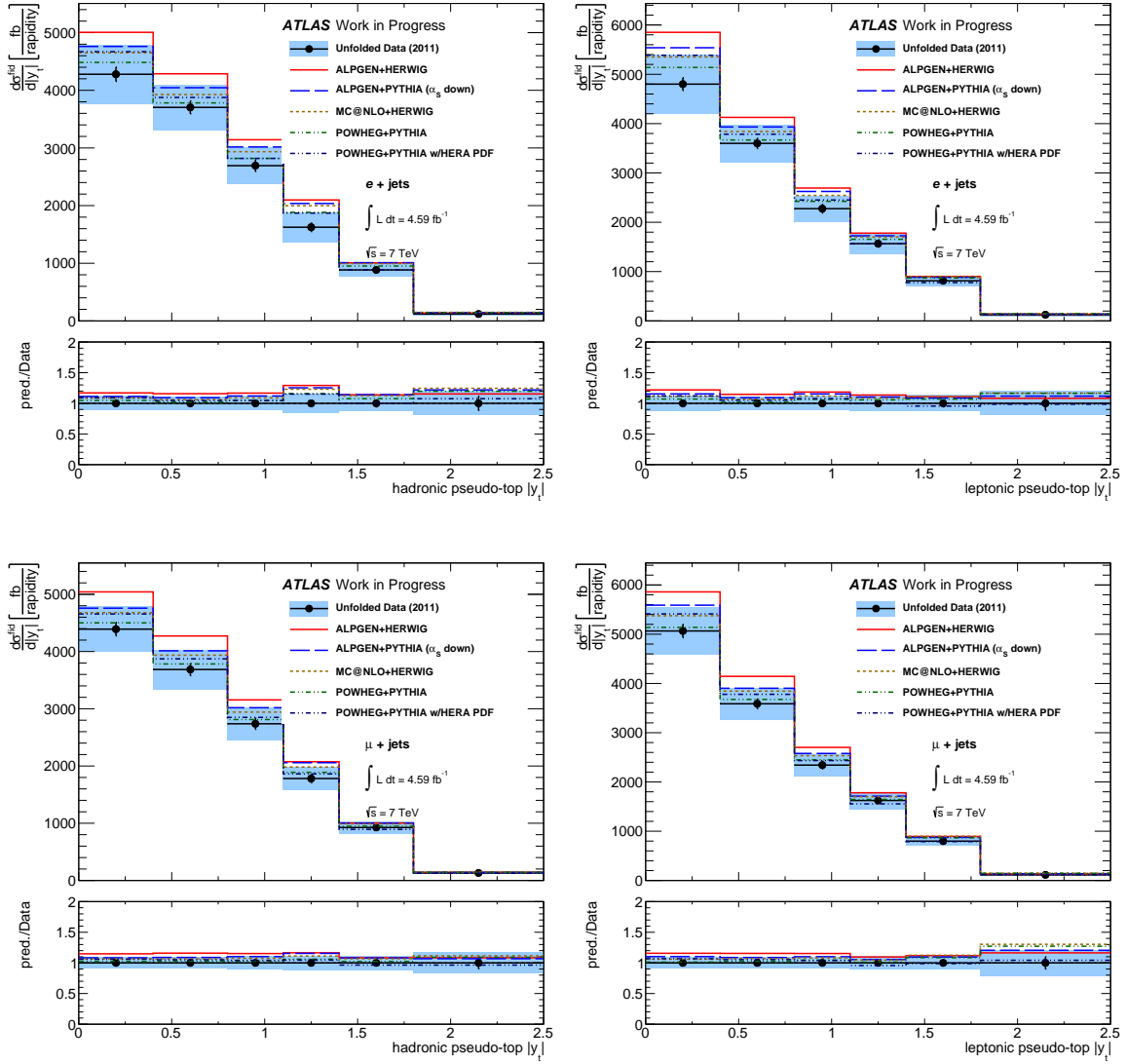


**Figure 6.6:** Unfolded and corrected distributions for (left to right) the hadronic and leptonic top distributions of top  $|y^t|$  in the electron (top) and muon (bottom) channels. The corrections used are derived from the POWHEG+PYTHIA  $t\bar{t}$  sample. Data points are shown with error bars for statistical uncertainties and error bands for total statistical and systematic uncertainties.

the estimate is given by

$$\hat{y} = \sum \alpha_i y_i \quad (6.5)$$

for some set of weighting factors  $\alpha_i$ . For this to be unbiased, assuming that  $y_i$  are unbiased, this implies

$$\sum \alpha_i = 1. \quad (6.6)$$

Finally, the variance for a given set of  $\alpha$  is given by

$$\sigma^2 = \alpha^T E \alpha, \quad (6.7)$$

so the BLUE technique is to simply minimise this equation by varying  $\alpha$  subject to the constraint 6.6. This can be solved analytically using the method of Lagrange multipliers to give

$$\alpha = (U^T E U)^{-1} E^{-1} U \quad (6.8)$$

where  $U$  is a  $n$ -vector with all entries unity. The  $\alpha$  can then be substituted back into equation 6.5 to give the estimate and 6.7 for the variance.

In our case, we are combining the electron and muon channels, and considering each bin of each distribution independently, so we have two measurements for each bin. The covariance matrix between the two channels is constructed by assuming zero or full correlation for channel-specific or common systematic uncertainty sources, respectively. That is, if the  $i$ th systematic source is only applicable to one of the channels, we construct a covariance matrix for that uncertainty of

$$\begin{pmatrix} \sigma_{e,i}^2 & 0 \\ 0 & 0 \end{pmatrix}, \begin{pmatrix} 0 & 0 \\ 0 & \sigma_{\mu,i}^2 \end{pmatrix} \quad (6.9)$$

for an electron or muon channel systematic respectively. For a systematic from a common source, we assume that the uncertainties between the channels are fully correlated

$$\begin{pmatrix} \sigma_{e,i}^2 & \sigma_{e,i}\sigma_{\mu,i} \\ \sigma_{e,i}\sigma_{\mu,i} & \sigma_{\mu,i}^2 \end{pmatrix}. \quad (6.10)$$

The full covariance matrix is then the sum of the individual sources of uncertainty  $E = \sum E_i$ . This matrix along with the data points from the channels  $y = (y_e, y_\mu)$  are then used in the BLUE method outlined above to give the combined result. Finally, the overall contribution of the  $i$ th systematic source  $\sigma_i$  to the final uncertainty can also be obtained from the method by calculating  $\sigma_i = \frac{\sqrt{\alpha^T E_i \alpha}}{\sqrt{\alpha^T E \alpha}}$ . The statistical uncertainties are treated as uncorrelated in the combination.

The uncertainties we take to be correlated are the JES components, jet efficiency, JVF and JER uncertainties, the data to MC uncertainties such as for the  $b$ -tagging scale factors, the lepton energy scale uncertainties, the  $E_T^{miss}$  uncertainties from pileup, the  $t\bar{t}$  modelling uncertainties, the PDF uncertainties and the luminosity uncertainty. The background components and MC statistical uncertainties are taken uncorrelated. The lepton efficiency uncertainties are only valid in the separate channels and so only included as an uncertainty component in the relevant distribution.

Figures 6.8 and 6.8 show the ratio of the electron and muon channels to the final combination for each bin of the analysis distributions for, respectively, the individual pseudo-top and the pseudo-top pair variables. The distributions can be seen to be in agreement with each within the uncertainties of the analysis, and slight reductions in the overall uncertainty can be seen after combination.

Results of the channel combination are presented in figures 6.12 to 6.15 for the pseudo-top  $p_T$  and  $|y^t|$ , and figures 6.9 to 6.11 for the pseudo-top pair distributions,  $m^{t\bar{t}}$ ,  $p_T^{t\bar{t}}$ , and  $|y^{t\bar{t}}|$  in comparison with several Monte Carlo simulation predictions. In appendix E, figures E.5 and E.6 present the combinations compared with the ALPGEN generator combined with different parton showers, and with the I/FSR up and down tunes. Figures E.3 and E.4 show the combinations and Monte Carlos normalised with respect to the cross-section. This enable us to compare just the shapes of the distributions. Also given in appendix D are tables for the contribution of each systematic source to the overall uncertainty.

## 6.4. Discussion

The individual top rapidity (figure 6.14 for the hadronic pseudo-top rapidity and figure 6.15 for the leptonic pseudo-top) is well described by all the MC samples in shape and mostly within uncertainties for the normalisation. The exception is the ALPGEN+HERWIG  $t\bar{t}$

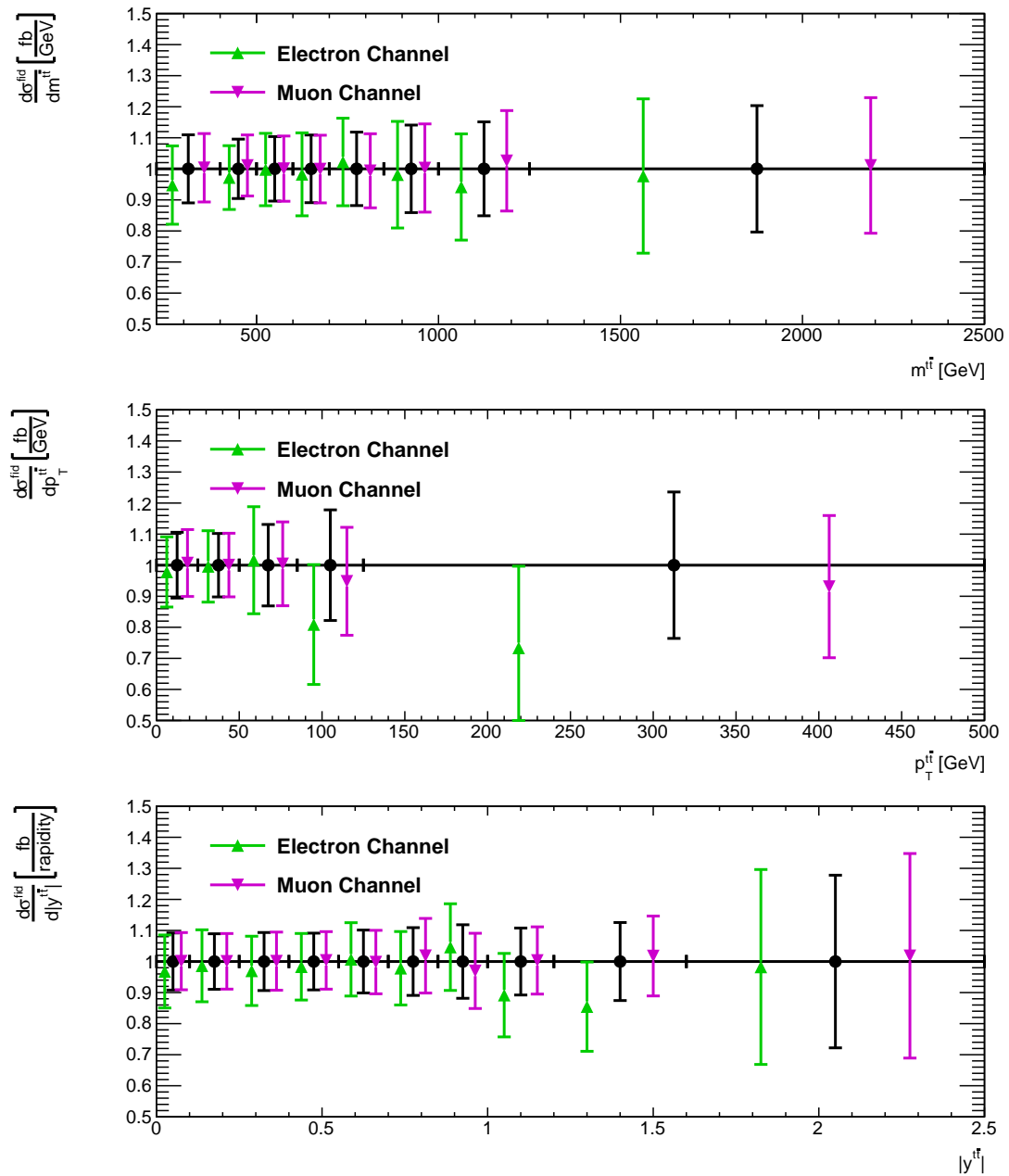


**Figure 6.7:** The ratio of the electron and muon channels to the output of the BLUE combination for the pseudo-top pair (top to bottom) mass,  $p_T$  and rapidity.

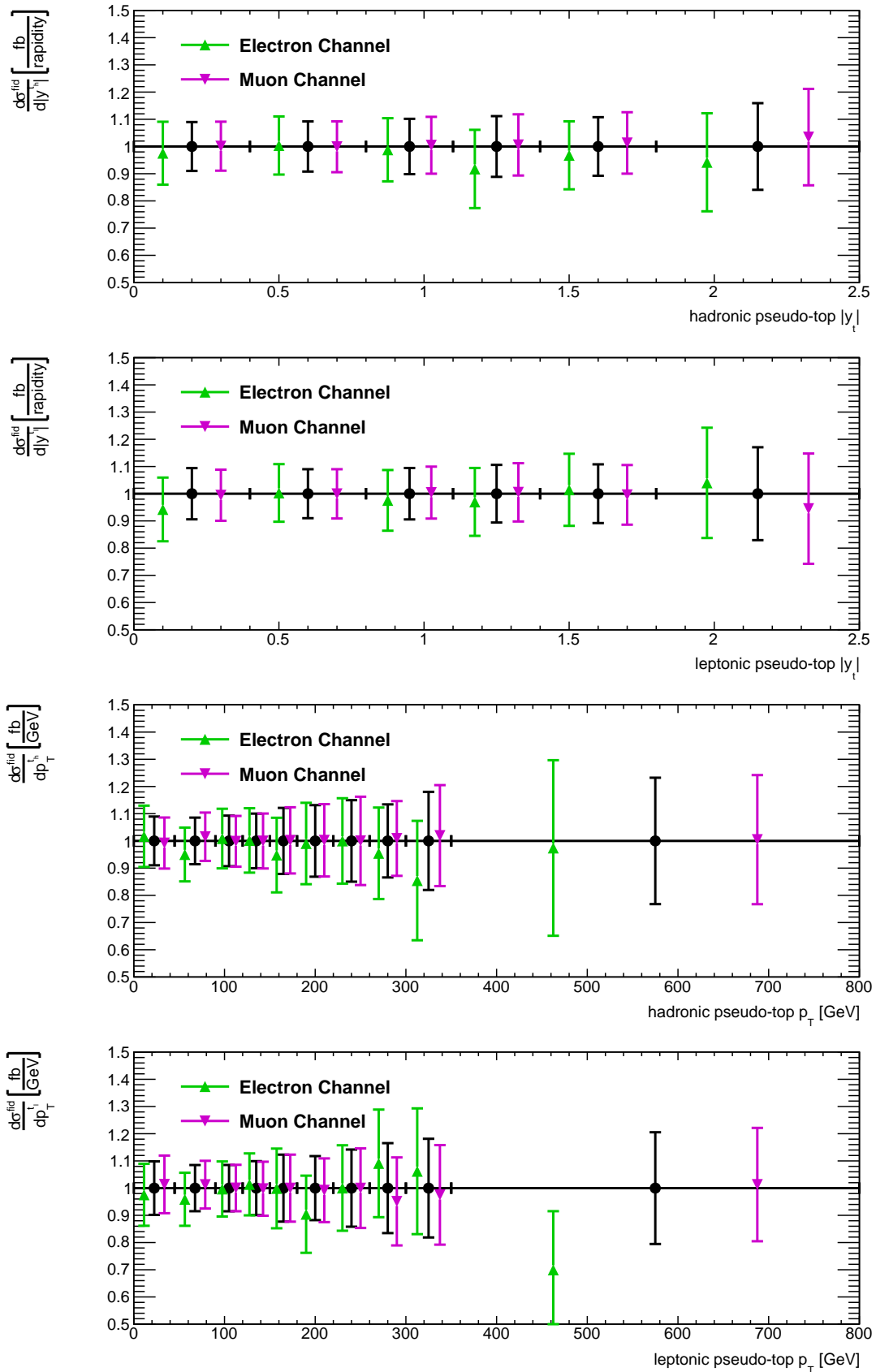


**Figure 6.8:** The ratio of the electron and muon channels to the output of the BLUE combination shown for the individual pseudo-top (top to bottom) hadronic rapidity, leptonic rapidity, hadronic  $p_T$ , and leptonic  $p_T$ .

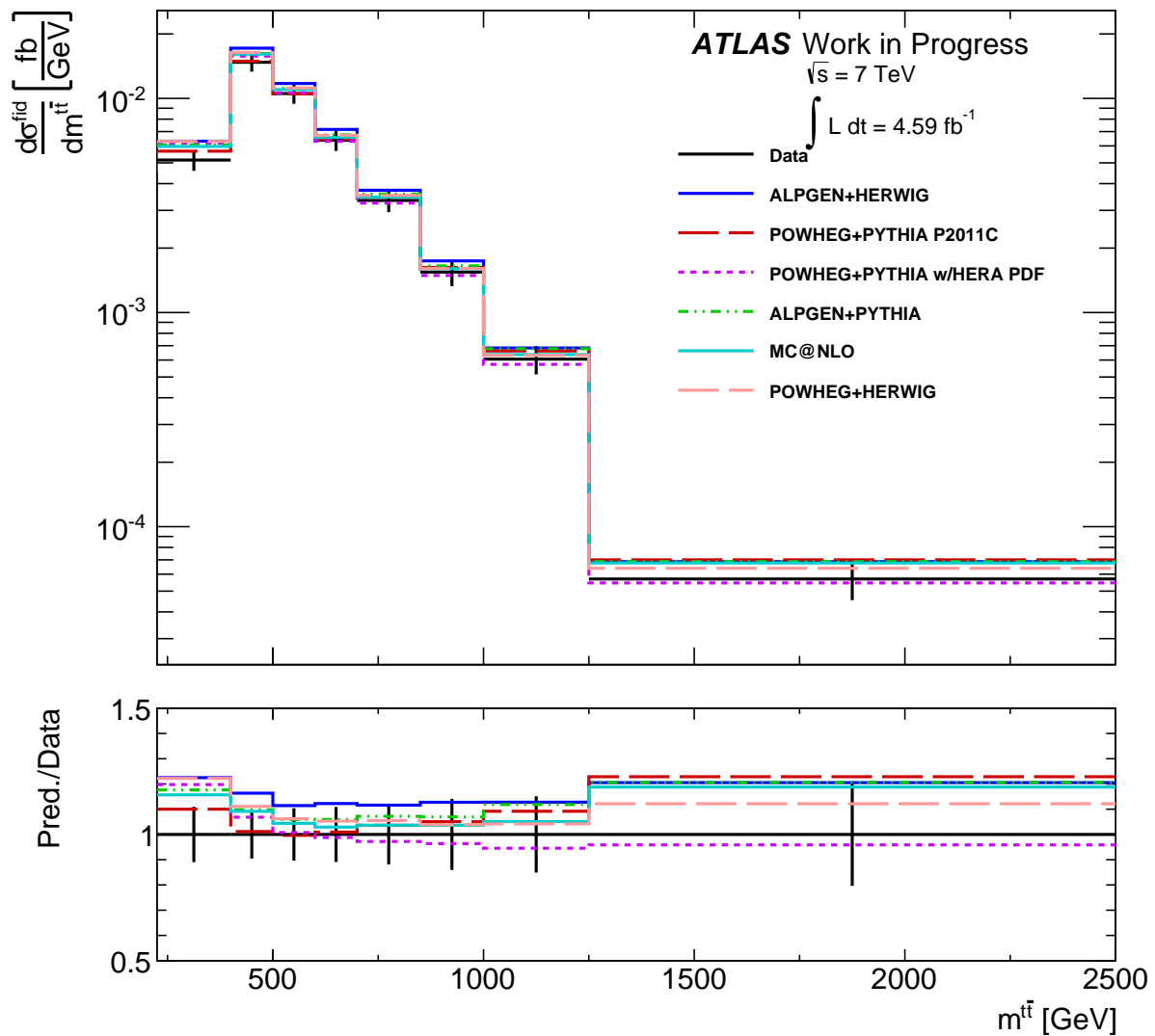


**Figure 6.9:** The fiducial differential  $t\bar{t}$  cross-section for pseudo-top pair  $m^{t\bar{t}}$  after the combination of electron and muon channel results compared against several  $t\bar{t}$  models predictions, which are shown in ratio against the data in the bottom figure. The data points are shown with the associated combined systematic and statistical uncertainties.

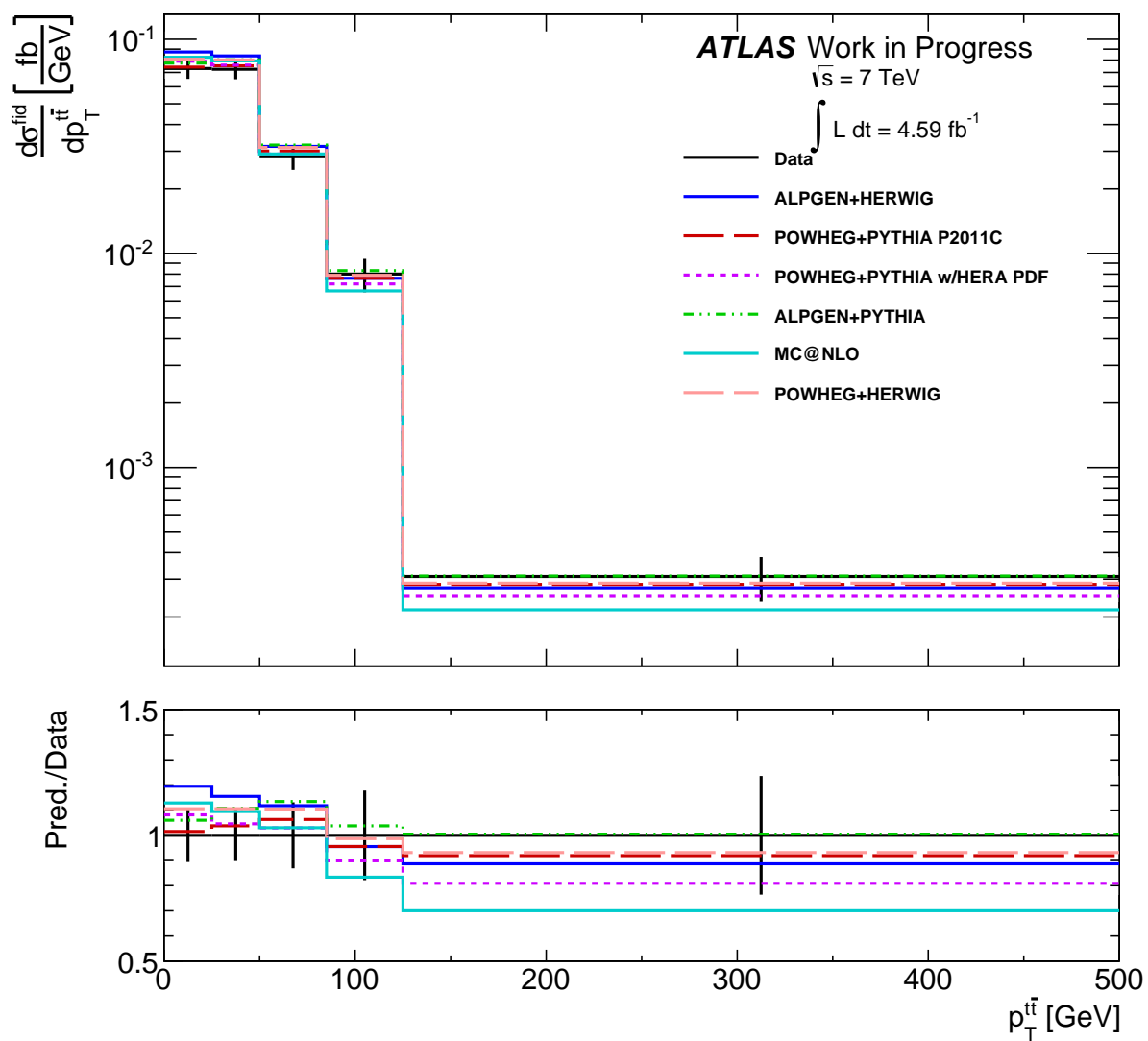


**Figure 6.10:** The fiducial differential  $t\bar{t}$  cross-section for pseudo-top pair  $p_T^{t\bar{t}}$  after the combination of electron and muon channel results compared against several  $t\bar{t}$  models predictions, which are shown in ratio against the data in the bottom figure. The data points are shown with the associated combined systematic and statistical uncertainties.

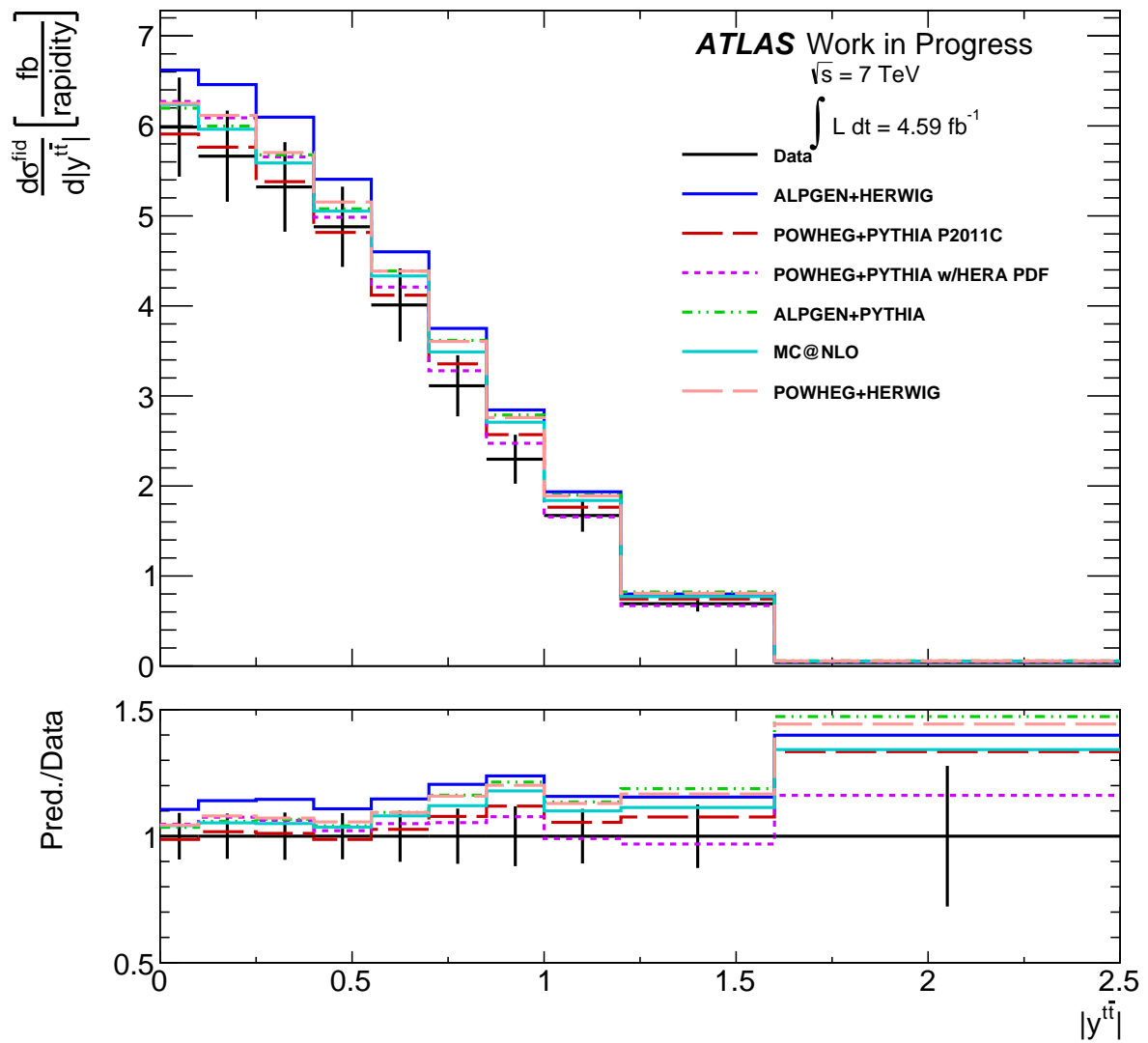


**Figure 6.11:** The fiducial differential  $t\bar{t}$  cross-section for pseudo-top pair  $|y^{t\bar{t}}|$  after the combination of electron and muon channel results compared against several  $t\bar{t}$  models predictions, which are shown in ratio against the data in the bottom figure. The data points are shown with the associated combined systematic and statistical uncertainties.

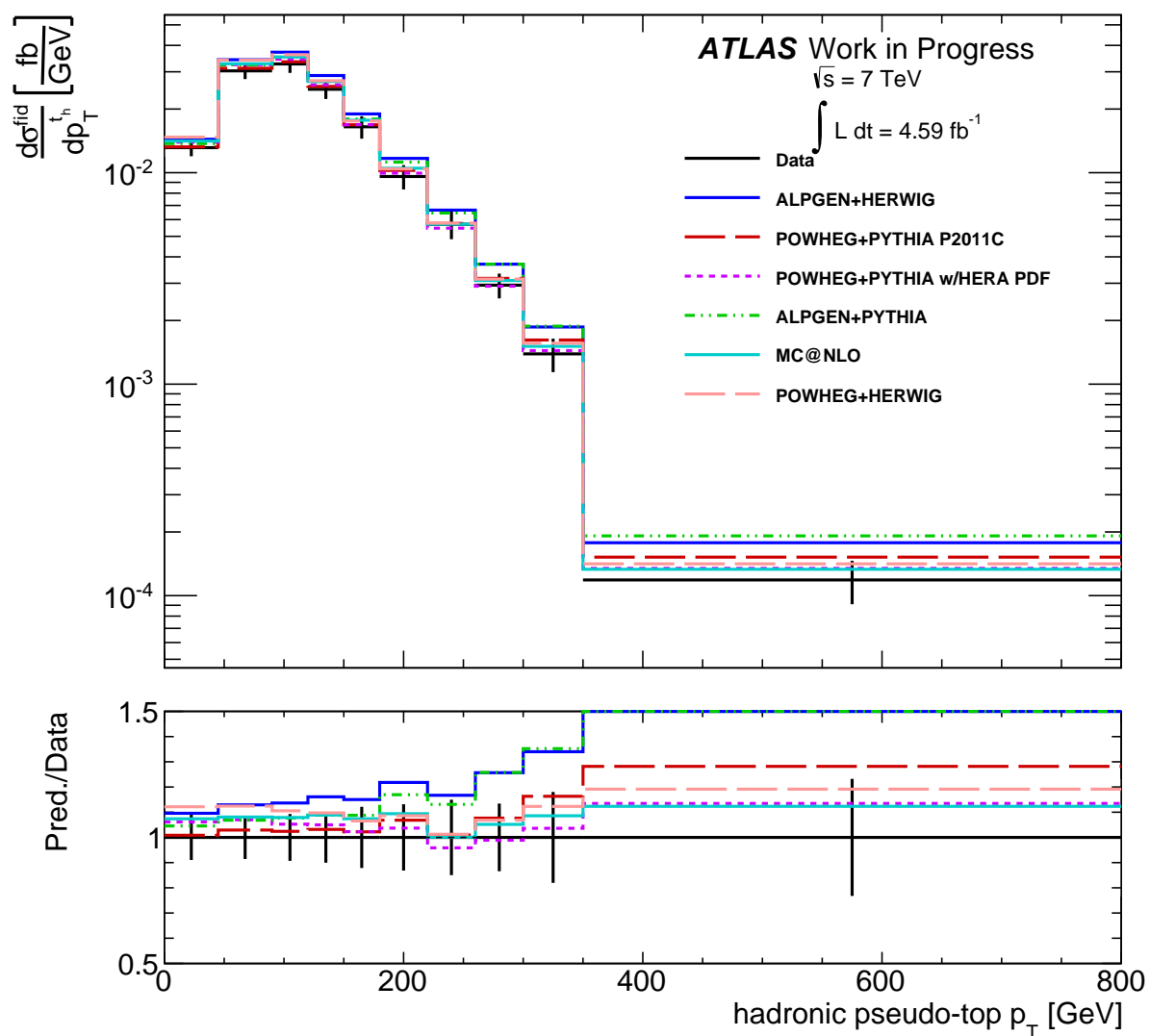


**Figure 6.12:** The fiducial differential  $t\bar{t}$  cross-section for individual pseudo-top kinematics  $p_T^t$  for the hadronic top after the combination of electron and muon channel results compared against several  $t\bar{t}$  models predictions, which are shown in ratio against the data in the bottom figure. The data points are shown with the associated combined systematic and statistical uncertainties.

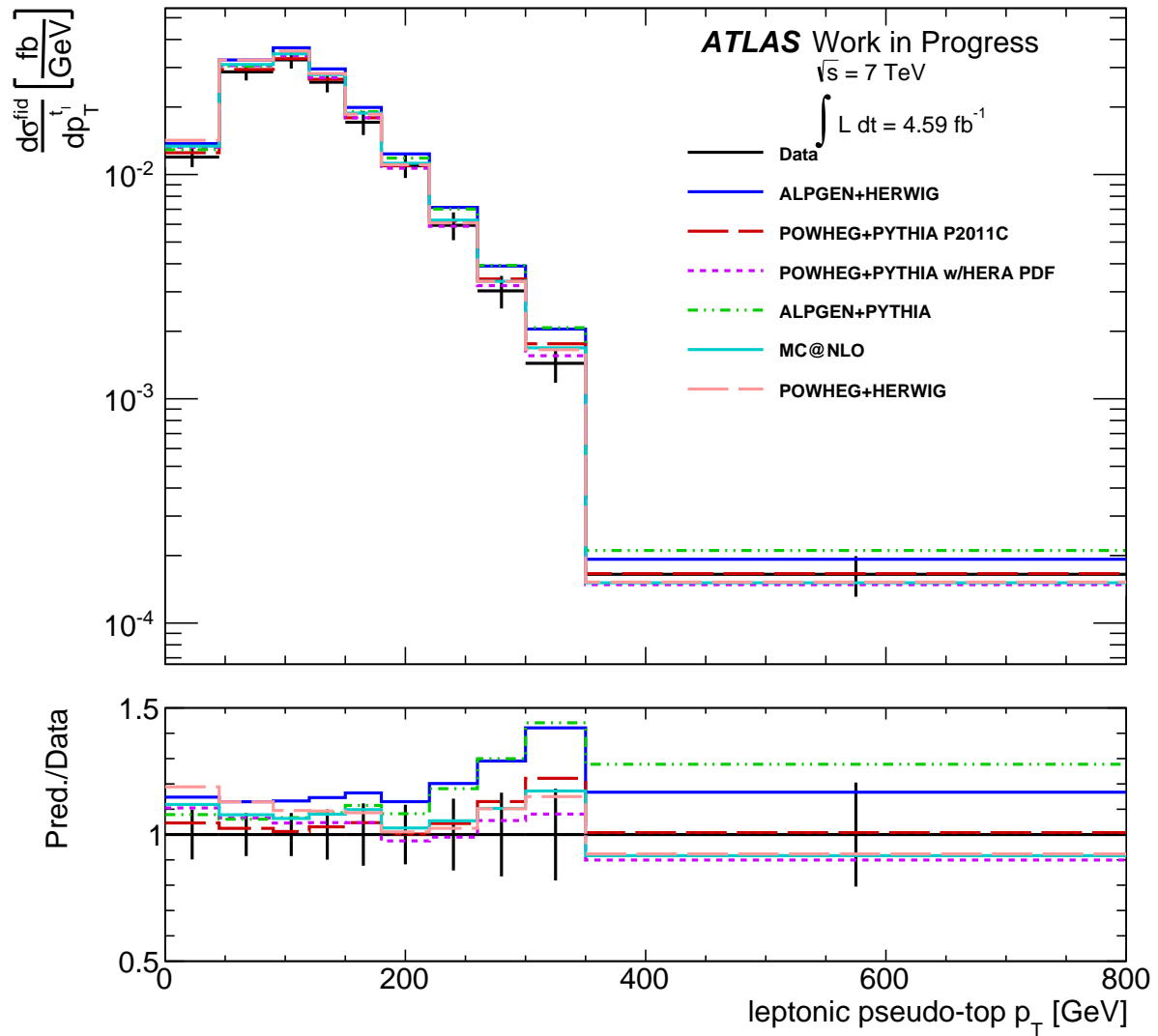


**Figure 6.13:** The fiducial differential  $t\bar{t}$  cross-section for individual pseudo-top  $p_T^t$  for the leptonic top after the combination of electron and muon channel results compared against several  $t\bar{t}$  models predictions, which are shown in ratio against the data in the bottom figure. The data points are shown with the associated combined systematic and statistical uncertainties.

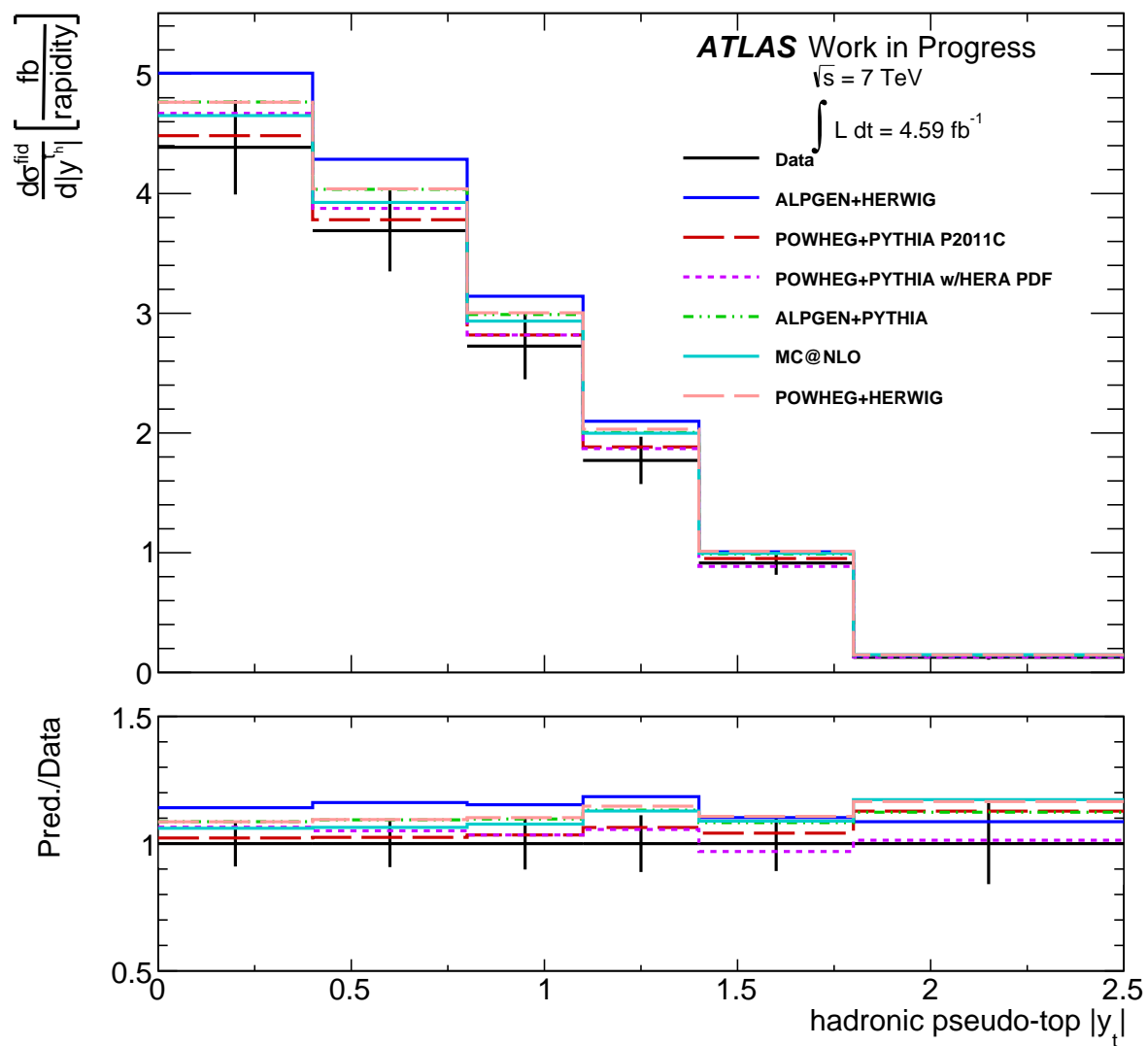


**Figure 6.14:** The fiducial differential  $t\bar{t}$  cross-section for individual pseudo-top  $|y_t^h|$  for the hadronic top after the combination of electron and muon channel results. The data points are shown with the associated combined systematic and statistical uncertainties.

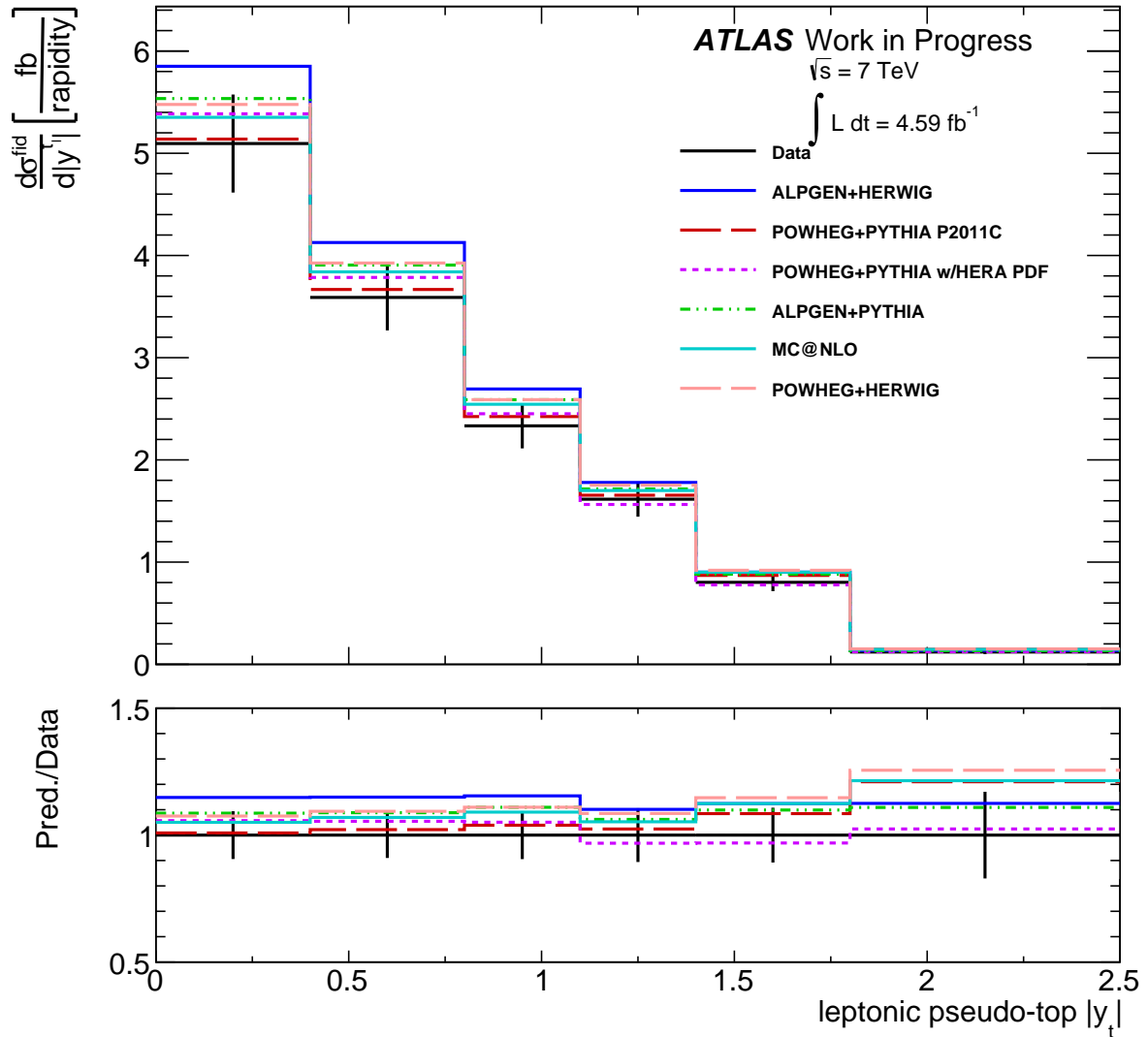


**Figure 6.15:** The fiducial differential  $t\bar{t}$  cross-section for individual pseudo-top  $|y^t|$  leptonic top after the combination of electron and muon channel results. The data points are shown with the associated combined systematic and statistical uncertainties.

sample, which has a higher normalisation than the other samples. As the samples are normalised to the same theoretical cross-section at parton-level, we can attribute this to the larger parton to particle-level acceptance for ALPGEN+HERWIG compared to the other MCs, which can be seen in figure B.6.

The individual top  $p_T$  is poorly described at high  $p_T$  for many of the samples. While generally, the distributions are within the uncertainties of the analysis, there is a systematic tendency to predict a higher cross-section than the data in the high  $p_T$  region for the ALPGEN  $t\bar{t}$  samples and one of the POWHEG+PYTHIA  $t\bar{t}$  sample. The POWHEG+PYTHIA  $t\bar{t}$  sample with the HERA PDF best describes the top  $p_T$  spectrum, while the POWHEG+PYTHIA with the P2011C tune sample begins to overestimate the high  $p_T$  regime. This implies that the HERA PDF, which predicts a softer gluon PDF, is a better description of the data than the currently used CT10 PDFs. This also implies that the data will provide useful inputs for the PDF fitting groups to use to adjust their gluon PDFs.

The  $t\bar{t}$  system variables are not, in general, as well predicted as the the kinematic variables of the individual top quarks. All the MCs over-predict the low  $m^{t\bar{t}}$  region (figure 6.9). This implies that the threshold region description used by the MCs is inadequate and higher order corrections need to be taken into account in order to fit this regime. The low mass  $m^{t\bar{t}}$  phase space is in any case hard to predict since at threshold soft gluon corrections become important and the resummation terms, hard to calculate within the MCs, dominate. The POWHEG+PYTHIA with HERA PDF sample here slightly underestimates the data at high  $m^{t\bar{t}}$ , while the other samples overestimate it. This is consistent with the HERA PDF predicting a softer gluon PDF (implying lower average centre of mass energy since the gluon PDF dominates production) than the other samples. All the samples, however, are within the  $1\sigma$  uncertainties of the measurement at high  $m^{t\bar{t}}$ .

The shape of the  $|y^{t\bar{t}}|$  distribution (figure 6.11) is generally well predicted for low  $|y^{t\bar{t}}|$ , but all the samples over-predict the high  $|y^{t\bar{t}}|$  region, again with the exception of the HERA PDF POWHEG+PYTHIA sample which provides a good prediction of the data across the entire  $|y^{t\bar{t}}|$  spectrum. Given that for  $|y^{t\bar{t}}| = 0$  it is required (at leading order), that  $x_1 = x_2 = m^{t\bar{t}}/\sqrt{s}$ , and that the more extreme the  $|y^{t\bar{t}}|$ , the further apart the two values of  $x$  become, this is again showing that the softer high- $x$  gluon spectrum of the HERA PDF sample gives a better description of the proton than the other PDFs.

The  $p_T^{t\bar{t}}$  spectrum (figure 6.10), as noted previously, is sensitive to the overall extra radiation produced in the parton collision process. The spectrum is poorly modelled by the MC@NLO+HERWIG sample, which predicts that the  $p_T^{t\bar{t}}$  should be larger at low  $p_T^{t\bar{t}}$  and smaller at high  $p_T^{t\bar{t}}$ . This trend is also present in the POWHEG+PYTHIA HERA PDF sample, though the prediction remains within  $1\sigma$  uncertainty of the measurement. This trend is also present in the ALPGEN+HERWIG  $t\bar{t}$  sample. The ALPGEN+PYTHIA and POWHEG+PYTHIA  $t\bar{t}$  samples with the Perugia tune both give good predictions of the data distribution. The Perugia tune of POWHEG+PYTHIA  $t\bar{t}$  was explicitly fitting data to achieve good descriptions of Initial and Final State Radiation, so as it is the only NLO sample to give a good description of this distribution, it implies that the distribution will be particularly useful for fitting the phenomenological radiation parameters in future MC tunes. The calculations of  $p_T^{t\bar{t}}$  are also only available to leading order, since it requires an additional parton, so the NLO generators will only include a tree-level Feynman diagram for this process. Thus, the difference may also be due to higher-order effects. There is an ongoing effort to produce differential distributions at NNLO, so this distribution is potentially an interesting test of the effect of higher-order corrections.

Ultimately, however, the utility of the measurements is not the comparison between the samples currently in use at ATLAS, but to allow for new generator parameter and PDF fits to be made based on the results presented. The deviations of the samples from the data show that there is scope for the results to be used in future tunes of the MCs that will be of benefit in future measurements which require detailed description of top production kinematics. This includes both precision measurements of the top quark, as well as searches and measurements where the top is a dominant background and where more precise top MCs would reduce the background uncertainty of the analysis. To facilitate this, a suitable function has been made for Rivet (discussed in section 5.2), which should allow automatic parameters fitters, such as Professor [190] to be able to use the data in future tunes.

## 6.5. Extrapolation to top partons

The final result that we present is the extrapolation of the fiducial cross-section to parton level. As mentioned, unlike previous results, this is not the main result being presented, but instead is done to allow quick cross checks with parton level calculations and for

comparison to the recent top parton measurements [171]. The POWHEG+PYTHIA  $t\bar{t}$  MC sample was used to derive bin-by-bin correction factors that were used to extrapolate from the pseudo-top measurements. The extrapolation factor used was defined as

$$C_i = N_i^{parton} / N_i^{particle} \quad (6.11)$$

where  $N_i^{parton}$  is the number of parton-level events with the parton-top variable in the bin range, and  $N_i^{particle}$  the number of particle level events with pseudo-top variable falling in the bin range for a given measurement variable. The POWHEG+PYTHIA  $t\bar{t}$  MC sample used to derive this cross-section did not include fully hadronic  $t\bar{t}$  events and we further restricted our signal definition to semi-leptonic events with the lepton being an electron, muon or tau decaying to an electron or muon. Therefore, an additional correction of  $1/0.378$  was applied to account for the branching fraction of these events.

For the top-pair variables:  $m^{t\bar{t}}$ ,  $p_T^{t\bar{t}}$ , and  $|y^{t\bar{t}}|$ , the electron and muon fiducial cross-sections were corrected to the parton level and then the two channels combined using the method of the previous section. For the top variables:  $p_T^t$  and  $|y^t|$ , at the parton level, before the top has decayed, there is no distinguishing the hadronic and leptonic tops. Thus, all of the pseudo-top distributions were corrected to the parton level using the individual correction factors for the given top decay-type and lepton channel, and then the four distributions were combined into a single result. Figure 6.17 shows the final results of the measurements to the parton level compared with several Monte Carlo predictions.

In figure 6.16, the parton level analysis distributions from the dedicated parton level analysis performed at ATLAS [171], and our distributions corrected to the parton level are displayed. The parton level analysis distributions are multiplied by the overall cross-section of our distribution to display them unnormalised. Due to the parton-level analysis correcting to normalised distributions, many systematics which only cause shifts in the overall normalisation cancel out in their analysis. No attempt has been made here to include these systematics, and therefore the uncertainties shown in the figure for the parton-level analysis are artificially smaller than those for our analysis. Similarly, no attempt has been made to estimate the size of the uncertainties of our analysis due to the particle to parton-level acceptance correction differences between the various  $t\bar{t}$  MCs. The figure shows good agreement between the two analysis methods with our results in accordance with the dedicated parton-level result. It should be noted that as the binnings in the analyses are different, and so one must be careful when interpreting the

figures to average across the bins where we have presented finer details. In particular, for the top-pair mass distribution the first two points of the parton-level analysis (in red) are of similar height, while our first two points jump from low to high. This is an effect of our smaller binning being on the edge of a rise in the expected cross-section, while the first data point of the parton analysis averages the first bin and a half of our analysis and therefore lies between them, similarly with the second bin of the parton-analysis.

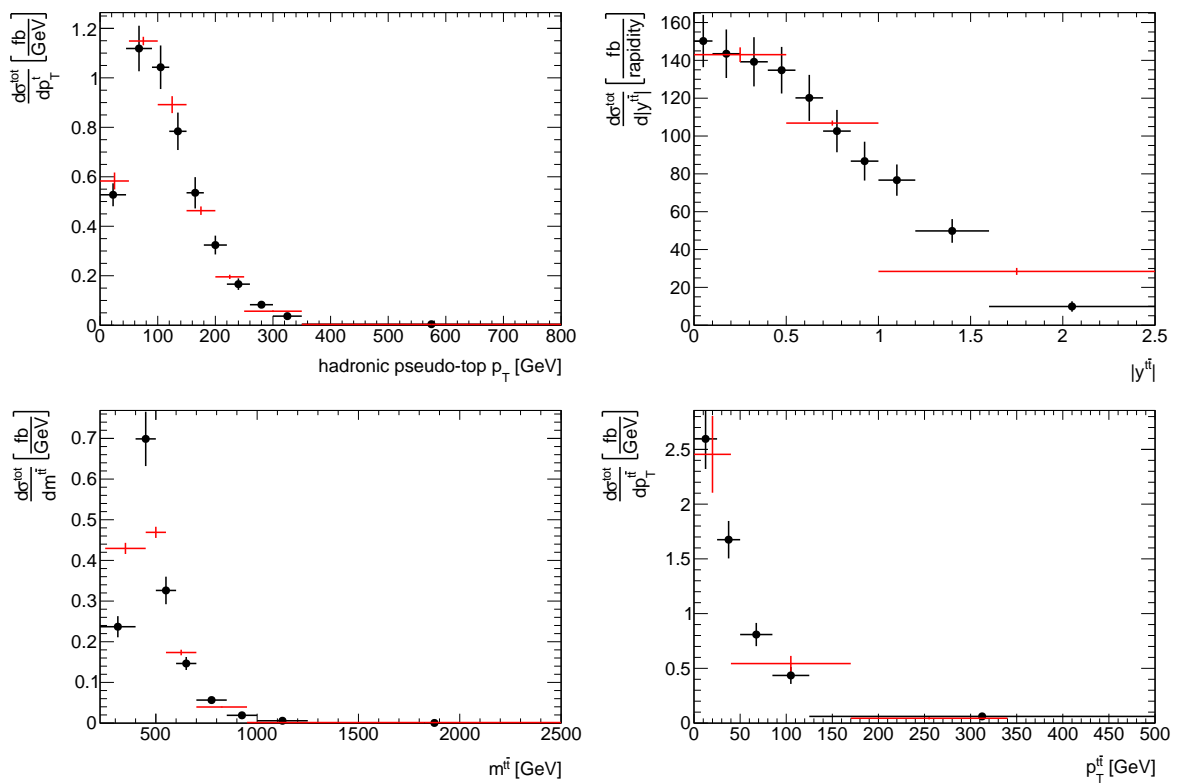


**Figure 6.16:** The  $t\bar{t}$  production cross-section after channel combination as a function of the leptonic-hadronic pseudo-top system (a) rapidity, (b) mass and (c)  $p_T$ . The data points are shown with the total statistical and systematic uncertainties. The data are compared with the parton level analysis results normalised to be the same as our distribution.

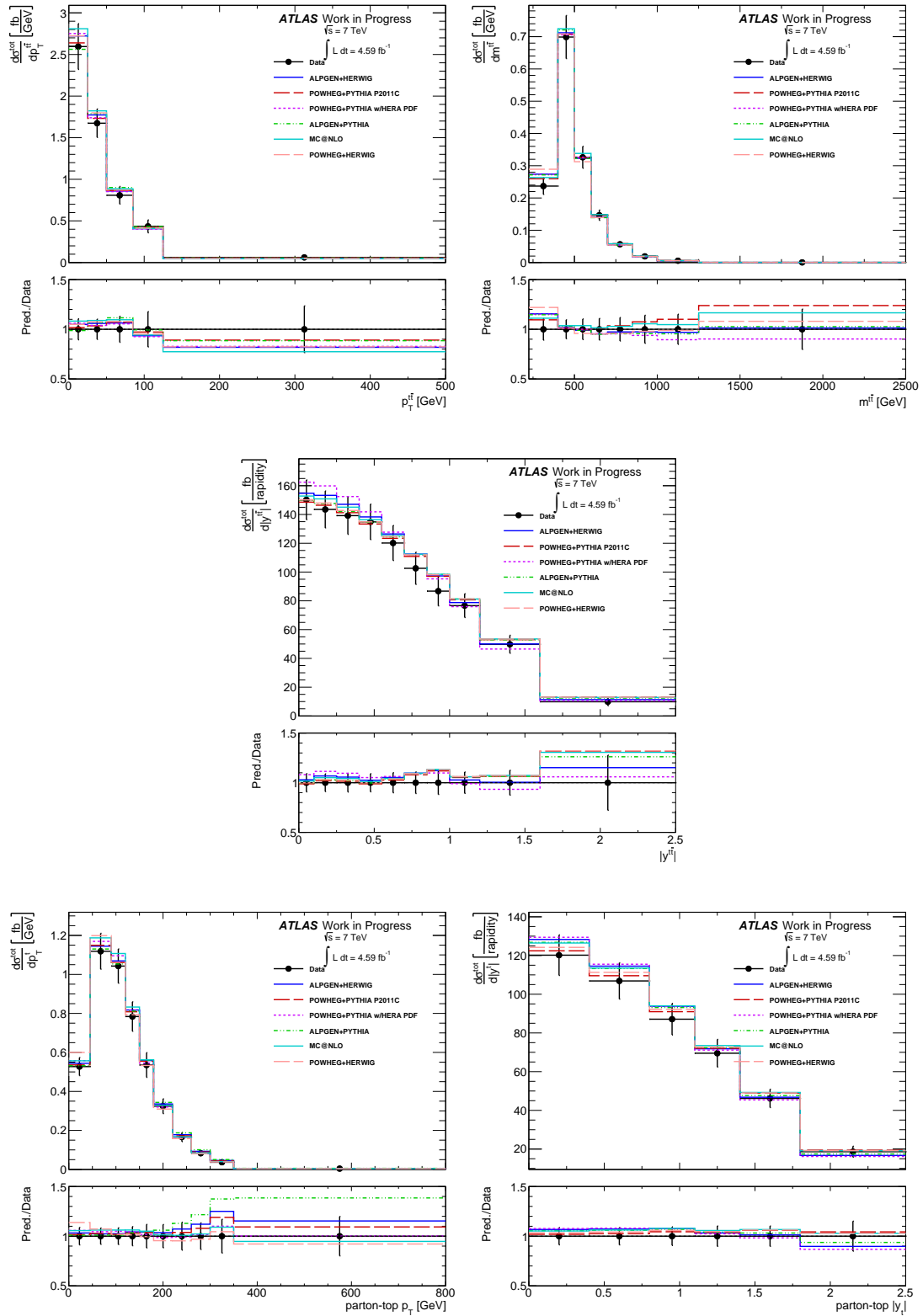


**Figure 6.17:** The inclusive  $t\bar{t}$  cross-section is shown after channel combination and extrapolation to the parton level, and in comparison to several MC generator predictions. The data points are shown with the total statistical and systematic uncertainties from the particle level unfolding. No model dependence uncertainty due to the parton level extrapolation is added.



# Chapter 7.

## Conclusion

The successful operation of the LHC since 2010 has given particle physicists an incredible opportunity to probe their theories at the highest energies ever achieved by a particle collider. This is most evident by the discovery of the Higgs boson, and therefore confirmation of the Higgs mechanism, by the ATLAS and CMS experiments in 2012. It also allowed broad, detailed studies of the known SM physics, such as the differential top cross-section analysis presented in this thesis using the 2011  $\sqrt{s} = 7$  TeV ATLAS dataset.

Where previous measurements sought to present the top-pair differential cross-sections corrected through to the top parton level, this analysis has taken a more conservative approach in the analysis of the data. This approach seeks to address the limitations of previous measurements, as requested by the theoretical community. In particular, we have presented an analysis of proxy observables related to the top decay. These “pseudo-top” observables are definable completely independently of the simulation description of the top. This has allowed us to avoid correcting the observables for effects only describable by theory or phenomenological models, some of which the measurements actually seek to constrain. It has also allowed us to present, for the first time, differential measurements of the top quark at the fiducial level – the experimentally accessible phase space of top quark decays. This allows us to avoid large, theory-dependent corrections into regions of phase space that cannot be probed by the detector. These considerations together should allow for more robust interpretations of the analysis results presented by the theory community than has previously been allowed.

After briefly reviewing the theory of top quarks (chapter 2) and the experimental setup of ATLAS on the LHC (chapters 3 and 4), we have presented in this thesis a set of observables for top pair production events which can be used for differential kinematic

studies (in chapter 5). The observables are applicable at the reconstruction and particle levels, and are independent of the parton-level definition of the top. We have called these observables “pseudo-top” to distinguish them from existing measurements extrapolating to the parton-level top, and to emphasize that the constructions are not directly related to the partonic top propagator. The observables are then useful for generator tunings of top production and fits of the proton parton distribution functions (PDFs). In particular, the gluon PDFs are currently only loosely constrained at large  $x$ , which is an important regime for top-pair production.

We then presented (in chapter 6) the first measurement of the pseudo-top observables. We measured the fiducial cross-section as a function of the differential pseudo-top  $p_T^t$ ,  $|y^t|$  and pseudo-top pair  $|y^{t\bar{t}}|$ ,  $m^{t\bar{t}}$ ,  $p_T^{t\bar{t}}$  using the 2011 ATLAS  $\sqrt{s} = 7$  TeV proton–proton collision data set with the complete evaluation of the systematic uncertainties. We compared the results to several models which are currently in use by the ATLAS experiment to model the production of top-pair events. We showed that no single one of these Monte Carlos currently reproduces all of the features of the distributions. The POWHEG+PYTHIA  $t\bar{t}$  sample produced with HERA PDF, however, gives the best description across most of the distributions. The discrepancies we find show that the results will be useful inputs for future tunings of the Monte Carlos and for improving the fits of the proton PDFs. As well as being useful for testing the predictions of perturbative QCD and for modelling the top for other top physics analyses, top production is generically an important background for new physics searches. These searches will therefore also benefit from better descriptions of the top production process through a reduction of the top modelling systematics, which the results of this thesis provide.

## 7.1. Future Work

There are several directions that this work may be taken from the baseline established in this thesis. In 2012, ATLAS collected  $20 \text{ fb}^{-1}$  of data from LHC proton–proton collisions with  $\sqrt{s} = 8$  TeV. At 8 TeV, the top cross-section also increases to  $240 \text{ pb}$  [191], so there is an order of magnitude more top events in the 2012 dataset than in the 2011 7 TeV data. As well as repeating the measurements presented in this thesis, the extra data would allow for doubly-differential measurements to be performed. For example, a measurement with respect to the top’s or top pair’s  $p_T$  and rapidity could be made simultaneously. This would provide better sensitivity to the gluon PDF which is dependent on both of

these quantities. Further reduction in the systematics is also possible in this dataset, since several of the sources of systematic uncertainty are estimated using data-driven techniques. For example, the b-tagging uses dileptonic top events to estimate the tagging efficiency uncertainties, so a larger dataset would allow these uncertainties to be reduced. Another route is to provide results of the ratio of 8 TeV to 7 TeV data. This allows a more robust theoretical interpretation of the results, since many of the theory uncertainties cancel in the ratio [162]. Similarly, the LHC is due to restart in 2015 with  $\sqrt{s} = 13$  TeV proton–proton collisions, and run at this energy for several years. This will bring both an additional increase in the cross-section for top pair production to 950 pb [69] and an expected order of magnitude more collision data. This would again allow the measurements to be performed at new energies with larger datasets, so the techniques presented in this thesis are the start of a programme of measurements which will continue to probe our understanding of the top quark for the next several years.



# Appendix A.

## Inner Detector Studies for the ATLAS Phase-II Upgrade

As of 2013, the LHC has provided  $5 \text{ fb}^{-1}$  of  $\sqrt{s} = 7 \text{ TeV}$  and  $20 \text{ fb}^{-1}$  of  $\sqrt{s} = 8 \text{ TeV}$  proton–proton collisions. The 2013–2014 shutdown is the first (Long Shutdown 1 or LS1) of a series of planned shutdowns, in which both the LHC machine and the detectors on the beamline will be upgraded. When collisions restart in 2015, the repairs to the LHC will allow it to deliver either 13 or 14 TeV collisions to the detectors. This period (Phase 0) will continue until 2018, when Long Shutdown 2 (LS2) will start and a new linear accelerator injector, LINAC4, will replace the current injector and the PS Booster upgraded to provide lower emittance. This will allow higher luminosities of around  $2 - 3 \times 10^{-34} \text{ cm}^{-2} \text{ sec}^{-1}$  during the subsequent phase I running of the LHC. A final shutdown (Long Shutdown 3) is then planned for 2022 when the LHC will be upgraded to the High Luminosity LHC (HL-LHC), which will deliver an instantaneous luminosity of approximately  $5 \times 10^{-34} \text{ cm}^{-2} \text{ sec}^{-1}$  during the subsequent Phase II operations. Phase 0 is expected to deliver a total luminosity of 50–100  $\text{fb}^{-1}$ , Phase 1 300–400  $\text{fb}^{-1}$  and Phase 2 3000  $\text{fb}^{-1}$  over the lifetime of the experiments. For each of these shutdowns, the ATLAS detector will also undergo upgrades so that it may maintain or improve performance with the higher pileup that the increased luminosity will entail. In particular, this chapter deals with the proposed new Inner Detector which will be installed in ATLAS during LS3. First, the ATLAS upgrades proposed for the shutdowns will be briefly outlined, then the initial, preliminary design and study of the proposed new tracker will be presented in the context of these upgrades. This work was performed as part of the mandate of the ATLAS Layout Task Force and is also documented in [192].

## A.1. The ATLAS Upgrade Schedule

A new innermost pixel layer is currently being constructed (as this is being written during LS1) as the first major upgrade of the ATLAS detector since operations began. This is the Insertable B-Layer (IBL) [193]. For the IBL upgrade, the beampipe is being replaced by a thinner, lighter beampipe, and a layer of pixels will be inserted between the new beampipe and the current innermost pixel layer. Since it gives a charged particle measurement closer to the interaction point, the IBL allows better vertexing resolution and therefore superior b-tagging performance. It also keeps the tracking robustness high in the face of failures. Since the pixel layers closest to the interaction point experience the highest radiation, they degrade faster than the outer layers. Therefore, the IBL will then compensate for these radiation-induced losses. It benefits from new technologies, and so is also more radiation hard and has fewer radiation lengths than the previous pixel layers, and so will stay performant over a longer period without adding a significant amount to the material budget (the IBL radiation length is 60% of the current pixel B-layer). The IBL will be integrated into the detector in time for the Phase 0 2015 LHC restart.

During the next shutdown, LS2 in 2018, ATLAS will undergo the “Phase I upgrade” [194]. During this phase, several of the detectors will be upgraded in order to exploit the luminosity increase provided by the LINAC4 upgrade. The granularity of the calorimeter information at the Level-1 trigger will be increased by installing new read-out boards in the EM and forward calorimeters and new muon triggers and tracking detectors will be installed in the forward direction. These upgrades will allow the ATLAS trigger to maintain low  $p_T$  lepton trigger thresholds at the larger expected luminosities.

Finally, during LS3 in 2022, the “Phase-II Upgrade” of ATLAS will be an extensive detector replacement and upgrade in order to maintain performance during the HL-LHC era [195]. The largest upgrade will be the complete replacement of the inner tracking detector, which is described in the remaining sections of this chapter.

A second major upgrade for Phase II is that of the trigger system. To cope with the intense luminosity expected from the HL-LHC, the complete trigger chain is planned to be replaced. The hardware L1 trigger will be split into two, a Level 0 and Level 1 trigger system, both on the hardware. The Level 0 will be approximately equivalent to the current L1; that is, it will use information from the EM and hadronic calorimeters

and muon spectrometer to make the initial trigger decision. The increase in luminosity means that the L0 trigger needs to operate at 500 kHz.

The L0 information will then be fed to the hardware-based Level 1 trigger, which adds hardware pattern-recognition to the inner detector to be able to perform tracking in the regions of interest defined by L0. This track information is then used for the L1 decision, and so the trigger will be able to do an initial electron and muon reconstruction and isolation test, b-tagging, and so on, at the hardware level. The L1 trigger will also use the full calorimeter granularity and the full MDT information from the muon spectrometer, which is restricted to the higher level triggers in the current ATLAS detector. It is expected that the L1 trigger will reduce the event rate to 200 kHz. The L1 information will then be passed to the high level trigger, which is expected to operate at an output rate of 5–10 kHz.

In order to accommodate the extra information needed by the hardware triggers, both the LAr and tile calorimeters will have the front end electronics replaced. In the LAr calorimeters, there will be a complete change of architecture: the hardware triggers will be moved to dedicated boards off the detector. This means that the trigger electronics will not be exposed to intense radiation, and therefore not degrade, and as well can be easily replaced as technology improves. This also implies that all the data recorded from the calorimeter will need to be transferred off the detector. This will require high transfer lines, outputting around 140 Tbps. Since the data is transferred off the detector, it also means there are no space limitations for the hardware triggers. This allows the full detector granularity to be used at L1. In the tile calorimeters, the front end will be replaced to adapt it to the L0/L1 split.

In the muon spectrometer, the front-end electronics will also be replaced. This is because the current information from the RPC and TGC detectors is not sufficient to keep the trigger rates sufficiently reduced to cope with the increased luminosity. Therefore, the MDT front-end electronics will be replaced to allow them to be used in the new hardware trigger chain.

## A.2. Inner Detector Requirements

The increase in luminosity provided by the HL-LHC comes with a corresponding increase in the pileup. It is expected that the mean number of pileup events per bunch crossing

will increase to  $\langle\mu\rangle \approx 140$ . For this level of pileup, the expected TRT occupancy will make it inadequate for track recognition. Also, by the time of the Phase-II upgrade, the current inner detector will have been in service for a decade, approximately the design lifetime of the inner detector layers due to accumulated radiation. The entire Inner Detector will therefore be replaced as part of the Phase-II upgrade. The detector is currently being designed as an all-Si tracker.

A highly performant tracker is key to the ATLAS physics program, and so the design of the upgrade to the tracking system needs careful consideration. The design study of the current chapter was performed in the context of preparing a preliminary simulation to be used in the Phase II Letter of Intent [195], which is distributed to funding agencies as the case for the upgrade. As such, it was decided to maintain a traditional barrel and end-cap design. Other, novel tracking layout proposals were welcome, but were not fleshed out in detail. Based on the experience from the initial running of ATLAS from 2009 – 2013, several design criteria have been formulated for the tracker upgrade.

The first point concerns the excellent tracker performance during this initial run period. As such, the goal of the upgrade is that the performance should not degrade. This is a more lofty goal than it might first appear, because tracking in the high pileup environment of Phase-II will need a more granular and more radiation resistant tracker than at present. This is required to allow robust pattern recognition performance to keep the fake rejection rate high, while maintaining excellent track reconstruction efficiency. From the current inner detector operations, at least 11 hits are judged necessary for good fake rejection. Including detector inefficiencies and hit misses from non-instrumented areas, the effect of modules damaged by radiation or other reasons, the design aims to allow 14 hits in the fiducial volume of the tracker. This requirement is to hold for both the nominal interaction point at the centre of the detector, and for points away from this point within 15 cm (nominally  $2\sigma$ ) along  $z$  of the interaction point. Adding the judgement based on current tracking performance that at least 4 pixel hits are required, this implies splitting the detector into 4 pixel layers close to the interaction point, and 5 double-sided Si strip layers further away from the interaction point. The 10 hits from the strip detectors also allow backtracking to enable photon conversion and bremsstrahlung recovery, as made done in the current detector by the TRT. The final hit should also be as close to the calorimeters as possible and of high precision, to allow an accurate extrapolation of tracks into the calorimetry. One of the major issues in tracking in the current detector is the distance between hits at high  $\eta$ , so the extrapolation distance between points across the entirety of the fiducial volume should be

kept to a minimum. Currently, there is also a mismatch in the tracking volume between the inner detector and the muon spectrometer: the inner detector tracks up to  $|\eta| < 2.5$ , while the muon spectrometer can reconstruct muons to  $|\eta| < 2.7$ . An additional design goal is to be able to match this tracking volume with the new detector, albeit with less traversed hits. Finally, the material budget should be kept to a minimum, both in order to minimize bremsstrahlung electrons and to keep the cost of the detector at a reasonable level. This final goal, of course, is at odds with the other criteria.

Several external constraints on the design have also been imposed. The inner pixel layers need to be removable separately from the rest of the inner detector. This is to facilitate extraction, since it is expected that over the course of the HL-LHC, the high levels of radiation that these layers will be exposed to means that these layers will need to be replaced. This implies that the inner layers will be contained in a support tube, the Inner Support Tube (IST), which traverses the length of the detector, so that these layers may be removed by removing the IST. For similar reasons, it was imposed that the entire pixel detector should be removable separately from the strip detectors, and are to be placed in a Pixel Support Tube (PST). These tubes also imply that the services (power and readout cables, cooling tubes and so on) must be routed down these tubes, since they are attached to the pixels and so must be removed simultaneously with them.

### A.3. Studies

The starting point for the studies was the Utopia layout [196]. Utopia was used for engineering studies and initial tracking simulation studies. The design studies were made on the basis of a single particle analytic tracking model program, IDRES [197]. The IDRES program calculates the error matrix of a single particle track as it propagates through a simplified model of the layout and a user specified magnetic field. The layout is specified in terms of idealized cylindrical and disc layers, which are given a material density in terms of radiation lengths. Each active detector element is also given a resolution in  $r\phi$  and  $z$  for cylindrical elements, and  $r\phi$  and  $r$  for discs. The model calculates the errors based on the multiple scattering of the particle in the material and the detector granularity. As an example of the description, the Utopia layout, as given to the program, is shown in figure A.1. This figure shows the components in a quarter  $r - z$  slice. This slice is sufficient to represent the entire detector, since the detector is nominally forward-backward and radially symmetric (so that horizontal lines in the image represent

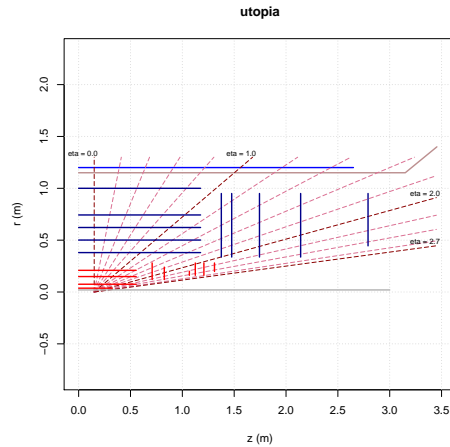


**Figure A.1:** IDRES description of the Utopia layout. Pixel detectors are shown in red, and silicon strip detectors in blue. Non-active components are in grey.

cylindrical components, while vertical lines are disc components). Charged particles will originate from collisions at the centre of the detector, the bottom-left corner in the figure, and will nominally travel in straight lines in the figure, since the solenoidal magnetic fields will bend the tracks in the  $\phi$  direction.

Figure A.2 shows the IDRES results for the Utopia layout. The most important observation is the problems in the barrel–end-cap transition region. At  $\eta \approx 1$ , the number of hits falls below the desired 14 when the track falls between the edge of the final barrel layer and the first end-cap disc. This effect is exacerbated with a track originating displaced from the exact origin of the detector, at a  $z$  value  $15 \text{ cm} = 1\sigma_z$  of the expected width of the interaction region away. This dropping off, and the subsequent dropping off of the subsequent end-cap disc layers, also leads to a reduction in momentum resolution of the tracks. This is due to a decrease of the lever arm for these tracks, the measurable length of the track perpendicular to the magnetic field (so, the length in the  $r$  direction for these tracks, assuming a constant field in  $z$ ). In the barrel, the lever arm is constant, while in the end-caps, the lever arm decreases with respect to  $\eta$  from the top of the end-cap, and decreases until the track can hit the next end-cap. This leads to the spiky behaviour seen in the resolution. For the final layer, the lever arm constantly decreases and so the  $p_T$  resolution quickly decreases ( $\sigma_{p_T} \sim 1/L^2$  for lever arm  $L$ ), since there is no detector past this layer. Finally, the tracking quickly degrades, both in terms of number of hits, and  $p_T$  resolution, above  $\eta = 2.5$  for the Utopia layout, with degradation occurring before this point for the  $z$ -displaced particles.

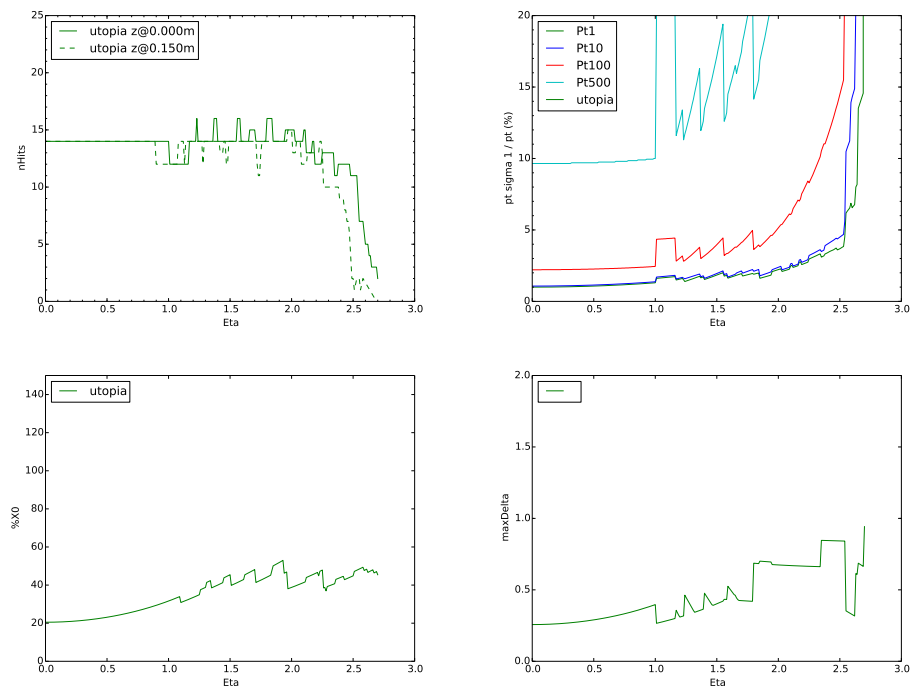


**Figure A.2:** Results of running IDRES over the Utopia layout. The distributions are all shown as a function of the  $\eta$  of a single particle. Starting top left and going clockwise, the figures are: the number of detector hits that the particle makes (also shown with the particle  $z$  position starting offset from the origin by 15 cm, the nominal interaction point spread of the upgraded LHC), the resolution of  $1/p_T$  (in %) for various  $p_T$  of the particle, the maximum distance between two subsequent hits, and the total detector material the particle passes through.

From this, several design considerations are apparent. There needs to be improvement in the barrel–end-cap region, by some means. The final disc needs to be placed as far in  $z$  as allowed in order to avoid the rapid tracking degradation as much as possible, to keep tracking ability for the full  $\eta$  range. Also, the pixel end-caps being confined to low  $z$  leads to very large distances between hits at high  $\eta$ . This is undesirable since it means a larger extrapolation between points is needed in this tracking, which leads to efficiency losses. It would thus be desirable for the layers to be more evenly spaced.

These considerations, after several discussions and refinements, led to the layout shown in figure A.3, referred to as the “cartigny” layout as it was presented during a layout retreat in Cartigny which brought together the layout task force, tracking experts and detector engineers to discuss the designs. The layout makes several radical modifications in order to achieve the criteria just discussed. A “stub-cylinder” layer is added between the final two layers of the barrel, in order to improve the number of hits in the barrel–end-cap region, and “stub-discs” are added between the disc layers to keep the hits at 14 and tame the  $p_T$  resolution spikes. In particular, the stub disc between the first and second “full” discs in the end-cap strips allow the second disc to move back slightly, to keep a more even spacing between the points. The pixel end-cap discs have also been spread further out to allow more pixel hits at larger  $\eta$  and to reduce the distance between the last pixel hit and the first strip hit, which was the largest extrapolation distance in the previous layouts (and the current ATLAS detector). Finally, the placement of the detectors allows the detector to maintain performance even with displaced tracks and at large  $\eta$ . Figure A.4 shows the results of running the layout through the IDRES program, and illustrates the above points.

Objections were raised, however, to the design by the engineering teams. In particular, the stub cylinders and discs would require additional manpower to design and implement the staves on which the detectors sit and the services to cool and power the detectors (the detectors themselves would be just one layer of a standard module, remembering that each barrel or endcap layer consists of overlapping modules to fill the space). The design also uses a larger number of detectors, leading to an increase in the cost of the detector relative to Utopia. These objections led to a final design for the ATLAS letter of intent layout.

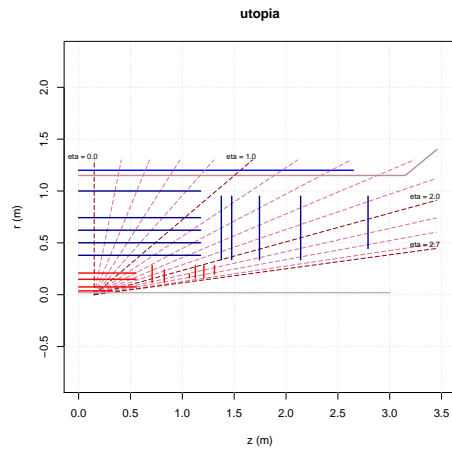


**Figure A.3:** IDRES description of the Cartigny layout. Pixel detectors are shown in red, and silicon strip detectors in blue. Non-active components are in grey.

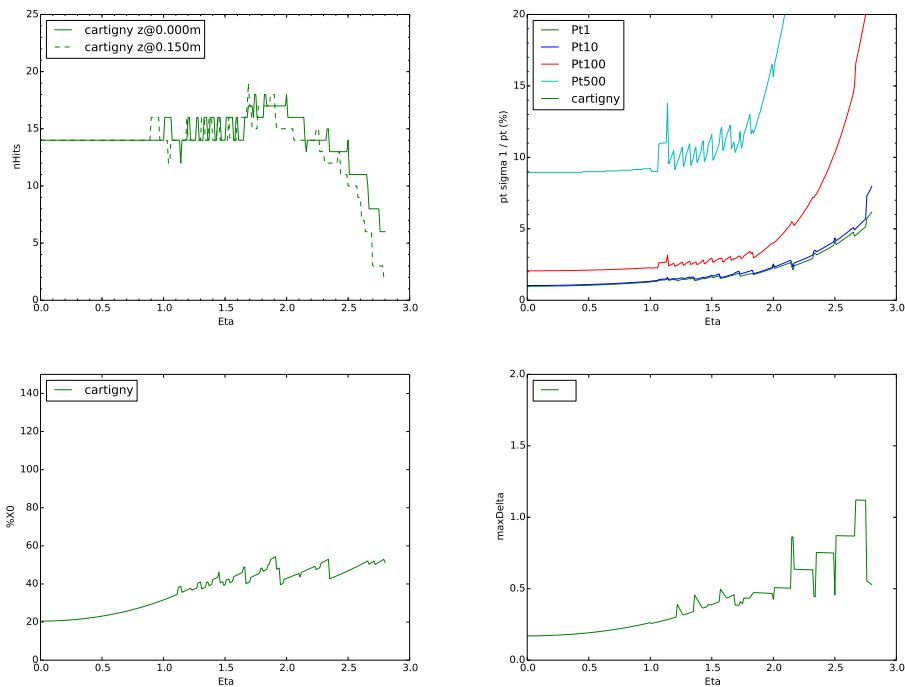


**Figure A.4:** Results of running IDRES over the Cartigny layout. The distributions are all shown as a function of the  $\eta$  of a single particle. Further description of the figure is as for figure A.2

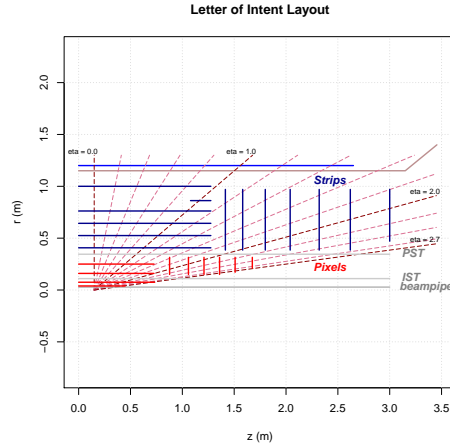


**Figure A.5:** LoI layout as input into the IDRES program.

## A.4. The Letter of Intent Layout

Figure A.5 shows a sketch of the layout that was the final design used for the Phase-II Letter of Intent studies, which we will call the LoI layout. The design keeps the stub cylinder to improve the barrel–end-cap gap performance, but drops the stub discs in the end-cap and reoptimizes the distances between layers. To maintain  $p_T$  resolution performance, it does however increase the number of layers to seven. Figure A.6 shows the results of running the layout through the IDRES program.

For the Letter of Intent, simulation studies using the layout have been performed using the full ATLAS GEANT4 simulation suite with a detailed description of the upgrade tracker and the standard ATLAS reconstruction algorithms, adapted to use the new detector geometry [195]. These studies have been performed to show the tracking capabilities of the detector for the expected  $\langle\mu\rangle = 140$  pileup events at the HL-LHC. Figure A.7 shows the material distribution as a function of  $\eta$  for the detailed, full simulation version of the upgrade tracker. Across the entire tracking volume range, the material is less than  $0.7X_0$  except in a few regions, while the current tracker has  $> 1.2X_0$  for  $|\eta| > 1$ . This is achieved mostly through the services for the pixels being routed out along the service tubes and so leaving the tracking volume as soon as possible, while in the current layout, all the services are routed up through the barrel–end-cap gap.

Figure A.8 shows the efficiency for reconstructing 100 GeV particles of various types with the full  $\langle\mu\rangle = 140$  pileup overlaid, showing that the detector is able to maintain very high efficiency even at very high pileup levels. In addition, the number of fake

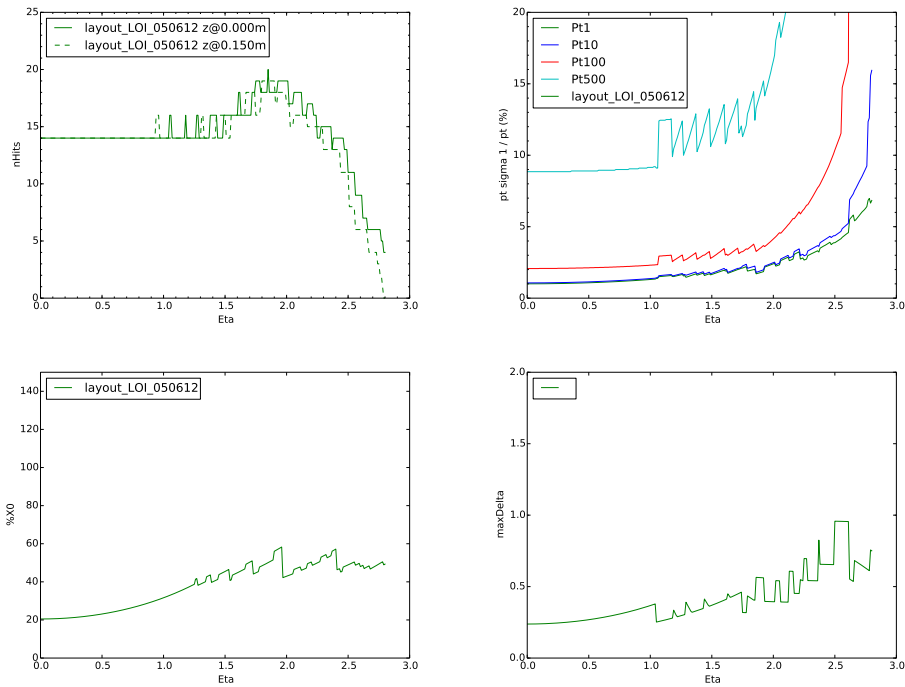


**Figure A.6:** Results of running IDRES over the letter of intent layout. The distributions are all shown as a function of the  $\eta$  of a single particle. Further description of the figure is as for figure A.2

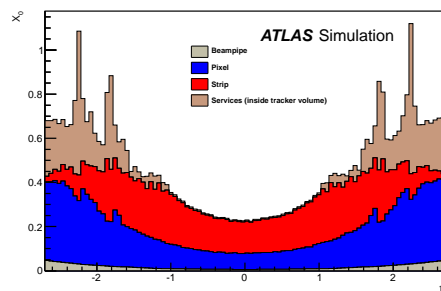


**Figure A.7:** The material in  $X_0$  as a function of  $\eta$  for the LoI layout. From [195].

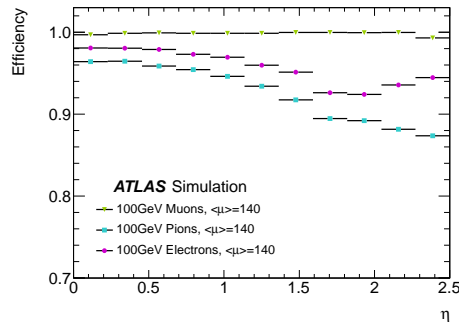


**Figure A.8:** Efficiencies as a function of  $\eta$  for  $p_T = 100$  GeV muons, pions and electrons for the LoI layout using full detector simulation at a pileup of 140. From [195].

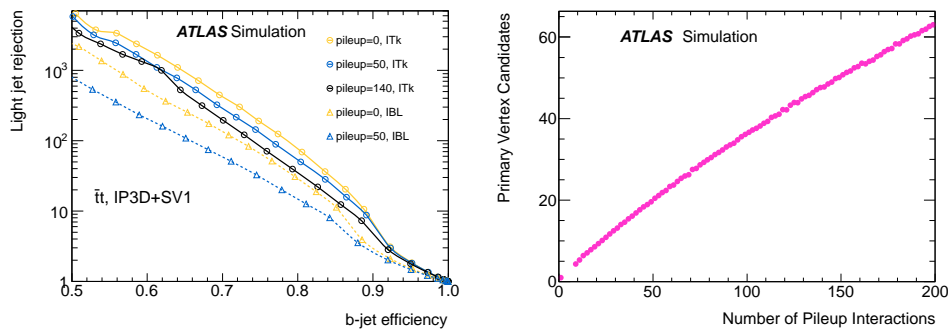


**Figure A.9:** The left figure shows the performance of  $b$ -tagging in  $t\bar{t}$  events, for a range of pileup levels for the LoI layout. The right figure shows the number of reconstructed primary vertex candidates as a function of the number of pileup interactions. From [195].

reconstructed tracks (that is, tracks reconstructed that cannot be associated to a single charged particle) was studying, and found to be less than  $10^{-3}$  of all reconstructed tracks. Figure A.9 shows the light-jet rejection for various  $b$ -tagging efficiencies, using the current ATLAS  $b$ -tagging algorithms. The upgrade tracker is able to reject more light-jets, even with higher pileup levels, than the current detector. The figure also shows the number of primary vertices reconstructed, as a function of the number of pileup events generated. Many of the pileup events do not have associated vertices because they have too few tracks, however, the fraction of vertices reconstructed is approximately independent of the number of pileup events, showing that the tracker is maintaining good primary vertexing capabilities at the expected level of pileup.

Thus, the simulation studies show that the upgrade tracker that has been designed maintains or exceeds the capabilities of the current tracker, even in the more extreme conditions of the HL-LHC.

## Appendix B.

# Correction Factors and Response Matrices

This appendix presents the correction factors and response matrix for each of the distributions we have measured. Also shown are the acceptance factor for a parton level event to be seen at particle level (figure [B.6](#)) and figures stepping through the analysis corrections from the reconstructed distributions (figure [B.5](#)).

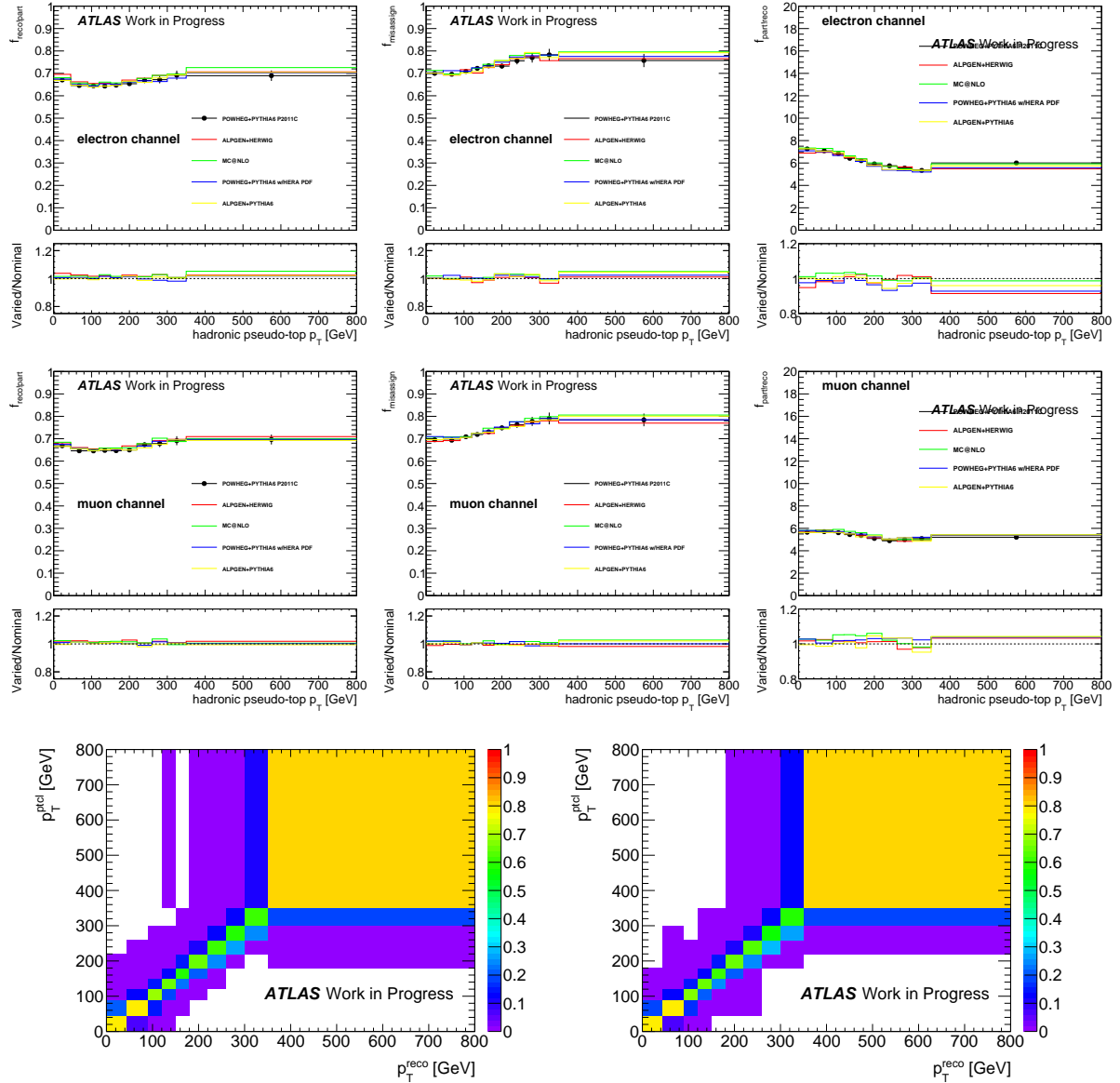


**Figure B.1:** Correction factors for the hadronic pseudo-top  $p_T$  in the electron channel (top) and muon channel (middle) and response matrices (bottom) using the POWHEG+PYTHIA  $t\bar{t}$  signal sample.

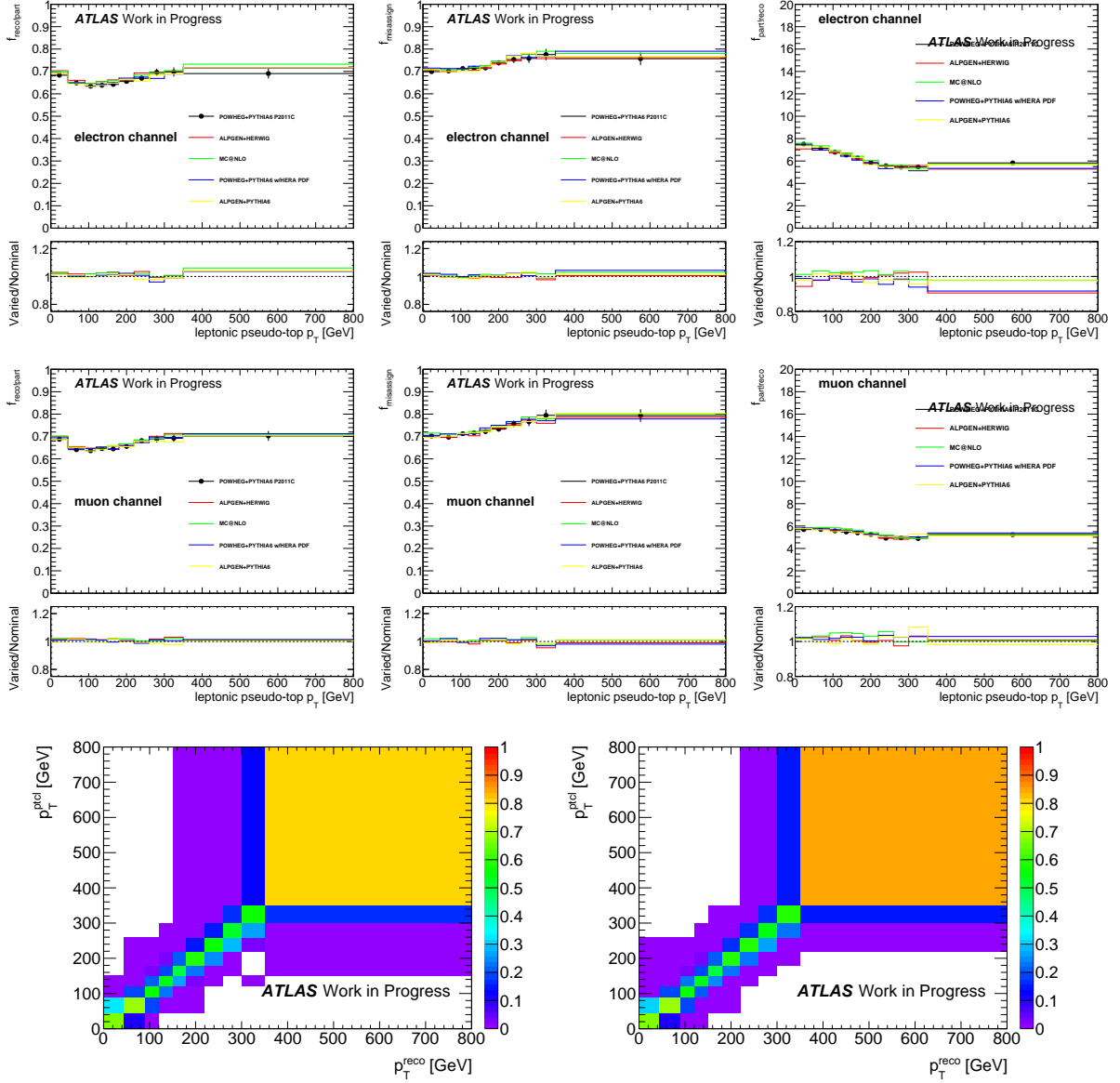


**Figure B.2:** Correction factors for the leptonic pseudo-top  $p_T$  in the electron channel (top) and muon channel (middle) and response matrices (bottom) using the POWHEG+PYTHIA  $t\bar{t}$  signal sample.

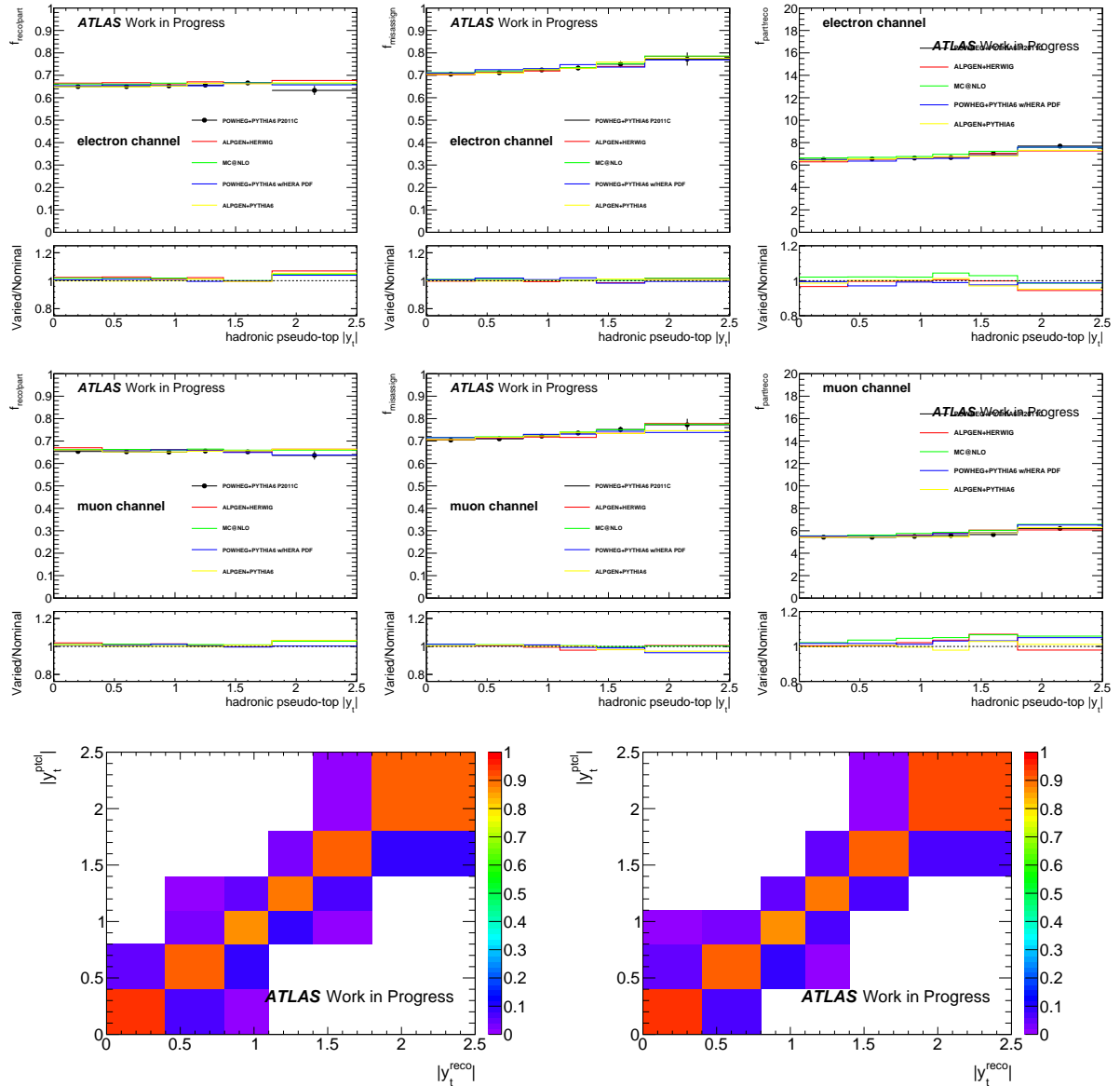


**Figure B.3:** Correction factors for the hadronic pseudo-top  $|y_t^t|$  in the electron channel (top) and muon channel (middle) and response matrices (bottom) using the POWHEG+PYTHIA  $t\bar{t}$  signal sample.

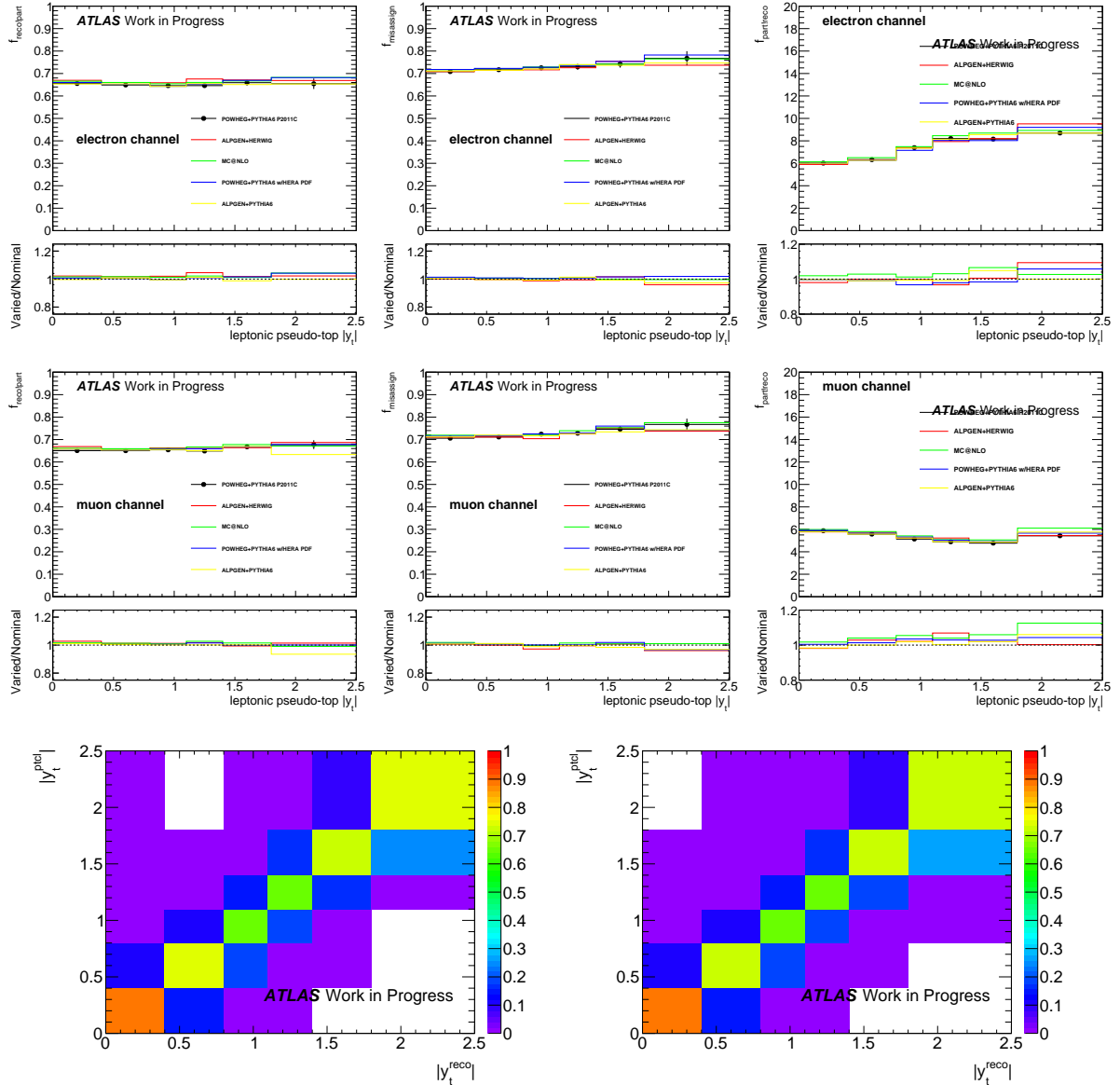


**Figure B.4:** Correction factors for the leptonic pseudo-top  $|y^t|$  in the electron channel (top) and muon channel (middle) and response matrices (bottom) using the POWHEG+PYTHIA  $t\bar{t}$  signal sample.

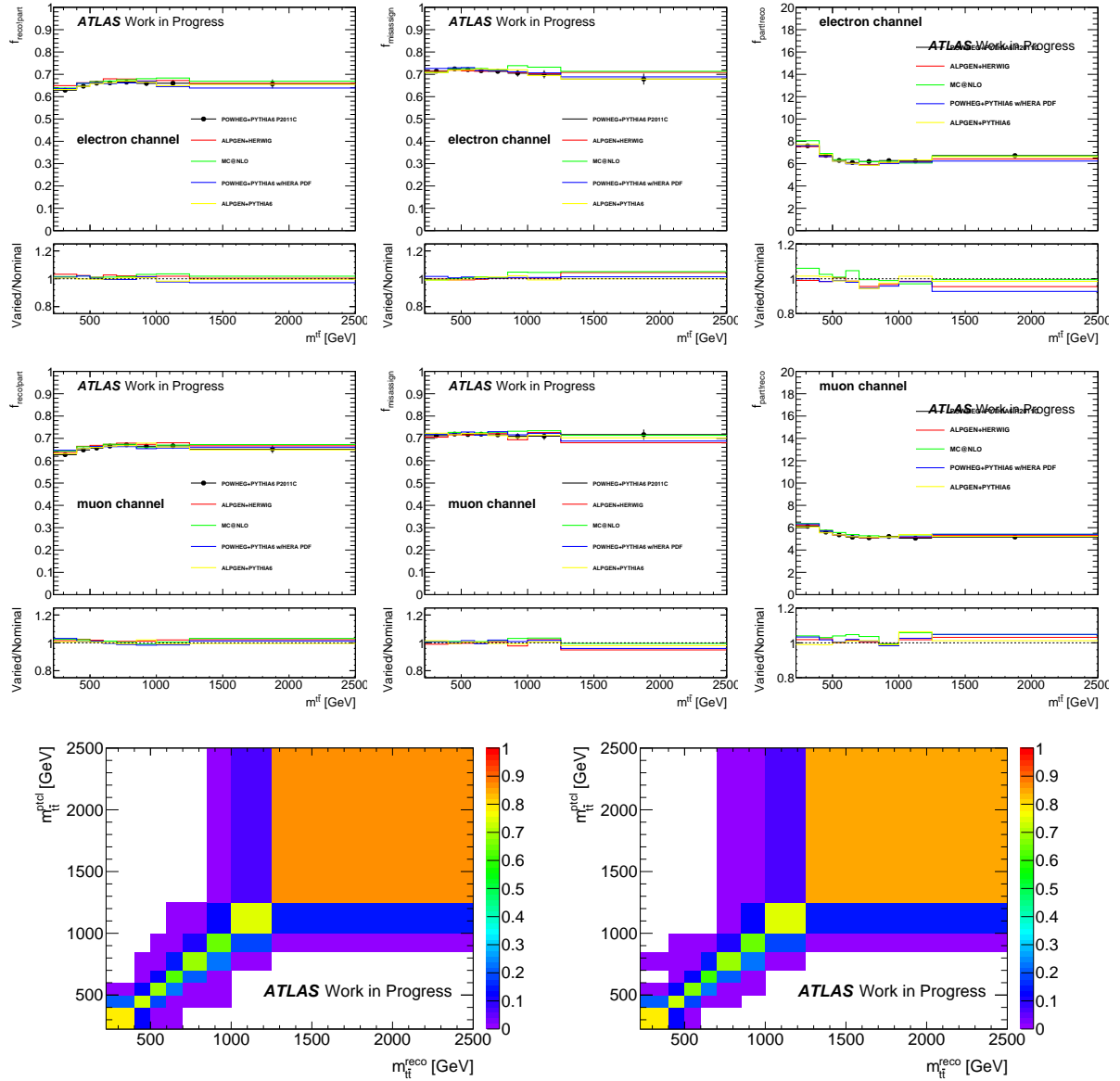


**Figure B.5:** Correction factors for the pseudo-top  $m_{tt}$  in the electron channel (top) and muon channel (middle) and response matrices (bottom) using the POWHEG+PYTHIA  $t\bar{t}$  signal sample.

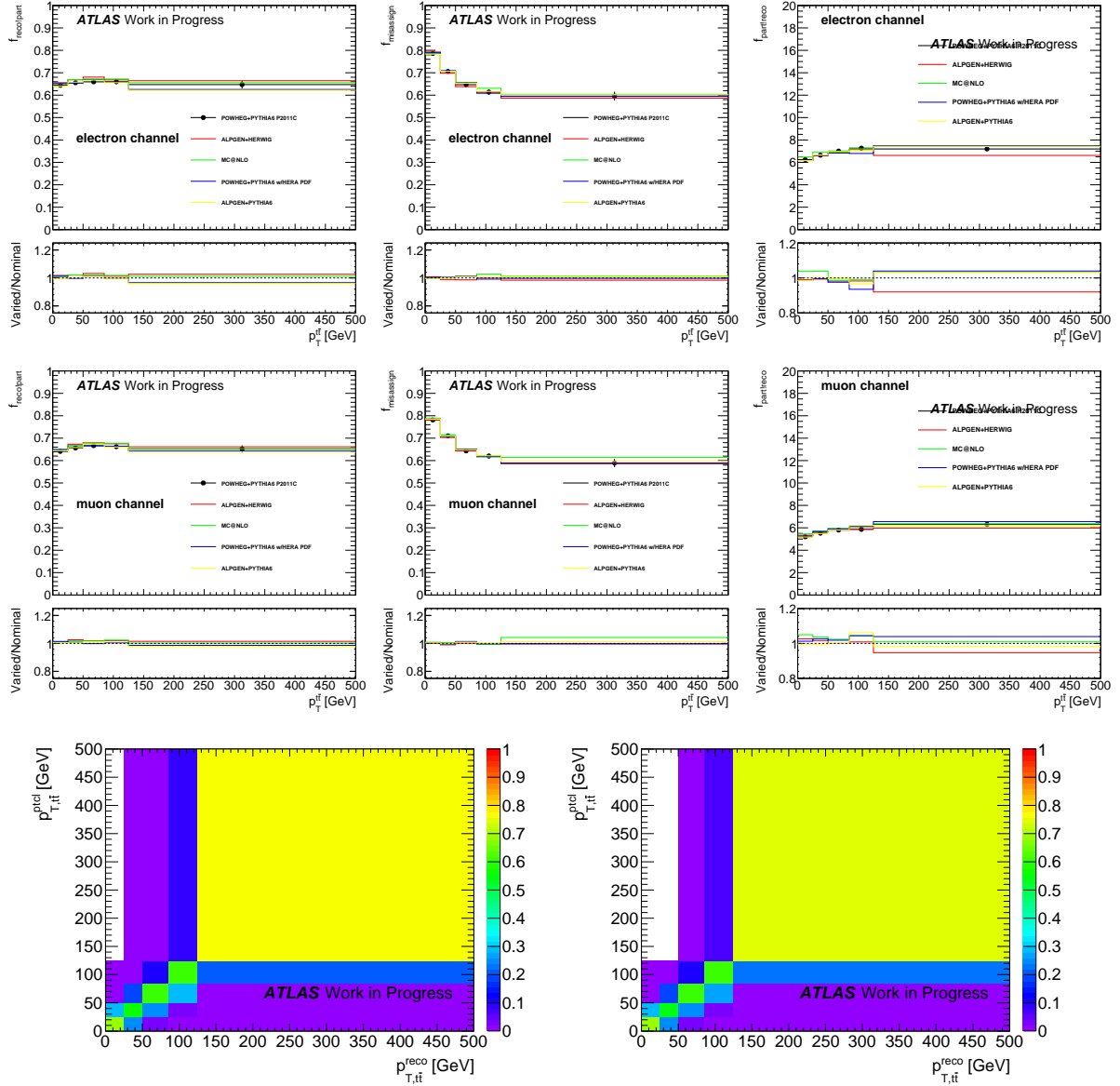


**Figure B.6:** Correction factors for the pseudo-top  $p_T^{tt}$  in the electron channel (top) and muon channel (middle) and response matrices (bottom) using the POWHEG+PYTHIA  $t\bar{t}$  signal sample.

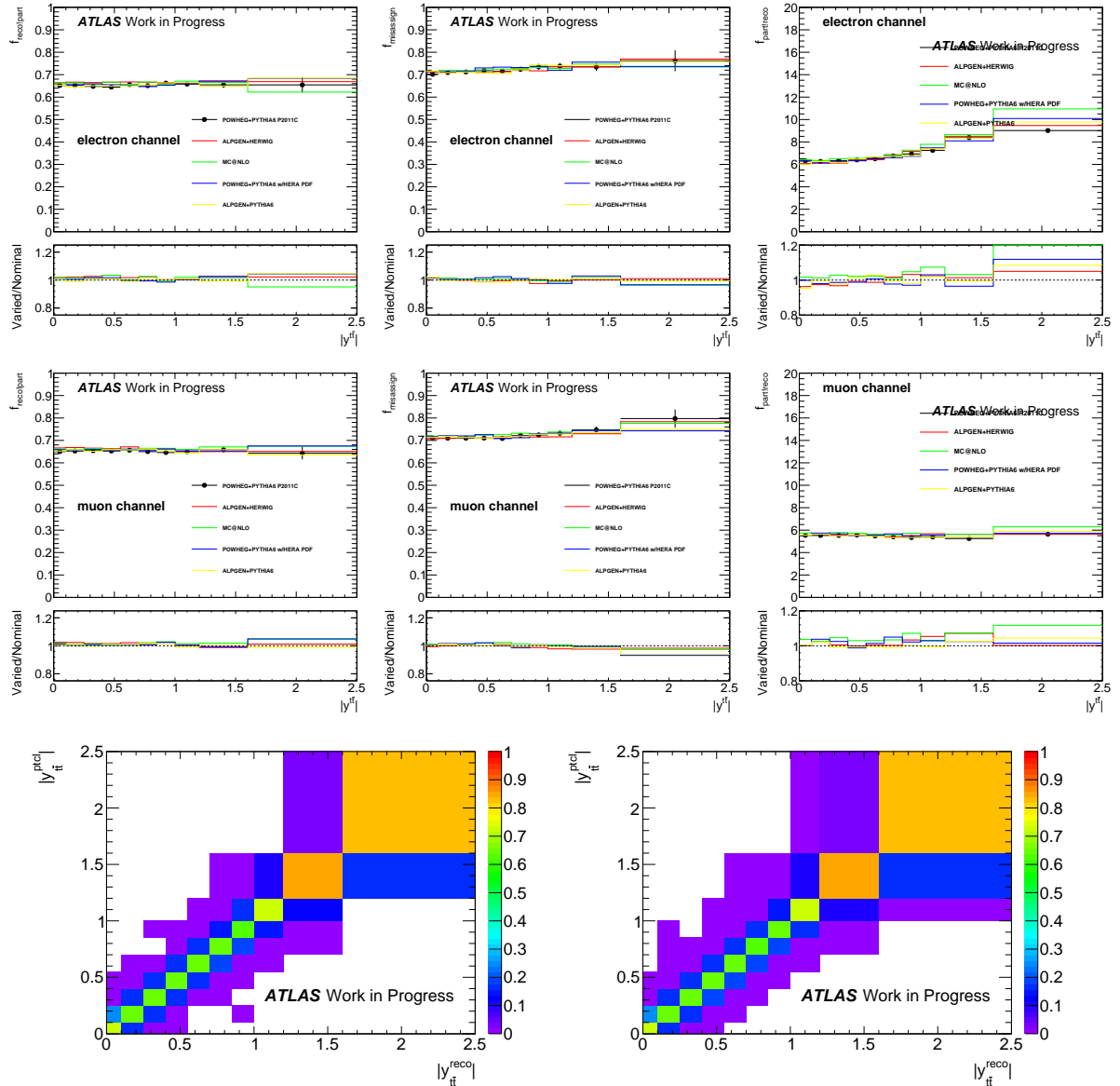
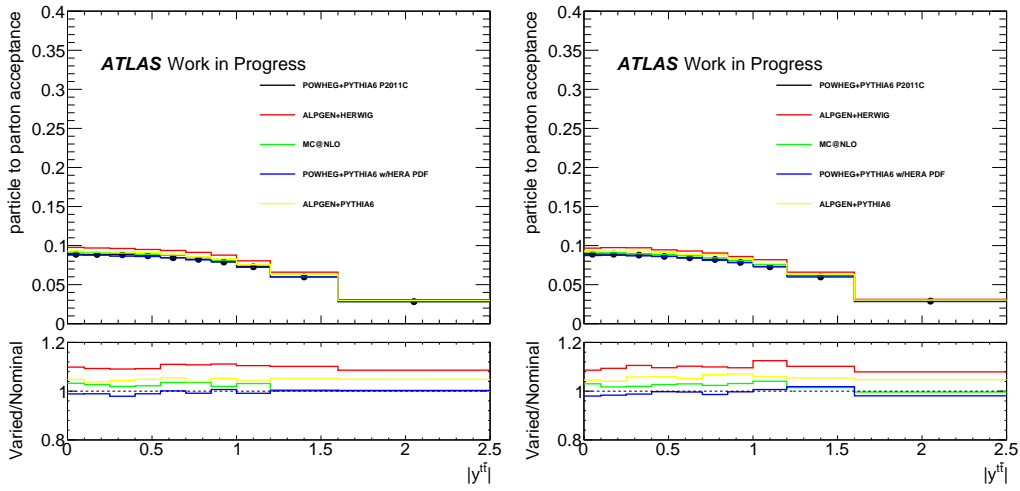
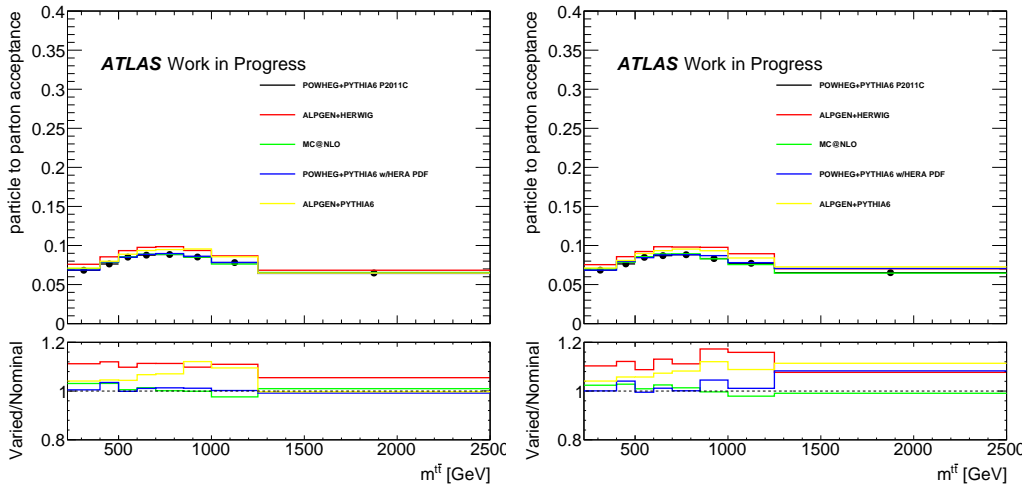


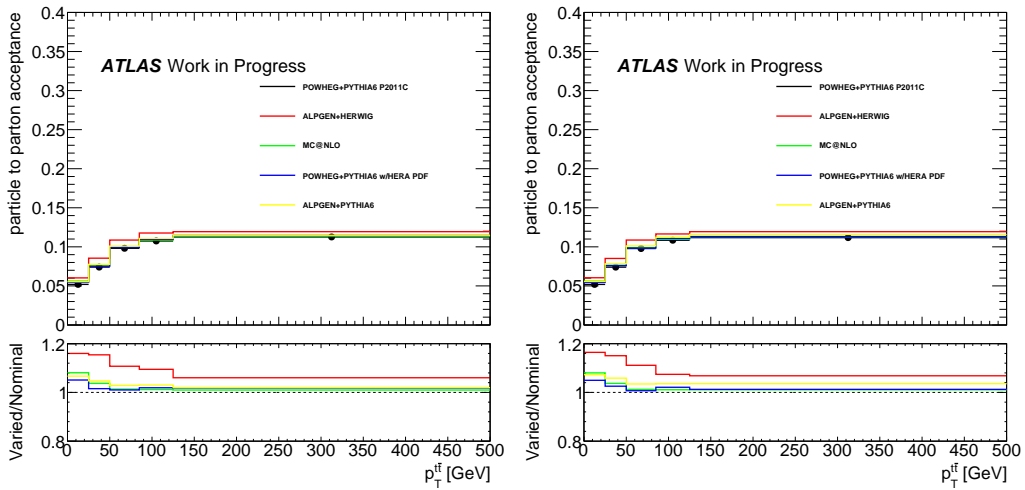
**Figure B.7:** Correction factors for the pseudo-top  $|y^{tt}|$  in the electron channel (top) and muon channel (middle) and response matrices (bottom) using the POWHEG+PYTHIA  $t\bar{t}$  signal sample.



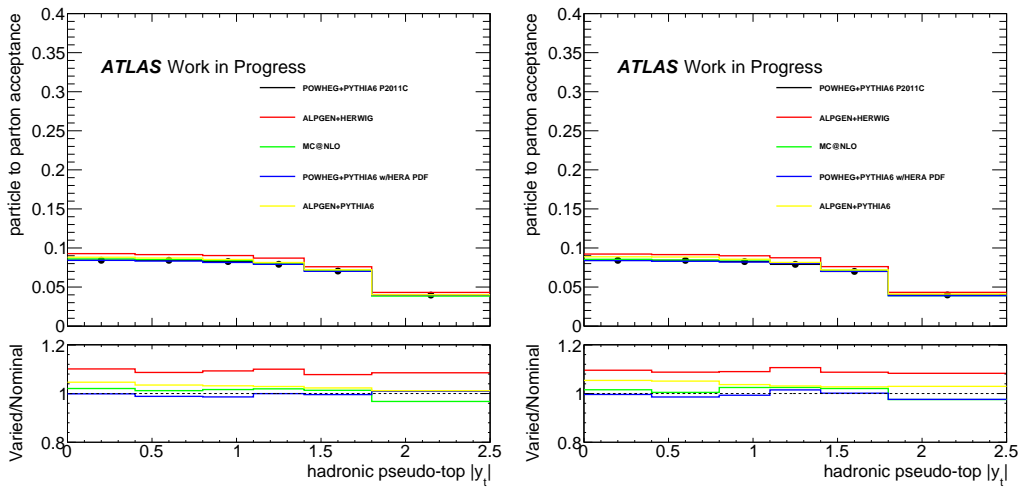
(a) Pseudo-top pair rapidity



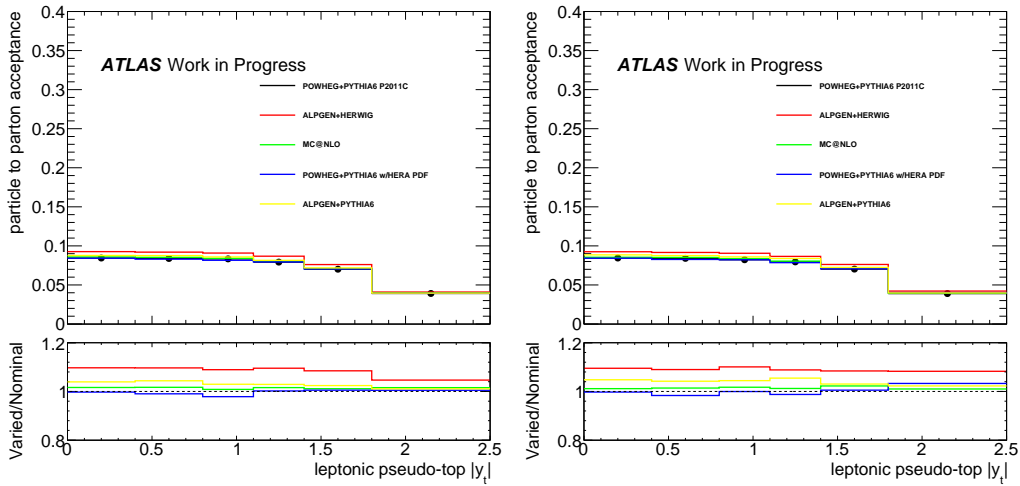
(b) Pseudo-top pair  $m^{t\bar{t}}$



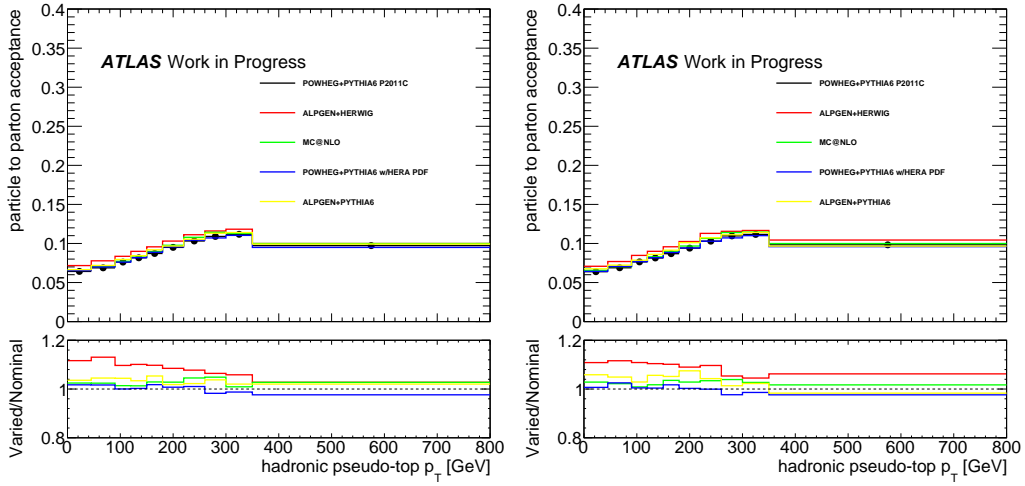
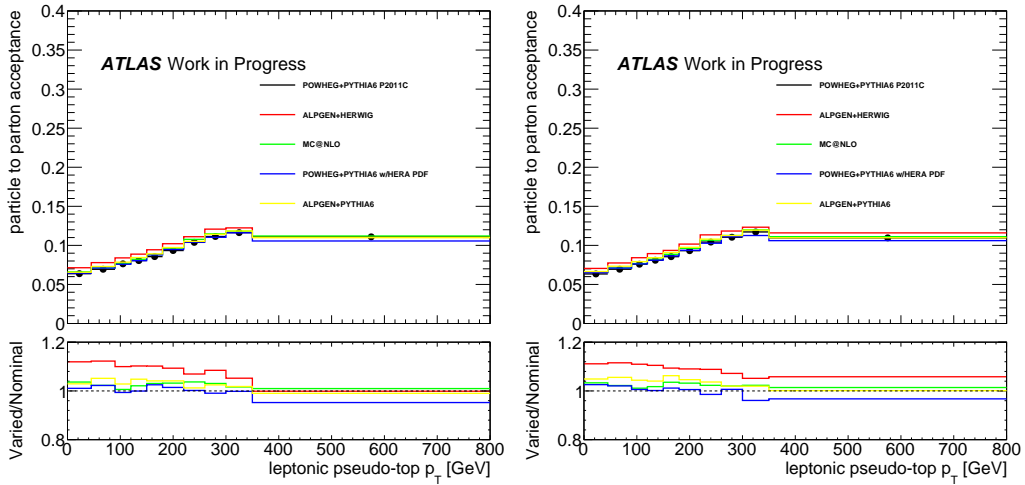
(c) Pseudo-top pair  $p_T^{t\bar{t}}$



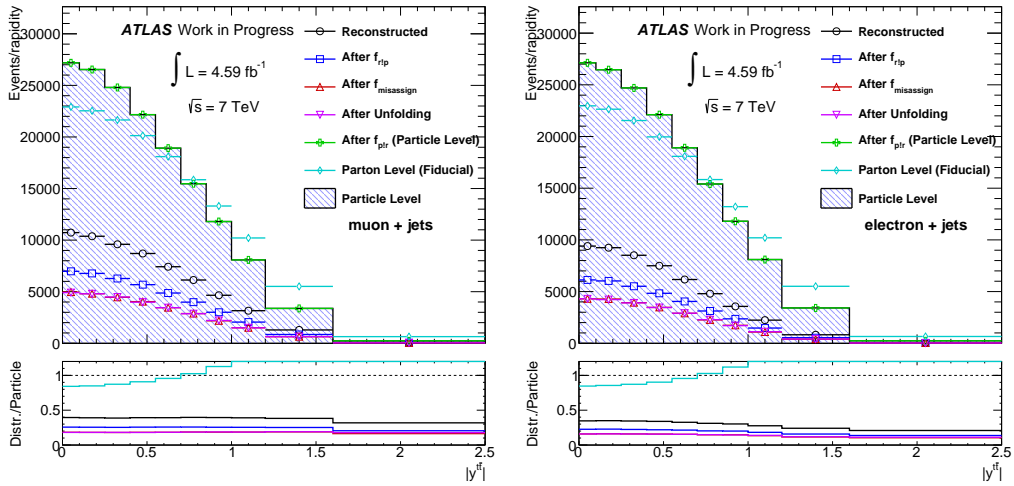
(d) Individual hadronic pseudo-top rapidity



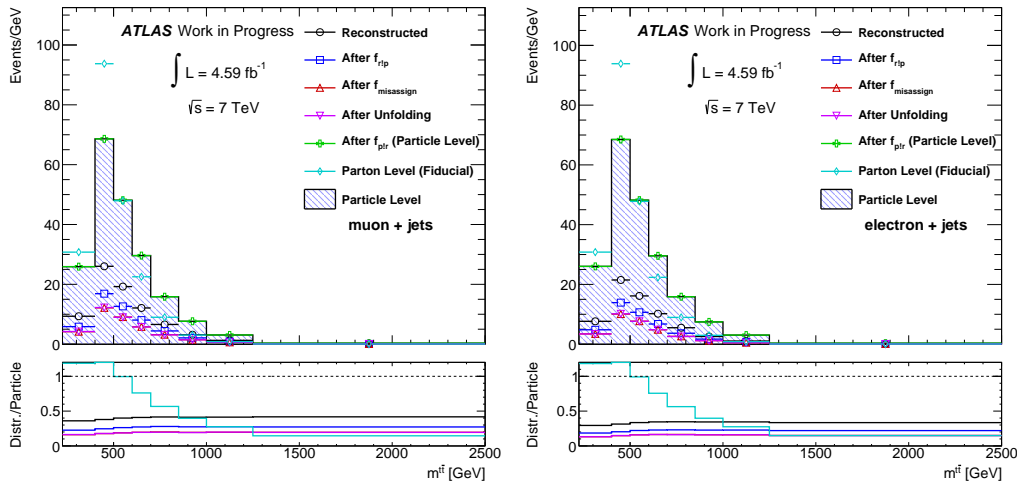
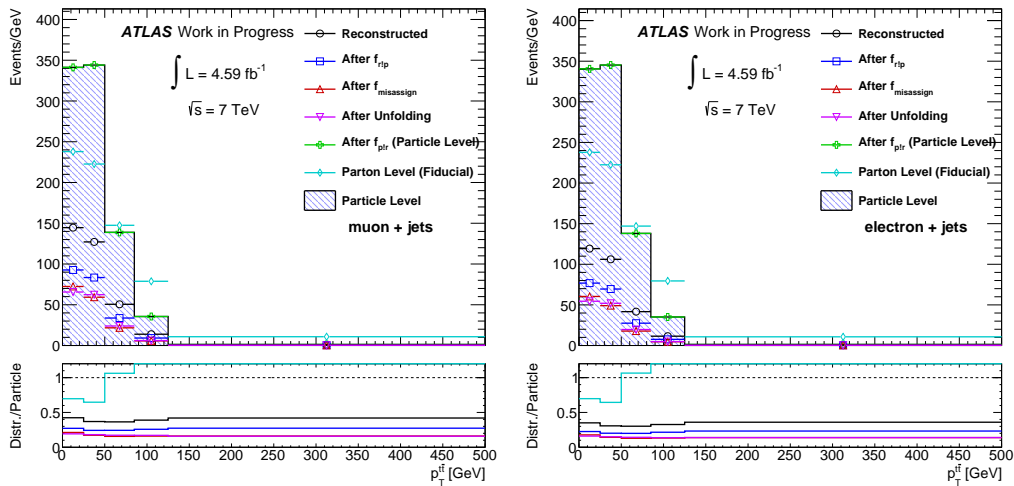
(e) Individual leptonic pseudo-top rapidity

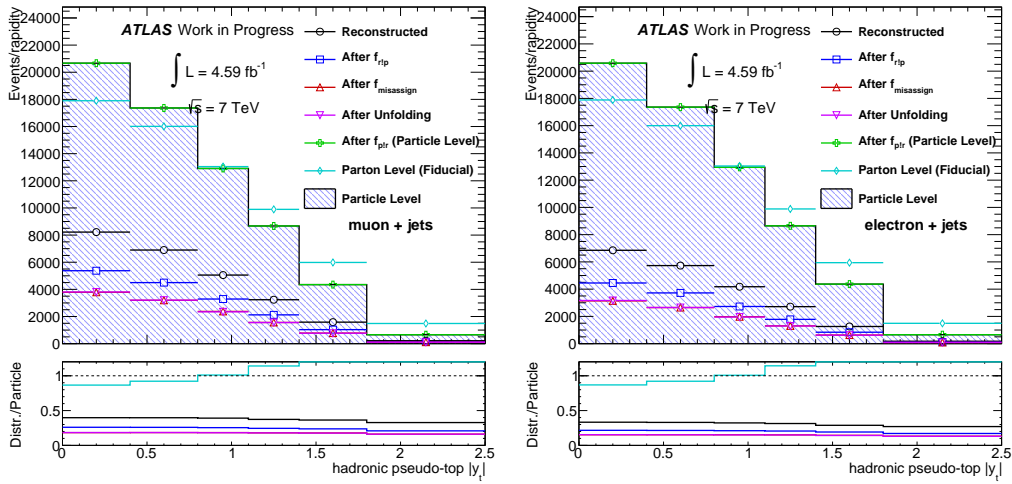
(f) Individual hadronic pseudo-top  $p_T$ (g) Individual leptonic pseudo-top  $p_T$ 

**Figure B.6:** Efficiency of a parton level event being inside the particle level fiducial volume. Each figure shows the muon channel on the left and the electron channel on the right.

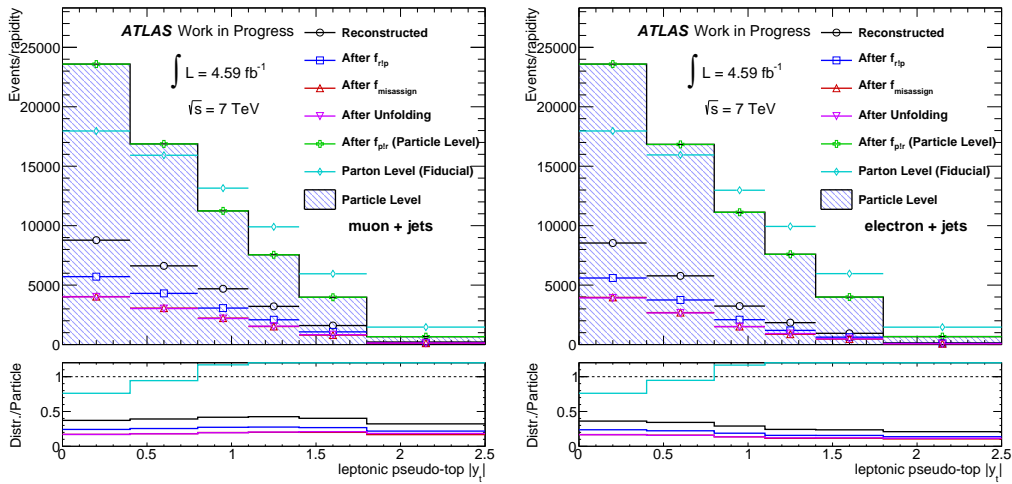


(a) Pseudo-top pair rapidity distribution

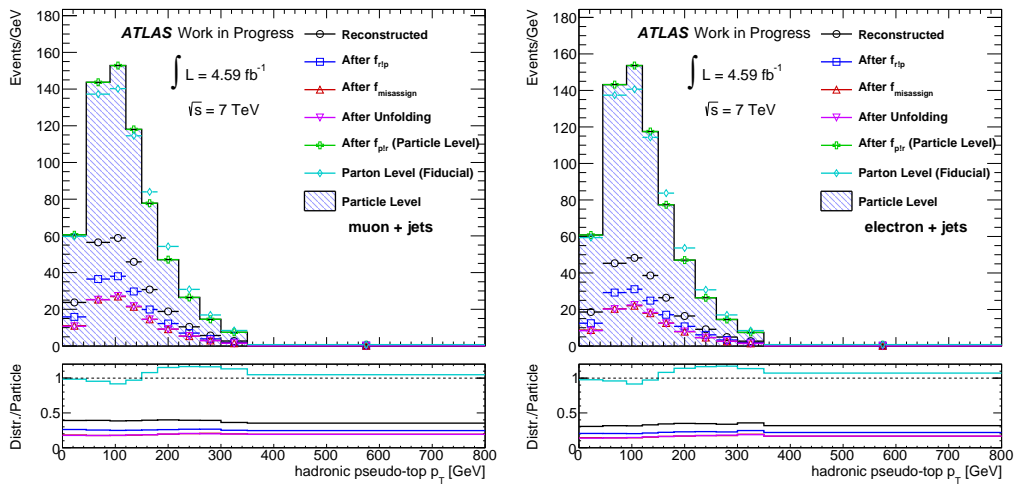
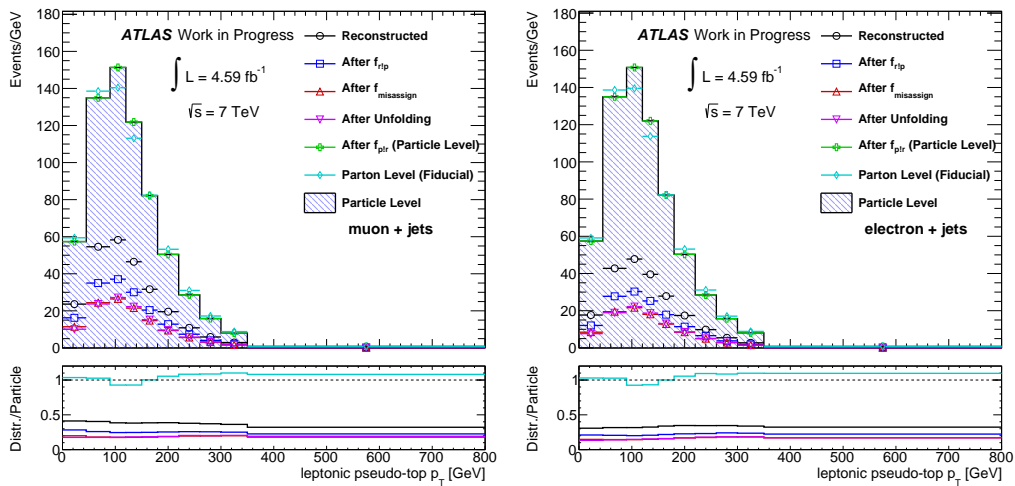
(b) Pseudo-top pair  $m^{t\bar{t}}$  distribution(c) Pseudo-top pair  $p_T^{t\bar{t}}$  distribution



(d) Individual hadronic pseudo-top rapidity



(e) Individual leptonic pseudo-top rapidity

(f) Individual hadronic pseudo-top  $p_T$ (g) Individual leptonic pseudo-top  $p_T$ 

**Figure B.5:** Distributions obtained using the POWHEG+PYTHIA  $t\bar{t}$  signal sample, showing the effect of applying each correction, in turn, on the reconstructed distribution and showing that the particle level distribution is reobtained by the correction factors. All figures display the muon channel on the left and the electron channel on the right.

# Appendix C.

## Tables of Systematic Uncertainties

This appendix presents table of the breakdown of the sources of systematic uncertainty in the measured distributions, for the individual lepton channels.

Bin Range [GeV]	[225, 400]	[400, 500]	[500, 600]	[600, 700]	[700, 850]	[850, 1000]	[1000, 1250]	[1250, 2500]
$d\sigma/dm(t\bar{t})$ [fb/GeV]	5.172	14.913	10.543	6.377	3.317	1.549	0.621	0.058
<b>Total Uncertainty [%]</b>	10.98	9.72	10.50	10.90	12.00	14.16	15.76	21.59
<b>Statistics [%]</b>	2.72	2.06	2.24	2.85	3.54	5.14	7.00	10.95
<b>Systematics [%]</b>	10.63	9.50	10.26	10.52	11.47	13.20	14.13	18.61
MC Stats on Correction Factors [%]	0.62	0.49	0.55	0.69	0.80	1.14	1.53	2.32
Background Subtraction Unc. [%]	1.45	1.09	1.87	1.91	2.78	3.52	4.56	7.55
Cellout [%]	0.30	0.34	0.21	0.06	0.03	0.17	0.25	0.51
Pileup [%]	0.22	0.22	0.09	0.03	0.06	0.18	0.28	0.31
Mistag [%]	0.92	0.73	0.79	0.94	1.06	1.42	1.50	2.66
Btag [%]	4.81	4.36	4.37	4.57	4.78	5.00	5.20	5.61
Ctag [%]	2.01	1.84	1.93	2.08	2.22	2.51	2.46	2.73
Jet Eff [%]	0.09	0.03	0.04	0.05	0.02	0.06	0.06	0.19
Jet Energy Resolution [%]	4.18	0.92	0.78	1.51	1.18	1.91	2.80	0.25
JVF [%]	1.53	1.48	1.50	1.58	1.73	1.92	1.86	2.22
Lepton Trigger Eff. [%]	1.40	1.33	1.27	1.33	1.35	1.34	1.37	1.60
Lepton Identification Eff. [%]	0.82	0.74	0.73	0.80	0.74	0.76	0.76	0.97
Lepton Reconstruction Eff. [%]	0.37	0.32	0.32	0.36	0.30	0.41	0.49	0.27
JES EffectiveNP STAT1 [%]	1.03	1.34	1.18	0.96	0.96	0.95	0.62	0.29
JES EffectiveNP STAT2 [%]	0.35	0.06	0.04	0.07	0.21	0.36	0.37	0.70
JES EffectiveNP STAT3 [%]	0.75	0.06	0.26	0.43	0.59	0.72	0.63	0.81
JES EffectiveNP MODEL1 [%]	0.28	2.02	2.38	2.09	2.14	1.97	1.47	1.65
JES EffectiveNP MODEL2 [%]	1.07	0.25	0.13	0.31	0.56	0.76	0.77	1.28
JES EffectiveNP MODEL3 [%]	1.31	0.26	0.26	0.47	0.69	0.93	0.70	0.93
JES EffectiveNP MODEL4 [%]	0.09	0.01	0.08	0.06	0.18	0.21	0.38	0.28
JES EffectiveNP DET1 [%]	2.43	0.45	1.32	1.71	2.31	2.83	3.68	4.03
JES EffectiveNP DET2 [%]	0.19	0.09	0.09	0.12	0.14	0.18	0.31	0.34
JES EffectiveNP MIXED1 [%]	0.16	0.04	0.07	0.10	0.27	0.13	0.43	0.81
JES EffectiveNP MIXED2 [%]	0.11	0.36	0.38	0.33	0.33	0.46	0.40	0.45
JES EtaIntercalibration TotalStat [%]	0.17	0.45	0.59	0.52	0.70	0.88	0.62	0.54
JES EtaIntercalibration Theory [%]	1.89	0.66	1.40	2.17	3.11	3.30	4.71	7.26
JES SingleParticle HighPt [%]	0.02	0.01	0.02	0.02	0.04	0.03	0.08	0.19
JES RelativeNonClosure MC11b [%]	0.27	0.22	0.36	0.41	0.73	0.90	0.51	0.75
JES Pileup OffsetMu [%]	0.31	0.31	0.07	0.28	0.26	0.36	0.05	0.79
JES Pileup OffsetNPV [%]	0.33	0.21	0.24	0.36	0.38	0.44	0.42	0.58
JES closeby [%]	1.90	2.73	3.21	3.08	3.06	2.75	3.15	3.09
JES flavor comp [%]	1.50	1.10	1.81	1.98	2.16	2.47	3.59	3.54
JES flavor response [%]	1.02	0.59	1.03	1.12	1.34	1.48	2.24	2.31
JES B Jes Unc. [%]	3.68	1.22	2.43	3.11	3.37	3.55	4.23	3.72
Muon ID [%]	0.03	0.01	0.04	0.04	0.05	0.01	0.14	0.01
Muon MS [%]	0.01	0.00	0.05	0.04	0.03	0.02	0.22	0.06
Muon Momentum Scaling [%]	0.12	0.25	0.35	0.18	0.36	0.38	0.01	0.60
Parton Shower [%]	0.13	3.01	3.65	1.62	2.35	1.53	0.74	0.43
I/FSR [%]	3.29	4.94	4.07	4.20	4.86	5.76	4.45	8.24
Color Reconnection [%]	0.18	0.93	0.39	0.06	1.53	0.90	3.20	2.32
Generator [%]	3.26	2.18	2.67	3.31	1.47	4.59	2.22	5.14
PDF [%]	0.35	0.43	0.24	0.21	0.17	0.13	1.05	2.43
Lumi. Uncertainty [%]	1.80	1.80	1.80	1.80	1.80	1.80	1.80	1.80

**Table C.1:** Relative uncertainties on the final differential  $t\bar{t}$  cross-section as a function of the hadronic-leptonic pseudo-top quark system  $m(t\bar{t})$  in the muon channel. The systematic uncertainties were propagated to the final distribution using correction factors from the nominal POWHEG+PYTHIA  $t\bar{t}$  MC sample.

Bin Range [GeV]	[225, 400]	[400, 500]	[500, 600]	[600, 700]	[700, 850]	[850, 1000]	[1000, 1250]	[1250, 2500]
$d\sigma/dm(t\bar{t})$ [fb/GeV]	4.885	14.338	10.513	6.269	3.412	1.516	0.570	0.056
<b>Total Uncertainty [%]</b>	13.31	10.57	11.68	13.60	13.79	17.49	18.16	25.43
<b>Statistics [%]</b>	3.35	2.22	2.51	3.16	3.74	5.96	7.92	13.20
<b>Systematics [%]</b>	12.88	10.33	11.41	13.23	13.28	16.45	16.35	21.73
MC Stats on Correction Factors [%]	0.71	0.51	0.60	0.74	0.86	1.24	1.55	2.49
Background Subtraction Unc. [%]	2.31	1.58	1.83	2.67	3.38	5.19	5.52	9.90
Cellout [%]	0.22	0.18	0.08	0.27	0.20	0.18	0.42	0.00
Pileup [%]	0.04	0.06	0.08	0.26	0.11	0.25	0.20	0.28
Mistag [%]	0.78	0.78	0.88	1.04	1.08	1.31	1.61	2.13
Btag [%]	5.17	4.54	4.47	4.69	4.70	5.04	5.41	5.75
Ctag [%]	2.13	1.90	1.88	1.99	2.31	2.53	2.89	2.74
Jet Eff [%]	0.14	0.09	0.02	0.02	0.03	0.19	0.07	0.07
Jet Energy Resolution [%]	3.89	0.72	0.40	0.90	2.42	2.05	2.03	2.53
JVF [%]	1.56	1.53	1.58	1.69	1.70	1.82	1.87	2.49
Lepton Trigger Eff. [%]	0.64	0.58	0.57	0.59	0.57	0.58	0.64	0.73
Lepton Identification Eff. [%]	2.57	2.30	2.23	2.35	2.26	2.38	2.62	2.97
Lepton Reconstruction Eff. [%]	1.06	0.95	0.88	0.84	0.86	0.93	1.00	0.91
JES EffectiveNP STAT1 [%]	1.16	1.44	1.26	1.10	0.79	0.67	0.39	0.17
JES EffectiveNP STAT2 [%]	0.35	0.00	0.03	0.15	0.20	0.08	0.17	0.77
JES EffectiveNP STAT3 [%]	0.74	0.11	0.25	0.50	0.57	0.82	0.81	0.73
JES EffectiveNP MODEL1 [%]	0.74	2.29	2.31	2.43	1.89	1.90	1.85	1.36
JES EffectiveNP MODEL2 [%]	1.20	0.31	0.14	0.26	0.50	0.75	1.17	1.06
JES EffectiveNP MODEL3 [%]	1.37	0.18	0.21	0.51	0.65	0.87	1.14	0.79
JES EffectiveNP MODEL4 [%]	0.14	0.12	0.03	0.12	0.25	0.30	0.33	0.61
JES EffectiveNP DET1 [%]	2.45	0.59	1.20	1.79	2.18	2.84	3.62	4.30
JES EffectiveNP DET2 [%]	0.16	0.12	0.13	0.12	0.16	0.15	0.25	0.19
JES EffectiveNP MIXED1 [%]	0.24	0.10	0.10	0.13	0.18	0.40	0.37	1.22
JES EffectiveNP MIXED2 [%]	0.03	0.45	0.43	0.42	0.30	0.27	0.35	0.38
JES EtaIntercalibration TotalStat [%]	0.18	0.57	0.59	0.59	0.63	0.66	0.56	0.54
JES EtaIntercalibration Theory [%]	1.85	0.98	1.66	2.47	3.04	3.94	5.06	8.17
JES SingleParticle HighPt [%]	0.01	0.05	0.04	0.01	0.00	0.01	0.03	0.00
JES RelativeNonClosure MC11b [%]	0.18	0.35	0.43	0.60	0.56	0.72	0.38	1.15
JES Pileup OffsetMu [%]	0.21	0.43	0.10	0.25	0.24	0.21	0.58	0.55
JES Pileup OffsetNPV [%]	0.24	0.42	0.29	0.28	0.29	0.52	0.99	0.51
JES closeby [%]	1.63	3.72	3.63	3.74	3.17	3.53	4.71	3.02
JES flavor comp [%]	1.59	1.44	1.76	2.21	2.29	2.99	3.94	3.63
JES flavor response [%]	0.98	0.79	1.09	1.34	1.34	1.82	2.73	2.13
JES B Jes Unc. [%]	3.93	1.34	2.34	3.19	3.23	3.68	4.02	3.51
Electron Energy Resolution [%]	0.02	0.06	0.21	0.21	0.21	0.14	0.30	0.18
Electron Energy Scale [%]	0.23	0.43	0.48	0.63	0.73	0.77	0.74	0.75
Parton Shower [%]	0.21	0.43	1.16	3.50	1.93	1.89	0.22	0.68
I/FSR [%]	6.45	5.24	6.55	7.36	5.82	9.75	6.44	10.64
Color Reconnection [%]	3.23	0.17	0.78	0.39	0.75	0.45	0.21	0.18
Generator [%]	3.08	3.20	3.13	3.25	5.53	4.58	4.82	5.31
PDF [%]	0.47	0.54	0.33	0.30	0.38	0.85	0.55	4.57
Lumi. Uncertainty [%]	1.80	1.80	1.80	1.80	1.80	1.80	1.80	1.80

**Table C.2:** Relative uncertainties on the final differential  $t\bar{t}$  cross-section as a function of the hadronic-leptonic pseudo-top quark system  $m(t\bar{t})$  in the electron channel. The systematic uncertainties were propagated to the final distribution using correction factors from the nominal POWHEG+PYTHIA  $t\bar{t}$  MC sample.

Bin Range [GeV]	[0, 25]	[25, 50]	[50, 85]	[85, 125]	[125, 500]
$d\sigma/dp_T(t\bar{t})$ [fb/GeV]	73.560	72.483	28.393	7.590	0.287
<b>Total Uncertainty [%]</b>	10.70	10.23	13.44	18.32	24.59
<b>Statistics [%]</b>	1.77	1.42	2.18	4.17	8.08
<b>Systematics [%]</b>	10.55	10.14	13.26	17.84	23.23
MC Stats on Correction Factors [%]	0.42	0.37	0.51	0.98	2.01
Background Subtraction Unc. [%]	2.09	1.39	1.66	2.13	3.90
Cellout [%]	3.45	2.65	2.99	3.35	3.26
Pileup [%]	2.00	1.61	1.81	2.02	1.81
Mistag [%]	0.79	0.92	1.12	1.17	0.98
Btag [%]	4.60	4.65	4.65	4.31	3.88
Ctag [%]	1.90	2.06	2.22	2.12	1.76
Jet Eff [%]	0.01	0.08	0.15	0.09	0.05
Jet Energy Resolution [%]	0.65	1.03	0.47	0.14	1.15
JVF [%]	1.31	1.53	1.90	2.18	2.33
Lepton Trigger Eff. [%]	1.33	1.35	1.38	1.39	1.29
Lepton Identification Eff. [%]	0.72	0.77	0.78	0.74	0.69
Lepton Reconstruction Eff. [%]	0.33	0.34	0.33	0.28	0.38
JES EffectiveNP STAT1 [%]	0.80	0.97	1.35	1.65	1.34
JES EffectiveNP STAT2 [%]	0.07	0.05	0.02	0.15	0.26
JES EffectiveNP STAT3 [%]	0.04	0.06	0.19	0.38	0.87
JES EffectiveNP MODEL1 [%]	1.43	1.65	2.51	3.36	3.24
JES EffectiveNP MODEL2 [%]	0.10	0.12	0.12	0.13	0.77
JES EffectiveNP MODEL3 [%]	0.09	0.08	0.09	0.33	0.78
JES EffectiveNP MODEL4 [%]	0.05	0.06	0.10	0.18	0.26
JES EffectiveNP DET1 [%]	0.45	0.51	1.00	2.01	3.03
JES EffectiveNP DET2 [%]	0.03	0.04	0.08	0.23	0.21
JES EffectiveNP MIXED1 [%]	0.01	0.03	0.07	0.18	0.19
JES EffectiveNP MIXED2 [%]	0.20	0.25	0.38	0.48	0.56
JES EtaIntercalibration TotalStat [%]	0.27	0.34	0.57	1.09	1.15
JES EtaIntercalibration Theory [%]	0.22	0.55	2.25	4.94	8.84
JES SingleParticle HighPt [%]	0.02	0.01	0.05	0.01	0.02
JES RelativeNonClosure MC11b [%]	0.11	0.17	0.49	0.89	1.36
JES Pileup OffsetMu [%]	0.46	0.26	0.28	0.55	0.86
JES Pileup OffsetNPV [%]	0.23	0.20	0.17	0.19	0.65
JES closeby [%]	1.40	1.73	3.20	5.33	7.34
JES flavor comp [%]	0.63	0.87	1.99	4.12	5.43
JES flavor response [%]	0.36	0.48	1.07	2.27	3.02
JES B Jes Unc. [%]	1.28	1.29	1.30	1.27	1.97
Muon ID [%]	0.01	0.02	0.02	0.06	0.03
Muon MS [%]	0.02	0.03	0.03	0.01	0.04
Muon Momentum Scaling [%]	0.28	0.26	0.30	0.22	0.16
Parton Shower [%]	6.76	2.40	3.69	6.42	5.86
I/FSR [%]	1.96	5.78	6.78	8.46	13.13
Color Reconnection [%]	0.17	0.45	1.81	1.62	0.63
Generator [%]	0.45	2.30	5.29	7.03	7.33
PDF [%]	0.57	0.45	0.32	0.18	3.36
Lumi. Uncertainty [%]	1.80	1.80	1.80	1.80	1.80

**Table C.3:** Relative uncertainties on the final differential  $t\bar{t}$  cross-section as a function of the hadronic-leptonic pseudo-top quark system  $p_T(t\bar{t})$  in the muon channel. The systematic uncertainties were propagated to the final distribution using correction factors from the nominal POWHEG+PYTHIA  $t\bar{t}$  MC sample.

Bin Range [GeV]	[0, 25]	[25, 50]	[50, 85]	[85, 125]	[125, 500]
$d\sigma/dp_T(t\bar{t})$ [fb/GeV]	71.460	72.159	28.721	6.475	0.226
<b>Total Uncertainty [%]</b>	11.54	11.54	16.96	23.86	35.89
<b>Statistics [%]</b>	2.02	1.64	2.44	4.96	10.18
<b>Systematics [%]</b>	11.36	11.43	16.79	23.33	34.42
MC Stats on Correction Factors [%]	0.44	0.38	0.57	1.00	2.07
Background Subtraction Unc. [%]	2.73	1.79	2.37	3.84	5.04
Cellout [%]	3.77	2.57	3.06	4.35	2.98
Pileup [%]	2.35	1.57	1.72	2.53	1.70
Mistag [%]	0.78	0.94	1.13	1.32	1.63
Btag [%]	4.73	4.72	4.60	4.99	5.06
Ctag [%]	1.97	2.08	2.18	2.27	1.94
Jet Eff [%]	0.06	0.11	0.12	0.02	0.26
Jet Energy Resolution [%]	0.56	0.86	0.51	0.38	0.73
JVF [%]	1.34	1.55	1.87	2.51	2.99
Lepton Trigger Eff. [%]	0.57	0.56	0.57	0.67	0.76
Lepton Identification Eff. [%]	2.34	2.34	2.33	2.59	2.90
Lepton Reconstruction Eff. [%]	0.92	0.94	0.96	1.07	1.32
JES EffectiveNP STAT1 [%]	0.84	1.04	1.53	1.88	1.77
JES EffectiveNP STAT2 [%]	0.03	0.04	0.08	0.25	0.60
JES EffectiveNP STAT3 [%]	0.07	0.06	0.25	0.66	1.00
JES EffectiveNP MODEL1 [%]	1.46	1.80	2.60	3.84	4.40
JES EffectiveNP MODEL2 [%]	0.08	0.15	0.09	0.43	0.87
JES EffectiveNP MODEL3 [%]	0.05	0.11	0.07	0.53	1.18
JES EffectiveNP MODEL4 [%]	0.00	0.03	0.13	0.29	0.44
JES EffectiveNP DET1 [%]	0.51	0.64	1.14	2.42	4.27
JES EffectiveNP DET2 [%]	0.03	0.01	0.11	0.25	0.36
JES EffectiveNP MIXED1 [%]	0.05	0.06	0.10	0.13	0.45
JES EffectiveNP MIXED2 [%]	0.27	0.32	0.44	0.67	0.68
JES EtaIntercalibration TotalStat [%]	0.29	0.39	0.66	1.05	1.67
JES EtaIntercalibration Theory [%]	0.44	0.74	2.29	5.81	10.78
JES SingleParticle HighPt [%]	0.02	0.01	0.02	0.05	0.16
JES RelativeNonClosure MC11b [%]	0.18	0.24	0.51	1.26	2.16
JES Pileup OffsetMu [%]	0.37	0.28	0.33	0.41	0.94
JES Pileup OffsetNPV [%]	0.34	0.22	0.09	0.38	0.25
JES closeby [%]	2.03	2.34	3.60	6.79	9.19
JES flavor comp [%]	0.84	0.98	2.08	4.75	7.31
JES flavor response [%]	0.44	0.51	1.20	2.89	4.35
JES B Jes Unc. [%]	1.32	1.27	1.42	2.20	1.78
Electron Energy Resolution [%]	0.01	0.04	0.04	0.18	0.39
Electron Energy Scale [%]	0.49	0.48	0.50	0.48	0.54
Parton Shower [%]	6.89	0.01	3.98	5.70	12.31
I/FSR [%]	1.76	6.86	11.44	15.09	22.05
Color Reconnection [%]	0.75	0.83	0.23	0.63	3.53
Generator [%]	0.81	3.89	6.18	6.96	10.29
PDF [%]	0.61	0.56	0.30	0.23	0.93
Lumi. Uncertainty [%]	1.80	1.80	1.80	1.80	1.80

**Table C.4:** Relative uncertainties on the final differential  $t\bar{t}$  cross-section as a function of the hadronic-leptonic pseudo-top quark system  $p_T(t\bar{t})$  in the electron channel. The systematic uncertainties were propagated to the final distribution using correction factors from the nominal POWHEG+PYTHIA  $t\bar{t}$  MC sample.

Bin Range [rapidity]	[0.0, 0.1]	[0.1, 0.2]	[0.2, 0.4]	[0.4, 0.6]	[0.6, 0.7]	[0.7, 0.8]	[0.8, 1.0]	[1.0, 1.2]	[1.2, 1.6]	[1.6, 2.5]
$d\sigma/d y(t\bar{t}) $ [fb/rapidity]	5993.229	5667.218	5328.119	4896.724	4003.569	3170.661	2227.882	1677.694	704.375	39.690
Total Uncertainty [%]	9.20	8.94	9.35	9.22	10.24	11.79	12.49	10.79	12.64	32.33
Statistics [%]	3.49	2.48	2.67	2.74	3.08	3.43	4.00	4.40	5.12	15.20
Systematics [%]	8.52	8.59	8.96	8.81	9.76	11.28	11.83	9.85	11.55	28.54
MC Stats on Correction Factors [%]	0.77	0.57	0.61	0.67	0.69	0.77	0.87	0.98	1.12	3.28
Background Subtraction Unc. [%]	1.73	1.79	1.87	1.92	1.81	1.78	1.75	1.61	1.81	2.92
Cellout [%]	0.26	0.21	0.32	0.15	0.36	0.28	0.40	0.15	0.44	0.67
Pileup [%]	0.05	0.21	0.26	0.16	0.30	0.15	0.23	0.30	0.30	0.13
Mistag [%]	0.87	0.91	0.95	0.86	0.83	0.94	1.09	0.94	0.91	0.09
Btag [%]	4.45	4.51	4.51	4.41	4.62	4.78	5.18	4.72	4.76	6.12
Ctag [%]	1.98	2.03	1.99	1.97	2.10	2.11	2.23	1.80	2.01	1.93
Jet Eff [%]	0.00	0.09	0.06	0.01	0.03	0.09	0.04	0.14	0.02	0.09
Jet Energy Resolution [%]	0.80	0.47	0.25	0.28	0.75	0.84	0.42	1.25	1.91	0.37
JVF [%]	1.56	1.61	1.56	1.52	1.56	1.58	1.68	1.57	1.45	2.04
Lepton Trigger Eff. [%]	1.35	1.41	1.34	1.29	1.36	1.39	1.43	1.28	1.19	1.39
Lepton Identification Eff. [%]	0.76	0.78	0.77	0.74	0.83	0.82	0.83	0.76	0.80	1.07
Lepton Reconstruction Eff. [%]	0.31	0.31	0.30	0.32	0.30	0.34	0.42	0.37	0.42	0.57
JES EffectiveNP STAT1 [%]	1.06	1.02	1.00	1.11	1.20	1.21	1.33	1.14	0.88	1.06
JES EffectiveNP STAT2 [%]	0.06	0.03	0.00	0.04	0.06	0.03	0.10	0.00	0.03	0.31
JES EffectiveNP STAT3 [%]	0.09	0.15	0.11	0.13	0.18	0.13	0.20	0.19	0.16	0.07
JES EffectiveNP MODEL1 [%]	1.75	1.74	1.79	1.87	2.06	1.92	2.06	1.83	1.80	2.26
JES EffectiveNP MODEL2 [%]	0.08	0.14	0.09	0.06	0.06	0.10	0.17	0.12	0.10	0.33
JES EffectiveNP MODEL3 [%]	0.03	0.08	0.13	0.08	0.00	0.04	0.03	0.00	0.02	0.23
JES EffectiveNP MODEL4 [%]	0.11	0.08	0.08	0.10	0.01	0.10	0.13	0.08	0.08	0.47
JES EffectiveNP DET1 [%]	0.76	0.71	0.65	0.70	0.75	0.74	1.10	0.76	0.90	1.75
JES EffectiveNP DET2 [%]	0.04	0.07	0.08	0.10	0.07	0.01	0.07	0.01	0.17	0.54
JES EffectiveNP MIXED1 [%]	0.06	0.04	0.03	0.09	0.09	0.13	0.17	0.01	0.07	0.10
JES EffectiveNP MIXED2 [%]	0.31	0.27	0.26	0.29	0.35	0.45	0.39	0.29	0.16	0.46
JES EtaIntercalibration TotalStat [%]	0.38	0.35	0.37	0.47	0.59	0.52	0.68	0.34	0.41	0.53
JES EtaIntercalibration Theory [%]	0.37	0.77	0.80	0.87	1.33	1.60	2.26	2.20	3.25	6.45
JES SingleParticle HighPt [%]	0.02	0.01	0.01	0.01	0.00	0.01	0.06	0.00	0.00	0.11
JES RelativeNonClosure MC11b [%]	0.01	0.15	0.25	0.43	0.32	0.43	0.61	0.32	0.58	2.06
JES Pileup OffsetMu [%]	0.36	0.27	0.28	0.20	0.28	0.20	0.23	0.23	0.49	0.01
JES Pileup OffsetNPV [%]	0.21	0.12	0.24	0.25	0.13	0.06	0.05	0.30	0.04	0.82
JES closeby [%]	2.17	2.01	1.85	1.83	2.16	2.35	2.92	2.56	2.69	4.42
JES flavor comp [%]	1.19	1.05	1.35	1.54	1.62	1.34	1.53	1.33	1.31	2.00
JES flavor response [%]	0.78	0.61	0.77	0.76	0.78	0.68	0.91	0.77	0.74	1.20
JES B Jes Unc. [%]	1.41	1.31	1.31	1.35	1.25	1.31	1.57	1.50	1.40	2.76
Muon ID [%]	0.05	0.02	0.01	0.05	0.02	0.09	0.10	0.08	0.06	0.37
Muon MS [%]	0.02	0.01	0.08	0.02	0.01	0.14	0.10	0.00	0.02	0.11
Muon Momentum Scaling [%]	0.08	0.30	0.25	0.25	0.35	0.14	0.46	0.44	0.41	0.14
Parton Shower [%]	0.74	1.92	0.92	2.89	2.65	1.58	5.32	3.35	1.12	18.95
I/FSR [%]	3.16	4.04	4.57	3.56	5.22	4.97	5.64	3.99	5.36	14.76
Color Reconnection [%]	1.40	1.67	0.02	0.36	0.81	0.78	0.18	0.09	0.49	7.81
Generator [%]	2.97	0.69	2.79	2.31	1.64	6.29	2.38	2.84	5.63	3.49
PDF [%]	0.48	0.25	0.24	0.22	0.20	0.25	0.12	0.21	0.34	1.71
Lumi. Uncertainty [%]	1.80	1.80	1.80	1.80	1.80	1.80	1.80	1.80	1.80	1.80

**Table C.5:** Relative uncertainties on the final differential  $t\bar{t}$  cross-section as a function of the hadronic-leptonic pseudo-top quark system  $|y(t\bar{t})|$  in the muon channel. The systematic uncertainties were propagated to the final distribution using correction factors from the nominal POWHEG+PYTHIA  $t\bar{t}$  MC sample.

Bin Range [rapidity]	[0.0, 0.1]	[0.1, 0.2]	[0.2, 0.4]	[0.4, 0.6]	[0.6, 0.7]	[0.7, 0.8]	[0.8, 1.0]	[1.0, 1.2]	[1.2, 1.6]	[1.6, 2.5]
$d\sigma/d y(t\bar{t}) $ [fb/rapidity]	5794.787	5585.784	5161.710	4796.959	4038.601	3045.171	2403.770	1491.000	591.524	38.287
<b>Total Uncertainty [%]</b>	12.14	11.75	11.50	10.90	11.73	12.08	13.33	15.07	16.82	31.94
<b>Statistics [%]</b>	3.65	2.71	2.93	3.02	3.36	3.80	4.53	5.47	6.68	19.85
<b>Systematics [%]</b>	11.58	11.43	11.12	10.47	11.23	11.47	12.54	14.04	15.44	25.03
MC Stats on Correction Factors [%]	0.80	0.62	0.65	0.73	0.73	0.85	1.00	1.16	1.37	3.78
Background Subtraction Unc. [%]	2.46	2.34	2.48	2.19	2.52	2.29	2.18	3.16	2.51	4.34
Cellout [%]	0.04	0.12	0.41	0.15	0.19	0.47	0.30	0.27	0.28	0.55
Pileup [%]	0.11	0.16	0.29	0.12	0.26	0.44	0.41	0.49	0.11	0.45
Mistag [%]	0.96	0.92	0.95	0.88	0.95	1.11	0.83	1.00	1.18	1.51
Btag [%]	4.55	4.52	4.70	4.54	4.61	5.04	4.91	5.42	5.72	6.56
Ctag [%]	2.00	2.07	2.00	1.99	1.99	2.10	1.91	2.35	2.53	1.63
Jet Eff [%]	0.03	0.07	0.02	0.05	0.05	0.07	0.05	0.10	0.02	0.34
Jet Energy Resolution [%]	0.40	0.60	0.34	0.77	0.73	0.32	1.45	0.97	1.36	7.44
JVF [%]	1.58	1.58	1.63	1.61	1.58	1.71	1.61	1.66	1.73	1.99
Lepton Trigger Eff. [%]	0.56	0.61	0.59	0.56	0.53	0.63	0.68	0.65	0.61	1.02
Lepton Identification Eff. [%]	2.20	2.27	2.31	2.20	2.27	2.45	2.42	2.74	3.02	3.55
Lepton Reconstruction Eff. [%]	0.95	0.94	0.98	0.94	0.92	0.91	0.90	0.91	0.74	0.89
JES EffectiveNP STAT1 [%]	1.14	1.08	1.06	1.14	1.03	1.29	1.58	1.50	1.36	1.28
JES EffectiveNP STAT2 [%]	0.00	0.01	0.08	0.04	0.01	0.00	0.00	0.07	0.07	0.51
JES EffectiveNP STAT3 [%]	0.17	0.08	0.12	0.17	0.15	0.17	0.31	0.22	0.27	0.66
JES EffectiveNP MODEL1 [%]	1.95	1.85	2.02	1.98	1.89	1.94	2.54	2.46	2.80	2.76
JES EffectiveNP MODEL2 [%]	0.11	0.06	0.08	0.10	0.05	0.14	0.14	0.07	0.02	0.71
JES EffectiveNP MODEL3 [%]	0.02	0.06	0.07	0.04	0.03	0.20	0.29	0.15	0.10	0.93
JES EffectiveNP MODEL4 [%]	0.07	0.08	0.08	0.06	0.11	0.16	0.11	0.07	0.08	0.47
JES EffectiveNP DET1 [%]	0.58	0.73	0.86	0.87	0.80	0.99	1.37	1.10	1.06	1.16
JES EffectiveNP DET2 [%]	0.08	0.14	0.08	0.07	0.08	0.12	0.17	0.25	0.12	0.39
JES EffectiveNP MIXED1 [%]	0.04	0.07	0.09	0.04	0.01	0.22	0.08	0.17	0.09	0.04
JES EffectiveNP MIXED2 [%]	0.33	0.29	0.34	0.31	0.29	0.47	0.46	0.31	0.52	0.88
JES EtaIntercalibration TotalStat [%]	0.30	0.40	0.47	0.51	0.45	0.58	0.90	0.46	0.80	0.54
JES EtaIntercalibration Theory [%]	0.45	0.63	0.65	1.11	1.66	1.95	2.76	3.90	5.54	4.98
JES SingleParticle HighPt [%]	0.02	0.00	0.04	0.02	0.00	0.06	0.07	0.11	0.03	0.28
JES RelativeNonClosure MC11b [%]	0.25	0.28	0.26	0.31	0.32	0.35	0.92	0.54	1.11	0.12
JES Pileup OffsetMu [%]	0.18	0.08	0.10	0.27	0.14	0.53	0.50	0.09	0.47	0.82
JES Pileup OffsetNPV [%]	0.16	0.19	0.26	0.22	0.26	0.46	0.69	0.21	0.46	0.23
JES closeby [%]	2.73	2.60	2.81	2.43	2.60	3.01	3.27	3.76	5.79	5.81
JES flavor comp [%]	1.42	1.16	1.34	1.51	1.20	1.39	2.17	1.74	2.59	1.79
JES flavor response [%]	0.74	0.69	0.80	0.98	0.71	0.90	1.46	0.93	1.38	0.26
JES B Jes Unc. [%]	1.21	1.49	1.35	1.07	1.31	1.57	1.79	2.10	2.16	4.08
Electron Energy Resolution [%]	0.20	0.13	0.16	0.16	0.08	0.24	0.21	0.21	0.43	0.50
Electron Energy Scale [%]	0.41	0.36	0.56	0.53	0.55	0.72	0.69	0.81	0.92	0.69
Parton Shower [%]	1.92	1.12	1.04	1.08	1.45	3.25	0.15	1.61	3.45	4.66
I/FSR [%]	5.68	6.77	6.82	5.61	7.33	6.56	6.12	8.07	8.12	16.72
Color Reconnection [%]	2.01	0.88	0.02	0.35	0.05	0.51	0.60	3.01	0.40	3.04
Generator [%]	5.66	4.67	3.19	3.90	2.31	0.49	5.23	2.79	1.15	1.41
PDF [%]	0.19	0.24	0.25	0.23	0.18	0.20	0.10	0.91	0.44	7.81
Lumi. Uncertainty [%]	1.80	1.80	1.80	1.80	1.80	1.80	1.80	1.80	1.80	1.80

**Table C.6:** Relative uncertainties on the final differential  $t\bar{t}$  cross-section as a function of the hadronic-leptonic pseudo-top quark system  $|y(t\bar{t})|$  in the electron channel. The systematic uncertainties were propagated to the final distribution using correction factors from the nominal POWHEG+PYTHIA  $t\bar{t}$  MC sample.

Bin Range [GeV]	[0, 45]	[45, 90]	[90, 120]	[120, 150]	[150, 180]	[180, 220]	[220, 260]	[260, 300]	[300, 350]	[350, 800]
$d\sigma/dp_T(t)$ [fb/GeV]	13.031	30.769	32.628	24.796	16.518	9.615	5.701	2.965	1.418	0.119
Total Uncertainty [%]	9.45	8.75	9.35	10.10	12.14	13.27	16.23	13.62	18.20	23.62
Statistics [%]	3.58	2.17	2.48	2.76	3.15	3.71	4.77	6.63	9.12	12.63
Systematics [%]	8.75	8.48	9.01	9.71	11.72	12.74	15.51	11.89	15.75	19.95
MC Stats on Correction Factors [%]	0.83	0.49	0.55	0.64	0.74	0.85	1.14	1.53	2.01	2.55
Background Subtraction Unc. [%]	2.70	1.91	1.80	1.65	1.69	1.73	1.74	1.97	1.92	5.03
Cellout [%]	0.14	0.26	0.37	0.36	0.33	0.04	0.25	0.29	0.18	0.93
Pileup [%]	0.07	0.18	0.19	0.22	0.12	0.02	0.08	0.14	0.09	0.92
Mistag [%]	1.03	1.01	0.85	0.89	0.96	0.89	0.83	0.83	0.96	1.24
Btag [%]	4.23	4.30	4.44	4.61	4.74	5.19	5.25	5.69	6.24	7.43
Ctag [%]	2.21	2.21	2.04	2.00	1.97	1.84	1.58	1.51	1.50	1.50
Jet Eff [%]	0.02	0.09	0.02	0.08	0.03	0.16	0.10	0.15	0.15	0.06
Jet Energy Resolution [%]	1.06	0.84	0.37	0.31	1.18	1.54	0.21	1.25	2.63	0.97
JVF [%]	1.48	1.53	1.55	1.61	1.62	1.66	1.62	1.68	1.90	2.18
Lepton Trigger Eff. [%]	1.33	1.28	1.31	1.30	1.32	1.42	1.39	1.43	1.61	1.86
Lepton Identification Eff. [%]	0.72	0.76	0.75	0.75	0.77	0.76	0.76	0.81	0.92	0.97
Lepton Reconstruction Eff. [%]	0.25	0.33	0.32	0.34	0.31	0.37	0.39	0.42	0.40	0.62
JES EffectiveNP STAT1 [%]	1.10	1.11	1.19	1.10	0.96	0.91	0.71	0.70	0.78	0.41
JES EffectiveNP STAT2 [%]	0.11	0.06	0.02	0.03	0.11	0.18	0.29	0.21	0.45	0.58
JES EffectiveNP STAT3 [%]	0.28	0.08	0.05	0.33	0.34	0.52	0.62	0.88	0.86	1.02
JES EffectiveNP MODEL1 [%]	1.42	1.59	1.91	2.02	2.08	2.00	1.69	2.29	2.08	1.37
JES EffectiveNP MODEL2 [%]	0.53	0.34	0.19	0.10	0.14	0.54	0.79	1.05	1.37	1.64
JES EffectiveNP MODEL3 [%]	0.53	0.30	0.13	0.14	0.32	0.63	0.79	0.94	1.03	0.58
JES EffectiveNP MODEL4 [%]	0.13	0.01	0.01	0.16	0.22	0.22	0.32	0.19	0.64	0.46
JES EffectiveNP DET1 [%]	0.51	0.04	0.30	1.11	1.69	2.07	2.00	2.91	4.90	5.87
JES EffectiveNP DET2 [%]	0.01	0.03	0.05	0.08	0.11	0.18	0.27	0.18	0.29	0.44
JES EffectiveNP MIXED1 [%]	0.09	0.03	0.04	0.08	0.13	0.34	0.31	0.23	0.82	1.67
JES EffectiveNP MIXED2 [%]	0.19	0.29	0.29	0.36	0.28	0.26	0.40	0.21	0.42	0.49
JES EtaIntercalibration TotalStat [%]	0.32	0.34	0.42	0.68	0.58	0.48	0.51	0.74	0.66	0.69
JES EtaIntercalibration Theory [%]	0.26	0.50	1.06	1.84	1.99	2.06	2.23	3.13	3.40	3.73
JES SingleParticle HighPt [%]	0.03	0.00	0.03	0.01	0.03	0.02	0.00	0.04	0.07	0.08
JES RelativeNonClosure MC11b [%]	0.22	0.17	0.26	0.30	0.31	0.50	0.56	0.52	0.66	0.46
JES Pileup OffsetMu [%]	0.18	0.30	0.14	0.10	0.28	0.09	0.28	0.13	0.34	0.87
JES Pileup OffsetNPV [%]	0.08	0.22	0.21	0.18	0.17	0.26	0.29	0.17	0.47	1.25
JES closeby [%]	1.13	1.22	1.87	2.82	3.17	3.49	2.60	3.41	5.08	5.16
JES flavor comp [%]	0.30	0.40	0.67	1.52	2.27	2.75	2.47	3.34	5.22	6.58
JES flavor response [%]	0.14	0.24	0.38	0.84	1.17	1.63	1.76	2.12	2.91	4.06
JES B Jes Unc. [%]	0.31	0.27	1.54	1.92	2.37	2.91	2.50	2.74	3.52	3.99
Muon ID [%]	0.02	0.00	0.02	0.05	0.05	0.09	0.12	0.16	0.22	0.22
Muon MS [%]	0.07	0.00	0.05	0.06	0.01	0.04	0.06	0.05	0.05	0.03
Muon Momentum Scaling [%]	0.37	0.32	0.35	0.25	0.28	0.18	0.01	0.12	0.13	0.06
Parton Shower [%]	3.69	3.61	1.26	0.58	3.33	1.06	2.95	2.00	4.61	3.95
I/FSR [%]	3.68	3.68	4.21	3.23	5.89	6.45	11.00	4.17	5.54	10.49
Color Reconnection [%]	0.06	1.09	0.37	0.17	1.40	0.86	0.75	1.07	2.52	0.96
Generator [%]	1.58	0.65	3.45	4.51	3.74	5.17	5.31	1.98	1.05	0.80
PDF [%]	0.23	0.40	0.24	0.21	0.20	0.25	0.89	0.20	0.67	1.05
Lumi. Uncertainty [%]	1.80	1.80	1.80	1.80	1.80	1.80	1.80	1.80	1.80	1.80

**Table C.7:** Relative uncertainties on the final differential  $t\bar{t}$  cross-section as a function of the hadronic pseudo-top quark  $p_T(t)$  in the muon channel. The systematic uncertainties were propagated to the final distribution using correction factors from the nominal POWHEG+PYTHIA  $t\bar{t}$  MC sample.

Bin Range [GeV]	[0, 45]	[45, 90]	[90, 120]	[120, 150]	[150, 180]	[180, 220]	[220, 260]	[260, 300]	[300, 350]	[350, 800]
$d\sigma/dp_T(t)$ [fb/GeV]	13.357	28.792	32.961	24.849	15.626	9.502	5.700	2.805	1.188	0.116
<b>Total Uncertainty [%]</b>	11.08	10.40	10.86	11.81	14.46	15.10	15.70	17.61	25.69	33.13
<b>Statistics [%]</b>	4.11	2.43	2.72	2.95	3.56	3.99	5.34	7.19	10.43	14.04
<b>Systematics [%]</b>	10.29	10.11	10.51	11.44	14.02	14.57	14.76	16.08	23.48	30.00
MC Stats on Correction Factors [%]	0.85	0.54	0.60	0.65	0.79	0.89	1.17	1.53	2.13	2.73
Background Subtraction Unc. [%]	3.18	3.16	2.31	1.76	2.05	2.18	2.11	2.80	3.48	4.96
Cellout [%]	0.11	0.01	0.24	0.33	0.39	0.37	0.14	0.10	0.47	0.06
Pileup [%]	0.14	0.08	0.17	0.23	0.27	0.00	0.01	0.11	0.17	0.27
Mistag [%]	0.92	1.03	0.94	0.90	0.93	0.99	0.77	0.61	0.91	1.09
Btag [%]	4.24	4.60	4.47	4.65	4.94	5.18	5.05	5.87	7.30	7.23
Ctag [%]	2.04	2.35	2.07	1.93	1.98	1.95	1.56	1.79	2.21	2.30
Jet Eff [%]	0.03	0.14	0.15	0.06	0.01	0.02	0.00	0.17	0.01	0.06
Jet Energy Resolution [%]	0.77	0.47	0.57	0.34	0.82	1.35	0.72	1.43	1.64	7.28
JVF [%]	1.47	1.61	1.51	1.52	1.69	1.67	1.61	1.75	2.23	2.53
Lepton Trigger Eff. [%]	0.63	0.62	0.54	0.58	0.62	0.60	0.68	0.67	0.71	0.96
Lepton Identification Eff. [%]	2.20	2.44	2.30	2.33	2.45	2.42	2.24	2.58	3.01	2.95
Lepton Reconstruction Eff. [%]	0.92	0.96	0.89	0.92	0.98	0.96	0.78	0.82	1.29	1.24
JES EffectiveNP STAT1 [%]	1.25	1.25	1.25	1.27	1.19	1.19	0.77	0.72	0.58	0.73
JES EffectiveNP STAT2 [%]	0.14	0.15	0.08	0.05	0.07	0.20	0.23	0.12	0.39	0.84
JES EffectiveNP STAT3 [%]	0.18	0.13	0.11	0.21	0.45	0.36	0.65	0.54	1.02	1.30
JES EffectiveNP MODEL1 [%]	1.63	1.95	1.86	2.22	2.54	2.49	2.19	1.48	2.18	2.09
JES EffectiveNP MODEL2 [%]	0.47	0.36	0.31	0.08	0.17	0.41	1.06	0.62	0.87	2.40
JES EffectiveNP MODEL3 [%]	0.45	0.41	0.28	0.06	0.24	0.53	0.86	0.79	1.67	0.68
JES EffectiveNP MODEL4 [%]	0.05	0.03	0.02	0.04	0.09	0.08	0.31	0.21	0.54	0.45
JES EffectiveNP DET1 [%]	0.60	0.09	0.37	1.35	1.51	1.74	2.53	3.10	4.22	7.36
JES EffectiveNP DET2 [%]	0.07	0.05	0.13	0.11	0.15	0.15	0.23	0.22	0.30	0.41
JES EffectiveNP MIXED1 [%]	0.02	0.07	0.07	0.06	0.10	0.09	0.45	0.10	0.45	2.02
JES EffectiveNP MIXED2 [%]	0.31	0.23	0.43	0.37	0.30	0.25	0.29	0.53	0.54	0.63
JES EtaIntercalibration TotalStat [%]	0.27	0.43	0.48	0.55	0.69	0.49	0.59	0.65	0.86	0.88
JES EtaIntercalibration Theory [%]	0.39	0.70	1.22	1.75	1.92	2.45	2.68	2.50	3.64	4.99
JES SingleParticle HighPt [%]	0.00	0.01	0.04	0.00	0.06	0.08	0.05	0.00	0.02	0.00
JES RelativeNonClosure MC11b [%]	0.29	0.24	0.33	0.37	0.54	0.46	0.55	0.19	0.96	0.81
JES Pileup OffsetMu [%]	0.42	0.17	0.48	0.24	0.38	0.30	0.22	0.30	0.65	0.81
JES Pileup OffsetNPV [%]	0.17	0.17	0.30	0.27	0.27	0.26	0.44	0.47	0.95	1.00
JES closeby [%]	2.13	2.08	2.24	3.62	3.65	3.82	4.18	3.90	4.65	6.21
JES flavor comp [%]	0.71	0.41	0.83	1.78	2.03	2.99	3.36	3.51	5.10	7.60
JES flavor response [%]	0.43	0.15	0.43	1.07	1.25	1.63	2.08	2.15	2.81	4.67
JES B Jes Unc. [%]	0.35	0.38	1.32	2.24	2.48	2.57	2.71	2.67	3.10	5.14
Electron Energy Resolution [%]	0.13	0.03	0.04	0.10	0.07	0.10	0.06	0.32	0.36	0.20
Electron Energy Scale [%]	0.63	0.56	0.52	0.38	0.39	0.48	0.49	0.36	0.85	1.01
Parton Shower [%]	0.04	0.91	0.28	1.54	0.80	4.65	5.43	0.55	0.71	7.53
I/FSR [%]	5.58	5.37	5.33	6.52	8.85	9.01	8.74	11.41	18.43	11.11
Color Reconnection [%]	2.16	0.13	1.03	0.58	0.49	0.63	1.21	0.83	0.22	0.10
Generator [%]	3.54	3.08	4.69	2.94	5.31	2.35	0.11	1.47	1.45	15.34
PDF [%]	0.32	0.43	0.38	0.39	0.47	0.46	0.58	0.54	0.39	8.61
Lumi. Uncertainty [%]	1.80	1.80	1.80	1.80	1.80	1.80	1.80	1.80	1.80	1.80

**Table C.8:** Relative uncertainties on the final differential  $t\bar{t}$  cross-section as a function of the hadronic pseudo-top quark  $p_T(t)$  in the electron channel. The systematic uncertainties were propagated to the final distribution using correction factors from the nominal POWHEG+PYTHIA  $t\bar{t}$  MC sample.

Bin Range [GeV]	[0, 45]	[45, 90]	[90, 120]	[120, 150]	[150, 180]	[180, 220]	[220, 260]	[260, 300]	[300, 350]	[350, 800]
$d\sigma/dp_T(t)$ [fb/GeV]	12.127	29.065	32.459	25.747	17.101	10.853	5.937	2.880	1.404	0.167
Total Uncertainty [%]	10.45	8.66	8.53	9.95	12.32	11.80	14.63	17.01	18.76	20.56
Statistics [%]	3.62	2.07	2.19	2.41	2.84	3.24	4.26	6.26	9.07	10.93
Systematics [%]	9.80	8.41	8.25	9.65	11.98	11.34	13.99	15.81	16.42	17.41
MC Stats on Correction Factors [%]	0.82	0.49	0.50	0.57	0.69	0.79	1.07	1.42	1.93	2.29
Background Subtraction Unc. [%]	2.92	1.72	1.35	1.35	1.52	1.63	1.64	1.76	3.07	3.42
Cellout [%]	0.38	0.35	0.25	0.31	0.21	0.14	0.58	0.80	0.68	0.56
Pileup [%]	0.22	0.27	0.17	0.13	0.24	0.25	0.35	0.24	0.25	0.63
Mistag [%]	1.12	0.95	0.84	0.85	0.84	0.82	0.88	1.14	1.01	0.52
Btag [%]	4.34	4.21	4.36	4.60	4.88	4.91	5.37	6.42	6.90	5.93
Ctag [%]	2.06	2.19	2.08	2.03	2.03	1.94	1.61	1.35	1.59	1.19
Jet Eff [%]	0.07	0.00	0.06	0.06	0.10	0.09	0.04	0.05	0.03	0.17
Jet Energy Resolution [%]	0.73	1.15	0.35	0.31	0.93	0.78	0.65	0.86	0.23	1.57
JVF [%]	1.52	1.53	1.53	1.58	1.63	1.57	1.61	1.88	1.96	1.99
Lepton Trigger Eff. [%]	1.32	1.33	1.30	1.32	1.38	1.36	1.39	1.66	1.72	1.37
Lepton Identification Eff. [%]	0.79	0.77	0.77	0.78	0.83	0.79	0.76	0.87	0.99	0.81
Lepton Reconstruction Eff. [%]	0.32	0.31	0.31	0.33	0.32	0.34	0.40	0.46	0.56	0.41
JES EffectiveNP STAT1 [%]	1.21	1.08	1.06	1.18	1.15	0.99	0.88	0.96	0.56	0.32
JES EffectiveNP STAT2 [%]	0.14	0.10	0.02	0.04	0.14	0.13	0.23	0.20	0.46	0.56
JES EffectiveNP STAT3 [%]	0.18	0.12	0.10	0.19	0.43	0.43	0.73	0.81	0.79	0.67
JES EffectiveNP MODEL1 [%]	1.62	1.53	1.74	2.12	2.28	2.08	2.15	2.10	2.01	1.22
JES EffectiveNP MODEL2 [%]	0.48	0.34	0.16	0.09	0.28	0.38	0.70	0.77	1.28	1.22
JES EffectiveNP MODEL3 [%]	0.49	0.32	0.11	0.12	0.37	0.43	0.73	0.72	0.69	0.68
JES EffectiveNP MODEL4 [%]	0.08	0.07	0.06	0.09	0.07	0.15	0.28	0.47	0.60	0.33
JES EffectiveNP DET1 [%]	0.38	0.18	0.39	0.92	1.60	1.79	2.53	3.35	5.17	5.41
JES EffectiveNP DET2 [%]	0.03	0.03	0.05	0.08	0.11	0.05	0.15	0.34	0.24	0.28
JES EffectiveNP MIXED1 [%]	0.09	0.00	0.00	0.09	0.15	0.17	0.37	0.51	1.00	1.40
JES EffectiveNP MIXED2 [%]	0.36	0.25	0.26	0.32	0.38	0.34	0.31	0.44	0.41	0.51
JES EtaIntercalibration TotalStat [%]	0.37	0.30	0.37	0.50	0.66	0.65	0.73	0.73	0.54	0.54
JES EtaIntercalibration Theory [%]	0.36	0.33	0.80	1.49	2.17	2.54	3.06	3.15	3.57	3.26
JES SingleParticle HighPt [%]	0.02	0.01	0.01	0.00	0.01	0.02	0.07	0.04	0.00	0.06
JES RelativeNonClosure MC11b [%]	0.22	0.17	0.18	0.30	0.52	0.55	0.59	0.58	0.50	0.47
JES Pileup OffsetMu [%]	0.12	0.24	0.16	0.13	0.22	0.27	0.55	0.35	0.33	0.25
JES Pileup OffsetNPV [%]	0.02	0.05	0.20	0.29	0.25	0.36	0.48	0.36	0.73	1.17
JES closeby [%]	1.06	1.18	1.66	2.48	3.09	3.54	4.04	4.23	5.78	5.36
JES flavor comp [%]	0.46	0.21	0.61	1.40	2.18	2.69	3.09	3.77	5.91	5.72
JES flavor response [%]	0.35	0.05	0.40	0.93	1.40	1.65	1.95	2.56	3.87	3.40
JES B Jes Unc. [%]	0.37	0.53	1.33	2.08	2.40	2.37	2.65	3.12	3.69	2.90
Muon ID [%]	0.08	0.02	0.01	0.03	0.02	0.06	0.18	0.17	0.08	0.17
Muon MS [%]	0.05	0.01	0.05	0.03	0.05	0.12	0.13	0.09	0.26	0.29
Muon Momentum Scaling [%]	0.41	0.38	0.28	0.24	0.19	0.14	0.13	0.16	0.16	0.12
Parton Shower [%]	4.05	3.42	1.70	1.55	2.03	1.27	0.30	3.02	3.07	4.61
I/FSR [%]	4.74	3.85	3.60	4.26	6.79	4.93	7.42	8.56	5.91	9.20
Color Reconnection [%]	0.04	0.90	1.13	0.14	1.24	0.86	0.97	0.34	0.42	0.45
Generator [%]	2.77	1.03	2.47	3.61	3.68	4.05	5.74	5.24	0.96	0.17
PDF [%]	0.40	0.36	0.25	0.21	0.19	0.25	0.16	0.18	1.14	0.26
Lumi. Uncertainty [%]	1.80	1.80	1.80	1.80	1.80	1.80	1.80	1.80	1.80	1.80

**Table C.9:** Relative uncertainties on the final differential  $t\bar{t}$  cross-section as a function of the leptonic pseudo-top quark  $p_T(t)$  in the muon channel. The systematic uncertainties were propagated to the final distribution using correction factors from the nominal POWHEG+PYTHIA  $t\bar{t}$  MC sample.

Bin Range [GeV]	[0, 45]	[45, 90]	[90, 120]	[120, 150]	[150, 180]	[180, 220]	[220, 260]	[260, 300]	[300, 350]	[350, 800]
$d\sigma/dp_T(t)$ [fb/GeV]	11.670	27.522	32.347	26.159	17.083	9.889	5.940	3.304	1.529	0.115
<b>Total Uncertainty [%]</b>	11.67	10.16	10.15	11.23	14.66	15.69	15.70	18.13	21.77	30.82
<b>Statistics [%]</b>	4.37	2.42	2.45	2.56	2.91	3.59	4.75	6.11	8.70	13.14
<b>Systematics [%]</b>	10.83	9.87	9.85	10.93	14.37	15.27	14.97	17.07	19.95	27.88
MC Stats on Correction Factors [%]	0.90	0.57	0.55	0.60	0.73	0.82	1.11	1.46	1.94	2.55
Background Subtraction Unc. [%]	4.47	2.86	2.09	1.69	1.79	2.16	1.87	2.33	3.16	4.65
Cellout [%]	0.50	0.24	0.20	0.41	0.28	0.37	0.99	0.74	0.84	0.65
Pileup [%]	0.46	0.18	0.22	0.35	0.23	0.17	0.80	0.60	0.52	0.52
Mistag [%]	1.09	0.98	0.94	0.89	0.95	0.97	0.80	0.62	0.69	1.16
Btag [%]	4.50	4.52	4.45	4.54	4.79	5.36	5.25	5.37	6.17	8.13
Ctag [%]	2.19	2.30	2.09	1.96	2.00	2.03	1.61	1.47	1.73	2.50
Jet Eff [%]	0.00	0.15	0.11	0.09	0.06	0.04	0.02	0.09	0.04	0.08
Jet Energy Resolution [%]	0.93	0.15	0.82	0.41	0.41	0.77	1.28	3.28	1.28	0.85
JVF [%]	1.58	1.58	1.49	1.51	1.64	1.73	1.67	1.64	1.83	2.78
Lepton Trigger Eff. [%]	0.69	0.62	0.54	0.56	0.59	0.62	0.69	0.64	0.65	1.06
Lepton Identification Eff. [%]	2.39	2.40	2.30	2.30	2.38	2.50	2.33	2.37	2.52	3.24
Lepton Reconstruction Eff. [%]	0.99	0.94	0.89	0.91	0.96	0.98	0.81	0.77	1.05	1.37
JES EffectiveNP STAT1 [%]	1.13	1.22	1.17	1.24	1.29	1.03	1.01	0.96	0.70	1.06
JES EffectiveNP STAT2 [%]	0.22	0.09	0.09	0.13	0.10	0.25	0.31	0.37	0.47	0.89
JES EffectiveNP STAT3 [%]	0.19	0.09	0.02	0.19	0.42	0.55	0.79	0.72	0.66	0.96
JES EffectiveNP MODEL1 [%]	1.76	1.88	1.89	2.15	2.51	2.40	2.40	1.97	2.11	2.68
JES EffectiveNP MODEL2 [%]	0.48	0.34	0.21	0.10	0.22	0.47	0.95	0.97	0.77	1.64
JES EffectiveNP MODEL3 [%]	0.51	0.36	0.21	0.11	0.26	0.55	0.91	0.94	0.91	0.80
JES EffectiveNP MODEL4 [%]	0.05	0.01	0.03	0.10	0.12	0.22	0.38	0.51	0.47	0.62
JES EffectiveNP DET1 [%]	0.59	0.18	0.38	1.06	1.76	1.98	2.48	3.01	4.28	5.96
JES EffectiveNP DET2 [%]	0.06	0.05	0.04	0.11	0.18	0.16	0.19	0.32	0.26	0.34
JES EffectiveNP MIXED1 [%]	0.00	0.02	0.08	0.14	0.20	0.27	0.50	0.66	0.60	1.49
JES EffectiveNP MIXED2 [%]	0.21	0.28	0.26	0.34	0.42	0.39	0.49	0.69	0.49	0.66
JES EtaIntercalibration TotalStat [%]	0.23	0.36	0.41	0.47	0.75	0.80	0.78	0.71	0.60	0.96
JES EtaIntercalibration Theory [%]	0.25	0.59	0.89	1.52	2.22	2.71	3.06	3.10	3.55	4.52
JES SingleParticle HighPt [%]	0.00	0.01	0.04	0.01	0.05	0.08	0.04	0.00	0.01	0.01
JES RelativeNonClosure MC11b [%]	0.20	0.27	0.28	0.36	0.48	0.65	0.88	0.59	0.59	0.79
JES Pileup OffsetMu [%]	0.43	0.31	0.07	0.07	0.27	0.42	0.51	0.31	0.45	0.15
JES Pileup OffsetNPV [%]	0.34	0.19	0.14	0.28	0.52	0.25	0.28	0.51	0.61	0.76
JES closeby [%]	1.90	2.04	2.24	2.93	3.86	4.21	4.49	4.16	4.52	7.07
JES flavor comp [%]	0.74	0.46	0.78	1.46	2.13	2.88	3.63	4.20	5.11	6.50
JES flavor response [%]	0.50	0.23	0.36	0.91	1.58	1.87	2.01	2.17	2.58	3.98
JES B Jes Unc. [%]	0.67	0.45	1.27	2.25	2.53	2.21	2.65	3.18	3.53	4.02
Electron Energy Resolution [%]	0.06	0.07	0.03	0.02	0.13	0.19	0.12	0.14	0.13	0.24
Electron Energy Scale [%]	0.62	0.60	0.47	0.43	0.37	0.56	0.50	0.39	0.55	0.81
Parton Shower [%]	0.52	0.64	1.54	0.86	0.04	4.34	4.59	1.46	2.80	9.29
I/FSR [%]	4.70	5.31	5.40	6.06	8.83	10.05	8.60	11.38	13.45	14.68
Color Reconnection [%]	0.07	1.49	0.62	0.54	0.14	0.04	1.88	2.04	0.58	0.29
Generator [%]	4.74	2.69	2.96	3.71	6.11	2.02	1.40	3.63	3.62	12.11
PDF [%]	0.30	0.45	0.36	0.33	0.49	0.60	0.57	0.87	4.17	1.22
Lumi. Uncertainty [%]	1.80	1.80	1.80	1.80	1.80	1.80	1.80	1.80	1.80	1.80

**Table C.10:** Relative uncertainties on the final differential  $t\bar{t}$  cross-section as a function of the leptonic pseudo-top quark  $p_T(t)$  in the electron channel. The systematic uncertainties were propagated to the final distribution using correction factors from the nominal POWHEG+PYTHIA  $t\bar{t}$  MC sample.

Bin Range [rapidity]	[0.0, 0.4]	[0.4, 0.8]	[0.8, 1.1]	[1.1, 1.4]	[1.4, 1.8]	[1.8, 2.5]
$d\sigma/d y(t) $ [fb/rapidity]	4391.421	3686.303	2738.081	1781.439	926.038	131.131
<b>Total Uncertainty [%]</b>	9.00	9.35	10.40	11.18	11.15	17.12
<b>Statistics [%]</b>	1.96	2.24	3.04	3.78	4.67	9.46
<b>Systematics [%]</b>	8.78	9.08	9.95	10.53	10.12	14.27
MC Stats on Correction Factors [%]	0.47	0.52	0.70	0.85	1.09	2.26
Background Subtraction Unc. [%]	2.25	2.10	1.82	1.74	1.53	1.89
Cellout [%]	0.19	0.23	0.23	0.43	0.01	0.33
Pileup [%]	0.07	0.19	0.20	0.23	0.21	0.49
Mistag [%]	0.93	0.94	0.84	0.93	0.94	0.97
Btag [%]	4.50	4.59	4.67	4.91	4.75	5.34
Ctag [%]	2.04	2.12	1.96	1.86	1.58	1.79
Jet Eff [%]	0.08	0.05	0.03	0.03	0.12	0.25
Jet Energy Resolution [%]	0.03	0.73	0.27	0.75	1.05	0.38
JVF [%]	1.61	1.56	1.59	1.71	1.65	1.49
Lepton Trigger Eff. [%]	1.34	1.36	1.34	1.34	1.28	1.47
Lepton Identification Eff. [%]	0.74	0.74	0.75	0.84	0.76	0.82
Lepton Reconstruction Eff. [%]	0.33	0.36	0.38	0.40	0.26	0.36
JES EffectiveNP STAT1 [%]	1.05	1.14	1.16	0.98	1.19	1.29
JES EffectiveNP STAT2 [%]	0.02	0.01	0.01	0.00	0.07	0.14
JES EffectiveNP STAT3 [%]	0.08	0.13	0.10	0.12	0.08	0.14
JES EffectiveNP MODEL1 [%]	1.80	1.94	1.89	1.91	1.92	2.05
JES EffectiveNP MODEL2 [%]	0.12	0.05	0.08	0.12	0.08	0.34
JES EffectiveNP MODEL3 [%]	0.06	0.05	0.11	0.08	0.01	0.20
JES EffectiveNP MODEL4 [%]	0.05	0.03	0.03	0.15	0.05	0.02
JES EffectiveNP DET1 [%]	0.77	0.77	0.71	0.77	0.83	1.36
JES EffectiveNP DET2 [%]	0.07	0.03	0.00	0.10	0.18	0.01
JES EffectiveNP MIXED1 [%]	0.04	0.05	0.00	0.06	0.07	0.12
JES EffectiveNP MIXED2 [%]	0.35	0.29	0.31	0.24	0.31	0.63
JES EtaIntercalibration TotalStat [%]	0.41	0.47	0.48	0.44	0.63	1.03
JES EtaIntercalibration Theory [%]	0.43	1.04	1.58	2.52	3.67	4.40
JES SingleParticle HighPt [%]	0.02	0.04	0.05	0.02	0.06	0.01
JES RelativeNonClosure MC11b [%]	0.16	0.18	0.32	0.44	0.82	1.52
JES Pileup OffsetMu [%]	0.24	0.33	0.34	0.13	0.19	0.14
JES Pileup OffsetNPV [%]	0.16	0.20	0.23	0.10	0.22	0.40
JES closeby [%]	2.10	2.11	2.36	2.40	2.51	3.17
JES flavor comp [%]	1.32	1.28	1.41	1.59	1.33	1.15
JES flavor response [%]	0.76	0.76	0.70	0.65	0.78	0.42
JES B Jes Unc. [%]	1.22	1.45	1.62	1.39	1.10	1.15
Muon ID [%]	0.02	0.01	0.02	0.03	0.03	0.06
Muon MS [%]	0.01	0.02	0.01	0.03	0.08	0.09
Muon Momentum Scaling [%]	0.28	0.22	0.35	0.18	0.25	0.17
Parton Shower [%]	2.13	1.32	3.57	2.38	3.84	3.32
I/FSR [%]	3.80	4.20	4.29	3.10	3.44	6.88
Color Reconnection [%]	1.66	0.32	0.58	1.09	1.19	0.66
Generator [%]	1.55	2.60	3.06	5.45	2.18	7.08
PDF [%]	0.51	0.42	0.34	0.17	0.50	0.51
Lumi. Uncertainty [%]	1.80	1.80	1.80	1.80	1.80	1.80

**Table C.11:** Relative uncertainties on the final differential  $t\bar{t}$  cross-section as a function of the hadronic pseudo-top quark  $|y(t)|$  in the muon channel. The systematic uncertainties were propagated to the final distribution using correction factors from the nominal POWHEG+PYTHIA  $t\bar{t}$  MC sample.

Bin Range [rapidity]	[0.0, 0.4]	[0.4, 0.8]	[0.8, 1.1]	[1.1, 1.4]	[1.4, 1.8]	[1.8, 2.5]
$d\sigma/d y(t) $ [fb/rapidity]	4278.304	3703.712	2693.016	1624.920	884.475	119.407
<b>Total Uncertainty [%]</b>	11.85	10.64	11.75	15.68	12.91	19.13
<b>Statistics [%]</b>	2.25	2.43	3.32	4.27	5.47	11.44
<b>Systematics [%]</b>	11.64	10.36	11.27	15.08	11.70	15.33
MC Stats on Correction Factors [%]	0.50	0.55	0.76	0.91	1.12	2.48
Background Subtraction Unc. [%]	2.71	2.77	2.51	2.55	2.51	2.75
Cellout [%]	0.17	0.12	0.06	0.22	0.05	0.20
Pileup [%]	0.09	0.03	0.09	0.13	0.08	0.38
Mistag [%]	0.99	0.94	0.85	1.05	0.99	0.79
Btag [%]	4.66	4.54	4.74	5.26	4.94	5.65
Ctag [%]	2.14	2.02	2.00	2.27	1.74	1.83
Jet Eff [%]	0.08	0.05	0.11	0.14	0.03	0.14
Jet Energy Resolution [%]	0.18	0.19	0.80	0.36	0.20	1.14
JVF [%]	1.63	1.53	1.58	1.71	1.51	1.83
Lepton Trigger Eff. [%]	0.60	0.60	0.61	0.64	0.60	0.67
Lepton Identification Eff. [%]	2.33	2.31	2.41	2.63	2.44	2.75
Lepton Reconstruction Eff. [%]	0.92	0.91	0.88	0.99	0.93	0.91
JES EffectiveNP STAT1 [%]	1.07	1.06	1.15	1.54	1.30	1.07
JES EffectiveNP STAT2 [%]	0.00	0.01	0.02	0.04	0.01	0.10
JES EffectiveNP STAT3 [%]	0.08	0.09	0.10	0.16	0.07	0.23
JES EffectiveNP MODEL1 [%]	1.97	1.78	1.86	2.58	2.05	2.59
JES EffectiveNP MODEL2 [%]	0.03	0.07	0.08	0.09	0.13	0.00
JES EffectiveNP MODEL3 [%]	0.01	0.06	0.08	0.13	0.01	0.04
JES EffectiveNP MODEL4 [%]	0.09	0.04	0.03	0.13	0.01	0.13
JES EffectiveNP DET1 [%]	0.73	0.81	0.94	1.00	0.99	0.82
JES EffectiveNP DET2 [%]	0.04	0.09	0.06	0.12	0.20	0.34
JES EffectiveNP MIXED1 [%]	0.10	0.04	0.08	0.20	0.08	0.05
JES EffectiveNP MIXED2 [%]	0.34	0.25	0.25	0.44	0.52	0.35
JES EtaIntercalibration TotalStat [%]	0.37	0.40	0.46	0.60	0.69	0.70
JES EtaIntercalibration Theory [%]	0.43	0.98	1.69	2.87	4.10	6.05
JES SingleParticle HighPt [%]	0.01	0.03	0.02	0.05	0.04	0.17
JES RelativeNonClosure MC11b [%]	0.23	0.25	0.35	0.82	0.82	0.68
JES Pileup OffsetMu [%]	0.06	0.10	0.28	0.75	0.09	0.21
JES Pileup OffsetNPV [%]	0.25	0.25	0.33	0.43	0.09	0.16
JES closeby [%]	2.67	2.61	3.06	3.19	3.68	3.59
JES flavor comp [%]	1.24	1.35	1.57	2.00	1.89	1.08
JES flavor response [%]	0.72	0.87	0.93	1.14	1.02	0.66
JES B Jes Unc. [%]	1.36	1.30	1.63	1.26	1.37	2.07
Electron Energy Resolution [%]	0.03	0.01	0.00	0.07	0.01	0.83
Electron Energy Scale [%]	0.54	0.45	0.54	0.46	0.54	0.26
Parton Shower [%]	0.33	2.90	0.06	2.39	0.35	1.96
I/FSR [%]	6.26	5.75	6.02	11.08	5.32	7.71
Color Reconnection [%]	0.34	0.97	1.23	0.14	1.28	0.07
Generator [%]	5.55	1.16	4.11	2.31	3.51	5.07
PDF [%]	0.49	0.52	0.33	0.40	0.32	3.66
Lumi. Uncertainty [%]	1.80	1.80	1.80	1.80	1.80	1.80

**Table C.12:** Relative uncertainties on the final differential  $t\bar{t}$  cross-section as a function of the hadronic pseudo-top quark  $|y(t)|$  in the electron channel. The systematic uncertainties were propagated to the final distribution using correction factors from the nominal POWHEG+PYTHIA  $t\bar{t}$  MC sample.

Bin Range [rapidity]	[0.0, 0.4]	[0.4, 0.8]	[0.8, 1.1]	[1.1, 1.4]	[1.4, 1.8]	[1.8, 2.5]
$d\sigma/d y(t) $ [fb/rapidity]	5065.907	3587.717	2342.454	1623.573	798.645	113.690
<b>Total Uncertainty [%]</b>	9.45	9.05	9.51	10.66	11.01	21.45
<b>Statistics [%]</b>	1.96	2.12	2.75	3.13	4.21	9.86
<b>Systematics [%]</b>	9.24	8.80	9.10	10.19	10.17	19.06
MC Stats on Correction Factors [%]	0.45	0.47	0.64	0.77	0.97	2.13
Background Subtraction Unc. [%]	1.70	1.93	1.90	1.73	2.37	4.53
Cellout [%]	0.22	0.16	0.34	0.39	0.11	1.09
Pileup [%]	0.13	0.14	0.12	0.28	0.08	0.44
Mistag [%]	0.92	0.96	0.90	0.90	0.84	0.86
Btag [%]	4.46	4.55	4.73	4.60	4.97	6.07
Ctag [%]	2.10	2.10	1.96	1.76	1.64	1.86
Jet Eff [%]	0.00	0.04	0.05	0.09	0.12	0.35
Jet Energy Resolution [%]	0.05	0.22	0.13	0.76	1.68	2.27
JVF [%]	1.53	1.55	1.58	1.53	1.64	1.90
Lepton Trigger Eff. [%]	1.40	1.47	1.31	1.05	1.02	1.43
Lepton Identification Eff. [%]	0.74	0.78	0.76	0.72	0.81	0.96
Lepton Reconstruction Eff. [%]	0.36	0.36	0.38	0.35	0.32	0.56
JES EffectiveNP STAT1 [%]	1.01	1.00	1.12	1.02	1.08	1.20
JES EffectiveNP STAT2 [%]	0.02	0.00	0.04	0.07	0.00	0.00
JES EffectiveNP STAT3 [%]	0.10	0.11	0.13	0.07	0.06	0.06
JES EffectiveNP MODEL1 [%]	1.79	1.84	1.87	1.75	1.91	2.71
JES EffectiveNP MODEL2 [%]	0.09	0.04	0.11	0.04	0.03	0.09
JES EffectiveNP MODEL3 [%]	0.07	0.05	0.00	0.11	0.03	0.13
JES EffectiveNP MODEL4 [%]	0.06	0.03	0.06	0.12	0.08	0.05
JES EffectiveNP DET1 [%]	0.68	0.71	0.78	0.84	0.83	1.57
JES EffectiveNP DET2 [%]	0.08	0.05	0.11	0.05	0.10	0.31
JES EffectiveNP MIXED1 [%]	0.05	0.06	0.04	0.06	0.03	0.27
JES EffectiveNP MIXED2 [%]	0.29	0.22	0.33	0.27	0.30	0.48
JES EtaIntercalibration TotalStat [%]	0.40	0.42	0.43	0.45	0.53	0.78
JES EtaIntercalibration Theory [%]	0.89	1.13	1.48	1.57	2.11	2.78
JES SingleParticle HighPt [%]	0.02	0.02	0.02	0.00	0.07	0.03
JES RelativeNonClosure MC11b [%]	0.23	0.24	0.30	0.38	0.42	0.46
JES Pileup OffsetMu [%]	0.19	0.20	0.16	0.16	0.24	0.71
JES Pileup OffsetNPV [%]	0.13	0.26	0.29	0.18	0.03	0.55
JES closeby [%]	2.11	2.15	2.16	2.11	2.45	2.75
JES flavor comp [%]	1.35	1.16	1.24	1.24	1.42	3.53
JES flavor response [%]	0.75	0.70	0.71	0.71	0.76	1.95
JES B Jes Unc. [%]	1.03	1.49	1.64	1.41	1.57	0.94
Muon ID [%]	0.01	0.04	0.03	0.08	0.03	0.13
Muon MS [%]	0.03	0.04	0.06	0.07	0.07	0.12
Muon Momentum Scaling [%]	0.12	0.25	0.42	0.33	0.53	0.92
Parton Shower [%]	2.47	1.51	1.11	3.82	2.25	0.81
I/FSR [%]	4.90	3.41	3.98	5.39	4.44	7.86
Color Reconnection [%]	0.18	0.58	1.03	0.68	1.14	2.93
Generator [%]	2.16	3.02	2.76	2.54	3.16	12.74
PDF [%]	0.58	0.40	0.18	0.32	0.42	0.35
Lumi. Uncertainty [%]	1.80	1.80	1.80	1.80	1.80	1.80

**Table C.13:** Relative uncertainties on the final differential  $t\bar{t}$  cross-section as a function of the leptonic pseudo-top quark  $|y(t)|$  in the muon channel. The systematic uncertainties were propagated to the final distribution using correction factors from the nominal POWHEG+PYTHIA  $t\bar{t}$  MC sample.

Bin Range [rapidity]	[0.0, 0.4]	[0.4, 0.8]	[0.8, 1.1]	[1.1, 1.4]	[1.4, 1.8]	[1.8, 2.5]
$d\sigma/d y(t) $ [fb/rapidity]	4800.593	3599.739	2275.813	1566.744	813.557	125.110
<b>Total Uncertainty [%]</b>	12.42	10.56	11.43	12.86	13.06	19.49
<b>Statistics [%]</b>	2.03	2.27	3.43	4.24	5.39	11.30
<b>Systematics [%]</b>	12.26	10.31	10.91	12.14	11.90	15.88
MC Stats on Correction Factors [%]	0.45	0.52	0.74	0.93	1.20	2.41
Background Subtraction Unc. [%]	2.43	2.20	2.78	2.91	3.08	4.45
Cellout [%]	0.09	0.03	0.19	0.73	0.79	0.22
Pileup [%]	0.02	0.08	0.21	0.51	0.53	1.01
Mistag [%]	0.97	0.92	0.93	0.88	0.86	1.11
Btag [%]	4.75	4.52	4.84	4.77	4.78	5.47
Ctag [%]	2.19	1.98	1.98	1.96	1.71	1.65
Jet Eff [%]	0.04	0.04	0.06	0.04	0.24	0.32
Jet Energy Resolution [%]	0.32	0.16	0.18	0.63	1.04	1.95
JVF [%]	1.64	1.55	1.63	1.66	1.59	1.81
Lepton Trigger Eff. [%]	0.60	0.59	0.57	0.57	0.62	0.89
Lepton Identification Eff. [%]	2.31	2.21	2.40	2.56	2.83	3.20
Lepton Reconstruction Eff. [%]	1.07	0.90	0.81	0.64	0.60	0.87
JES EffectiveNP STAT1 [%]	1.16	1.01	1.15	1.28	1.03	1.19
JES EffectiveNP STAT2 [%]	0.00	0.04	0.04	0.03	0.08	0.20
JES EffectiveNP STAT3 [%]	0.12	0.10	0.11	0.21	0.31	0.01
JES EffectiveNP MODEL1 [%]	1.98	1.87	2.00	1.93	1.81	2.74
JES EffectiveNP MODEL2 [%]	0.06	0.08	0.04	0.26	0.20	0.00
JES EffectiveNP MODEL3 [%]	0.04	0.07	0.05	0.10	0.09	0.01
JES EffectiveNP MODEL4 [%]	0.12	0.05	0.04	0.05	0.09	0.09
JES EffectiveNP DET1 [%]	0.78	0.77	0.81	0.77	0.89	1.39
JES EffectiveNP DET2 [%]	0.05	0.01	0.10	0.09	0.13	0.15
JES EffectiveNP MIXED1 [%]	0.12	0.07	0.01	0.06	0.09	0.02
JES EffectiveNP MIXED2 [%]	0.38	0.30	0.32	0.34	0.28	0.76
JES EtaIntercalibration TotalStat [%]	0.41	0.39	0.46	0.54	0.66	0.61
JES EtaIntercalibration Theory [%]	0.98	1.23	1.66	2.39	2.21	3.02
JES SingleParticle HighPt [%]	0.01	0.01	0.03	0.07	0.01	0.12
JES RelativeNonClosure MC11b [%]	0.32	0.24	0.42	0.52	0.64	0.67
JES Pileup OffsetMu [%]	0.02	0.26	0.20	0.21	0.15	0.63
JES Pileup OffsetNPV [%]	0.12	0.28	0.21	0.24	0.35	0.96
JES closeby [%]	2.81	2.63	2.98	3.02	2.92	3.47
JES flavor comp [%]	1.60	1.29	1.22	1.39	1.55	1.42
JES flavor response [%]	0.80	0.79	0.77	0.94	0.97	0.56
JES B Jes Unc. [%]	1.27	1.34	1.66	1.50	1.50	2.52
Electron Energy Resolution [%]	0.06	0.10	0.19	0.16	0.17	0.54
Electron Energy Scale [%]	0.22	0.58	0.79	0.93	0.84	0.60
Parton Shower [%]	0.23	3.81	0.90	1.18	2.97	5.37
I/FSR [%]	8.02	4.85	6.42	6.78	6.80	7.25
Color Reconnection [%]	0.76	0.83	0.12	0.30	0.99	4.56
Generator [%]	4.19	2.64	1.98	4.57	2.31	0.57
PDF [%]	0.56	0.39	0.23	0.47	0.39	4.78
Lumi. Uncertainty [%]	1.80	1.80	1.80	1.80	1.80	1.80

**Table C.14:** Relative uncertainties on the final differential  $t\bar{t}$  cross-section as a function of the leptonic pseudo-top quark  $|y(t)|$  in the electron channel. The systematic uncertainties were propagated to the final distribution using correction factors from the nominal POWHEG+PYTHIA  $t\bar{t}$  MC sample.



# Appendix D.

## BLUE Combination Systematic Uncertainties

This appendix presents information and table of the breakdown of the sources of systematic uncertainty in the measured distributions after the electron and muon combination with the BLUE method.

From running f2av [198], a program which performs a measurement combination similar to BLUE, over the particle level distributions, the  $\chi^2$  and the number of degrees of freedom (equivalent to the number of bins here) of the combination is obtained:

distr.	chi2	ndof
absyttu2	2.03	10
mttu2	0.70	8
ptttu2	1.33	6
thptutt12	0.96	10
tlptutt12	2.49	10
absthyul2	0.70	6
abstlyul2	0.42	6

showing compatibility between the channels.

The BLUE combinations also have as an output tables of systematics for the overall uncertainty contribution of each systematic to the combination systematic. These are given in tables [D.1](#) to [D.7](#).

Bin Range	[225, 400]	[400, 500]	[500, 600]	[600, 700]	[700, 850]	[850, 1000]	[1000, 1250]	[1250, 2500]
$d\sigma/dm(t\bar{t})$ [fb/GeV]	5.15	14.75	10.54	6.38	3.34	1.55	0.61	0.06
Total Uncertainty [%]	10.97	9.56	10.38	10.90	11.83	14.09	15.12	20.35
Statistics [%]	2.57	1.61	1.83	2.97	2.88	4.57	5.43	8.56
Systematics [%]	10.66	9.42	10.22	10.48	11.47	13.33	14.11	18.46
Background Subtraction Unc.	1.37	0.90	1.51	2.00	2.29	3.15	3.59	6.03
Btag	4.83	4.41	4.39	4.56	4.76	5.00	5.26	5.66
Cellout	0.29	0.29	0.18	0.05	0.07	0.17	0.30	0.35
Color Reconnection	0.37	0.72	0.48	0.05	1.36	0.85	2.28	1.63
Ctag	2.02	1.86	1.92	2.09	2.24	2.51	2.59	2.73
Electron Energy Resolution	0.00	0.02	0.05	0.01	0.05	0.02	0.09	0.06
Electron Energy Scale	0.01	0.12	0.11	0.03	0.16	0.09	0.23	0.24
Electron Identification Eff.	0.16	0.64	0.49	0.10	0.50	0.29	0.80	0.95
Electron Reconstruction Eff.	0.07	0.27	0.19	0.04	0.19	0.11	0.31	0.29
Electron Trigger Eff.	0.04	0.16	0.13	0.03	0.13	0.07	0.20	0.23
Generator	3.24	2.46	2.77	3.32	2.37	4.59	3.02	5.19
I/FSR	3.49	5.02	4.62	4.07	5.07	6.25	5.06	9.01
JES B Jes Unc.	3.69	1.25	2.41	3.11	3.34	3.57	4.16	3.66
JES EffectiveNP DET1	2.43	0.49	1.29	1.71	2.28	2.83	3.66	4.12
JES EffectiveNP DET2	0.19	0.10	0.10	0.12	0.14	0.17	0.29	0.29
JES EffectiveNP MIXED1	0.17	0.06	0.08	0.10	0.25	0.16	0.41	0.94
JES EffectiveNP MIXED2	0.10	0.38	0.39	0.32	0.32	0.43	0.39	0.42
JES EffectiveNP MODEL1	0.31	2.09	2.36	2.08	2.08	1.97	1.59	1.55
JES EffectiveNP MODEL2	1.07	0.27	0.14	0.32	0.55	0.76	0.89	1.21
JES EffectiveNP MODEL3	1.32	0.24	0.25	0.46	0.68	0.92	0.84	0.89
JES EffectiveNP MODEL4	0.09	0.04	0.07	0.06	0.19	0.22	0.36	0.39
JES EffectiveNP STAT1	1.03	1.37	1.20	0.96	0.92	0.91	0.55	0.25
JES EffectiveNP STAT2	0.35	0.04	0.04	0.07	0.21	0.32	0.31	0.72
JES EffectiveNP STAT3	0.75	0.07	0.26	0.43	0.59	0.73	0.69	0.79
JES EtaIntercalibration Theory	1.89	0.75	1.45	2.16	3.09	3.38	4.82	7.55
JES EtaIntercalibration TotalStat	0.17	0.48	0.59	0.51	0.68	0.86	0.60	0.54
JES Pileup OffsetMu	0.30	0.34	0.08	0.28	0.25	0.34	0.21	0.71
JES Pileup OffsetNPV	0.32	0.27	0.25	0.36	0.36	0.45	0.60	0.56
JES RelativeNonClosure MC11b	0.26	0.26	0.37	0.41	0.69	0.88	0.47	0.88
JES SingleParticle HighPt	0.02	0.02	0.02	0.02	0.03	0.03	0.06	0.13
JES closeby	1.88	3.01	3.31	3.05	3.09	2.85	3.63	3.07
JES flavor comp	1.51	1.19	1.80	1.97	2.19	2.53	3.70	3.57
JES flavor response	1.02	0.64	1.05	1.11	1.34	1.52	2.39	2.25
JVF	1.53	1.49	1.52	1.57	1.72	1.91	1.87	2.31
Jet Eff	0.10	0.05	0.03	0.05	0.02	0.08	0.06	0.15
Jet Energy Resolution	4.16	0.87	0.69	1.53	1.45	1.92	2.56	0.98
Luminosity	1.69	1.39	1.46	1.88	1.46	1.60	1.36	1.35
MC Stats on Correction Factors	0.58	0.38	0.45	0.72	0.65	1.01	1.16	1.77
Mistag	0.91	0.75	0.81	0.94	1.07	1.41	1.53	2.48
Muon ID	0.03	0.01	0.03	0.04	0.04	0.01	0.09	0.01
Muon Identification Eff.	0.77	0.54	0.57	0.84	0.58	0.67	0.53	0.66
Muon MS	0.01	0.00	0.04	0.05	0.02	0.02	0.15	0.04
Muon Momentum Scaling	0.11	0.18	0.27	0.18	0.28	0.33	0.01	0.41
Muon Reconstruction Eff.	0.35	0.23	0.25	0.37	0.23	0.36	0.34	0.19
Muon Trigger Eff.	1.31	0.96	0.99	1.39	1.05	1.18	0.95	1.09
PDF	0.35	0.46	0.26	0.21	0.22	0.22	0.89	3.12
Parton Shower	0.13	2.29	3.10	1.54	2.26	1.57	0.58	0.51
Pileup	0.21	0.17	0.09	0.02	0.07	0.19	0.25	0.30

**Table D.1:** Relative uncertainties on the final, particle-level differential  $t\bar{t}$  cross-section as a function of the pseudo-top pair mass after the channel combination. The systematic uncertainties were propagated to the final distribution using correction factors from the nominal POWHEG+PYTHIA P2011C  $t\bar{t}$  MC sample.

Bin Range	[0, 25]	[25, 50]	[50, 85]	[85, 125]	[125, 500]
$d\sigma/dp_T(t\bar{t})$ [fb/GeV]	73.05	72.45	28.27	8.01	0.31
Total Uncertainty [%]	10.59	10.21	13.11	17.81	23.57
Statistics [%]	1.43	1.28	3.14	6.01	11.48
Systematics [%]	10.50	10.13	12.73	16.77	20.59
Background Subtraction Unc.	1.71	1.26	2.45	3.26	5.55
Btag	4.63	4.66	4.67	4.06	3.46
Cellout	3.53	2.64	2.97	2.98	3.36
Color Reconnection	0.31	0.49	2.40	1.98	0.38
Ctag	1.92	2.06	2.24	2.07	1.70
Electron Energy Resolution	0.00	0.00	0.01	0.07	0.14
Electron Energy Scale	0.12	0.05	0.19	0.18	0.19
Electron Identification Eff.	0.57	0.25	0.88	0.96	1.02
Electron Reconstruction Eff.	0.22	0.10	0.36	0.40	0.46
Electron Trigger Eff.	0.14	0.06	0.22	0.25	0.26
Generator	0.54	2.47	4.95	7.06	6.30
I/FSR	1.91	5.89	5.03	6.00	10.01
JES B Jes Unc.	1.29	1.29	1.25	0.92	2.04
JES EffectiveNP DET1	0.47	0.53	0.95	1.86	2.59
JES EffectiveNP DET2	0.03	0.04	0.06	0.23	0.15
JES EffectiveNP MIXED1	0.02	0.03	0.06	0.20	0.11
JES EffectiveNP MIXED2	0.22	0.26	0.35	0.41	0.52
JES EffectiveNP MODEL1	1.44	1.67	2.48	3.19	2.83
JES EffectiveNP MODEL2	0.09	0.12	0.13	0.01	0.74
JES EffectiveNP MODEL3	0.08	0.08	0.10	0.26	0.65
JES EffectiveNP MODEL4	0.04	0.06	0.08	0.14	0.20
JES EffectiveNP STAT1	0.81	0.98	1.28	1.57	1.19
JES EffectiveNP STAT2	0.06	0.05	0.00	0.12	0.15
JES EffectiveNP STAT3	0.04	0.06	0.17	0.27	0.82
JES EtaIntercalibration Theory	0.27	0.57	2.24	4.62	8.16
JES EtaIntercalibration TotalStat	0.27	0.34	0.54	1.11	0.97
JES Pileup OffsetMu	0.44	0.27	0.26	0.60	0.83
JES Pileup OffsetNPV	0.25	0.20	0.19	0.12	0.79
JES RelativeNonClosure MC11b	0.13	0.18	0.49	0.75	1.08
JES SingleParticle HighPt	0.02	0.01	0.06	0.00	0.03
JES closeby	1.56	1.79	3.05	4.79	6.69
JES flavor comp	0.68	0.88	1.95	3.88	4.77
JES flavor response	0.38	0.48	1.02	2.04	2.55
JVF	1.31	1.53	1.91	2.05	2.09
Jet Eff	0.02	0.08	0.16	0.11	0.03
Jet Energy Resolution	0.63	1.01	0.45	0.04	1.30
Luminosity	1.43	1.62	2.57	2.56	2.51
MC Stats on Correction Factors	0.33	0.33	0.73	1.40	2.81
Mistag	0.79	0.92	1.11	1.11	0.76
Muon ID	0.01	0.02	0.02	0.08	0.04
Muon Identification Eff.	0.55	0.69	1.08	1.02	0.93
Muon MS	0.01	0.02	0.04	0.01	0.05
Muon Momentum Scaling	0.21	0.24	0.41	0.30	0.22
Muon Reconstruction Eff.	0.25	0.30	0.45	0.38	0.52
Muon Trigger Eff.	1.01	1.20	1.90	1.91	1.75
PDF	0.58	0.47	0.33	0.17	4.21
Parton Shower	6.79	2.15	3.58	6.68	3.60
Pileup	2.08	1.61	1.84	1.83	1.85

**Table D.2:** Relative uncertainties on the final, particle-level differential  $t\bar{t}$  cross-section as a function of the pseudo-top pair  $p_T$  after the channel combination. The systematic uncertainties were propagated to the final distribution using correction factors from the nominal POWHEG+PYTHIA P2011C  $t\bar{t}$  MC sample.

And there are parton-level combinations systematic tables resulting from the BLUE method, given in tables D.8 to D.12.

Bin Range	[0.0, 0.1]	[0.1, 0.2]	[0.2, 0.4]	[0.4, 0.6]	[0.6, 0.7]	[0.7, 0.8]	[0.8, 1.0]	[1.0, 1.2]	[1.2, 1.6]	[1.6, 2.5]
$d\sigma/d y(t\bar{t}) $ [fb/rapidity]	5986.46	5663.52	5321.77	4879.07	4010.64	3112.57	2297.11	1672.06	692.04	38.97
<b>Total Uncertainty [%]</b>	9.20	8.94	9.34	9.14	10.13	10.91	11.84	10.78	12.56	27.80
<b>Statistics [%]</b>	3.37	2.37	2.57	2.32	2.55	2.55	3.01	4.27	4.61	12.58
<b>Systematics [%]</b>	8.56	8.62	8.98	8.84	9.80	10.61	11.45	9.90	11.68	24.79
Background Subtraction Unc.	1.67	1.71	1.80	1.63	1.53	1.43	1.36	1.57	1.64	2.64
Btag	4.45	4.51	4.51	4.43	4.62	4.90	5.07	4.74	4.86	6.35
Cellout	0.25	0.20	0.33	0.15	0.33	0.37	0.36	0.16	0.42	0.61
Color Reconnection	1.42	1.64	0.02	0.36	0.66	0.66	0.34	0.18	0.48	5.37
Ctag	1.98	2.03	1.99	1.98	2.08	2.10	2.10	1.82	2.06	1.78
Electron Energy Resolution	0.01	0.01	0.01	0.03	0.02	0.11	0.08	0.01	0.05	0.26
Electron Energy Scale	0.01	0.02	0.02	0.09	0.11	0.33	0.27	0.02	0.10	0.35
Electron Identification Eff.	0.08	0.10	0.09	0.39	0.46	1.13	0.95	0.08	0.33	1.82
Electron Reconstruction Eff.	0.03	0.04	0.04	0.17	0.19	0.42	0.35	0.03	0.08	0.45
Electron Trigger Eff.	0.02	0.03	0.02	0.10	0.11	0.29	0.27	0.02	0.07	0.52
Generator	3.06	0.87	2.80	2.59	1.78	3.61	3.50	2.84	5.14	2.42
I/FSR	3.24	4.17	4.65	3.92	5.65	5.71	5.83	4.12	5.66	15.76
JES B Jes Unc.	1.41	1.31	1.32	1.30	1.26	1.43	1.65	1.52	1.48	3.44
JES EffectiveNP DET1	0.76	0.71	0.66	0.73	0.76	0.85	1.21	0.77	0.92	1.45
JES EffectiveNP DET2	0.05	0.07	0.08	0.09	0.07	0.06	0.11	0.02	0.16	0.46
JES EffectiveNP MIXED1	0.06	0.04	0.03	0.08	0.08	0.17	0.14	0.01	0.07	0.07
JES EffectiveNP MIXED2	0.31	0.27	0.26	0.29	0.33	0.46	0.42	0.29	0.20	0.67
JES EffectiveNP MODEL1	1.75	1.74	1.79	1.89	2.03	1.93	2.25	1.85	1.91	2.51
JES EffectiveNP MODEL2	0.08	0.13	0.09	0.06	0.06	0.12	0.16	0.12	0.09	0.52
JES EffectiveNP MODEL3	0.02	0.08	0.13	0.07	0.01	0.11	0.13	0.01	0.03	0.59
JES EffectiveNP MODEL4	0.11	0.08	0.08	0.09	0.03	0.13	0.12	0.08	0.08	0.47
JES EffectiveNP STAT1	1.06	1.02	1.00	1.12	1.17	1.25	1.43	1.15	0.93	1.17
JES EffectiveNP STAT2	0.05	0.03	0.01	0.04	0.05	0.02	0.06	0.01	0.03	0.41
JES EffectiveNP STAT3	0.09	0.15	0.11	0.14	0.17	0.15	0.24	0.19	0.17	0.37
JES EtaIntercalibration Theory	0.37	0.76	0.79	0.91	1.40	1.76	2.46	2.26	3.50	5.70
JES EtaIntercalibration TotalStat	0.38	0.35	0.38	0.48	0.56	0.55	0.77	0.34	0.46	0.53
JES Pileup OffsetMu	0.35	0.26	0.28	0.21	0.25	0.35	0.34	0.22	0.49	0.43
JES Pileup OffsetNPV	0.21	0.13	0.24	0.25	0.15	0.25	0.30	0.30	0.08	0.52
JES RelativeNonClosure MC11b	0.02	0.16	0.25	0.41	0.32	0.39	0.73	0.33	0.64	1.07
JES SingleParticle HighPt	0.02	0.01	0.01	0.01	0.00	0.04	0.06	0.01	0.00	0.20
JES closeby	2.19	2.03	1.88	1.94	2.25	2.66	3.06	2.59	3.03	5.13
JES flavor comp	1.19	1.06	1.35	1.53	1.53	1.36	1.79	1.34	1.45	1.89
JES flavor response	0.78	0.61	0.77	0.80	0.77	0.79	1.13	0.77	0.81	0.72
JVF	1.56	1.61	1.56	1.54	1.56	1.64	1.65	1.58	1.48	2.01
Jet Eff	0.00	0.08	0.06	0.02	0.04	0.08	0.05	0.14	0.02	0.21
Jet Energy Resolution	0.78	0.48	0.25	0.37	0.74	0.60	0.83	1.24	1.85	3.99
Luminosity	1.74	1.72	1.73	1.52	1.48	1.28	1.30	1.75	1.62	1.27
MC Stats on Correction Factors	0.74	0.54	0.59	0.56	0.57	0.57	0.66	0.95	1.01	2.51
Mistag	0.87	0.91	0.95	0.86	0.85	1.02	0.98	0.94	0.94	0.81
Muon ID	0.05	0.02	0.01	0.04	0.02	0.05	0.06	0.08	0.06	0.18
Muon Identification Eff.	0.73	0.74	0.74	0.61	0.66	0.44	0.50	0.73	0.71	0.52
Muon MS	0.02	0.01	0.07	0.02	0.01	0.07	0.06	0.00	0.02	0.05
Muon Momentum Scaling	0.08	0.29	0.24	0.21	0.28	0.07	0.28	0.42	0.37	0.07
Muon Reconstruction Eff.	0.30	0.30	0.29	0.27	0.24	0.18	0.25	0.36	0.37	0.28
Muon Trigger Eff.	1.30	1.34	1.29	1.06	1.08	0.74	0.87	1.24	1.06	0.68
PDF	0.47	0.25	0.24	0.22	0.20	0.23	0.11	0.23	0.35	4.84
Parton Shower	0.78	1.89	0.92	2.57	2.41	2.35	3.28	3.30	1.38	11.63
Pileup	0.05	0.21	0.27	0.15	0.29	0.28	0.30	0.31	0.28	0.30

**Table D.3:** Relative uncertainties on the final, particle-level differential  $t\bar{t}$  cross-section as a function of the pseudo-top pair rapidity after the channel combination. The systematic uncertainties were propagated to the final distribution using correction factors from the nominal POWHEG+PYTHIA P2011C  $t\bar{t}$  MC sample.

Bin Range	[0.0, 0.4]	[0.4, 0.8]	[0.8, 1.1]	[1.1, 1.4]	[1.4, 1.8]	[1.8, 2.5]
$d\sigma/d y(t) $ [fb/rapidity]	4386.44	3690.28	2725.83	1771.17	914.12	126.76
<b>Total Uncertainty [%]</b>	8.99	9.22	10.17	11.16	10.77	15.93
<b>Statistics [%]</b>	1.88	1.82	2.39	3.54	3.68	7.31
<b>Systematics [%]</b>	8.79	9.04	9.88	10.58	10.12	14.15
Background Subtraction Unc.	2.15	1.74	1.49	1.63	1.31	1.57
Btag	4.50	4.58	4.69	4.94	4.80	5.45
Cellout	0.19	0.21	0.18	0.42	0.02	0.28
Color Reconnection	1.60	0.47	0.75	1.03	1.21	0.44
Ctag	2.05	2.10	1.97	1.88	1.62	1.81
Electron Energy Resolution	0.00	0.00	0.00	0.00	0.00	0.31
Electron Energy Scale	0.02	0.10	0.15	0.03	0.15	0.10
Electron Identification Eff.	0.10	0.53	0.66	0.17	0.70	1.03
Electron Reconstruction Eff.	0.04	0.21	0.24	0.06	0.27	0.34
Electron Trigger Eff.	0.03	0.14	0.17	0.04	0.17	0.25
Generator	1.73	2.27	3.35	5.24	2.57	6.33
I/FSR	3.91	4.55	4.76	3.63	3.98	7.19
JES B Jes Unc.	1.22	1.42	1.62	1.38	1.18	1.49
JES EffectiveNP DET1	0.77	0.78	0.77	0.79	0.88	1.16
JES EffectiveNP DET2	0.07	0.04	0.02	0.11	0.19	0.13
JES EffectiveNP MIXED1	0.04	0.05	0.02	0.07	0.07	0.09
JES EffectiveNP MIXED2	0.35	0.28	0.29	0.25	0.37	0.53
JES EffectiveNP MODEL1	1.81	1.90	1.88	1.96	1.95	2.25
JES EffectiveNP MODEL2	0.11	0.06	0.08	0.12	0.09	0.21
JES EffectiveNP MODEL3	0.06	0.06	0.10	0.08	0.01	0.14
JES EffectiveNP MODEL4	0.05	0.03	0.03	0.15	0.04	0.06
JES EffectiveNP STAT1	1.05	1.12	1.16	1.02	1.22	1.21
JES EffectiveNP STAT2	0.02	0.01	0.01	0.01	0.05	0.12
JES EffectiveNP STAT3	0.08	0.12	0.10	0.12	0.08	0.18
JES EtaIntercalibration Theory	0.43	1.02	1.61	2.55	3.79	5.01
JES EtaIntercalibration TotalStat	0.41	0.45	0.47	0.45	0.65	0.91
JES Pileup OffsetMu	0.23	0.28	0.32	0.17	0.16	0.17
JES Pileup OffsetNPV	0.16	0.21	0.26	0.12	0.18	0.31
JES RelativeNonClosure MC11b	0.16	0.19	0.33	0.47	0.82	1.21
JES SingleParticle HighPt	0.02	0.04	0.04	0.02	0.05	0.07
JES closeby	2.12	2.23	2.55	2.45	2.85	3.33
JES flavor comp	1.32	1.30	1.45	1.61	1.49	1.12
JES flavor response	0.76	0.78	0.76	0.68	0.85	0.51
JVF	1.61	1.55	1.59	1.71	1.61	1.62
Jet Eff	0.08	0.05	0.05	0.03	0.09	0.21
Jet Energy Resolution	0.04	0.61	0.41	0.72	0.81	0.66
Luminosity	1.72	1.45	1.40	1.69	1.38	1.31
MC Stats on Correction Factors	0.45	0.42	0.55	0.80	0.84	1.69
Mistag	0.93	0.94	0.84	0.94	0.96	0.90
Muon ID	0.02	0.01	0.01	0.03	0.02	0.04
Muon Identification Eff.	0.71	0.57	0.55	0.78	0.54	0.52
Muon MS	0.01	0.02	0.01	0.03	0.06	0.05
Muon Momentum Scaling	0.27	0.17	0.26	0.17	0.18	0.10
Muon Reconstruction Eff.	0.32	0.28	0.28	0.37	0.19	0.23
Muon Trigger Eff.	1.28	1.05	0.98	1.25	0.92	0.92
PDF	0.51	0.44	0.34	0.19	0.45	1.69
Parton Shower	2.05	1.68	2.61	2.38	2.84	2.81
Pileup	0.07	0.15	0.17	0.22	0.17	0.45

**Table D.4:** Relative uncertainties on the final, particle-level differential  $t\bar{t}$  cross-section as a function of the hadronic pseudo-top rapidity after the channel combination. The systematic uncertainties were propagated to the final distribution using correction factors from the nominal POWHEG+PYTHIA P2011C  $t\bar{t}$  MC sample.

Bin Range	[0.0, 0.4]	[0.4, 0.8]	[0.8, 1.1]	[1.1, 1.4]	[1.4, 1.8]	[1.8, 2.5]
$d\sigma/d y(t) $ [fb/rapidity]	5095.10	3589.56	2332.97	1615.44	802.04	120.31
<b>Total Uncertainty [%]</b>	9.41	9.00	9.45	10.59	10.79	17.07
<b>Statistics [%]</b>	2.19	1.83	2.41	2.75	3.47	7.75
<b>Systematics [%]</b>	9.15	8.81	9.13	10.23	10.22	15.21
Background Subtraction Unc.	1.91	1.67	1.67	1.54	1.96	3.21
Btag	4.43	4.54	4.74	4.62	4.93	5.72
Cellout	0.23	0.14	0.32	0.44	0.27	0.58
Color Reconnection	0.12	0.62	0.90	0.62	1.11	3.88
Ctag	2.09	2.08	1.96	1.79	1.66	1.74
Electron Energy Resolution	0.01	0.02	0.03	0.02	0.04	0.31
Electron Energy Scale	0.02	0.09	0.11	0.13	0.19	0.35
Electron Identification Eff.	0.25	0.34	0.34	0.37	0.64	1.86
Electron Reconstruction Eff.	0.12	0.14	0.12	0.09	0.14	0.50
Electron Trigger Eff.	0.07	0.09	0.08	0.08	0.14	0.52
Generator	1.93	2.97	2.65	2.83	2.96	5.68
I/FSR	4.55	3.63	4.32	5.59	4.98	7.50
JES B Jes Unc.	1.00	1.47	1.65	1.42	1.55	1.86
JES EffectiveNP DET1	0.66	0.72	0.79	0.83	0.85	1.47
JES EffectiveNP DET2	0.08	0.05	0.11	0.05	0.10	0.22
JES EffectiveNP MIXED1	0.04	0.06	0.03	0.06	0.05	0.13
JES EffectiveNP MIXED2	0.28	0.23	0.32	0.28	0.29	0.64
JES EffectiveNP MODEL1	1.76	1.84	1.89	1.78	1.89	2.73
JES EffectiveNP MODEL2	0.09	0.04	0.10	0.07	0.07	0.04
JES EffectiveNP MODEL3	0.07	0.06	0.01	0.11	0.05	0.06
JES EffectiveNP MODEL4	0.06	0.03	0.06	0.11	0.08	0.07
JES EffectiveNP STAT1	0.99	1.00	1.13	1.06	1.07	1.20
JES EffectiveNP STAT2	0.02	0.01	0.04	0.06	0.02	0.12
JES EffectiveNP STAT3	0.10	0.11	0.13	0.09	0.12	0.03
JES EtaIntercalibration Theory	0.88	1.14	1.50	1.69	2.13	2.92
JES EtaIntercalibration TotalStat	0.39	0.42	0.44	0.46	0.56	0.68
JES Pileup OffsetMu	0.21	0.21	0.16	0.16	0.22	0.67
JES Pileup OffsetNPV	0.13	0.26	0.28	0.19	0.11	0.79
JES RelativeNonClosure MC11b	0.22	0.24	0.32	0.40	0.47	0.58
JES SingleParticle HighPt	0.02	0.02	0.02	0.01	0.05	0.08
JES closeby	2.03	2.23	2.28	2.24	2.56	3.16
JES flavor comp	1.32	1.18	1.24	1.27	1.45	2.31
JES flavor response	0.75	0.72	0.72	0.75	0.81	1.15
JVF	1.51	1.55	1.59	1.55	1.63	1.85
Jet Eff	0.00	0.04	0.05	0.08	0.15	0.33
Jet Energy Resolution	0.02	0.21	0.13	0.74	1.54	2.08
Luminosity	2.01	1.55	1.56	1.56	1.45	1.29
MC Stats on Correction Factors	0.50	0.41	0.56	0.68	0.80	1.66
Mistag	0.91	0.96	0.90	0.90	0.85	1.00
Muon ID	0.01	0.04	0.03	0.07	0.02	0.05
Muon Identification Eff.	0.82	0.66	0.65	0.62	0.62	0.40
Muon MS	0.04	0.04	0.06	0.06	0.05	0.05
Muon Momentum Scaling	0.14	0.21	0.36	0.28	0.41	0.39
Muon Reconstruction Eff.	0.40	0.31	0.32	0.30	0.25	0.23
Muon Trigger Eff.	1.55	1.24	1.12	0.90	0.79	0.60
PDF	0.58	0.40	0.19	0.34	0.41	2.92
Parton Shower	2.71	1.86	1.08	3.44	2.42	3.45
Pileup	0.14	0.13	0.13	0.31	0.18	0.77

**Table D.5:** Relative uncertainties on the final, particle-level differential  $t\bar{t}$  cross-section as a function of the leptonic pseudo-top rapidity after the channel combination. The systematic uncertainties were propagated to the final distribution using correction factors from the nominal POWHEG+PYTHIA P2011C  $t\bar{t}$  MC sample.

Bin Range	[0, 45]	[45, 90]	[90, 120]	[120, 150]	[150, 180]	[180, 220]	[220, 260]	[260, 300]	[300, 350]	[350, 800]
$d\sigma/dp_T(t)$ [fb/GeV]	13.13	30.30	32.68	24.80	16.48	9.59	5.70	2.94	1.39	0.12
Total Uncertainty [%]	8.96	8.56	9.30	10.04	12.14	13.15	14.97	13.43	18.03	23.23
Statistics [%]	2.77	1.76	2.15	2.38	3.04	3.10	3.67	5.66	8.13	10.91
Systematics [%]	8.52	8.38	9.05	9.75	11.75	12.78	14.52	12.18	16.09	20.50
Background Subtraction Unc.	2.10	1.64	1.57	1.42	1.63	1.46	1.42	1.71	1.74	4.33
Btag	4.23	4.37	4.44	4.62	4.75	5.19	5.14	5.72	6.36	7.40
Cellout	0.13	0.20	0.35	0.35	0.33	0.11	0.19	0.26	0.22	0.79
Color Reconnection	0.73	0.87	0.46	0.24	1.37	0.81	1.01	1.03	2.25	0.83
Ctag	2.16	2.24	2.05	1.98	1.97	1.86	1.56	1.56	1.59	1.62
Electron Energy Resolution	0.04	0.01	0.01	0.01	0.00	0.02	0.03	0.05	0.04	0.03
Electron Energy Scale	0.20	0.13	0.08	0.06	0.01	0.09	0.28	0.06	0.10	0.15
Electron Identification Eff.	0.70	0.57	0.34	0.36	0.09	0.46	1.28	0.43	0.36	0.45
Electron Reconstruction Eff.	0.29	0.22	0.13	0.14	0.04	0.18	0.44	0.14	0.15	0.19
Electron Trigger Eff.	0.20	0.15	0.08	0.09	0.02	0.11	0.39	0.11	0.08	0.15
Generator	2.20	1.22	3.63	4.27	3.79	4.63	2.34	1.90	1.09	3.03
I/FSR	4.28	4.08	4.38	3.73	6.00	6.94	9.71	5.37	7.06	10.58
JES B Jes Unc.	0.32	0.29	1.51	1.97	2.37	2.84	2.62	2.73	3.47	4.17
JES EffectiveNP DET1	0.54	0.05	0.31	1.15	1.68	2.01	2.30	2.94	4.82	6.10
JES EffectiveNP DET2	0.03	0.04	0.06	0.09	0.11	0.17	0.25	0.19	0.29	0.43
JES EffectiveNP MIXED1	0.07	0.04	0.05	0.08	0.13	0.29	0.39	0.21	0.78	1.73
JES EffectiveNP MIXED2	0.22	0.28	0.32	0.36	0.28	0.26	0.34	0.26	0.44	0.51
JES EffectiveNP MODEL1	1.49	1.68	1.91	2.05	2.10	2.09	1.97	2.15	2.09	1.48
JES EffectiveNP MODEL2	0.51	0.35	0.21	0.10	0.14	0.52	0.95	0.98	1.31	1.75
JES EffectiveNP MODEL3	0.51	0.32	0.15	0.13	0.31	0.61	0.83	0.91	1.11	0.60
JES EffectiveNP MODEL4	0.11	0.02	0.01	0.14	0.22	0.19	0.32	0.19	0.63	0.46
JES EffectiveNP STAT1	1.15	1.15	1.20	1.13	0.97	0.96	0.74	0.70	0.75	0.46
JES EffectiveNP STAT2	0.12	0.09	0.03	0.04	0.10	0.19	0.26	0.20	0.44	0.62
JES EffectiveNP STAT3	0.25	0.09	0.06	0.31	0.34	0.49	0.64	0.82	0.88	1.07
JES EtaIntercalibration Theory	0.30	0.55	1.09	1.82	1.99	2.14	2.49	3.03	3.43	3.92
JES EtaIntercalibration TotalStat	0.30	0.36	0.43	0.66	0.59	0.48	0.56	0.72	0.69	0.72
JES Pileup OffsetMu	0.26	0.27	0.19	0.13	0.29	0.13	0.24	0.16	0.37	0.86
JES Pileup OffsetNPV	0.11	0.21	0.22	0.19	0.18	0.26	0.37	0.22	0.53	1.21
JES RelativeNonClosure MC11b	0.24	0.19	0.27	0.32	0.31	0.49	0.56	0.46	0.69	0.51
JES SingleParticle HighPt	0.02	0.00	0.03	0.01	0.03	0.04	0.03	0.03	0.06	0.07
JES closeby	1.45	1.42	1.92	2.95	3.18	3.55	3.50	3.49	5.03	5.32
JES flavor comp	0.43	0.40	0.69	1.56	2.26	2.79	2.98	3.37	5.21	6.73
JES flavor response	0.23	0.22	0.38	0.88	1.18	1.63	1.94	2.12	2.90	4.15
JVF	1.48	1.55	1.54	1.60	1.62	1.66	1.62	1.69	1.94	2.23
Jet Eff	0.02	0.10	0.04	0.08	0.03	0.13	0.04	0.15	0.14	0.06
Jet Energy Resolution	0.97	0.75	0.40	0.31	1.16	1.50	0.50	1.28	2.51	1.93
Luminosity	1.36	1.44	1.56	1.55	1.73	1.50	1.29	1.53	1.60	1.55
MC Stats on Correction Factors	0.63	0.40	0.47	0.55	0.72	0.71	0.83	1.30	1.79	2.20
Mistag	0.99	1.01	0.86	0.89	0.96	0.91	0.80	0.79	0.96	1.22
Muon ID	0.01	0.00	0.02	0.04	0.05	0.07	0.05	0.13	0.19	0.18
Muon Identification Eff.	0.50	0.58	0.64	0.64	0.74	0.62	0.33	0.67	0.81	0.83
Muon MS	0.05	0.00	0.04	0.05	0.01	0.03	0.03	0.04	0.05	0.02
Muon Momentum Scaling	0.25	0.24	0.29	0.21	0.27	0.14	0.00	0.10	0.11	0.05
Muon Reconstruction Eff.	0.17	0.25	0.28	0.28	0.30	0.30	0.17	0.35	0.36	0.53
Muon Trigger Eff.	0.91	0.98	1.12	1.10	1.27	1.15	0.60	1.19	1.42	1.58
PDF	0.26	0.40	0.26	0.24	0.21	0.29	0.71	0.25	0.64	2.21
Parton Shower	2.53	2.98	1.12	0.73	3.24	1.74	4.37	1.76	4.15	4.50
Pileup	0.09	0.15	0.18	0.22	0.13	0.02	0.04	0.14	0.10	0.82

**Table D.6:** Relative uncertainties on the final, particle-level differential  $t\bar{t}$  cross-section as a function of the hadronic pseudo-top  $p_T$  after the channel combination. The systematic uncertainties were propagated to the final distribution using correction factors from the nominal POWHEG+PYTHIA P2011C  $t\bar{t}$  MC sample.

Bin Range	[0, 45]	[45, 90]	[90, 120]	[120, 150]	[150, 180]	[180, 220]	[220, 260]	[260, 300]	[300, 350]	[350, 800]
$d\sigma/dp_T(t)$ [fb/GeV]	11.96	28.70	32.45	25.80	17.10	10.94	5.94	3.03	1.44	0.16
Total Uncertainty [%]	9.83	8.48	8.51	9.91	12.31	11.77	14.18	16.53	18.13	20.54
Statistics [%]	2.80	1.68	1.99	2.11	3.04	3.55	3.23	4.60	6.94	10.49
Systematics [%]	9.42	8.32	8.28	9.69	11.93	11.22	13.81	15.88	16.75	17.65
Background Subtraction Unc.	2.47	1.48	1.23	1.18	1.62	1.79	1.25	1.41	2.37	3.29
Btag	4.40	4.28	4.37	4.59	4.88	4.87	5.33	6.05	6.70	6.02
Cellout	0.42	0.33	0.24	0.33	0.21	0.12	0.72	0.78	0.72	0.56
Color Reconnection	0.05	1.04	1.08	0.19	1.31	0.93	1.29	0.93	0.47	0.45
Ctag	2.11	2.22	2.08	2.02	2.03	1.93	1.61	1.39	1.63	1.24
Electron Energy Resolution	0.02	0.02	0.00	0.00	0.01	0.02	0.04	0.05	0.04	0.01
Electron Energy Scale	0.22	0.14	0.05	0.06	0.02	0.05	0.17	0.14	0.16	0.03
Electron Identification Eff.	0.86	0.57	0.22	0.32	0.16	0.22	0.81	0.83	0.72	0.13
Electron Reconstruction Eff.	0.36	0.22	0.09	0.13	0.06	0.09	0.28	0.27	0.30	0.06
Electron Trigger Eff.	0.25	0.15	0.05	0.08	0.04	0.06	0.24	0.23	0.19	0.04
Generator	3.48	1.42	2.51	3.63	3.52	4.23	4.23	4.68	1.72	0.67
I/FSR	4.72	4.19	3.78	4.51	6.66	4.48	7.83	9.55	8.07	9.43
JES B Jes Unc.	0.48	0.51	1.33	2.10	2.40	2.38	2.65	3.14	3.65	2.95
JES EffectiveNP DET1	0.46	0.18	0.39	0.94	1.59	1.77	2.51	3.23	4.92	5.44
JES EffectiveNP DET2	0.04	0.03	0.04	0.09	0.11	0.04	0.17	0.33	0.25	0.29
JES EffectiveNP MIXED1	0.06	0.01	0.01	0.09	0.15	0.17	0.42	0.56	0.89	1.40
JES EffectiveNP MIXED2	0.30	0.25	0.26	0.33	0.37	0.33	0.37	0.53	0.44	0.52
JES EffectiveNP MODEL1	1.67	1.61	1.75	2.13	2.26	2.05	2.24	2.06	2.04	1.28
JES EffectiveNP MODEL2	0.48	0.34	0.16	0.09	0.29	0.37	0.79	0.84	1.13	1.24
JES EffectiveNP MODEL3	0.50	0.33	0.12	0.12	0.37	0.42	0.79	0.80	0.75	0.69
JES EffectiveNP MODEL4	0.07	0.05	0.06	0.09	0.07	0.14	0.31	0.48	0.56	0.35
JES EffectiveNP STAT1	1.18	1.11	1.07	1.18	1.14	0.99	0.92	0.96	0.60	0.35
JES EffectiveNP STAT2	0.17	0.09	0.02	0.06	0.14	0.11	0.26	0.26	0.46	0.58
JES EffectiveNP STAT3	0.18	0.11	0.09	0.19	0.43	0.42	0.75	0.78	0.75	0.68
JES EtaIntercalibration Theory	0.32	0.39	0.81	1.50	2.17	2.52	3.06	3.14	3.56	3.32
JES EtaIntercalibration TotalStat	0.32	0.32	0.37	0.49	0.66	0.64	0.74	0.72	0.56	0.56
JES Pileup OffsetMu	0.23	0.26	0.16	0.12	0.22	0.26	0.54	0.34	0.36	0.24
JES Pileup OffsetNPV	0.14	0.08	0.19	0.29	0.23	0.37	0.41	0.41	0.69	1.16
JES RelativeNonClosure MC11b	0.21	0.19	0.19	0.31	0.52	0.54	0.69	0.59	0.53	0.49
JES SingleParticle HighPt	0.01	0.01	0.01	0.00	0.00	0.01	0.06	0.03	0.01	0.06
JES closeby	1.36	1.38	1.71	2.54	3.04	3.48	4.20	4.21	5.42	5.43
JES flavor comp	0.56	0.27	0.63	1.41	2.19	2.68	3.28	3.92	5.68	5.75
JES flavor response	0.40	0.09	0.40	0.93	1.38	1.63	1.97	2.42	3.50	3.42
JVF	1.54	1.54	1.53	1.57	1.63	1.56	1.63	1.80	1.92	2.03
Jet Eff	0.04	0.04	0.06	0.07	0.10	0.10	0.03	0.07	0.03	0.17
Jet Energy Resolution	0.80	0.91	0.39	0.32	0.96	0.79	0.87	1.70	0.53	1.54
Luminosity	1.32	1.44	1.63	1.57	1.92	1.97	1.33	1.33	1.38	1.73
MC Stats on Correction Factors	0.62	0.40	0.45	0.50	0.74	0.86	0.80	1.05	1.49	2.20
Mistag	1.11	0.96	0.85	0.86	0.84	0.80	0.86	0.96	0.92	0.55
Muon ID	0.05	0.01	0.01	0.02	0.02	0.07	0.11	0.11	0.05	0.17
Muon Identification Eff.	0.51	0.59	0.69	0.67	0.89	0.86	0.50	0.57	0.71	0.78
Muon MS	0.03	0.01	0.05	0.03	0.05	0.14	0.08	0.06	0.18	0.28
Muon Momentum Scaling	0.27	0.29	0.25	0.21	0.20	0.15	0.09	0.11	0.12	0.11
Muon Reconstruction Eff.	0.20	0.24	0.28	0.29	0.34	0.37	0.26	0.30	0.40	0.39
Muon Trigger Eff.	0.85	1.02	1.18	1.13	1.47	1.48	0.91	1.08	1.23	1.32
PDF	0.36	0.38	0.26	0.23	0.17	0.21	0.30	0.42	2.01	0.30
Parton Shower	2.78	2.76	1.68	1.45	2.16	1.00	1.79	2.48	2.99	4.80
Pileup	0.31	0.25	0.18	0.16	0.24	0.25	0.51	0.36	0.33	0.62

**Table D.7:** Relative uncertainties on the final, particle-level differential  $t\bar{t}$  cross-section as a function of the leptonic pseudo-top  $p_T$  after the channel combination. The systematic uncertainties were propagated to the final distribution using correction factors from the nominal POWHEG+PYTHIA P2011C  $t\bar{t}$  MC sample.

Bin Range	[225, 400]	[400, 500]	[500, 600]	[600, 700]	[700, 850]	[850, 1000]	[1000, 1250]	[1250, 2500]
$d\sigma/dm(t\bar{t})$ [fb/GeV]	236.95	698.83	326.14	146.55	56.57	19.07	5.66	0.34
Total Uncertainty [%]	10.97	9.56	10.38	10.90	11.83	14.09	15.12	20.35
Statistics [%]	2.57	1.61	1.83	2.97	2.88	4.57	5.43	8.56
Systematics [%]	10.66	9.42	10.22	10.48	11.47	13.33	14.11	18.46
Background Subtraction Unc.	1.37	0.90	1.51	2.00	2.29	3.15	3.59	6.03
Btag	4.83	4.41	4.39	4.56	4.76	5.00	5.26	5.66
Cellout	0.29	0.29	0.18	0.05	0.07	0.17	0.30	0.35
Color Reconnection	0.37	0.72	0.48	0.05	1.36	0.85	2.28	1.63
Ctag	2.02	1.86	1.92	2.09	2.24	2.51	2.59	2.73
Electron Energy Resolution	0.00	0.02	0.05	0.01	0.05	0.02	0.09	0.06
Electron Energy Scale	0.01	0.12	0.11	0.03	0.16	0.09	0.23	0.24
Electron Identification Eff.	0.16	0.64	0.49	0.10	0.50	0.29	0.80	0.95
Electron Reconstruction Eff.	0.07	0.27	0.19	0.04	0.19	0.11	0.31	0.29
Electron Trigger Eff.	0.04	0.16	0.13	0.03	0.13	0.07	0.20	0.23
Generator	3.24	2.46	2.77	3.32	2.37	4.59	3.02	5.19
I/FSR	3.49	5.02	4.62	4.07	5.07	6.25	5.06	9.01
JES B Jes Unc.	3.69	1.25	2.41	3.11	3.34	3.57	4.16	3.66
JES EffectiveNP DET1	2.43	0.49	1.29	1.71	2.28	2.83	3.66	4.12
JES EffectiveNP DET2	0.19	0.10	0.10	0.12	0.14	0.17	0.29	0.29
JES EffectiveNP MIXED1	0.17	0.06	0.08	0.10	0.25	0.16	0.41	0.94
JES EffectiveNP MIXED2	0.10	0.38	0.39	0.32	0.32	0.43	0.39	0.42
JES EffectiveNP MODEL1	0.31	2.09	2.36	2.08	2.08	1.97	1.59	1.55
JES EffectiveNP MODEL2	1.07	0.27	0.14	0.32	0.55	0.76	0.89	1.21
JES EffectiveNP MODEL3	1.32	0.24	0.25	0.46	0.68	0.92	0.84	0.89
JES EffectiveNP MODEL4	0.09	0.04	0.07	0.06	0.19	0.22	0.36	0.39
JES EffectiveNP STAT1	1.03	1.37	1.20	0.96	0.92	0.91	0.55	0.25
JES EffectiveNP STAT2	0.35	0.04	0.04	0.07	0.21	0.32	0.31	0.72
JES EffectiveNP STAT3	0.75	0.07	0.26	0.43	0.59	0.73	0.69	0.79
JES EtaIntercalibration Theory	1.89	0.75	1.45	2.16	3.09	3.38	4.82	7.55
JES EtaIntercalibration TotalStat	0.17	0.48	0.59	0.51	0.68	0.86	0.60	0.54
JES Pileup OffsetMu	0.30	0.34	0.08	0.28	0.25	0.34	0.21	0.71
JES Pileup OffsetNPV	0.32	0.27	0.25	0.36	0.36	0.45	0.60	0.56
JES RelativeNonClosure MC11b	0.26	0.26	0.37	0.41	0.69	0.88	0.47	0.88
JES SingleParticle HighPt	0.02	0.02	0.02	0.02	0.03	0.03	0.06	0.13
JES closeby	1.88	3.01	3.31	3.05	3.09	2.85	3.63	3.07
JES flavor comp	1.51	1.19	1.80	1.97	2.19	2.53	3.70	3.57
JES flavor response	1.02	0.64	1.05	1.11	1.34	1.52	2.39	2.25
JVF	1.53	1.49	1.52	1.57	1.72	1.91	1.87	2.31
Jet Eff	0.10	0.05	0.03	0.05	0.02	0.08	0.06	0.15
Jet Energy Resolution	4.16	0.87	0.69	1.53	1.45	1.92	2.56	0.98
Luminosity	1.69	1.39	1.46	1.88	1.46	1.60	1.36	1.35
MC Stats on Correction Factors	0.58	0.38	0.45	0.72	0.65	1.01	1.16	1.77
Mistag	0.91	0.75	0.81	0.94	1.07	1.41	1.53	2.48
Muon ID	0.03	0.01	0.03	0.04	0.04	0.01	0.09	0.01
Muon Identification Eff.	0.77	0.54	0.57	0.84	0.58	0.67	0.53	0.66
Muon MS	0.01	0.00	0.04	0.05	0.02	0.02	0.15	0.04
Muon Momentum Scaling	0.11	0.18	0.27	0.18	0.28	0.33	0.01	0.41
Muon Reconstruction Eff.	0.35	0.23	0.25	0.37	0.23	0.36	0.34	0.19
Muon Trigger Eff.	1.31	0.96	0.99	1.39	1.05	1.18	0.95	1.09
PDF	0.35	0.46	0.26	0.21	0.22	0.22	0.89	3.12
Parton Shower	0.13	2.29	3.10	1.54	2.26	1.57	0.58	0.51
Pileup	0.21	0.17	0.09	0.02	0.07	0.19	0.25	0.30

**Table D.8:** Relative uncertainties on the final, parton-level differential  $t\bar{t}$  cross-section as a function of the top-pair mass after the channel combination. The systematic uncertainties were propagated to the final distribution using correction factors from the nominal POWHEG+PYTHIA P2011C  $t\bar{t}$  MC sample.

Bin Range	[0, 25]	[25, 50]	[50, 85]	[85, 125]	[125, 500]
$d\sigma/dp_T(t\bar{t})$ [fb/GeV]	2596.03	1675.22	808.81	435.07	60.94
<b>Total Uncertainty [%]</b>	10.59	10.21	13.11	17.81	23.57
<b>Statistics [%]</b>	1.43	1.28	3.14	6.01	11.48
<b>Systematics [%]</b>	10.50	10.13	12.73	16.77	20.59
Background Subtraction Unc.	1.71	1.26	2.45	3.26	5.55
Btag	4.63	4.66	4.67	4.06	3.46
Cellout	3.53	2.64	2.97	2.98	3.36
Color Reconnection	0.31	0.49	2.40	1.98	0.38
Ctag	1.92	2.06	2.24	2.07	1.70
Electron Energy Resolution	0.00	0.00	0.01	0.07	0.14
Electron Energy Scale	0.12	0.05	0.19	0.18	0.19
Electron Identification Eff.	0.57	0.25	0.88	0.96	1.02
Electron Reconstruction Eff.	0.22	0.10	0.36	0.40	0.46
Electron Trigger Eff.	0.14	0.06	0.22	0.25	0.26
Generator	0.54	2.47	4.95	7.06	6.30
I/FSR	1.91	5.89	5.03	6.00	10.01
JES B Jes Unc.	1.29	1.29	1.25	0.92	2.04
JES EffectiveNP DET1	0.47	0.53	0.95	1.86	2.59
JES EffectiveNP DET2	0.03	0.04	0.06	0.23	0.15
JES EffectiveNP MIXED1	0.02	0.03	0.06	0.20	0.11
JES EffectiveNP MIXED2	0.22	0.26	0.35	0.41	0.52
JES EffectiveNP MODEL1	1.44	1.67	2.48	3.19	2.83
JES EffectiveNP MODEL2	0.09	0.12	0.13	0.01	0.74
JES EffectiveNP MODEL3	0.08	0.08	0.10	0.26	0.65
JES EffectiveNP MODEL4	0.04	0.06	0.08	0.14	0.20
JES EffectiveNP STAT1	0.81	0.98	1.28	1.57	1.19
JES EffectiveNP STAT2	0.06	0.05	0.00	0.12	0.15
JES EffectiveNP STAT3	0.04	0.06	0.17	0.27	0.82
JES EtaIntercalibration Theory	0.27	0.57	2.24	4.62	8.16
JES EtaIntercalibration TotalStat	0.27	0.34	0.54	1.11	0.97
JES Pileup OffsetMu	0.44	0.27	0.26	0.60	0.83
JES Pileup OffsetNPV	0.25	0.20	0.19	0.12	0.79
JES RelativeNonClosure MC11b	0.13	0.18	0.49	0.75	1.08
JES SingleParticle HighPt	0.02	0.01	0.06	0.00	0.03
JES closeby	1.56	1.79	3.05	4.79	6.69
JES flavor comp	0.68	0.88	1.95	3.88	4.77
JES flavor response	0.38	0.48	1.02	2.04	2.55
JVF	1.31	1.53	1.91	2.05	2.09
Jet Eff	0.02	0.08	0.16	0.11	0.03
Jet Energy Resolution	0.63	1.01	0.45	0.04	1.30
Luminosity	1.43	1.62	2.57	2.56	2.51
MC Stats on Correction Factors	0.33	0.33	0.73	1.40	2.81
Mistag	0.79	0.92	1.11	1.11	0.76
Muon ID	0.01	0.02	0.02	0.08	0.04
Muon Identification Eff.	0.55	0.69	1.08	1.02	0.93
Muon MS	0.01	0.02	0.04	0.01	0.05
Muon Momentum Scaling	0.21	0.24	0.41	0.30	0.22
Muon Reconstruction Eff.	0.25	0.30	0.45	0.38	0.52
Muon Trigger Eff.	1.01	1.20	1.90	1.91	1.75
PDF	0.58	0.47	0.33	0.17	4.21
Parton Shower	6.79	2.15	3.58	6.68	3.60
Pileup	2.08	1.61	1.84	1.83	1.85

**Table D.9:** Relative uncertainties on the final, parton-level differential  $t\bar{t}$  cross-section as a function of the top-pair  $p_T$  after the channel combination. The systematic uncertainties were propagated to the final distribution using correction factors from the nominal POWHEG+PYTHIA P2011C  $t\bar{t}$  MC sample.

Bin Range	[0.0, 0.1]	[0.1, 0.2]	[0.2, 0.4]	[0.4, 0.6]	[0.6, 0.7]	[0.7, 0.8]	[0.8, 1.0]	[1.0, 1.2]	[1.2, 1.6]	[1.6, 2.5]
$d\sigma/d y(t\bar{t}) $ [fb/rapidity]	150221.20	143499.08	139236.58	134795.62	120157.10	102610.50	86729.88	76696.91	49835.21	9885.04
<b>Total Uncertainty [%]</b>	9.20	8.94	9.34	9.14	10.13	10.91	11.84	10.78	12.56	27.80
<b>Statistics [%]</b>	3.37	2.37	2.57	2.32	2.55	2.55	3.01	4.27	4.61	12.58
<b>Systematics [%]</b>	8.56	8.62	8.98	8.84	9.80	10.61	11.45	9.90	11.68	24.79
Background Subtraction Unc.	1.67	1.71	1.80	1.63	1.53	1.43	1.36	1.57	1.64	2.64
Btag	4.45	4.51	4.51	4.43	4.62	4.90	5.07	4.74	4.86	6.35
Cellout	0.25	0.20	0.33	0.15	0.33	0.37	0.36	0.16	0.42	0.61
Color Reconnection	1.42	1.64	0.02	0.36	0.66	0.66	0.34	0.18	0.48	5.37
Ctag	1.98	2.03	1.99	1.98	2.08	2.10	2.10	1.82	2.06	1.78
Electron Energy Resolution	0.01	0.01	0.01	0.03	0.02	0.11	0.08	0.01	0.05	0.26
Electron Energy Scale	0.01	0.02	0.02	0.09	0.11	0.33	0.27	0.02	0.10	0.35
Electron Identification Eff.	0.08	0.10	0.09	0.39	0.46	1.13	0.95	0.08	0.33	1.82
Electron Reconstruction Eff.	0.03	0.04	0.04	0.17	0.19	0.42	0.35	0.03	0.08	0.45
Electron Trigger Eff.	0.02	0.03	0.02	0.10	0.11	0.29	0.27	0.02	0.07	0.52
Generator	3.06	0.87	2.80	2.59	1.78	3.61	3.50	2.84	5.14	2.42
I/FSR	3.24	4.17	4.65	3.92	5.65	5.71	5.83	4.12	5.66	15.76
JES B Jes Unc.	1.41	1.31	1.32	1.30	1.26	1.43	1.65	1.52	1.48	3.44
JES EffectiveNP DET1	0.76	0.71	0.66	0.73	0.76	0.85	1.21	0.77	0.92	1.45
JES EffectiveNP DET2	0.05	0.07	0.08	0.09	0.07	0.06	0.11	0.02	0.16	0.46
JES EffectiveNP MIXED1	0.06	0.04	0.03	0.08	0.08	0.17	0.14	0.01	0.07	0.07
JES EffectiveNP MIXED2	0.31	0.27	0.26	0.29	0.33	0.46	0.42	0.29	0.20	0.67
JES EffectiveNP MODEL1	1.75	1.74	1.79	1.89	2.03	1.93	2.25	1.85	1.91	2.51
JES EffectiveNP MODEL2	0.08	0.13	0.09	0.06	0.06	0.12	0.16	0.12	0.09	0.52
JES EffectiveNP MODEL3	0.02	0.08	0.13	0.07	0.01	0.11	0.13	0.01	0.03	0.59
JES EffectiveNP MODEL4	0.11	0.08	0.08	0.09	0.03	0.13	0.12	0.08	0.08	0.47
JES EffectiveNP STAT1	1.06	1.02	1.00	1.12	1.17	1.25	1.43	1.15	0.93	1.17
JES EffectiveNP STAT2	0.05	0.03	0.01	0.04	0.05	0.02	0.06	0.01	0.03	0.41
JES EffectiveNP STAT3	0.09	0.15	0.11	0.14	0.17	0.15	0.24	0.19	0.17	0.37
JES EtaIntercalibration Theory	0.37	0.76	0.79	0.91	1.40	1.76	2.46	2.26	3.50	5.70
JES EtaIntercalibration TotalStat	0.38	0.35	0.38	0.48	0.56	0.55	0.77	0.34	0.46	0.53
JES Pileup OffsetMu	0.35	0.26	0.28	0.21	0.25	0.35	0.34	0.22	0.49	0.43
JES Pileup OffsetNPV	0.21	0.13	0.24	0.25	0.15	0.25	0.30	0.30	0.08	0.52
JES RelativeNonClosure MC11b	0.02	0.16	0.25	0.41	0.32	0.39	0.73	0.33	0.64	1.07
JES SingleParticle HighPt	0.02	0.01	0.01	0.01	0.00	0.04	0.06	0.01	0.00	0.20
JES closeby	2.19	2.03	1.88	1.94	2.25	2.66	3.06	2.59	3.03	5.13
JES flavor comp	1.19	1.06	1.35	1.53	1.53	1.36	1.79	1.34	1.45	1.89
JES flavor response	0.78	0.61	0.77	0.80	0.77	0.79	1.13	0.77	0.81	0.72
JVF	1.56	1.61	1.56	1.54	1.56	1.64	1.65	1.58	1.48	2.01
Jet Eff	0.00	0.08	0.06	0.02	0.04	0.08	0.05	0.14	0.02	0.21
Jet Energy Resolution	0.78	0.48	0.25	0.37	0.74	0.60	0.83	1.24	1.85	3.99
Luminosity	1.74	1.72	1.73	1.52	1.48	1.28	1.30	1.75	1.62	1.27
MC Stats on Correction Factors	0.74	0.54	0.59	0.56	0.57	0.57	0.66	0.95	1.01	2.51
Mistag	0.87	0.91	0.95	0.86	0.85	1.02	0.98	0.94	0.94	0.81
Muon ID	0.05	0.02	0.01	0.04	0.02	0.05	0.06	0.08	0.06	0.18
Muon Identification Eff.	0.73	0.74	0.74	0.61	0.66	0.44	0.50	0.73	0.71	0.52
Muon MS	0.02	0.01	0.07	0.02	0.01	0.07	0.06	0.00	0.02	0.05
Muon Momentum Scaling	0.08	0.29	0.24	0.21	0.28	0.07	0.28	0.42	0.37	0.07
Muon Reconstruction Eff.	0.30	0.30	0.29	0.27	0.24	0.18	0.25	0.36	0.37	0.28
Muon Trigger Eff.	1.30	1.34	1.29	1.06	1.08	0.74	0.87	1.24	1.06	0.68
PDF	0.47	0.25	0.24	0.22	0.20	0.23	0.11	0.23	0.35	4.84
Parton Shower	0.78	1.89	0.92	2.57	2.41	2.35	3.28	3.30	1.38	11.63
Pileup	0.05	0.21	0.27	0.15	0.29	0.28	0.30	0.31	0.28	0.30

**Table D.10:** Relative uncertainties on the final, parton-level differential  $t\bar{t}$  cross-section as a function of the top-pair rapidity after the channel combination. The systematic uncertainties were propagated to the final distribution using correction factors from the nominal POWHEG+PYTHIA P2011C  $t\bar{t}$  MC sample.

Bin Range	[0.0, 0.4]	[0.4, 0.8]	[0.8, 1.1]	[1.1, 1.4]	[1.4, 1.8]	[1.8, 2.5]
<b>d<math>\sigma</math>/d [fb/GeV]</b>	120181.04	106866.74	87109.56	69519.51	46179.42	18639.89
<b>Total Uncertainty [%]</b>	8.71	8.78	9.35	10.28	10.24	15.12
<b>Statistics [%]</b>	1.43	1.31	1.90	2.17	2.53	5.39
<b>Systematics [%]</b>	8.60	8.68	9.15	10.05	9.93	14.13
Background Subtraction Unc.	1.52	1.22	1.30	1.14	1.17	1.57
Btag	4.47	4.56	4.73	4.74	4.86	5.56
Cellout	0.20	0.17	0.29	0.43	0.14	0.40
Color Reconnection	1.03	0.56	0.86	0.78	1.16	1.77
Ctag	2.06	2.09	1.96	1.83	1.64	1.78
Electron Energy Resolution	0.00	0.01	0.02	0.01	0.02	0.23
Electron Energy Scale	0.02	0.07	0.09	0.08	0.12	0.15
Electron Identification Eff.	0.12	0.30	0.30	0.24	0.48	0.95
Electron Reconstruction Eff.	0.05	0.12	0.11	0.06	0.15	0.29
Electron Trigger Eff.	0.03	0.08	0.07	0.05	0.11	0.25
Generator	1.81	2.68	2.83	3.72	2.76	6.08
I/FSR	4.15	4.01	4.44	4.86	4.48	7.31
JES B Jes Unc.	1.14	1.45	1.64	1.41	1.36	1.64
JES EffectiveNP DET1	0.73	0.74	0.78	0.82	0.86	1.28
JES EffectiveNP DET2	0.07	0.05	0.09	0.07	0.15	0.17
JES EffectiveNP MIXED1	0.04	0.06	0.03	0.06	0.06	0.11
JES EffectiveNP MIXED2	0.32	0.25	0.32	0.27	0.33	0.57
JES EffectiveNP MODEL1	1.79	1.87	1.89	1.84	1.92	2.43
JES EffectiveNP MODEL2	0.10	0.05	0.10	0.09	0.08	0.14
JES EffectiveNP MODEL3	0.06	0.06	0.03	0.10	0.03	0.11
JES EffectiveNP MODEL4	0.06	0.03	0.05	0.12	0.06	0.07
JES EffectiveNP STAT1	1.03	1.05	1.13	1.04	1.15	1.20
JES EffectiveNP STAT2	0.02	0.01	0.03	0.04	0.04	0.12
JES EffectiveNP STAT3	0.08	0.12	0.12	0.10	0.10	0.12
JES EtaIntercalibration Theory	0.60	1.09	1.53	2.01	2.97	4.20
JES EtaIntercalibration TotalStat	0.40	0.43	0.45	0.46	0.60	0.82
JES Pileup OffsetMu	0.22	0.24	0.21	0.17	0.19	0.36
JES Pileup OffsetNPV	0.15	0.24	0.28	0.17	0.14	0.49
JES RelativeNonClosure MC11b	0.18	0.22	0.32	0.42	0.65	0.96
JES SingleParticle HighPt	0.02	0.03	0.02	0.02	0.05	0.08
JES closeby	2.09	2.23	2.35	2.32	2.70	3.26
JES flavor comp	1.32	1.23	1.29	1.39	1.47	1.58
JES flavor response	0.75	0.75	0.73	0.72	0.83	0.75
JVF	1.57	1.55	1.59	1.61	1.62	1.70
Jet Eff	0.05	0.04	0.05	0.07	0.12	0.26
Jet Energy Resolution	0.03	0.37	0.20	0.73	1.17	1.21
Luminosity	1.31	1.09	1.22	1.17	1.00	0.95
MC Stats on Correction Factors	0.34	0.29	0.44	0.52	0.58	1.22
Mistag	0.92	0.95	0.89	0.91	0.90	0.94
Muon ID	0.01	0.02	0.02	0.04	0.01	0.03
Muon Identification Eff.	0.54	0.45	0.50	0.49	0.41	0.35
Muon MS	0.01	0.02	0.04	0.04	0.04	0.04
Muon Momentum Scaling	0.17	0.14	0.28	0.19	0.22	0.16
Muon Reconstruction Eff.	0.25	0.21	0.25	0.23	0.15	0.17
Muon Trigger Eff.	0.99	0.85	0.87	0.73	0.60	0.61
PDF	0.53	0.42	0.23	0.28	0.43	2.16
Parton Shower	2.31	1.79	1.47	3.05	2.63	3.06
Pileup	0.10	0.14	0.14	0.28	0.18	0.57

**Table D.11:** Relative uncertainties on the final, parton-level differential  $t\bar{t}$  cross-section as a function of the top rapidity after the channel combination. The systematic uncertainties were propagated to the final distribution using correction factors from the nominal POWHEG+PYTHIA P2011C  $t\bar{t}$  MC sample.

Bin Range	[0, 45]	[45, 90]	[90, 120]	[120, 150]	[150, 180]	[180, 220]	[220, 260]	[260, 300]	[300, 350]	[350, 800]
$d\sigma/d$ [fb/GeV]	527.25	1118.63	1042.81	783.90	535.32	324.08	165.99	82.86	36.65	3.99
<b>Total Uncertainty [%]</b>	8.80	8.23	8.44	9.66	11.81	11.72	14.03	13.42	17.00	19.86
<b>Statistics [%]</b>	2.14	1.22	1.63	1.58	2.16	3.07	2.54	5.52	5.37	8.03
<b>Systematics [%]</b>	8.53	8.14	8.29	9.53	11.61	11.31	13.80	12.23	16.13	18.16
Background Subtraction Unc.	1.66	1.10	1.02	0.91	1.15	1.55	0.98	1.67	1.46	2.64
Btag	4.28	4.32	4.39	4.60	4.81	4.92	5.28	5.73	6.53	6.44
Cellout	0.21	0.27	0.27	0.34	0.28	0.12	0.57	0.27	0.46	0.63
Color Reconnection	0.54	0.96	0.95	0.21	1.34	0.92	1.21	1.03	1.38	0.56
Ctag	2.14	2.23	2.07	2.00	2.00	1.92	1.60	1.55	1.61	1.36
Electron Energy Resolution	0.03	0.01	0.00	0.01	0.00	0.01	0.03	0.05	0.03	0.01
Electron Energy Scale	0.16	0.10	0.04	0.04	0.01	0.04	0.15	0.06	0.09	0.05
Electron Identification Eff.	0.56	0.40	0.19	0.24	0.09	0.20	0.68	0.42	0.40	0.17
Electron Reconstruction Eff.	0.23	0.16	0.07	0.09	0.03	0.08	0.24	0.13	0.17	0.07
Electron Trigger Eff.	0.16	0.10	0.04	0.06	0.02	0.05	0.20	0.11	0.10	0.05
Generator	2.56	1.33	2.76	3.92	3.67	4.29	3.70	1.96	1.40	1.38
I/FSR	4.40	4.14	3.91	4.16	6.29	4.83	8.36	5.47	7.55	9.78
JES B Jes Unc.	0.37	0.41	1.37	2.04	2.38	2.45	2.64	2.74	3.56	3.32
JES EffectiveNP DET1	0.52	0.12	0.37	1.03	1.64	1.80	2.45	2.95	4.87	5.64
JES EffectiveNP DET2	0.04	0.03	0.05	0.09	0.11	0.06	0.19	0.19	0.27	0.33
JES EffectiveNP MIXED1	0.07	0.02	0.02	0.09	0.13	0.18	0.41	0.22	0.83	1.50
JES EffectiveNP MIXED2	0.25	0.26	0.27	0.34	0.32	0.32	0.36	0.27	0.44	0.52
JES EffectiveNP MODEL1	1.54	1.64	1.79	2.09	2.17	2.05	2.16	2.15	2.07	1.34
JES EffectiveNP MODEL2	0.50	0.34	0.17	0.09	0.21	0.39	0.83	0.97	1.22	1.40
JES EffectiveNP MODEL3	0.50	0.33	0.13	0.12	0.34	0.45	0.80	0.91	0.93	0.66
JES EffectiveNP MODEL4	0.10	0.04	0.05	0.11	0.15	0.15	0.31	0.20	0.60	0.38
JES EffectiveNP STAT1	1.16	1.13	1.10	1.16	1.05	0.99	0.87	0.71	0.68	0.39
JES EffectiveNP STAT2	0.14	0.09	0.02	0.05	0.12	0.12	0.26	0.20	0.45	0.59
JES EffectiveNP STAT3	0.23	0.10	0.09	0.24	0.38	0.43	0.72	0.82	0.82	0.80
JES EtaIntercalibration Theory	0.31	0.46	0.87	1.64	2.07	2.47	2.90	3.03	3.49	3.50
JES EtaIntercalibration TotalStat	0.31	0.34	0.39	0.57	0.62	0.62	0.69	0.72	0.62	0.61
JES Pileup OffsetMu	0.25	0.26	0.16	0.12	0.26	0.24	0.46	0.16	0.37	0.43
JES Pileup OffsetNPV	0.12	0.14	0.20	0.25	0.20	0.35	0.40	0.22	0.61	1.17
JES RelativeNonClosure MC11b	0.23	0.19	0.21	0.31	0.41	0.54	0.65	0.47	0.61	0.49
JES SingleParticle HighPt	0.02	0.01	0.01	0.01	0.02	0.01	0.05	0.03	0.04	0.06
JES closeby	1.43	1.40	1.76	2.72	3.12	3.49	4.00	3.51	5.22	5.40
JES flavor comp	0.47	0.33	0.64	1.48	2.23	2.69	3.19	3.38	5.44	6.05
JES flavor response	0.28	0.15	0.40	0.90	1.27	1.63	1.96	2.13	3.19	3.64
JVF	1.50	1.54	1.53	1.59	1.62	1.57	1.63	1.69	1.93	2.09
Jet Eff	0.03	0.07	0.06	0.07	0.06	0.10	0.04	0.15	0.08	0.13
Jet Energy Resolution	0.92	0.84	0.39	0.32	1.07	0.89	0.77	1.29	1.54	1.66
Luminosity	1.04	1.02	1.32	1.11	1.29	1.70	1.02	1.49	1.06	1.29
MC Stats on Correction Factors	0.48	0.28	0.37	0.37	0.52	0.74	0.62	1.27	1.17	1.67
Mistag	1.03	0.98	0.85	0.87	0.91	0.82	0.84	0.79	0.94	0.75
Muon ID	0.02	0.01	0.01	0.02	0.03	0.06	0.08	0.13	0.10	0.13
Muon Identification Eff.	0.38	0.41	0.56	0.47	0.57	0.74	0.37	0.66	0.54	0.60
Muon MS	0.03	0.01	0.04	0.03	0.02	0.12	0.06	0.04	0.09	0.19
Muon Momentum Scaling	0.20	0.19	0.21	0.15	0.17	0.13	0.06	0.10	0.08	0.08
Muon Reconstruction Eff.	0.14	0.17	0.23	0.20	0.23	0.32	0.19	0.34	0.27	0.32
Muon Trigger Eff.	0.70	0.71	0.95	0.80	0.96	1.28	0.68	1.16	0.94	1.03
PDF	0.29	0.39	0.26	0.24	0.19	0.23	0.42	0.26	1.31	0.87
Parton Shower	2.60	2.86	1.56	1.13	2.76	1.10	2.51	1.78	3.59	4.71
Pileup	0.15	0.20	0.18	0.19	0.18	0.22	0.38	0.14	0.21	0.68

**Table D.12:** Relative uncertainties on the final, parton-level differential  $t\bar{t}$  cross-section as a function of the top  $p_T$  after the channel combination. The systematic uncertainties were propagated to the final distribution using correction factors from the nominal POWHEG+PYTHIA P2011C  $t\bar{t}$  MC sample.



# Appendix E.

## Additional Results

This appendix presents further final results from the analysis in chapter 6. Section E.1 shows the final unfolded distributions after dividing through by the cross-section, that is, showing the  $\frac{1}{\sigma} \frac{d\sigma}{dX}$  distributions. These figures thus compare the shape of the data distributions to the MC predictions, independent of the normalization. These are not the default results as the full cross-section distributions add information about the fiducial cross-section, and since the fiducial acceptance changing across the distributions, as shown in figures in section B. Section E.2 shows the results of the fiducial cross-section measurement after the channel combination compared against further signal MC models not included in section 6.3.

### E.1. Normalized Unfolded Results

This section presents the normalised differential cross-sections,  $\frac{1}{\sigma^{fid}} \frac{d\sigma^{fid}}{dX}$ , for the distributions  $X$  analysed in the thesis. Figures E.1 and E.2 present the individual electron and muon channels for the, respectively, pseudo-top pair and individual pseudo-top distributions. Figure E.3 and E.4 show these distributions after combination of the channels.

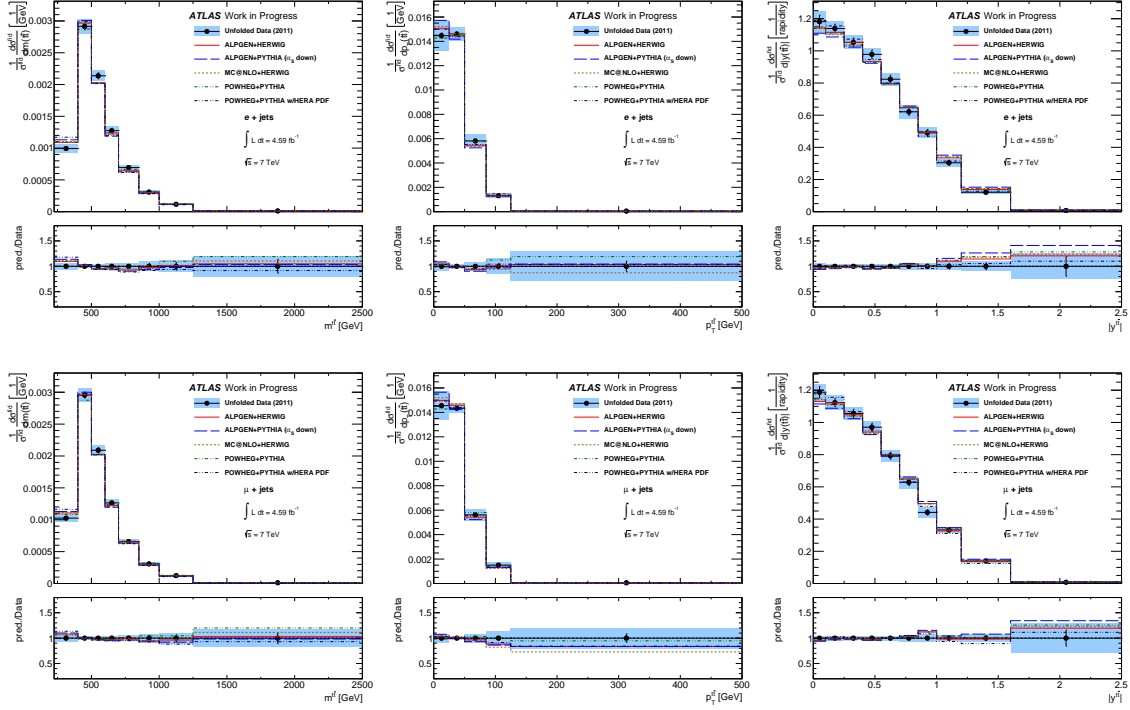


**Figure E.1:** Unfolded, corrected and normalized distributions for (left to right) the the  $m^{t\bar{t}}$ ,  $p_T^{t\bar{t}}$ ,  $|y^{t\bar{t}}|$  in the electron (top) and muon (bottom) channels.

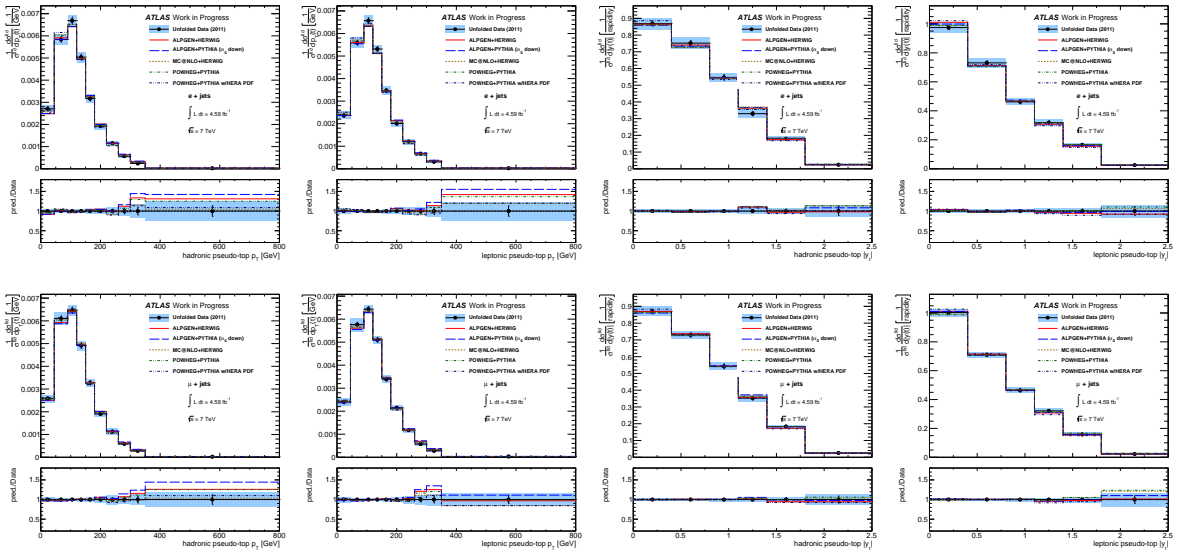


**Figure E.2:** Unfolded, corrected and normalized distributions for (left to right) the hadronic and leptonic top  $p_T$ , and the hadronic and leptonic top  $|y^t|$  in the electron (top) and muon (bottom) channels.

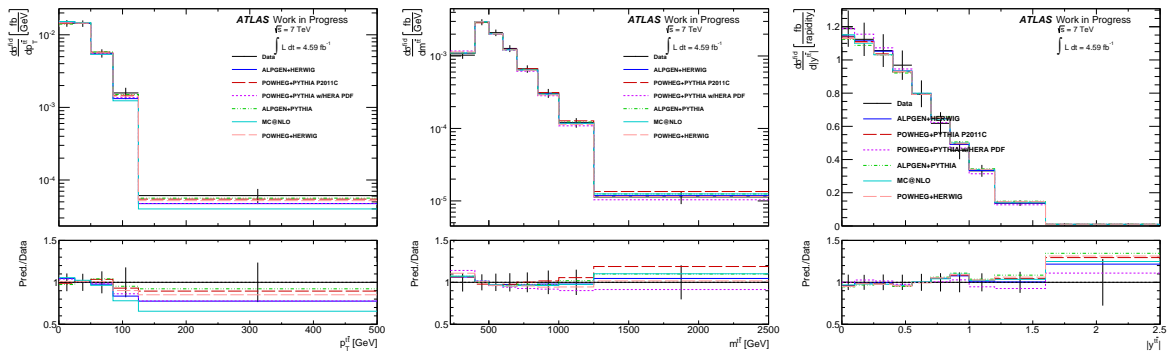


**Figure E.3:** The fiducial differential  $t\bar{t}$  cross-section for pseudo-top pair kinematics (left to right)  $p_T^{t\bar{t}}$ ,  $m^{t\bar{t}}$ , and  $|y^{t\bar{t}}|$ , after the combination of electron and muon channel results. The data points are shown with the associated combined systematic and statistical uncertainties.

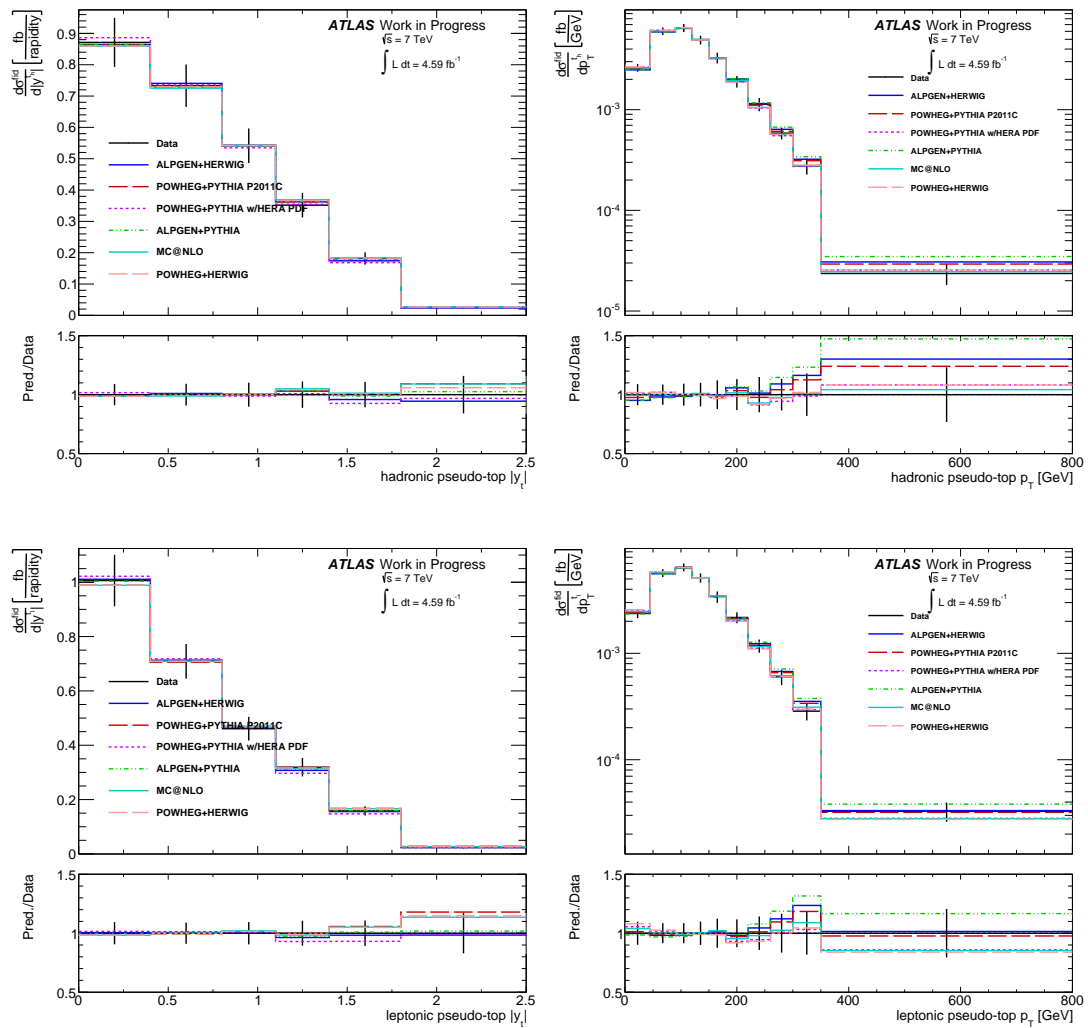


**Figure E.4:** The fiducial differential  $t\bar{t}$  cross-section for individual pseudo-top kinematics  $|y_t|$  (left) and  $p_{T,t}$  (right), for the hadronic (top) and leptonic (bottom) tops after the combination of electron and muon channel results. The data points are shown with the associated combined systematic and statistical uncertainties.

## E.2. Combination Results with Alternate Signal Models

Figures E.5 and E.6 present the combinations compared with the ALPGEN generator combined with different parton showers, and with the I/FSR up and down tunes.

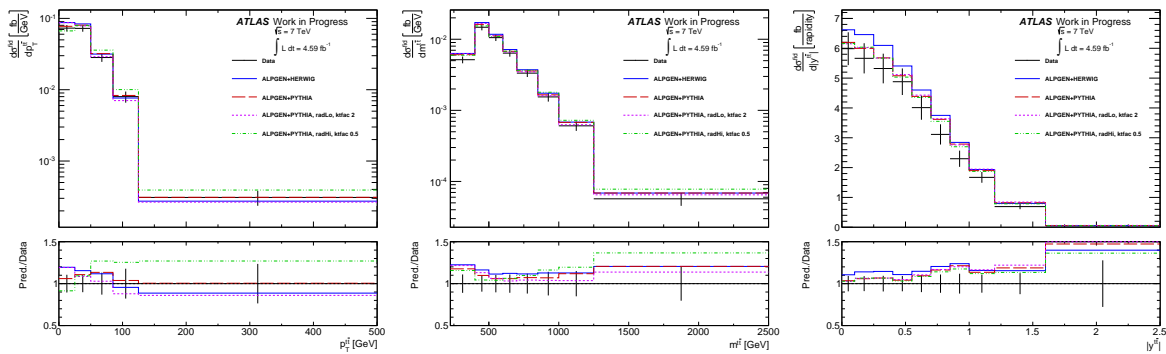


**Figure E.5:** The fiducial differential  $t\bar{t}$  cross-section for pseudo-top pair kinematics (left to right)  $p_T^{t\bar{t}}$ ,  $m^{t\bar{t}}$ , and  $|y^{t\bar{t}}|$ , after the combination of electron and muon channel results. The data points are shown with the associated combined systematic and statistical uncertainties.

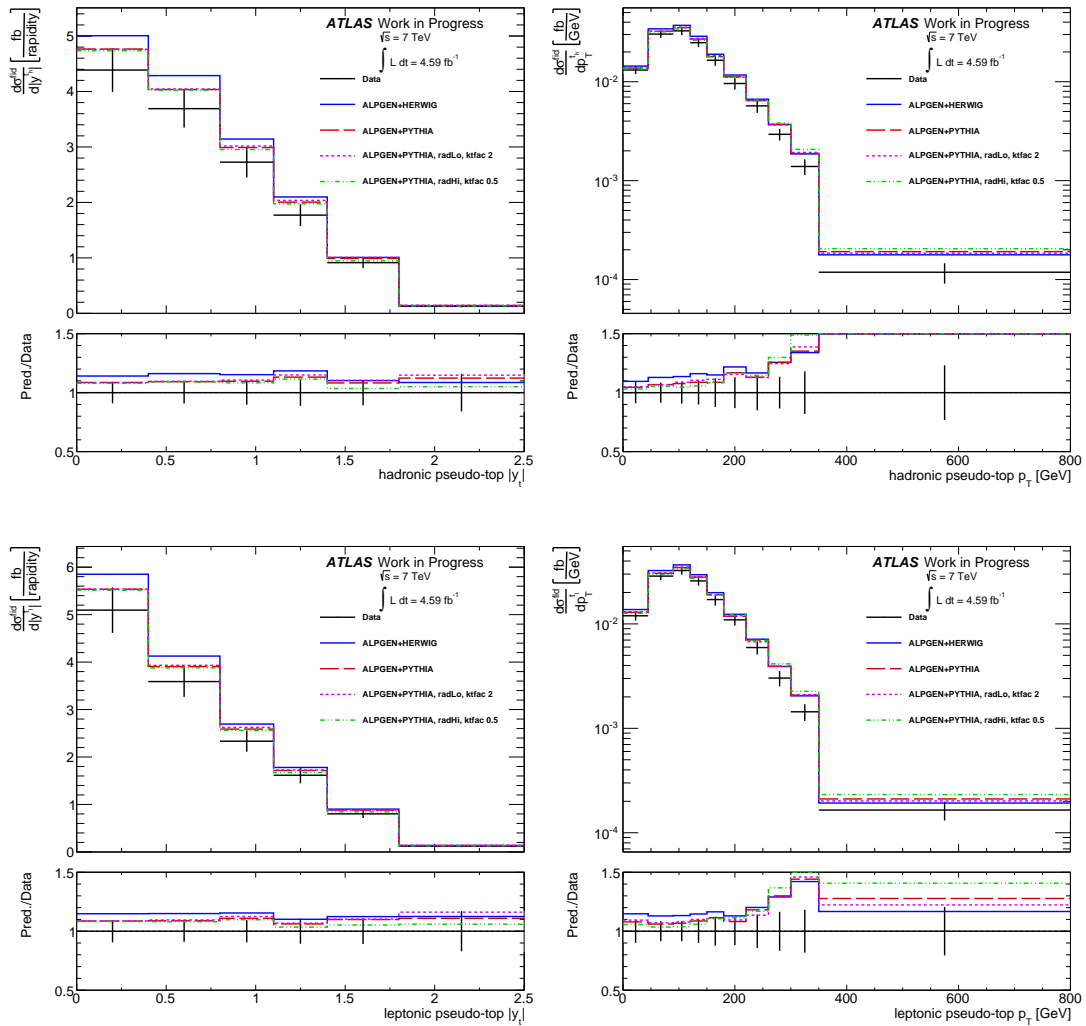


**Figure E.6:** The fiducial differential  $t\bar{t}$  cross-section for individual pseudo-top kinematics  $|y_t|$  (left) and  $p_{T,t}$  (right), for the hadronic (top) and leptonic (bottom) tops after the combination of electron and muon channel results. The data points are shown with the associated combined systematic and statistical uncertainties.





# List of Figures

2.1.	Summary of measurements of $\alpha_s$ as a function of the energy scale $Q$ . The respective degree of QCD perturbation theory used in the extraction of $\alpha_s$ is indicated in brackets. Taken from[4]. . . . .	10
2.2.	Feynman diagrams for the process $Z \rightarrow \gamma\gamma$ . . . . .	15
2.3.	Feynman diagrams for the process $K \rightarrow \mu\mu$ which illustrates the working of the GIM mechanism. . . . .	16
2.4.	Feynman diagrams for the process $B_d - \bar{B}_d$ mixing mediated by a $W$ (left) or $Z$ (right). In the Standard Model, the vertex in the right diagram does not exist. . . . .	16
2.5.	Evolution of the knowledge of the top quark mass with time. Includes fits to electroweak observables (green dots), 95% confidence limit lower bounds from $e^+e^-$ annihilation (solid line) and $p\bar{p}$ collisions (broken line), indirect lower bounds from the $W$ boson width (dot-dash line) and direct measurements from CDF (blue triangles) and D0 (red triangles). The Tevatron average is shown in magenta. Taken from[50]. . . . .	17
2.6.	Summary of the cross-sections of various physics processes at the Tevatron and the LHC. The cross-sections are plotted with respect to the centre of mass energy of the hadron collision and are shown for $p\bar{p}$ collisions below 3 TeV and for $pp$ collisions above 3 TeV. Also shown are the energies at which the Tevatron and LHC have taken data, and the expected 13 TeV LHC run in 2015, as dashed and solid (for the current data under analysis at the LHC) blue lines. Taken from[57]. . . . .	19

- 2.7. Figure showing parton distribution function  $xf(x, Q^2)$  against  $x$  for the various partons using the MSTW2008 NNLO PDF set [68, 72]. The left figure shows the PDF for  $Q^2 = 10$  GeV, and the right figure shows the PDF for  $Q^2 = 100^2$  GeV, an energy scale typical for LHC collisions. The error bands represent the 68% CL uncertainties of the fits. Figures from [73]. 22
- 2.8. Feynman diagrams for the production and decay of the top quark at hadron colliders. The top rows show the top pair production and include the decay of the top into  $W$  and  $b$  in various configurations as indicated. The bottom rows show the single top production modes. . . . . 23
- 2.9. Summary of the measurements of the top cross-section. Results given for top pair production from the Tevatron and the LHC (left) and single top production in the various sub-channels which are measured independently at ATLAS (right). Taken from [78]. . . . . 24
- 2.10. Top mass measurements from ATLAS, also including a comparison of the combination of the results from CMS and the Tevatron. Taken from [78]. . 26
- 2.11.  $W$  mass plotted versus top mass with blue (grey) contours showing the allowed mass regions at the 68% and 95% confidence level based on global fit to electroweak observables when including (excluding) the Higgs mass in the fit. The direct top and  $W$  mass measurements are always excluded from the fit. The vertical and horizontal bands (green) indicate the  $1\sigma$  regions of the direct measurements. Taken from [86] . . . . . 27
- 2.12. Top cross-section plotted versus top mass with predictions at NNLO with various PDFs with the CMS cross-section measurement shown as well as the Tevatron combined, direct pole mass measurement [87]. . . . . 27
- 3.1. Schematic drawing of the CERN accelerator complex. The protons beams are passed through the LINAC2, PSB, PS, and SPS accelerators before being injected into the LHC. Taken from [94]. . . . . 30
- 3.2. Integrated luminosity delivered and collected by ATLAS for the 2011 and 2012 runs (left) and the distribution of the average number of proton–proton interactions occurring per bunch crossing (right). Taken from [95]. . 32
- 3.3. Overview of the ATLAS detector, including most of its subsystems shown in a cut-away view. From [92] . . . . . 35

3.4. Event display of a top pair $e\text{-}\mu$ dilepton candidate with two $b$ -tagged jets. The electron is shown by the green track and calorimeter cluster in the 3D view, and the muon by the long red track intersecting the muon chambers. The two $b$ -tagged jets are shown by the purple cones, whose sizes are proportional to the jet energies. The inset shows the XY view of the vertex region, with the secondary vertices of the two $b$ -tagged jets indicated by the orange ellipses. Taken from[99] . . . . .	36
3.5. Schematic view of the ATLAS Inner Detector (ID). The diagram shows a $r - z$ slice of the cylindrical barrel, disc endcaps along with the support tubes and solenoid providing charged particle bending inside the ID. Lines of constant $\eta$ are indicated. Taken from[92]. . . . .	37
3.6. Cut-away view of the ATLAS Inner Detector in the barrel region (left) and of the entire Inner Detector (right). Taken from[92]. . . . .	38
3.7. The probability for a charged particle producing a high-threshold hit as a function of the particle's $p_T$ in the barrel (left) and end-cap (right), illustrating the electron/pion discrimination capabilities of the TRT. Taken from[104]. . . . .	40
3.8. Amount of material in the inner detector as a function of $\eta$ in terms of the radiation length (left) and interaction length (right). Taken from[92].	41
3.9. Cut-away view of the ATLAS calorimeter system. Taken from[92]. . . . .	41
3.10. Cumulative amount of material in the EM and hadronic calorimeters. The left figures show the number of radiation lengths of material before the accordions, and for each accordion layer for the barrel (leftmost) and endcap (right). The rightmost figure shows the number of interaction lengths of material before the calorimeters, for the EM calorimeter as a whole, and for the various sections of the hadronic calorimeters. Taken from[92]. . . . .	42
3.11. Figure showing the segmentation and accordion structure of the EM calorimeters. Taken from[92]. . . . .	44
3.12. Illustration of the tile calorimeter absorber/scintillator layout and the readout. Taken from[92]. . . . .	45

3.13. Illustration of the structure of the forward calorimeter. The EM calorimeter electrode in copper matrix is shown on the left, the hadronic tungsten electrodes surrounded by tungsten slugs is shown left. Taken from[92]. . . .	46
3.14. $r - \phi$ (left) and $r - z$ cross-sections of the muon detection system. . . . .	47
3.15. Muon (top) and electron (bottom) trigger rates for the 2011 data periods versus luminosity. For the muons, displayed is the L1 trigger rates for different $p_T$ thresholds (left) and the trigger rate for the EF mu18_medium stream (right) versus luminosity. For electrons, the event rates for the various EF triggers are shown versus luminosity. Taken from[111] for electrons and[112] for muons. . . . .	52
4.1. Electron reconstruction (top) and identification efficiencies with respect to the $\eta$ (bottom left) and $E_T$ (bottom right) of the electron. Note that this thesis only uses electrons satisfying the tight criteria. Taken from[117].	59
4.2. Muon reconstruction efficiencies as a function of $p_T$ . “Chain 2” refers to the refit ID and MS muons that are used in this analysis (other reconstructions used at ATLAS are not considered here). CB are combined muons that are used here; ST are “segment tagged” muons, where a ID track was not found, or the refit failed. ST muons are not used for this analysis. Taken from[119]. . . . .	61
4.3. Average number of jets in $Z \rightarrow \ell\ell$ ( $\ell = \mu, e$ ) for data and simulation, before and after a $ JVF  > 0.75$ requirement. Taken from[125]. . . . .	65
4.4. Light jet rejection factor (inverse of the probability to tag a light jet as a $b$ -jet) against $b$ -jet efficiency for the MV1 tagger used in the thesis and the component taggers. Taken from[116]. . . . .	68
4.5. Example Feynman diagrams of $W$ +jets processes which have similar topology to our $t\bar{t}$ signal. The diagram on the left shows the $W$ being produced in association with $b$ quarks; the diagram on the left shows a $W$ +jets event. . . . .	81
4.6. The fake (left) and real (right) efficiencies with respect to the muon $ \eta $ for the multijet matrix method in the muon channel, method A. The different curves show the efficiency for different leading jet $p_T$ ranges. . . . .	87

- 4.7. The fake (left) and real (right) efficiencies with respect to the muon  $|\eta|$  for the multijet matrix method in the muon channel, method B. The different curves show the efficiency for different number of jets in the event. . . . . 87
- 4.8. The fake (left) and real (right) efficiencies for the multijet matrix method in the electron channel. The efficiencies are calculated for different values of the electron's  $\eta$  and by the  $\Delta R$  between the electron and the nearest jet. 88
- 4.9. Data and MC distributions for leptonic quantities which include the lepton  $\eta$  (top) and  $p_T$  (bottom) for the electron (left) and muon (right) channels. The shown uncertainties are statistical on the data, and from the systematics as the hashed band on the Monte Carlo stack. POWHEG+PYTHIA MC is used for the signal expectation. At least two  $b$ -tags are required in the event. . . . . 90
- 4.10. Data and MC distributions for missing transverse energy quantities which include the  $E_T^{miss}$  (top) and  $m_T^W$  (bottom) for the electron (left) and muon (right) channels. The uncertainties are statistical on the data, and from the systematics as the hashed band on the Monte Carlo stack. POWHEG+PYTHIA MC is used for the signal expectation. At least two  $b$ -tags are required in the event. . . . . 91
- 4.11. Data and MC distributions for jet quantities which include the leading jet  $\eta$  (top),  $p_T$  (middle) and the number of jets (bottom) for the electron (left) and muon (right) channels. The uncertainties are statistical on the data, and from the systematics as the hashed band on the Monte Carlo stack. POWHEG+PYTHIA MC is used for the signal expectation. At least two  $b$ -tags are required in the event. . . . . 92
- 5.1. Gluon (left) and up quark (right) proton PDF uncertainty bands for  $Q^2 = 172.5 \text{ GeV}^2$  from the CT10 PDF fit[75]. Produced using[163]. . . . . 96
- 5.2. The measured gap fraction as a function of  $Q_0$ , the jet  $p_T$  threshold for additional jet activity, for  $|y| < 0.8$  (left) and  $|y| < 2.1$  (right). The measurement is compared to the ACERMC generator, where different settings of the PYTHIA parton shower parameters are used to produce samples with nominal, increased and decreased initial state radiation. From[150]. . . . . 97

- 5.3. The  $m^{t\bar{t}}$  parton-level distribution for the ALPGEN+HERWIG (left) and POWHEG+PYTHIA (right)  $t\bar{t}$  signal samples, reweighted using various PDFs. The bottom of the figures show the ratio of the varied PDFs to the MSTW2008 NLO PDF. . . . . 98
- 5.4. The  $|y^{t\bar{t}}|$  parton-level distribution for the ALPGEN+HERWIG, ALPGEN+PYTHIA, and ALPGEN+PYTHIA  $t\bar{t}$  generated with extra gluon radiation fitted to the gap analysis, both for the high radiation (radHi) and low radiation (radLo) limits. The right figure shows the various PDF distributions in ALPGEN+HERWIG  $t\bar{t}$  as for figure 5.3. The “nominal” sample used as denominator of the ratio in the lower half of the figures the is indicated by dots on the histogram in the upper half of the figures. 99
- 5.5. The top  $p_T$  parton-level distribution for the ALPGEN+HERWIG, ALPGEN+PYTHIA, and ALPGEN+PYTHIA  $t\bar{t}$  generated with extra gluon radiation fitted to the gap analysis, both for the high radiation (radHi) and low radiation (radLo) limits. The right figure shows the various PDF distributions in ALPGEN+HERWIG  $t\bar{t}$  as for figure 5.3. . . . . 99
- 5.6. The  $|y^t|$  top parton-level distribution for the ALPGEN+HERWIG, ALPGEN+PYTHIA, and ALPGEN+PYTHIA  $t\bar{t}$  generated with extra gluon radiation fitted to the gap analysis, both for the high radiation (radHi) and low radiation (radLo) limits. The right figure shows the various PDF distributions in ALPGEN+HERWIG  $t\bar{t}$  as for figure 5.3. The “nominal” sample used as denominator of the ratio in the lower half of the figures the is indicated by dots on the histogram in the upper half of the figures. 100
- 5.7. The  $p_T^{t\bar{t}}$  parton-level distribution for the ALPGEN+HERWIG, ALPGEN+PYTHIA, and ALPGEN+PYTHIA  $t\bar{t}$  generated with extra gluon radiation fitted to the gap analysis, both for the high radiation (radHi) and low radiation (radLo) limits. The right figure shows the various PDF distributions in MC@NLO+HERWIG  $t\bar{t}$  as for figure 5.3. The “nominal” sample used as denominator of the ratio in the lower half of the figures the is indicated by dots on the histogram in the upper half of the figures. . . . . 101

- 5.8. Results from the ATLAS top parton analysis, showing ratios of the NLO QCD predictions to the measured normalised differential cross-sections for different PDF sets (CT10, MSTW2008NLO, NNPDF2.3 and HERA-PDF1.5) (points) for  $p_T^t$  (top left),  $m^{t\bar{t}}$  (top right),  $p_T^{t\bar{t}}$  (bottom left), and  $|y^{t\bar{t}}|$  (bottom right). The points are slightly offset in each bin to allow for better visibility. The gray bands show the total statistical and systematic uncertainty on the unfolded distributions, while the error bars denote the uncertainties on the PDFs which include the internal PDF set variations and also fixed scale uncertainties. From[171]. . . . . 104
- 5.9. Selection efficiencies for the parton-level ATLAS analysis for the top pair mass (left) and transverse momentum (right) obtained using ALPGEN+HERWIG MC. From[171]. . . . . 105
- 5.10. The pre-tag construction in data compared with Monte Carlo predictions in the muon channel. Shown are the hadronic pseudo- $W$  mass (top, left), the hadronic pseudo-top mass (top, right) and the leptonic pseudo-top mass (bottom). POWHEG+PYTHIA is used as the top pair signal MC. The uncertainty bands show the total systematic uncertainty on the combined signal and background estimation. . . . . 111
- 5.11. The number of jets (left) and the number of tagged jets (right) in the muon channel after all  $t\bar{t}$  event selection requirements except  $b$ -tagging. . 112
- 5.12. Efficiency to completely match the pseudo-tops constructed at reconstruction and particle level as a function of the hadronic top  $p_T$  in the muon (left) and electron (right) channels. POWHEG+PYTHIA MC is used and pre-tag, single-tag and double-tag constructions are compared. . . . . 113
- 5.13. The two tag construction based on the pre-tag construction in data compared with Monte Carlo predictions in the muon channel showing the hadronic pseudo- $W$  mass (top left) and pseudo-top mass (top right) and leptonic pseudo-top mass (bottom left). POWHEG+PYTHIA is used as the signal sample. The lower right figure shows the matching efficiency between reconstruction and particle level for the semi-leptonic top pair signal for various MCs with respect to the hadronic top  $p_T$ . . . . . 114

- 5.14. Comparison of the various  $W$  hadronic mass construction techniques using the POWHEG+PYTHIA signal sample in the electron channel. The left figure shows the reconstructed mass distributions, and the right figure shows the particle-level mass distributions for the hadronic pseudo- $W$  (top) and pseudo-top (bottom). . . . . 115
- 5.15. Comparison of the various  $W$  hadronic mass construction techniques using the POWHEG+PYTHIA signal sample in the electron channel. The figures show the matching efficiency for the various constructions between the reconstruction and particle levels for the hadronic pseudo-top  $p_T$  (top left), leptonic pseudo-top  $p_T$  (top left), pseudo-top pair  $p_T$  (bottom left) and mass (bottom right). . . . . 116
- 5.16. Comparison of the various top association techniques using the POWHEG+PYTHIA signal sample in the electron channel. For all the methods, the two hardest remaining jets are associated to the hadronic  $W$ . . . . . 117
- 5.17.  $\Delta R$  between the top jet and the lepton for the parton matched top construction using the POWHEG+PYTHIA signal sample in reconstruction (left) and at particle level (right). . . . . 118
- 5.18. Comparison of the various top jet association techniques using the POWHEG+PYTHIA signal sample in the electron channel. For all the methods, the two hardest remaining jets are associated to the hadronic  $W$ . The figures show the matching efficiency for the various constructions between the reconstruction and particle levels. The bottom part of the figure shows the ratio of the method to the nominal lepton  $\Delta R$  method, which is represented as the data points in the plots. The top row shows this as a function of the hadronic (left) and leptonic (right) pseudo-top  $p_T$ , the bottom row shows the top pair  $p_T^{t\bar{t}}$  (left) and  $m^{t\bar{t}}$  (right). . . . . 119

- 5.19. The distribution of the relative difference between the particle-level pseudo-top and the parton top (left) and between the reconstruction level and particle level pseudo-top (right, i.e.) for the leptonic top rapidity in the POWHEG+PYTHIA sample for several different methods of neutrino  $p_z$  reconstruction methods. For each event in the signal sample, the  $\frac{\text{particle-parton}}{\text{parton}}$  and  $\frac{\text{particle-parton}}{\text{parton}}$  is calculated and added into the respective distribution. The ratio of a given method is given compared with the nominal imaginary part dropped if a non-real solution is found, and take the lowest  $|p_z|$  for multiple solutions method. . . . . 122
- 5.20. Reconstructed mass distributions for (left to right) the hadronic  $W$ , hadronic top, and leptonic top in the electron (top) and muon (bottom) channels. . . . . 123
- 5.21. Reconstructed distributions for (top to bottom) the the  $m^{t\bar{t}}$ ,  $p_T^{t\bar{t}}$ ,  $|y^{t\bar{t}}|$  in the electron (left) and muon (right) channels. . . . . 125
- 5.22. Reconstructed distributions for (left to right) the hadronic and leptonic top  $p_T$  in the electron (top) and muon (bottom) channels. . . . . 126
- 5.23. Reconstructed distributions for (left to right) the hadronic and leptonic top  $|y^t|$  in the electron (top) and muon (bottom) channels. . . . . 127
- 6.1. Response matrix (left) and RMS of the reconstructed pseudo-top  $m^{t\bar{t}}$  at a given particle level  $m^{t\bar{t}}$  based on the response matrix (right), for the POWHEG+PYTHIA signal in the electron channel. . . . . 136
- 6.2. The fraction of  $t\bar{t}$  signal events at particle level that are accepted at reconstruction level (left), and similarly, the parton to particle level acceptance fraction (right). The acceptances are shown as a function of the top pair  $p_T$  in the muon channel. Several  $t\bar{t}$  MC model for these quantities are compared and shown in ratio to the nominal POWHEG+PYTHIA sample (shown with points points) in the bottom of the figure. . . . . 138
- 6.3. Distributions stepping through the analysis corrections with the leptonic pseudo-top  $p_T$  in the muon channel (left) and electron channel (right) using the POWHEG+PYTHIA signal sample. The bottom of the figure shows the ratio of the particle-level leptonic pseudo-top  $p_T$  restricted to the fiducial region to the given distribution. . . . . 139

- 6.4. Unfolded and corrected distributions for (top to bottom) the the  $m^{t\bar{t}}$ ,  $p_T^{t\bar{t}}$ ,  $|y^{t\bar{t}}|$  in the electron (left) and muon (right) channels. The corrections used are derived from the POWHEG+PYTHIA  $t\bar{t}$  sample. Data points are shown with error bars for statistical uncertainties and error bands for total statistical and systematic uncertainties. . . . . 149
- 6.5. Unfolded and corrected distributions for (left to right) the hadronic and leptonic top distributions of top  $p_T^t$  in the electron (top) and muon (bottom) channels. The corrections used are derived from the POWHEG+PYTHIA  $t\bar{t}$  sample. Data points are shown with error bars for statistical uncertainties and error bands for total statistical and systematic uncertainties. . . 150
- 6.6. Unfolded and corrected distributions for (left to right) the hadronic and leptonic top distributions of top  $|y^t|$  in the electron (top) and muon (bottom) channels. The corrections used are derived from the POWHEG+PYTHIA  $t\bar{t}$  sample. Data points are shown with error bars for statistical uncertainties and error bands for total statistical and systematic uncertainties. . . 151
- 6.7. The ratio of the electron and muon channels to the output of the BLUE combination for the pseudo-top pair (top to bottom) mass,  $p_T$  and rapidity. 154
- 6.8. The ratio of the electron and muon channels to the output of the BLUE combination shown for the individual pseudo-top (top to bottom) hadronic rapidity, leptonic rapidity, hadronic  $p_T$ , and leptonic  $p_T$ . . . . . 155
- 6.9. The fiducial differential  $t\bar{t}$  cross-section for pseudo-top pair  $m^{t\bar{t}}$  after the combination of electron and muon channel results compared against several  $t\bar{t}$  models predictions, which are shown in ratio against the data in the bottom figure. The data points are shown with the associated combined systematic and statistical uncertainties. . . . . 156
- 6.10. The fiducial differential  $t\bar{t}$  cross-section for pseudo-top pair  $p_T^{t\bar{t}}$  after the combination of electron and muon channel results compared against several  $t\bar{t}$  models predictions, which are shown in ratio against the data in the bottom figure. The data points are shown with the associated combined systematic and statistical uncertainties. . . . . 157

- 6.11. The fiducial differential  $t\bar{t}$  cross-section for pseudo-top pair  $|y^{t\bar{t}}|$  after the combination of electron and muon channel results compared against several  $t\bar{t}$  models predictions, which are shown in ratio against the data in the bottom figure. The data points are shown with the associated combined systematic and statistical uncertainties. . . . . 158
- 6.12. The fiducial differential  $t\bar{t}$  cross-section for individual pseudo-top kinematics  $p_T^t$  for the hadronic top after the combination of electron and muon channel results compared against several  $t\bar{t}$  models predictions, which are shown in ratio against the data in the bottom figure. The data points are shown with the associated combined systematic and statistical uncertainties. 159
- 6.13. The fiducial differential  $t\bar{t}$  cross-section for individual pseudo-top  $p_T^t$  for the leptonic top after the combination of electron and muon channel results compared against several  $t\bar{t}$  models predictions, which are shown in ratio against the data in the bottom figure. The data points are shown with the associated combined systematic and statistical uncertainties. . . . . 160
- 6.14. The fiducial differential  $t\bar{t}$  cross-section for individual pseudo-top  $|y^t|$  for the hadronic top after the combination of electron and muon channel results. The data points are shown with the associated combined systematic and statistical uncertainties. . . . . 161
- 6.15. The fiducial differential  $t\bar{t}$  cross-section for individual pseudo-top  $|y^t|$  leptonic top after the combination of electron and muon channel results. The data points are shown with the associated combined systematic and statistical uncertainties. . . . . 162
- 6.16. The  $t\bar{t}$  production cross-section after channel combination as a function of the leptonic-hadronic pseudo-top system (a) rapidity, (b) mass and (c)  $p_T$ . The data points are shown with the total statistical and systematic uncertainties. The data are compared with the parton level analysis results normalised to be the same as our distribution. . . . . 166
- 6.17. The inclusive  $t\bar{t}$  cross-section is shown after channel combination and extrapolation to the parton level, and in comparison to several MC generator predictions. The data points are shown with the total statistical and systematic uncertainties from the particle level unfolding. No model dependence uncertainty due to the parton level extrapolation is added. . . 167

A.1. IDRES description of the Utopia layout. Pixel detectors are shown in red, and silicon strip detectors in blue. Non-active components are in grey. . .	178
A.2. Results of running IDRES over the Utopia layout. The distributions are all shown as a function of the $\eta$ of a single particle. Starting top left and going clockwise, the figures are: the number of detector hits that the particle makes (also shown with the particle $z$ position starting offset from the origin by 15 cm, the nominal interaction point spread of the upgraded LHC), the resolution of $1/p_T$ (in %) for various $p_T$ of the particle, the maximum distance between two subsequent hits, and the total detector material the particle passes through. . . . .	179
A.3. IDRES description of the Cartigny layout. Pixel detectors are shown in red, and silicon strip detectors in blue. Non-active components are in grey.	181
A.4. Results of running IDRES over the Cartigny layout. The distributions are all shown as a function of the $\eta$ of a single particle. Further description of the figure is as for figure A.2 . . . . .	181
A.5. LoI layout as input into the IDRES program. . . . .	182
A.6. Results of running IDRES over the letter of intent layout. The distributions are all shown as a function of the $\eta$ of a single particle. Further description of the figure is as for figure A.2 . . . . .	183
A.7. The material in $X_0$ as a function of $\eta$ for the LoI layout. From[195]. . . .	183
A.8. Efficiencies as a function of $\eta$ for $p_T = 100$ GeV muons, pions and electrons for the LoI layout using full detector simulation at a pileup of 140. From [195]. . . . .	184
A.9. The left figure shows the performance of $b$ -tagging in $t\bar{t}$ events, for a range of pileup levels for the LoI layout. The right figure shows the number of reconstructed primary vertex candidates as a function of the number of pileup interactions. From[195]. . . . .	184
B.1. Correction factors for the hadronic pseudo-top $p_T$ in the electron channel (top) and muon channel (middle) and response matrices (bottom) using the POWHEG+PYTHIA $t\bar{t}$ signal sample. . . . .	186

B.2. Correction factors for the leptonic pseudo-top $p_T$ in the electron channel (top) and muon channel (middle) and response matrices (bottom) using the POWHEG+PYTHIA $t\bar{t}$ signal sample. . . . .	187
B.3. Correction factors for the hadronic pseudo-top $ y^t $ in the electron channel (top) and muon channel (middle) and response matrices (bottom) using the POWHEG+PYTHIA $t\bar{t}$ signal sample. . . . .	188
B.4. Correction factors for the leptonic pseudo-top $ y^t $ in the electron channel (top) and muon channel (middle) and response matrices (bottom) using the POWHEG+PYTHIA $t\bar{t}$ signal sample. . . . .	189
B.5. Correction factors for the pseudo-top $m^{t\bar{t}}$ in the electron channel (top) and muon channel (middle) and response matrices (bottom) using the POWHEG+PYTHIA $t\bar{t}$ signal sample. . . . .	190
B.6. Correction factors for the pseudo-top $p_T^{t\bar{t}}$ in the electron channel (top) and muon channel (middle) and response matrices (bottom) using the POWHEG+PYTHIA $t\bar{t}$ signal sample. . . . .	191
B.7. Correction factors for the pseudo-top $ y^{t\bar{t}} $ in the electron channel (top) and muon channel (middle) and response matrices (bottom) using the POWHEG+PYTHIA $t\bar{t}$ signal sample. . . . .	192
B.6. Efficiency of a parton level event being inside the particle level fiducial volume. Each figure shows the muon channel on the left and the electron channel on the right. . . . .	195
B.5. Distributions obtained using the POWHEG+PYTHIA $t\bar{t}$ signal sample, showing the effect of applying each correction, in turn, on the reconstructed distribution and showing that the particle level distribution is reobtained by the correction factors. All figures display the muon channel on the left and the electron channel on the right. . . . .	198
E.1. Unfolded, corrected and normalized distributions for (left to right) the the $m^{t\bar{t}}$ , $p_T^{t\bar{t}}$ , $ y^{t\bar{t}} $ in the electron (top) and muon (bottom) channels. . . . .	230
E.2. Unfolded, corrected and normalized distributions for (left to right) the hadronic and leptonic top $p_T$ , and the hadronic and leptonic top $ y^t $ in the electron (top) and muon (bottom) channels. . . . .	230

- E.3. The fiducial differential  $t\bar{t}$  cross-section for pseudo-top pair kinematics (left to right)  $p_T^{t\bar{t}}$ ,  $m^{t\bar{t}}$ , and  $|y^{t\bar{t}}|$ , after the combination of electron and muon channel results. The data points are shown with the associated combined systematic and statistical uncertainties. . . . . 231
- E.4. The fiducial differential  $t\bar{t}$  cross-section for individual pseudo-top kinematics  $|y_t|$  (left) and  $p_{T,t}$  (right), for the hadronic (top) and leptonic (bottom) tops after the combination of electron and muon channel results. The data points are shown with the associated combined systematic and statistical uncertainties. . . . . 232
- E.5. The fiducial differential  $t\bar{t}$  cross-section for pseudo-top pair kinematics (left to right)  $p_T^{t\bar{t}}$ ,  $m^{t\bar{t}}$ , and  $|y^{t\bar{t}}|$ , after the combination of electron and muon channel results. The data points are shown with the associated combined systematic and statistical uncertainties. . . . . 233
- E.6. The fiducial differential  $t\bar{t}$  cross-section for individual pseudo-top kinematics  $|y_t|$  (left) and  $p_{T,t}$  (right), for the hadronic (top) and leptonic (bottom) tops after the combination of electron and muon channel results. The data points are shown with the associated combined systematic and statistical uncertainties. . . . . 234

# List of Tables

2.1.	The Standard Model particles[4]. Charges are in units of $e$ , the absolute value of the charge of the electron. The masses of the neutrinos are small but non-zero. The mass of the light quarks ( $u,d,s$ ) are given for the $\overline{MS}$ subtraction scheme at a scale $\mu \approx 2$ GeV. There is an anti-particle for each fermion with oppositely-signed charge and quantum numbers. Each quark is a triplet under $SU(3)$ , meaning that there are 3 fields for each quark, denoted red, blue and green. The leptons are singlets under $SU(3)$ and therefore do not experience the strong force. . . . .	9
3.1.	Typical beamline parameters for the LHC during the 2010, 2011 and 2012 data-taking compared with the nominal design parameters. . . . .	32
3.2.	General performance goals of the ATLAS detector. Note that, for high- $p_T$ muons, the muon-spectrometer performance is independent of the inner-detector system. The units for $E$ and $p_T$ are in GeV. . . . .	35
3.3.	Amount of data collected in each run period in 2011 by the ATLAS detector, determined to be of good quality and used in this thesis. Periods are merged together when there is no change in the conditions for the triggers collected in this thesis. . . . .	50
4.1.	Summary of the dataset number, process, generator, PDF, cross-section, and $k$ -factor for each signal Monte Carlo sample used. . . . .	77
4.2.	Summary of the dataset number, process, generator, PDF, cross-section, and $k$ -factor for each background Monte Carlo sample used. . . . .	78

4.3.	Table of scaling factors for the $W$ in association with $n$ jets MC samples based on the CA method. Pretag refers to the analysis selection without the requirement of any $b$ -tagged jets, tagged means the analysis selection requires at least 1 jet to be $b$ -tagged. . . . .	82
4.4.	Heavy flavour fraction scaling factors for the 2-jet bin. The scaling factors are applied to each category separately, then an additional scaling factor to all the samples so that the pretag number of events is the same as the value obtained by the charge asymmetry method. . . . .	84
4.5.	Event yields for data, MC simulation and data driven background estimates, in the electron and muon channels. The expected background yields include statistical and systematic uncertainties for each channel, while the data yield shows the statistical uncertainty. The $t\bar{t}$ prediction is from the POWHEG+PYTHIA P2011C sample and all MC samples are normalised to $4591.01 \text{ pb}^{-1}$ . . . . .	89
4.6.	Table summarising the event selections used for the analysis of this thesis.	94
6.1.	Numbers entering the simple example calculation of the measured $t\bar{t}$ cross-section. . . . .	131
6.2.	The relative statistical uncertainty on the reconstruction-level leptonic pseudo-top $p_T$ in the electron channel data. . . . .	134
6.3.	The relative statistical uncertainty on the $t\bar{t}$ production cross-section, as a function of the leptonic pseudo-top $p_T$ in the electron channel and the number of iterations used for the Bayesian unfolding. The correction factors from the nominal POWHEG+PYTHIA MC sample are used in the pseudo-experiments to derive the statistical uncertainty on the unfolded distribution. . . . .	134
6.4.	The fully corrected differential $t\bar{t}$ production cross-section, as a function of the leptonic pseudo-top $p_T$ in the electron channel and the number of iterations used for the Bayesian unfolding. The results were propagated to the final distribution using correction factors from the nominal POWHEG+PYTHIA MC sample. . . . .	135

6.5. The total (statistical $\oplus$ systematic) relative uncertainty on the differential $t\bar{t}$ production cross-section, as a function of the leptonic pseudo-top $p_T$ in the electron channel and the number of iterations used for the Bayesian unfolding. The systematic uncertainties were propagated to the final distribution using correction factors from the nominal POWHEG+PYTHIA MC sample. . . . .	135
6.6. Bin edges used in the analysis of the given kinematic distribution. . . . .	137
C.1. Relative uncertainties on the final differential $t\bar{t}$ cross-section as a function of the hadronic-leptonic pseudo-top quark system $m(t\bar{t})$ in the muon channel. The systematic uncertainties were propagated to the final distribution using correction factors from the nominal POWHEG+PYTHIA $t\bar{t}$ MC sample. . . . .	200
C.2. Relative uncertainties on the final differential $t\bar{t}$ cross-section as a function of the hadronic-leptonic pseudo-top quark system $m(t\bar{t})$ in the electron channel. The systematic uncertainties were propagated to the final distribution using correction factors from the nominal POWHEG+PYTHIA $t\bar{t}$ MC sample. . . . .	201
C.3. Relative uncertainties on the final differential $t\bar{t}$ cross-section as a function of the hadronic-leptonic pseudo-top quark system $p_T(t\bar{t})$ in the muon channel. The systematic uncertainties were propagated to the final distribution using correction factors from the nominal POWHEG+PYTHIA $t\bar{t}$ MC sample. . . . .	202
C.4. Relative uncertainties on the final differential $t\bar{t}$ cross-section as a function of the hadronic-leptonic pseudo-top quark system $p_T(t\bar{t})$ in the electron channel. The systematic uncertainties were propagated to the final distribution using correction factors from the nominal POWHEG+PYTHIA $t\bar{t}$ MC sample. . . . .	203
C.5. Relative uncertainties on the final differential $t\bar{t}$ cross-section as a function of the hadronic-leptonic pseudo-top quark system $ y(t\bar{t}) $ in the muon channel. The systematic uncertainties were propagated to the final distribution using correction factors from the nominal POWHEG+PYTHIA $t\bar{t}$ MC sample. . . . .	204

- C.6. Relative uncertainties on the final differential  $t\bar{t}$  cross-section as a function of the hadronic-leptonic pseudo-top quark system  $|y(t\bar{t})|$  in the electron channel. The systematic uncertainties were propagated to the final distribution using correction factors from the nominal POWHEG+PYTHIA  $t\bar{t}$  MC sample. . . . . 205
- C.7. Relative uncertainties on the final differential  $t\bar{t}$  cross-section as a function of the hadronic pseudo-top quark  $p_T(t)$  in the muon channel. The systematic uncertainties were propagated to the final distribution using correction factors from the nominal POWHEG+PYTHIA  $t\bar{t}$  MC sample. 206
- C.8. Relative uncertainties on the final differential  $t\bar{t}$  cross-section as a function of the hadronic pseudo-top quark  $p_T(t)$  in the electron channel. The systematic uncertainties were propagated to the final distribution using correction factors from the nominal POWHEG+PYTHIA  $t\bar{t}$  MC sample. 207
- C.9. Relative uncertainties on the final differential  $t\bar{t}$  cross-section as a function of the leptonic pseudo-top quark  $p_T(t)$  in the muon channel. The systematic uncertainties were propagated to the final distribution using correction factors from the nominal POWHEG+PYTHIA  $t\bar{t}$  MC sample. . . . . 208
- C.10. Relative uncertainties on the final differential  $t\bar{t}$  cross-section as a function of the leptonic pseudo-top quark  $p_T(t)$  in the electron channel. The systematic uncertainties were propagated to the final distribution using correction factors from the nominal POWHEG+PYTHIA  $t\bar{t}$  MC sample. 209
- C.11. Relative uncertainties on the final differential  $t\bar{t}$  cross-section as a function of the hadronic pseudo-top quark  $|y(t)|$  in the muon channel. The systematic uncertainties were propagated to the final distribution using correction factors from the nominal POWHEG+PYTHIA  $t\bar{t}$  MC sample. 210
- C.12. Relative uncertainties on the final differential  $t\bar{t}$  cross-section as a function of the hadronic pseudo-top quark  $|y(t)|$  in the electron channel. The systematic uncertainties were propagated to the final distribution using correction factors from the nominal POWHEG+PYTHIA  $t\bar{t}$  MC sample. 211
- C.13. Relative uncertainties on the final differential  $t\bar{t}$  cross-section as a function of the leptonic pseudo-top quark  $|y(t)|$  in the muon channel. The systematic uncertainties were propagated to the final distribution using correction factors from the nominal POWHEG+PYTHIA  $t\bar{t}$  MC sample. . . . . 212

- C.14. Relative uncertainties on the final differential  $t\bar{t}$  cross-section as a function of the leptonic pseudo-top quark  $|y(t)|$  in the electron channel. The systematic uncertainties were propagated to the final distribution using correction factors from the nominal POWHEG+PYTHIA  $t\bar{t}$  MC sample. 213
- D.1. Relative uncertainties on the final, particle-level differential  $t\bar{t}$  cross-section as a function of the pseudo-top pair mass after the channel combination. The systematic uncertainties were propagated to the final distribution using correction factors from the nominal POWHEG+PYTHIA P2011C  $t\bar{t}$  MC sample. . . . . 216
- D.2. Relative uncertainties on the final, particle-level differential  $t\bar{t}$  cross-section as a function of the pseudo-top pair  $p_T$  after the channel combination. The systematic uncertainties were propagated to the final distribution using correction factors from the nominal POWHEG+PYTHIA P2011C  $t\bar{t}$  MC sample. . . . . 217
- D.3. Relative uncertainties on the final, particle-level differential  $t\bar{t}$  cross-section as a function of the pseudo-top pair rapidity after the channel combination. The systematic uncertainties were propagated to the final distribution using correction factors from the nominal POWHEG+PYTHIA P2011C  $t\bar{t}$  MC sample. . . . . 218
- D.4. Relative uncertainties on the final, particle-level differential  $t\bar{t}$  cross-section as a function of the hadronic pseudo-top rapidity after the channel combination. The systematic uncertainties were propagated to the final distribution using correction factors from the nominal POWHEG+PYTHIA P2011C  $t\bar{t}$  MC sample. . . . . 219
- D.5. Relative uncertainties on the final, particle-level differential  $t\bar{t}$  cross-section as a function of the leptonic pseudo-top rapidity after the channel combination. The systematic uncertainties were propagated to the final distribution using correction factors from the nominal POWHEG+PYTHIA P2011C  $t\bar{t}$  MC sample. . . . . 220

D.6. Relative uncertainties on the final, particle-level differential $t\bar{t}$ cross-section as a function of the hadronic pseudo-top $p_T$ after the channel combination. The systematic uncertainties were propagated to the final distribution using correction factors from the nominal POWHEG+PYTHIA P2011C $t\bar{t}$ MC sample. . . . .	221
D.7. Relative uncertainties on the final, particle-level differential $t\bar{t}$ cross-section as a function of the leptonic pseudo-top $p_T$ after the channel combination. The systematic uncertainties were propagated to the final distribution using correction factors from the nominal POWHEG+PYTHIA P2011C $t\bar{t}$ MC sample. . . . .	222
D.8. Relative uncertainties on the final, parton-level differential $t\bar{t}$ cross-section as a function of the top-pair mass after the channel combination. The systematic uncertainties were propagated to the final distribution using correction factors from the nominal POWHEG+PYTHIA P2011C $t\bar{t}$ MC sample. . . . .	223
D.9. Relative uncertainties on the final, parton-level differential $t\bar{t}$ cross-section as a function of the top-pair $p_T$ after the channel combination. The systematic uncertainties were propagated to the final distribution using correction factors from the nominal POWHEG+PYTHIA P2011C $t\bar{t}$ MC sample. . . . .	224
D.10. Relative uncertainties on the final, parton-level differential $t\bar{t}$ cross-section as a function of the top-pair rapidity after the channel combination. The systematic uncertainties were propagated to the final distribution using correction factors from the nominal POWHEG+PYTHIA P2011C $t\bar{t}$ MC sample. . . . .	225
D.11. Relative uncertainties on the final, parton-level differential $t\bar{t}$ cross-section as a function of the top rapidity after the channel combination. The systematic uncertainties were propagated to the final distribution using correction factors from the nominal POWHEG+PYTHIA P2011C $t\bar{t}$ MC sample. . . . .	226

- D.12. Relative uncertainties on the final, parton-level differential  $t\bar{t}$  cross-section as a function of the top  $p_T$  after the channel combination. The systematic uncertainties were propagated to the final distribution using correction factors from the nominal POWHEG+PYTHIA P2011C  $t\bar{t}$  MC sample. . 227



# Bibliography

- [1] D. Griffiths, *Introduction to elementary particles*. Wiley. com, 2008. Cited on page 7.
- [2] M. E. Peskin, D. V. Schroeder, and E. Martinec, “An introduction to quantum field theory,” *Physics Today*, vol. 49, p. 69, 1996. Cited on page 7.
- [3] R. N. Cahn and G. Goldhaber, *The experimental foundations of particle physics*. Cambridge University Press, 2009. Cited on page 7.
- [4] J. Beringer *et al.*, “Review of Particle Physics,” *Physical Review D*, vol. 86, no. 1, 2012. Cited on pages 9, 10, 13, 25, 70, 113, 237, and 251.
- [5] S. L. Glashow, “Partial-symmetries of weak interactions,” *Nuclear Physics*, vol. 22, no. 4, pp. 579–588, 1961. Cited on page 11.
- [6] S. Weinberg, “A Model of Leptons. 1967,” *Phys. Rev. Lett*, vol. 19, p. 12641266, 1967. Cited on page 11.
- [7] A. Salam, “Elementary particle physics, ed. N. Svartholm,” in *Nobel Symposium*, no. 8, p. 367, 1968. Cited on page 11.
- [8] F. Hasert *et al.*, “Observation of neutrino-like interactions without muon or electron in the Gargamelle neutrino experiment,” *Physics Letters B*, vol. 46, no. 1, pp. 138–140, 1973. Cited on page 11.
- [9] G. Arnison *et al.*, “Experimental observation of isolated large transverse energy electrons with associated missing energy at  $s = 540 \text{ GeV}$ ,” *Physics Letters B*, vol. 122, no. 1, pp. 103–116, 1983. Cited on page 11.
- [10] G. Arnison *et al.*, “Experimental observation of lepton pairs of invariant mass around  $95 \text{ GeV}/c^2$  at the CERN SPS collider,” *Physics Letters B*, vol. 126, no. 5, pp. 398–410, 1983. Cited on page 11.

- [11] M. Banner *et al.*, “Observation of single isolated electrons of high transverse momentum in events with missing transverse energy at the CERN  $\bar{p}p$  collider,” *Physics Letters B*, vol. 122, no. 5, pp. 476–485, 1983. Cited on page 11.
- [12] P. Bagnaia *et al.*, “Evidence for  $Z^0 \rightarrow e^+e^-$  at the CERN  $\bar{p}p$  collider,” *Physics Letters B*, vol. 129, no. 1, pp. 130–140, 1983. Cited on page 11.
- [13] “Observation of a new particle in the search for the Standard Model Higgs boson with the ATLAS detector at the LHC,” *Physics Letters B*, vol. 716, no. 1, pp. 1 – 29, 2012. Cited on page 12.
- [14] “Observation of a new boson at a mass of 125 GeV with the CMS experiment at the LHC,” *Physics Letters B*, vol. 716, no. 1, pp. 30 – 61, 2012. Cited on page 12.
- [15] “Evidence for Higgs Boson Decays to the  $\tau^+\tau^-$  Final State with the ATLAS Detector,” Tech. Rep. ATLAS-CONF-2013-108, CERN, Geneva, Nov 2013. Cited on page 12.
- [16] “Evidence for the 125 GeV Higgs boson decaying to a pair of  $\tau$  leptons,” Tech. Rep. arXiv:1401.5041, CERN, Geneva, Jan 2014. Cited on page 12.
- [17] B. Aubert *et al.*, “The BABAR detector,” *Nuclear Instruments and Methods in Physics Research Section A: Accelerators, Spectrometers, Detectors and Associated Equipment*, vol. 479, no. 1, pp. 1–116, 2002. Cited on page 13.
- [18] A. Abashian *et al.*, “The Belle Detector,” *Nuclear Instruments and Methods in Physics Research Section A: Accelerators, Spectrometers, Detectors and Associated Equipment*, vol. 479, no. 1, pp. 117–232, 2002. Cited on page 13.
- [19] R. Davis Jr, D. S. Harmer, and K. C. Hoffman, “Search for neutrinos from the sun,” *Physical Review Letters*, vol. 20, no. 21, p. 1205, 1968. Cited on page 13.
- [20] Y. Fukuda *et al.*, “Evidence for Oscillation of Atmospheric Neutrinos,” *Phys. Rev. Lett.*, vol. 81, pp. 1562–1567, Aug 1998. Cited on page 13.
- [21] P. Minkowski, “ $\mu \rightarrow e\gamma$  at a rate of one out of  $10^9$  muon decays?,” *Physics Letters B*, vol. 67, pp. 421–428, Apr. 1977. Cited on page 13.
- [22] Z. Maki, M. Nakagawa, and S. Sakata, “Remarks on the unified model of elementary particles,” *Progress of Theoretical Physics*, vol. 28, no. 5, pp. 870–880, 1962. Cited on page 13.

- [23] B. Pontecorvo, “Mesonium and antimesonium,” *Zhur. Eksptl'. i Teoret. Fiz.*, vol. 33, 1957. Cited on page 13.
- [24] B. Pontecorvo, “Neutrino experiments and the problem of conservation of leptonic charge,” *Sov. Phys. JETP*, vol. 26, no. 984-988, p. 165, 1968. Cited on page 13.
- [25] A. Balantekin and W. Haxton, “Neutrino Oscillations,” *Prog.Part.Nucl.Phys.*, vol. 71, pp. 150–161, 2013. Cited on page 13.
- [26] O. Greenberg, “Resource Letter Q-1: Quarks,” *American Journal of Physics*, vol. 50, no. 12, pp. 1074–1089, 1982. Cited on page 14.
- [27] E. D. Bloom *et al.*, “High-Energy Inelastic  $e^-p$  Scattering at 6 and 10,” *Phys. Rev. Lett.*, vol. 23, pp. 930–934, Oct 1969. Cited on page 14.
- [28] M. Breidenbach *et al.*, “Observed Behavior of Highly Inelastic Electron-Proton Scattering,” *Phys. Rev. Lett.*, vol. 23, pp. 935–939, Oct 1969. Cited on page 14.
- [29] S. L. Glashow, J. Iliopoulos, and L. Maiani, “Weak Interactions with Lepton-Hadron Symmetry,” *Phys. Rev. D*, vol. 2, pp. 1285–1292, Oct 1970. Cited on page 14.
- [30] J. E. Augustin *et al.*, “Discovery of a Narrow Resonance in  $e^+e^-$  Annihilation,” *Phys. Rev. Lett.*, vol. 33, pp. 1406–1408, Dec 1974. Cited on page 14.
- [31] J. J. Aubert *et al.*, “Experimental Observation of a Heavy Particle  $J$ ,” *Phys. Rev. Lett.*, vol. 33, pp. 1404–1406, Dec 1974. Cited on page 14.
- [32] M. L. Perl *et al.*, “Evidence for Anomalous Lepton Production in  $e^+ - e^-$  Annihilation,” *Phys. Rev. Lett.*, vol. 35, pp. 1489–1492, Dec 1975. Cited on page 15.
- [33] S. Herb *et al.*, “Observation of a Dimuon Resonance at 9.5 GeV in 400-GeV Proton-Nucleus Collisions,” *Physical Review Letters*, vol. 39, no. 5, pp. 252–255, 1977. Cited on page 15.
- [34] W. R. Innes *et al.*, “Observation of Structure in the  $\Upsilon$  Region,” *Phys. Rev. Lett.*, vol. 39, pp. 1240–1242, Nov 1977. Cited on page 15.
- [35] G. L. Kane and M. E. Peskin, “A constraint from B decay on models with no t quark,” *Nuclear Physics B*, vol. 195, no. 1, pp. 29–38, 1982. Cited on page 15.
- [36] C. Matteuzzi *et al.*, “Limits on  $J/\psi$  and  $\Upsilon$  production in  $e^+e^-$  interactions at  $s =$

- 29 GeV,” *Physics Letters B*, vol. 129, no. 1, pp. 141–144, 1983. Cited on page 15.
- [37] D. Roy and S. U. Sankar, “Upper limit on  $B_d^0 - \bar{B}_d^0$  mixing as evidence for the existence of the top quark,” *Physics Letters B*, vol. 243, no. 3, pp. 296 – 300, 1990. Cited on page 16.
- [38] H. Albrecht *et al.*, “Observation of  $B^0 - \bar{B}^0$  mixing,” *Physics Letters B*, vol. 192, no. 1, pp. 245–252, 1987. Cited on page 16.
- [39] H.-J. Behrend *et al.*, “Search for new heavy quarks in  $e^+e^-$  collisions up to 46.78 GeV CM energy,” *Physics Letters B*, vol. 144, no. 3, pp. 297–301, 1984. Cited on page 16.
- [40] M. Althoff *et al.*, “Measurement of R and search for the top quark in  $e^+e^-$  annihilation between 39.8 and 45.2 GeV,” *Physics Letters B*, vol. 138, no. 5, pp. 441–448, 1984. Cited on page 16.
- [41] K. Abe *et al.*, “Measurement of R and search for new quark flavors decaying into multi-jet final states in  $e^+e^-$  collisions between 54.0 and 61.4 GeV {CM} energies,” *Physics Letters B*, vol. 234, no. 3, pp. 382 – 388, 1990. Cited on page 16.
- [42] P. Abreu *et al.*, “Search for the t and b’quarks in hadronic decays of the  $Z^0$  boson,” *Physics Letters B*, vol. 242, no. 3, pp. 536–546, 1990. Cited on page 17.
- [43] D. Decamp *et al.*, “A search for new quarks and leptons from  $Z^0$  decay at LEP,” *Physics Letters B*, vol. 236, no. 4, pp. 511–522, 1990. Cited on page 17.
- [44] M. Akrawy *et al.*, “A search for the top and b quarks in hadronic  $Z^0$  decays,” *Physics Letters B*, vol. 236, no. 3, pp. 364–374, 1990. Cited on page 17.
- [45] G. Abrams *et al.*, “Searches for new quarks and leptons produced in Z-boson decay,” *Physical review letters*, vol. 63, no. 22, p. 2447, 1989. Cited on page 17.
- [46] G. Arnison *et al.*, “Experimental observation of events with large missing transverse energy accompanied by a jet or a photon (S) in pp collisions at s= 540 GeV,” *Physics Letters B*, vol. 139, no. 1, pp. 115–125, 1984. Cited on page 17.
- [47] J.-P. Revol, “Search for the Top Quark at the CERN Proton-Antiproton Collider with UA1,” in *Sixth Workshop on Grand Unification*, vol. 1, p. 275, 1986. Cited on page 17.
- [48] C. Albajar *et al.*, “Search for new heavy quarks at the CERN proton-antiproton

- collider,” *Zeitschrift für Physik C Particles and Fields*, vol. 37, no. 4, pp. 505–525, 1988. Cited on page 17.
- [49] T. Åkesson *et al.*, “Search for top quark production at the CERN  $\bar{p}p$  collider,” *Zeitschrift für Physik C Particles and Fields*, vol. 46, no. 2, pp. 179–189, 1990. Cited on page 17.
- [50] C. Quigg, “Unanswered questions in the electroweak theory,” *arXiv preprint arXiv:0905.3187*, 2009. Cited on pages 17 and 237.
- [51] T. Group, “Design Report Tevatron 1 project,” 1984. Cited on page 17.
- [52] F. Abe *et al.*, “The CDF detector: an overview,” *Nuclear Instruments and Methods in Physics Research Section A: Accelerators, Spectrometers, Detectors and Associated Equipment*, vol. 271, no. 3, pp. 387–403, 1988. Cited on page 18.
- [53] S. Abachi *et al.*, “The DØ detector,” *Nuclear Instruments and Methods in Physics Research Section A: Accelerators, Spectrometers, Detectors and Associated Equipment*, vol. 338, no. 2, pp. 185–253, 1994. Cited on page 18.
- [54] F. Abe *et al.*, “Evidence for top quark production in  $p\bar{p}$  collisions at  $\sqrt{s} = 1.8$  TeV,” *Phys. Rev. D*, vol. 50, pp. 2966–3026, Sep 1994. Cited on page 18.
- [55] F. Abe *et al.*, “Observation of Top Quark Production in  $\bar{p}p$  Collisions with the Collider Detector at Fermilab,” *Phys. Rev. Lett.*, vol. 74, pp. 2626–2631, Apr 1995. Cited on page 18.
- [56] S. Abachi *et al.*, “Search for High Mass Top Quark Production in  $p\bar{p}$  Collisions at  $\sqrt{s} = 1.8$  TeV,” *Phys. Rev. Lett.*, vol. 74, pp. 2422–2426, Mar 1995. Cited on page 18.
- [57] W. J. Stirling. private communication. Cited on pages 19 and 237.
- [58] M. L. Mangano, “Two Lectures on QCD and Hadron Collider Physics,” *Corfu Summer Institute on Elementary Particle Physics*, 1998. Cited on page 18.
- [59] Y. L. Dokshitzer, “Calculation of the Structure Functions for Deep Inelastic Scattering and  $e^+e^-$  Annihilation by Perturbation Theory in Quantum Chromodynamics,” *Sov. Phys. JETP*, vol. 46, pp. 641–653, 1977. Cited on page 20.
- [60] V. N. Gribov and L. N. Lipatov, “Deep inelastic e p scattering in perturbation theory,” *Sov. J. Nucl. Phys.*, vol. 15, pp. 438–450, 1972. Cited on page 20.

- [61] G. Altarelli and G. Parisi, “Asymptotic freedom in parton language,” *Nuclear Physics B*, vol. 126, no. 2, pp. 298–318, 1977. Cited on page 20.
- [62] F. D. Aaron *et al.*, “Combined measurement and QCD analysis of the inclusive  $e^+p$  scattering cross sections at HERA,” *Journal of High Energy Physics*, vol. 1, p. 109, Jan. 2010. Cited on page 20.
- [63] T. Affolder *et al.*, “Measurement of the inclusive jet cross section in  $p\bar{p}$  collisions at  $\sqrt{s} = 1.8$  TeV,” *Physical Review D*, vol. 64, no. 3, p. 032001, 2001. Cited on page 20.
- [64] T. Aaltonen *et al.*, “Measurement of the inclusive jet cross section at the Fermilab Tevatron  $p\bar{p}$  collider using a cone-based jet algorithm,” *Physical Review D*, vol. 78, no. 5, p. 052006, 2008. Cited on page 20.
- [65] B. Abbott *et al.*, “Inclusive Jet Production in  $p\bar{p}$  Collisions,” *Physical Review Letters*, vol. 86, no. 9, p. 1707, 2001. Cited on page 20.
- [66] V. Abazov *et al.*, “Measurement of the Inclusive Jet Cross Section in  $p\bar{p}$  Collisions at  $\sqrt{s} = 1.96$  TeV,” *Physical Review Letters*, vol. 101, no. 6, p. 062001, 2008. Cited on page 20.
- [67] R. Placakyte, “Structure functions and PDF determination at HERA,” in *Proceedings, 48th Rencontres de Moriond on QCD and High Energy Interactions*, 2013. Cited on page 20.
- [68] A. Martin, W. Stirling, R. Thorne, and G. Watt, “Parton distributions for the LHC,” *The European Physical Journal C*, vol. 63, no. 2, pp. 189–285, 2009. Cited on pages 20, 22, 83, and 238.
- [69] M. Czakon, P. Fiedler, and A. Mitov, “Total Top-Quark Pair-Production Cross Section at Hadron Colliders Through  $\mathcal{O}(\alpha_s^4)$ ,” *Phys. Rev. Lett.*, vol. 110, p. 252004, Jun 2013. Cited on pages 21, 48, 76, and 171.
- [70] R. Bonciani, S. Catani, M. L. Mangano, and P. Nason, “Erratum to: NLL resummation of the heavy-quark hadroproduction cross-section [Nucl. Phys. B 529 (12) (1998) 424450],” *Nuclear Physics B*, vol. 803, no. 12, pp. 234 –, 2008. Cited on page 21.
- [71] M. Czakon and A. Mitov, “Top++: a program for the calculation of the top-pair cross-section at hadron colliders,” *arXiv preprint hep-ph/1112.5675*, 2011. Cited

- on pages 21 and 22.
- [72] A. Martin, W. Stirling, R. Thorne, and G. Watt, “Uncertainties on  $\alpha_S$  in global PDF analyses and implications for predicted hadronic cross sections,” *The European Physical Journal C*, vol. 64, no. 4, pp. 653–680, 2009. Cited on pages 22 and 238.
- [73] G. Watt. private communication. Cited on pages 22 and 238.
- [74] M. Botje *et al.*, “The PDF4LHC Working Group Interim Recommendations,” *arXiv preprint hep-ph/1101.0538*, 2011. Cited on page 22.
- [75] H.-L. Lai *et al.*, “New parton distributions for collider physics,” *Phys. Rev. D*, vol. 82, p. 074024, Oct 2010. Cited on pages 22, 76, 96, and 241.
- [76] J. Gao *et al.*, “The CT10 NNLO Global Analysis of QCD,” *arXiv preprint hep-ph/1302.6246*, 2013. Cited on page 22.
- [77] R. D. Ball *et al.*, “Parton distributions with {LHC} data,” *Nuclear Physics B*, vol. 867, no. 2, pp. 244 – 289, 2013. Cited on page 22.
- [78] ATLAS Collaboration, “Summary plots from the ATLAS Top physics group.” . <https://atlas.web.cern.ch/Atlas/GROUPS/PHYSICS/CombinedSummaryPlots/TOP/>. Cited on pages 24, 26, and 238.
- [79] N. Kidonakis, “Next-to-next-to-leading-order collinear and soft gluon corrections for t-channel single top quark production,” *Phys.Rev.*, vol. D83, p. 091503, 2011. Cited on page 24.
- [80] N. Kidonakis, “NNLL resummation for s-channel single top quark production,” *Phys.Rev.*, vol. D81, p. 054028, 2010. Cited on page 24.
- [81] N. Kidonakis, “Two-loop soft anomalous dimensions for single top quark associated production with a W- or H-,” *Phys.Rev.*, vol. D82, p. 054018, 2010. Cited on page 24.
- [82] F.-P. Schilling, “Top quark physics at the LHC: A review of the first two years,” *International Journal of Modern Physics A*, vol. 27, no. 17, 2012. Cited on page 25.
- [83] K. Chetyrkin *et al.*, “Second order QCD corrections to  $\Gamma(t W b)$ ,” *Physical Review D*, vol. 60, no. 11, p. 114015, 1999. Cited on page 25.
- [84] “Measurement of the  $t\bar{t}$  production cross section in the all-hadronic channel in

- ATLAS with  $\sqrt{s} = 7$  TeV data,” Tech. Rep. ATLAS-CONF-2012-031, CERN, Geneva, Mar 2012. Cited on page 25.
- [85] “Determination of the Top Quark Mass with a Template Method in the All Hadronic Decay Channel using 2.04/fb of ATLAS DATA,” Tech. Rep. ATLAS-CONF-2012-030, CERN, Geneva, Mar 2012. Cited on page 25.
- [86] M. Baak *et al.*, “The Electroweak Fit of the Standard Model after the Discovery of a New Boson at the LHC,” *arXiv:1209.2716v2 [hep-ph]*, 2012. Cited on pages 27 and 238.
- [87] CMS Collaboration, “Determination of the top-quark pole mass and strong coupling constant from the  $t\bar{t}$  production cross section in pp collisions at  $\sqrt{s} = 7$  TeV,” *arXiv preprint 1307.1907 [hep-ex]*, 2013. Cited on pages 27 and 238.
- [88] ATLAS Collaboration, “Measurement of the top quark charge in pp collisions at  $\sqrt{s} = 7$  TeV with the ATLAS detector,” *arXiv preprint 1307.4568 [hep-ex]*, 2011. Cited on page 27.
- [89] ATLAS Collaboration, “Measurement of top quark polarization in top-antitop events from proton-proton collisions at  $\sqrt{s} = 7$  TeV using the ATLAS detector,” *arXiv preprint 1307.6511 [hep-ex]*, 2013. Cited on page 28.
- [90] ATLAS Collaboration, “Observation of spin correlation in  $t\bar{t}$  events from pp collisions at  $\sqrt{s} = 7$  TeV using the ATLAS detector,” *arXiv preprint 1203.4081 [hep-ex]*, 2012. Cited on page 28.
- [91] L. Evans and P. Bryant, “LHC Machine,” *Journal of Instrumentation*, vol. 3, no. 08, p. S08001, 2008. Cited on page 29.
- [92] G. Aad *et al.*, “The ATLAS Experiment at the CERN Large Hadron Collider,” *JINST*, vol. 3, p. S08003, 2008. Cited on pages 29, 31, 35, 37, 38, 41, 42, 44, 45, 46, 238, 239, and 240.
- [93] M. Benedikt, “A walk through the LHC injector chain.” CERN Academic Training Lecture Regular Programme, 2005. <http://indico.cern.ch/conferenceDisplay.py?confId=a042795>. Cited on page 29.
- [94] Forthommel, “Map of the CERN accelerator complex.” May 2011. Cited on pages 30 and 238.
- [95] ATLAS Collaboration, “Luminosity Public Results.” . <https://twiki.cern.ch/>

- [twiki/bin/view/AtlasPublic/LuminosityPublicResults](#). Cited on pages 32 and 238.
- [96] S. Chatrchyan *et al.*, “The CMS experiment at the CERN LHC,” *JINST*, vol. 3, p. S08004, 2008. Cited on page 33.
- [97] J. Alves, A. Augusto *et al.*, “The LHCb Detector at the LHC,” *JINST*, vol. 3, p. S08005, 2008. Cited on page 33.
- [98] K. Aamodt *et al.*, “The ALICE experiment at the CERN LHC,” *JINST*, vol. 3, p. S08002, 2008. Cited on page 33.
- [99] ATLAS Collaboration, “ATLAS Stand-Alone Event Displays.” . <https://twiki.cern.ch/twiki/bin/view/AtlasPublic/EventDisplayStandAlone>. Cited on pages 36 and 239.
- [100] G. Aad *et al.*, “ATLAS pixel detector electronics and sensors,” *Journal of Instrumentation*, vol. 3, no. 07, p. P07007, 2008. Cited on page 37.
- [101] Y. Unno, “ATLAS silicon microstrip detector system (SCT),” *Nuclear Instruments and Methods in Physics Research Section A: Accelerators, Spectrometers, Detectors and Associated Equipment*, vol. 511, no. 1, pp. 58–63, 2003. Cited on page 38.
- [102] ATLAS TRT collaboration, “The ATLAS TRT Barrel Detector,” *Journal of Instrumentation*, vol. 3, no. 02, p. P02014, 2008. Cited on page 39.
- [103] E. Abat *et al.*, “The ATLAS TRT end-cap detectors,” *Journal of Instrumentation*, vol. 3, no. 10, p. P10003, 2008. Cited on page 39.
- [104] ATLAS Collaboration, “Public TRT Plots for Collision Data.” . <https://twiki.cern.ch/twiki/bin/view/AtlasPublic/TRTPublicResults>. Cited on pages 40 and 239.
- [105] ATLAS Collaboration, “Performance of the ATLAS Inner Detector Track and Vertex Reconstruction in the High Pile-Up LHC Environment,” Tech. Rep. ATLAS-CONF-2012-042, CERN, Geneva, Mar 2012. Cited on page 39.
- [106] ATLAS Collaboration, “Improved electron reconstruction in ATLAS using the Gaussian Sum Filter-based model for bremsstrahlung,” Tech. Rep. ATLAS-CONF-2012-047, CERN, Geneva, May 2012. Cited on page 40.
- [107] ATLAS Collaboration, “Electron performance measurements with the ATLAS

- detector using the 2010 LHC proton-proton collision data,” 2011. Cited on pages 43, 57, and 58.
- [108] G. Aad *et al.*, “Single hadron response measurement and calorimeter jet energy scale uncertainty with the ATLAS detector at the LHC,” *The European Physical Journal C*, vol. 73, no. 3, pp. 1–34, 2013. Cited on page 45.
- [109] “Preliminary results on the muon reconstruction efficiency, momentum resolution, and momentum scale in ATLAS 2012 pp collision data,” Tech. Rep. ATLAS-CONF-2013-088, CERN, Geneva, Aug 2013. Cited on page 48.
- [110] TOTEM Collaboration, “First measurement of the total proton-proton cross-section at the LHC energy of  $\sqrt{s} = 7\text{TeV}$ ,” *EPL (Europhysics Letters)*, vol. 96, no. 2, p. 21002, 2011. Cited on page 48.
- [111] ATLAS Collaboration, “Performance of the ATLAS Electron and Photon Trigger in p-p Collisions at  $\sqrt{s} = 7\text{TeV}$  in 2011,” tech. rep., 2012. [ATLAS-CONF-2012-048](#). Cited on pages 49, 50, 52, and 240.
- [112] ATLAS Collaboration, “Performance of the ATLAS muon trigger in 2011,” tech. rep., 2012. [ATLAS-CONF-2012-099](#). Cited on pages 52, 53, and 240.
- [113] “Performance of primary vertex reconstruction in proton-proton collisions at  $\sqrt{s} = 7\text{TeV}$  in the ATLAS experiment,” Tech. Rep. ATLAS-CONF-2010-069, CERN, Geneva, Jul 2010. Cited on page 56.
- [114] W. Waltenberger, R. Frühwirth, and P. Vanlaer, “Adaptive vertex fitting,” *Journal of Physics G: Nuclear and Particle Physics*, vol. 34, no. 12, p. N343, 2007. Cited on page 56.
- [115] W. Lampl *et al.*, “Calorimeter Clustering Algorithms: Description and Performance,” Cited on page 57.
- [116] B. Acharya *et al.*, “Object selection and calibration, background estimations and MC samples for the Autumn 2012 Top Quark analyses with 2011 data,” ATLAS-COM-PHYS-2012-1197. Cited on pages 58, 68, 85, 144, 145, and 240.
- [117] S. Heim *et al.*, “Update of Electron Efficiency Plots (Sep 2013): For Approval,” Tech. Rep. ATLAS-COM-PHYS-2013-1287, CERN, Geneva, Sep 2013. Cited on pages 59 and 240.
- [118] T. Lagouri *et al.*, “A muon identification and combined reconstruction procedure for

- the ATLAS detector at the LHC at CERN,” *Nuclear Science, IEEE Transactions on*, vol. 51, no. 6, pp. 3030–3033, 2004. Cited on page 60.
- [119] W. Spearman *et al.*, “Muon Efficiency Plots Using J/psi Tag and Probe in 2011 Data,” Tech. Rep. ATL-COM-MUON-2012-013, CERN, Geneva, May 2012. Cited on pages 61 and 240.
- [120] G. P. Salam, “Elements of QCD for hadron colliders,” *arXiv preprint arXiv:1011.5131*, 2010. Cited on page 62.
- [121] M. Cacciari, G. P. Salam, and G. Soyez, “The Anti-k(t) jet clustering algorithm,” *JHEP*, vol. 0804, p. 063, 2008. Cited on page 62.
- [122] W. Lampl *et al.*, “Calorimeter Clustering Algorithms: Description and Performance,” Tech. Rep. ATL-LARG-PUB-2008-002. ATL-COM-LARG-2008-003, CERN, Geneva, Apr 2008. Cited on page 62.
- [123] ATLAS Collaboration, “Jet energy measurement with the ATLAS detector in proton-proton collisions at  $\sqrt{s} = 7$  TeV,” *EUROPEAN PHYSICAL JOURNAL C*, vol. 73, MAR 2013. Cited on page 63.
- [124] D. W. Miller *et al.*, “Pile-up jet energy scale corrections using the jet-vertex fraction method,” Tech. Rep. ATL-COM-PHYS-2009-180, CERN, Geneva, Apr 2009. Cited on page 64.
- [125] ATLAS Collaboration, “JetEtmissApproved2011PileupOffsetAndJVF.” . <https://twiki.cern.ch/twiki/bin/view/AtlasPublic/JetEtmissApproved2011PileupOffsetAndJVF>. Cited on pages 65 and 240.
- [126] N. Makovec, “Selection of jets produced in proton-proton collisions with the ATLAS detector using 2011 data,” Tech. Rep. ATL-COM-PHYS-2012-067, CERN, Geneva, Jan 2012. Cited on page 65.
- [127] ATLAS Collaboration, “Commissioning of the ATLAS high-performance b-tagging algorithms in the 7 TeV collision data,” Tech. Rep. ATLAS-CONF-2011-102, CERN, Geneva, Jul 2011. Cited on page 66.
- [128] G. Piacquadio and C. Weiser, “A new inclusive secondary vertex algorithm for b-jet tagging in ATLAS,” in *Journal of Physics: Conference Series*, vol. 119, p. 032032, IOP Publishing, 2008. Cited on page 67.
- [129] ATLAS Collaboration, “Flavour Tagging: Analysis17.” . <https://twiki.cern>.

- [ch/twiki/bin/viewauth/AtlasProtected/Analysis17](#). Cited on page 67.
- [130] G. Aad *et al.*, “Performance of missing transverse momentum reconstruction in proton-proton collisions at  $\sqrt{s} = 7$  TeV with ATLAS,” *The European Physical Journal C*, vol. 72, no. 1, pp. 1–35, 2012. Cited on page 69.
- [131] “Measurement of the jet multiplicity in top anti-top final states produced in 7 TeV proton-proton collisions with the ATLAS detector,” Tech. Rep. ATLAS-CONF-2012-155, CERN, Geneva, Nov 2012. Cited on pages 71 and 75.
- [132] G. Aad *et al.*, “Expected performance of the ATLAS experiment-detector, trigger and physics,” *arXiv preprint arXiv:0901.0512*, 2008. Cited on page 72.
- [133] T. Sjöstrand, “Monte carlo generators,” *arXiv preprint hep-ph/0611247*, 2006. Cited on page 72.
- [134] M. L. Mangano *et al.*, “ALPGEN, a generator for hard multiparton processes in hadronic collisions,” *JHEP*, vol. 0307, p. 001, 2003. Cited on pages 73 and 75.
- [135] S. Alioli *et al.*, “A general framework for implementing NLO calculations in shower Monte Carlo programs: the POWHEG BOX,” *JHEP*, vol. 1006, p. 043, 2010. Cited on pages 73 and 75.
- [136] B. P. Kersevan and E. Richter-Was, “The Monte Carlo event generator AcerMC version 2.0 with interfaces to PYTHIA 6.2 and HERWIG 6.5,” 2004. Cited on pages 73 and 76.
- [137] S. Frixione *et al.*, “Matching NLO QCD computations and parton shower simulations,” *JHEP*, vol. 0206, p. 029, 2002. Cited on pages 73 and 76.
- [138] T. Sjostrand *et al.*, “PYTHIA 6.4 Physics and Manual,” *JHEP*, vol. 0605, p. 026, 2006. Cited on pages 73 and 76.
- [139] G. Corcella *et al.*, “HERWIG 6: An Event generator for hadron emission reactions with interfering gluons (including supersymmetric processes),” *JHEP*, vol. 0101, p. 010, 2001. Cited on pages 73 and 75.
- [140] J. Butterworth *et al.*, “Multiparton interactions in photoproduction at HERA,” *Z. Phys. C*, vol. 72, p. 637, 1996. Cited on pages 73 and 79.
- [141] G. Aad *et al.*, “The ATLAS Simulation Infrastructure,” *Eur.Phys.J.*, vol. C70, pp. 823–874, 2010. Cited on pages 73 and 79.

- [142] S. Agostinelli *et al.*, “GEANT4: A simulation toolkit,” *Nucl. Instrum. Meth. A*, vol. 506, p. 250, 2003. Cited on pages 73 and 79.
- [143] W. Lukas, “Fast simulation for atlas: Atlfast-ii and isf,” in *Journal of Physics: Conference Series*, vol. 396, p. 022031, IOP Publishing, 2012. Cited on page 74.
- [144] M. Beckingham *et al.*, “The simulation principle and performance of the ATLAS fast calorimeter simulation FastCaloSim,” Tech. Rep. ATL-PHYS-PUB-2010-013, CERN, Geneva, Oct 2010. Cited on page 74.
- [145] B. Cooper *et al.*, “Monte Carlo tuning in the presence of Matching,” 2011. Cited on pages 75 and 76.
- [146] P. Z. Skands, “Tuning Monte Carlo Generators: The Perugia Tunes,” *Phys.Rev.*, vol. D82, p. 074018, 2010. Cited on pages 75 and 76.
- [147] D. Stump *et al.*, “Inclusive jet production, parton distributions, and the search for new physics,” *JHEP*, vol. 0310, p. 046, 2003. Cited on page 75.
- [148] H. L. Lai *et al.*, “Global QCD Analysis of Parton Structure of the Nucleon: CTEQ5 Parton Distributions,” *Eur. Phys. J.*, vol. C12, pp. 375–392, 2000. Cited on page 76.
- [149] B. Cooper *et al.*, “Importance of a consistent choice of  $\alpha_s$  in the matching of AlpGen and Pythia,” *European Physical Journal C*, vol. 72, p. 2078, July 2012. Cited on page 76.
- [150] ATLAS Collaboration, “Measurement of  $t\bar{t}$  production with a veto on additional central jet activity in pp collisions at  $\sqrt{s} = 7$  TeV using the ATLAS detector,” *Eur.Phys.J.*, vol. C72, p. 2043, 2012. Cited on pages 76, 96, 97, 146, and 241.
- [151] N. Kidonakis, “Next-to-next-to-leading-order collinear and soft gluon corrections for t-channel single top quark production,” *Phys. Rev.*, vol. D83, p. 091503, 2012. Cited on page 77.
- [152] N. Kidonakis, “NNLL resummation for s-channel single top quark production,” *Phys. Rev.*, vol. D81, p. 054028, 2010. Cited on page 77.
- [153] N. Kidonakis, “Two-loop soft anomalous dimensions for single top quark associated production with a W- or H-,” *Phys. Rev.*, vol. D82, p. 054018, 2010. Cited on page 77.

- [154] J. M. Butterworth *et al.*, “Single Boson and Diboson Production Cross Sections in pp Collisions at  $\sqrt{s} = 7$  TeV.” ATLAS-CONF-2010-695, Oct 2010. Cited on page 77.
- [155] The ATLAS Collaboration, “First tuning of HERWIG/JIMMY to ATLAS data.” ATL-PHYS-PUB-2010-014, 2010. Cited on page 79.
- [156] “New ATLAS event generator tunes to 2010 data,” 2011. Cited on page 79.
- [157] G. Aad *et al.*, “Charged-particle multiplicities in pp interactions measured with the ATLAS detector at the LHC,” *New J.Phys.*, vol. 13, p. 053033, 2011. Cited on page 79.
- [158] H.L. Lai *et al.*, “New parton distributions for collider physics,” *Phys. Rev. D*, vol. 82, p. 074024, 2010. Cited on page 83.
- [159] K. Becker *et al.*, “Estimation of Fake Lepton Background for Top Analyses Using the  $\sqrt{s} = 8$  TeV Dataset,” Tech. Rep. ATL-COM-PHYS-2013-1100, CERN, Geneva, Aug 2013. Cited on page 85.
- [160] M. Guzzi *et al.*, “Top-quark pair production at hadron colliders: differential cross section and phenomenological applications with DiffTop,” *ArXiv e-prints*, June 2014. Cited on page 96.
- [161] M. Beneke *et al.*, “Inclusive top-pair production phenomenology with TOPIXS,” *Journal of High Energy Physics*, vol. 7, p. 194, July 2012. Cited on page 96.
- [162] M. Czakon *et al.*, “Constraints on the gluon PDF from top quark pair production at hadron colliders,” *Journal of High Energy Physics*, vol. 7, p. 167, July 2013. Cited on pages 96 and 171.
- [163] Durham HepData Project, “Online PDF plotting and calculation.” Oct 2013. Cited on pages 96 and 241.
- [164] J. M. Campbell, J. Huston, and W. Stirling, “Hard interactions of quarks and gluons: a primer for LHC physics,” *Reports on Progress in Physics*, vol. 70, no. 1, p. 89, 2007. Cited on pages 97 and 98.
- [165] R. Frederix and F. Maltoni, “Top pair invariant mass distribution: a window on new physics,” *Journal of High Energy Physics*, vol. 2009, no. 01, p. 047, 2009. Cited on page 101.

- [166] C. T. Hill and S. J. Parke, “Top quark production: Sensitivity to new physics,” *Phys. Rev. D*, vol. 49, pp. 4454–4462, May 1994. Cited on page 101.
- [167] T. Aaltonen *et al.*, “Measurement of the top quark forward-backward production asymmetry and its dependence on event kinematic properties,” *Phys. Rev. D*, vol. 87, p. 092002, May 2013. Cited on page 102.
- [168] V. M. Abazov *et al.*, “Forward-backward asymmetry in top quark-antiquark production,” *Phys. Rev. D*, vol. 84, p. 112005, Dec 2011. Cited on page 102.
- [169] A. collaboration *et al.*, “Measurement of the top quark pair production charge asymmetry in proton-proton collisions at 7 TeV using the ATLAS detector,” *arXiv preprint arXiv:1311.6724*, 2013. Cited on page 102.
- [170] J.-F. Arguin, “Experimental interplay between the top quark and Supersymmetry at the LHC and Tevatron,” tech. rep., ATL-COM-PHYS-2013-019, 2013. Cited on page 102.
- [171] ATLAS Collaboration, “Measurement of top-quark pair differential cross-sections in the  $l$ +jets channel in  $pp$  collisions at  $\sqrt{s} = 7$  TeV using the ATLAS detector,” Tech. Rep. ATLAS-CONF-2013-099, CERN, Geneva, Sep 2013. Cited on pages 103, 104, 105, 129, 165, and 243.
- [172] A. Buckley *et al.*, “Rivet user manual,” *arXiv:1003.0694v8 [hep-ph]*, 2013. Cited on page 106.
- [173] T. Gleisberg *et al.*, “Event generation with SHERPA 1.1,” *JHEP*, vol. 02, p. 007, 2009. Cited on page 107.
- [174] ATLAS Collaboration, “Measurement of the top quark pair production cross-section with ATLAS in  $pp$  collisions at  $\sqrt{s} = 7$  TeV in the single-lepton channel using semileptonic  $b$  decays,” Tech. Rep. ATLAS-CONF-2012-131, CERN, Geneva, Sep 2012. Cited on page 131.
- [175] G. D’Agostini, “A Multidimensional unfolding method based on Bayes’ theorem,” *Nucl. Instr. Meth.*, vol. A362, pp. 487–498, 1995. Cited on page 133.
- [176] T. Adye, “Unfolding algorithms and tests using RooUnfold.” PHYSTAT 2011, arXiv:1105.1160v1, 2011. Cited on page 133.
- [177] “Muon Momentum Resolution in First Pass Reconstruction of  $pp$  Collision Data Recorded by ATLAS in 2010,” Tech. Rep. ATLAS-CONF-2011-046, CERN, Geneva,

- Mar 2011. Cited on page 141.
- [178] “Muon reconstruction efficiency in reprocessed 2010 LHC proton-proton collision data recorded with the ATLAS detector,” Tech. Rep. ATLAS-CONF-2011-063, CERN, Geneva, Apr 2011. Cited on page 142.
- [179] N. Benekos *et al.*, “Lepton Trigger and Identification for the first *Top quark* observation,” Tech. Rep. ATL-COM-PHYS-2010-826, CERN, Geneva, Oct 2010. Supporting document for top paper’ (full list is here <https://twiki.cern.ch/twiki/bin/view/AtlasProtected/FirstTopPaper>). Cited on page 142.
- [180] N. Benekos *et al.*, “Lepton trigger and identification for the Winter 2011 top quark analyses,” Tech. Rep. ATL-COM-PHYS-2011-123, CERN, Geneva, Feb 2011. Supporting document for Winter 2011 top physics measurements. Cited on page 142.
- [181] G. Aad *et al.*, “Jet energy measurement and its systematic uncertainty in proton-proton collisions at  $\sqrt{s} = 7$  TeV with the ATLAS detector,” 2014. Cited on page 142.
- [182] G. Romeo *et al.*, “Jet Energy Resolution from In-situ Techniques with the ATLAS Detector Using Proton-Proton Collisions at a Center of Mass Energy  $\sqrt{s} = 7$  TeV,” Tech. Rep. ATL-COM-PHYS-2011-240, CERN, Geneva, Mar 2011. Cited on page 143.
- [183] B. Butler and A. Schwartzman, “Track-Jet Reconstruction and Performance,” Tech. Rep. ATL-PHYS-INT-2010-040, CERN, Geneva, Apr 2010. Cited on page 144.
- [184] “Jet energy resolution and selection efficiency relative to track jets from in-situ techniques with the ATLAS Detector Using Proton-Proton Collisions at a Center of Mass Energy  $\sqrt{s} = 7$  TeV,” Tech. Rep. ATLAS-CONF-2010-054, CERN, Geneva, Jul 2010. Cited on page 144.
- [185] G. Piacquadio, “Calibration of *b*-tagging using di-leptonic top pair events and a combinatorial likelihood approach,” Tech. Rep. ATL-COM-PHYS-2013-395, CERN, Geneva, Apr 2013. *b*-tagging calibration aiming at being approved in time for analyses to be presented at LHCP. Cited on page 145.
- [186] G. Piacquadio, “Calibration of *b*-tagging using di-leptonic top pair events applying the combinatorial likelihood approach to 2011 data,” Tech. Rep. ATL-COM-PHYS-

- 2013-1083, CERN, Geneva, Aug 2013. Cited on page 145.
- [187] “Performance of Missing Transverse Momentum Reconstruction in ATLAS with 2011 Proton-Proton Collisions at  $\sqrt{s} = 7$  TeV,” Tech. Rep. ATLAS-CONF-2012-101, CERN, Geneva, Jul 2012. Cited on page 145.
- [188] ATLAS Collaboration, “Improved Luminosity Determination in **pp** Collisions at  $\sqrt{s} = 7$  TeV using the ATLAS Detector at the LHC,” Tech. Rep. ATLAS-CONF-2012-080, CERN, Geneva, Jul 2012. Cited on page 147.
- [189] L. Lyons, D. Gibaut, and P. Clifford, “How to combine correlated estimates of a single physical quantity,” *Nuclear Instruments and Methods in Physics Research Section A: Accelerators, Spectrometers, Detectors and Associated Equipment*, vol. 270, no. 1, pp. 110–117, 1988. Cited on page 148.
- [190] A. Buckley *et al.*, “Systematic event generator tuning for the LHC,” *The European Physical Journal C*, vol. 65, no. 1-2, pp. 331–357, 2010. Cited on page 164.
- [191] ATLAS Collaboration, “Measurement of the top quark pair production cross section in the single-lepton channel with ATLAS in proton-proton collisions at 8 TeV using kinematic fits with b-tagging,” Tech. Rep. ATLAS-CONF-2012-149, CERN, Geneva, Nov 2012. Cited on page 170.
- [192] A. Clark *et al.*, “Final Report: ATLAS Phase-2 Tracker Upgrade Layout Task Force,” Tech. Rep. ATL-UPGRADE-PUB-2012-004, CERN, Geneva, Oct 2012. Cited on page 173.
- [193] M. Capeans *et al.*, “ATLAS Insertable B-Layer Technical Design Report,” Tech. Rep. CERN-LHCC-2010-013. ATLAS-TDR-19, CERN, Geneva, Sep 2010. Cited on page 174.
- [194] ATLAS Collaboration, “Letter of Intent for the Phase-I Upgrade of the ATLAS Experiment,” Tech. Rep. CERN-LHCC-2011-012. LHCC-I-020, CERN, Geneva, Nov 2011. Cited on page 174.
- [195] ATLAS Collaboration, “Letter of Intent for the Phase-II Upgrade of the ATLAS Experiment,” Tech. Rep. CERN-LHCC-2012-022. LHCC-I-023, CERN, Geneva, Dec 2012. Draft version for comments. Cited on pages 174, 176, 182, 183, 184, and 248.
- [196] ATLAS Collaboration, “The Utopia Layout Specifications.” . <https://edms.cern>.

- [ch/document/1064078](#). Cited on page 177.
- [197] N. Hessey, “The IDRES Program.” . <http://www.nikhef.nl/~r29/upgrade/idres.html>. Cited on page 177.
- [198] F. Aaron *et al.*, “Measurement of the Inclusive ep Scattering Cross Section at Low  $Q^2$  and  $x$  at HERA,” *Eur.Phys.J.*, vol. C63, pp. 625–678, 2009. Cited on page 215.